1D NANOWIRES: UNDERSTANDING GROWTH AND PROPERTIES AS STEPS TOWARD BIOMEDICAL AND ELECTRICAL APPLICATION

A Dissertation
Presented to
The Academic Faculty

by

Jenny Ruth Morber

In Partial Fulfillment
of the Requirements for the Degree
Doctor of Philosophy in the
School of Materials Science and Engineering

Georgia Institute of Technology
August 2008

1D NANOWIRES: UNDERSTANDING GROWTH AND PROPERTIES AS STEPS TOWARD BIOMEDICAL AND ELECTRICAL APPLICATION

Approved by:

Dr. Robert Snyder, Advisor
School of Materials Science and Engineering
Georgia Institute of Technology

Dr. Zhong Lin Wang, Advisor
School of Materials Science and Engineering
Georgia Institute of Technology

Dr. Valeria Milam
School of Materials Science and Engineering
Georgia Institute of Technology

Dr. Christopher Summers
School of Materials Science and Engineering
Georgia Institute of Technology

Dr. Mostafa A. El-Sayed
School of Chemistry and Biochemistry
Georgia Institute of Technology

Dr. C. P. Wong
School of Materials Science and Engineering
Georgia Institute of Technology

Date Approved: June 13, 2008

ACKNOWLEDGEMENTS

I cannot fully express the extent of my gratitude to my husband, Shaun Morber, who without whom every day would be a little darker, and without whose consistent support, I am not sure I could have finished this endeavor. I thank him for his financial assistance, which has allowed me to eat and live far better than many of my peers. I thank him also for his emotional reinforcement, for getting excited when I was excited, concerned when I was concerned, and angry when I was angry, and for listening with actual interest each evening to the minutiae of my day. I especially would like to thank him for pulling me out of those deep holes that graduate students sometimes may trip into, and for handing me back the confidence that I more than once let slip away. I am also extremely grateful that never once did he indicate that there was any career path he would not support. Because of him, I still hold fast to that childhood tenet, "You can be anything you decide to be."

I would also like to thank my father and mother. My father I thank as the first professor I knew, for showing me how one goes about doing this PhD thing, and for demonstrating to me the benefits of both loving a career and being a good parent. I thank him also for the exposure to the academic environment he provided me at a very young age. The casual experiences of growing up in a university have impacted me far greater than he could have known. My mother I thank as well, for her undying love, constant support, and strict parenting, without which I would be a different, and I believe, inferior person.

With regards to Georgia Tech, I have been here now a large part of my life and she has become both a loved and hated teacher. Still, I would like to thank those admissions people who allowed me to call myself a yellow jacket, without whose approval, my life certainly would have been very different. I would also like to thank Susan Bowman, who has more than once answered a stupid question, or helped me out of a sticky situation.

I count myself very lucky to have met and worked with so many incredible people in my research group. Among these, I would like to thank Dr. William Hughes for allowing me to pester him as a young student, and for shutting off the power in time the day I almost electrocuted myself after flooding the lab. For providing a wonderful working environment and solving many difficult equations, I thank my office mate Dr. Rusen Yang. I owe Dr. Yong Ding the highest recognition for his assistance, and thank him also for his many interesting conversations. I thank Dr. Daniel Moore for always providing alternative points of view, even if I didn't always ask for them, and later, for actually giving sound advice. And finally I owe considerable gratitude to Dr. Xudong Wang for his constant patience, abundant assistance, and great friendship.

I would not be here today if it were not for the support of my two advisers, Dr. Robert Snyder and Dr. Z.L. Wang. I would like to thank both of them for taking a chance on me as a student, for providing me the opportunity, means, space, direction, and encouragement to do my work, and helping me to achieve my personal and professional goals. I hope they feel that their gamble was worthwhile. I also thank my committee for donating the considerable time it requires to read and evaluate a thesis work. Finally, if

someone outside of those named here is reading this work, then my committee has most likely allowed me to call myself “doctor” and for that I thank them wholeheartedly.

TABLE OF CONTENTS

Page

ACKNOWLEDGEMENTS iii

LIST OF TABLES viii

LIST OF FIGURES ix

SUMMARY xvi

CHAPTER

1 INTRODUCTION 1

1.1 What is Nanotechnology? 1

1.2 Why Now? 3

1.3 Nanotechnology's Current Impact and Direction 12

1.4 Thesis Question and Motivation 18

2 ONE-DIMENSIONAL NANOSTRUCTURES 20

2.1 Definition and Types of 1D Nanostructures 20

2.2 Nanowire Synthesis and Theory 22

2.2.1 Vapor Synthesis 24

2.2.1.1 The VLS and VS processes 25

2.2.1.2 Vapor Synthesis 28

2.2.1.3 Laser Assisted Vapor Synthesis 34

2.2.2 Solution Based Synthesis 37

3 MAGNETIC IRON OXIDE NANOWIRES 39

3.1 Background 41

3.1.1 Magnetic Materials Theory 41

3.1.2 Magnetic Iron Oxide 46

3.1.2.1 Magnetic Iron Oxide Nanostructures 50
3.1.2.2 0D Magnetic Iron Oxide Nanostructures 53
3.1.2.3 Applications and Motivation for 1D Magnetic Iron Oxide Nanostructures 63
3.2 PLD Fabricated Iron Oxide Nanowires 79
3.2.1 Fabrication Method 82
3.2.2 Characterization 86
3.2.3 Properties 96
3.3 Epsilon – A Novel Iron Oxide Nanowire Phase 102
3.3.1 Epsilon Iron Oxide Background 104
3.3.2 Epsilon Iron Oxide Nanowires Characterization 109
4 CORE-SHELL ZINC OXIDE–SILICON DIOXIDE NANOWIRES 127
4.1 Background 129
4.2 Fabricated Core-Shell ZnO-SiO2 Nanowires 131
4.2.1 Fabrication Method 131
4.2.2 Characterization 132
4.2.3 Growth Mechanism 136
5 FUNDAMENTAL UNDERSTANDING OF NANOWIRE SYNTHESIS 157
6 FUTURE WORK 222
6.1 Engineering and Testing for *In Vivo* Application 222
6.2 Far Future Magnetic 1D Nanostructure Application: BCI 226
7 CONCLUSION 231
APPENDIX A: BIOLOGICAL STUDIES OF 1D NANOSTRUCTURES 234
REFERENCES 242
VITA 263

LIST OF TABLES

Page

Table 2.1: Classifying nanostructure fabrication techniques 24

Table 3.1: Table with properties of some common iron oxide phases 50

Table 3.2: Quantitative results from COMSOL simulation demonstrating greater magnetic forces in the x and z directions under application of a permanent magnet on a magnetite rod compared to a magnetite sphere of the same volume. 68

Table 3.3: Values for drag and lift coefficients calculated from the simulations shown pictorially in Figures 3.12 and 3.13. Areas of the immovable obstacles are also given.. 77

Table 5.1: Tests on gold-only systems using MMFF94 and MOE's MD software. The first column contains information on the system illustrated in Figure 5.4, while the second column contains information based on the gold box illustrated in Figure 5.5.... 184

Table 5.2: Tests on gold-only systems using MMFF94 for minimization and provided software for MD simulations. These tests were all run on the "50 atom" gold box illustrated in Figure 5.5. 185

Table 5.3: Values representing gold interaction parameters input into modeling program 187

Table 5.4: Gold-only NVT simulations using the modified empirical force field for energy minimization 189

Table 5.5: NVT simulations with Zn ions as solute, with varying solvent density and solute concentration 191

Table 5.6: NVT simulations with O^{2-} ions as solute, with varying solvent density and solute concentration 193

Table 5.7: NVT simulations with Si ions as solute, with varying solvent density and solute concentration 196

Table 5.8: NVT simulations with ZnS molecules and stoichiometric ions as solute, with varying solvent density and solute concentration 197

Table 5.9: NVT simulations with SiO molecules and stoichiometric ions as solute, with varying solvent density and solute concentration 200

LIST OF FIGURES

Page

Figure 1.1: (a) an 18th century Chinese vase, demonstrating use of red glaze pigments (b) a medieval stained glass window illustrating use of nanopowders in art glass processing (c) a magnetotatic bacteria, with internal magnetic nanoparticles clearly visible (d) a to-scale computer model of the polio virus 4

Figure 1.2: (a) A simple energy band diagram of a single free atom showing single potential energy states (b) The corresponding wider energy bands emerging in larger bulk materials in which several states at each level are possible 6

Figure 1.3: Schematic illustrating color change in a quantum dot resulting from a shift in possible energy states corresponding to size change 7

Figure 1.4: Vials containing varying sizes of CdSe quantum dots, growing larger from left to right 8

Figure 1.5: Computer generated structures of single-wall carbon nanotubes with different chiral angles between 0° and 30° 9

Figure 1.6: Graph illustrating the exponential growth of IC transistors according to Moore's Law from 1971 to 2000. 11

Figure 1.7: Conceptual graph illustrating that nanotech's slow growth period should soon be giving way to rapid development. 14

Figure 1.8: Pie chart illustrating predicted importance of nanotechnology in several key industries, according to the National Science Foundation 16

Figure 2.1: Images demonstrating nanomaterial classifications 21

Figure 2.2.: Schematic illustration of proposed VLS nanowire growth mechanism including alloying, nucleation, and axial growth stages 25

Figure 2.3: Furnace, gas flow, and pressure control systems used for vapor evaporation synthesis of 1D nanomaterials. 29

Figure 2.4: A photograph of a Themolyne 79300 Single Zone Split Tube Furnace 30

Figure 2.5: Graph illustrating thermal gradient in tube furnace at several maximum center temperatures. Distances are in centimeters. 32

Figure 2.6: Schematic of a PLD System 35

Figure 2.7: Schematic diagram of typical tube furnace PLD apparatus 36

Figure 3.1: A schematic image showing a magnetic moment arising from a single electron's spin and orbital movement. 42

Figure 3.2: A ball and stick diagram of a magnetite unit cell 47

Figure 3.3: Magnetite's "easy" axis of orientation is in the [111] direction 48

Figure 3.4: Phase diagram illustrating chemical relation between several iron oxide phases. 49

Figure 3.5: An MRI image showing the same location in the brain of a human patient before (left) and after (right) addition of magnetic nanoparticles for MRI contrast enhancement. 55

Figure 3.6: A schematic illustrating basic molecular target or cell separations with specially functionalized magnetic nanoparticles. 56

Figure 3.7: (A) Schematic illustration of magnetic nanoparticles as labels for DNA sensing. The particles are attached to a magnetic sensor via DNA hybridization. (B) Hysteresis loop of superparamagnetic particles. 56

Figure 3.8: Schematic illustrating basic steps in localized cancer treatment process 58

Figure 3.9: Schematic images illustrating traditional recording media (top) and the benefit of smaller bit sizes through perpendicular recording media (bottom) 63

Figure 3.10: Arrow plot of magnetic flux density as it acts upon magnetite material with a spherical geometry. The sidebar indicates the magnetic potential from the applied bar magnet. 67

Figure 3.11: Arrow plot of magnetic flux density as it acts upon magnetite material with a rod-like 1D geometry. The sidebar indicates the magnetic potential from the applied bar magnet. 67

Figure 3.12: Flow profiles for fluid with a Reynolds number of 20. Axes are dimensionless. Coloration shows fluid velocity variation from 0 (blue) to a maximum of 0.358 (m/s) 73

Figure 3.13: Flow profiles for fluid with a Reynolds number of 100. Axes are dimensionless. Coloration shows fluid velocity variation from 0 (blue) to a maximum of 0.358 (m/s) 75

Figure 3.14: Lift force variation in time for Reynolds 100 flow simulations. (a) Lift force plot corresponding to simulation shown in Figure 3.13 part a (b) lift force plot corresponding to the simulation shown in Figure 3.13 part b. 76

Figure 3.15: (a) Table showing tested pressure/temperature combinations and observed outcomes. Each cell represents a unique experiment. Green cells indicate combinations

that produced high-density 1D nanowire growth. Red cells indicate no or very low growth. White cells indicate untested parameter combinations or those in which results were inconclusive. All other parameters were kept constant in these experiments. (b) SEM image showing short rods synthesized at 700°C, 10 mbar. (c) SEM image showing long belts synthesized at 900°C, 10mbar. (d) SEM image displaying greater secondary growth after 120 min of laser energy exposure compared to usual 60 min growth time at 900°C, 10 mbar. (e) SEM image showing no 1D growth at 900°C, 10 mbar, without laser energy..... 83

Figure 3.16: SEM images of Mg-doped and pure iron oxide 1D nanostructures. (a) Low-magnification SEM image of aligned iron oxide nanowires doped with Mg showing local alignment along alumina crystallites. Inset shows EDS chemical signature. (b) Higher magnification SEM image showing aligned Mg-doped iron oxide nanorods. (c) SEM image showing long nanobelt structure most likely having ε-Fe2O3 microstructure, without presence of Mg. (d) SEM image showing group of aligned iron oxide nanowires with Mg absent..... 88

Figure 3.17: TEM data on magnetite and hematite nanostructures. (a) Low-magnification bright field TEM image of magnetite nanowire. (b) High-resolution TEM image of nanowire taken from the side edge of the wire in (a), illustrating high-quality single-crystalline nature of the wire. (c) Low-magnification bright field TEM image of hematite nanorods with Au particle tips. (d) Electron diffraction image taken from dark rod in previous image shows single-crystalline nature of the rod. (e) High-magnification TEM image of the section outlined in (c), showing well ordered structure and very little amorphous material on the nanorod surface. 91

Figure 3.18: XRD data taken from samples grown at 800°C, 10 mbar, and 750°C 10 mbar, respectively. (a) XRD signal from grazing incidence measurements of iron oxide nanobelts and nanowires grown on polycrystalline alumina. (b) Similar measurements on iron oxide nanostructures grown on a *c*-plane sapphire substrate. 94

Figure 3.19: Magnetic hysteresis behavior of iron oxide nanostructures grown at 700oC, measured with SQUID. (a) M-H loop at 300K showing ferromagnetic behavior and wasp-waist shape most likely derived from multi-phase nature of sample. (b) M-H loop at 5K with low-field region expanded, showing soft magnetic behavior with a saturation magnetization around 5 Tesla. Right inset: M-H loop from -5 to 5 T. (c) and (d) show similar results in a sample prepared at 900C. In (c) the presence of the soft phase is more pronounced, consistent with observations of increased hematite concentration in this sample. 97

Figure 3.20: Temperature-dependent magnetization under ZFC-FC (zero field cooling-field cooling) conditions at applied field of 100-1000 Oe. (a) Effect of temperature on magnetization for iron oxide nanowire sample on alumina substrate prepared at 700 °C at 1000 Oe field strength. (b) Effect of temperature on magnetization for iron oxide nanowire sample on alumina prepared at 900 °C under 1000 Oe. (c) ZFC-FC curve for same sample as (a) under 100 Oe field strength**.** 101

Figure 3.21: General morphology of the nanowires. TEM (a) bright-field and (b) dark-field images of the [111] growth magnetite nanowire. (c) SAED pattern of the wire. (d) HRTEM image recorded from the white rectangular area in (b). 110

Figure 3.22: (a) HRTEM image and (b) SAED pattern of a magnetite nanowire grown along the <211> direction. Stacking faults and (111) twins can be observed in the HRTEM image. 111

Figure 3.23: (a) Low-magnification TEM image of a [110] growth magnetite nanowire. The SAED patterns from the whole wire, and circled areas “C” and “D” are displayed in (b), (c), and (d), respectively. 112

Figure 3.24: Multiple directional examination of the diffraction behavior of the ε-Fe_2O_3 nanowires. (a–e) A series of zone-axis diffraction patterns of the ε-Fe_2O_3 phased wire with beam directions along the [001], [1¯02] [1¯01], [2¯01], and [–401] directions, respectively. These diffraction patterns provide a systematic expression about the 3D structure of the ε-Fe_2O_3 phase. (f) Schematic of the reciprocal space lattice built up from these patterns, where the reciprocal planes corresponding to the patterns displayed in (A–E) are marked. 114

Figure 3.25: Domain structure in a single nanowire. a, b) HRTEM images recorded from the wire shown in Figure 3a. c–f) FFT patterns from the 1–4 areas shown in (a) and (b). 115

Figure 3.26: Atomic models of a) magnetite, b) ε-Fe_2O_3, and c) ε-Fe_2O_3 d, e) Experimental and simulated (inset) HRTEM images of the ε-Fe_2O_3 phase with the beam along the [1¯01] and [001] directions, respectively. The insets are the simulated images based on model I and model II as displayed in (b) and (c), respectively, for the ε-Fe_2O_3 phase. 117

Figure 3.27: Structural evolution among the three phases along a single nanowire. a,b) Low-magnification TEM images showing different parts of the same nanowire. c) Enlarged image of the enclosed rectangular area in (a). 118

Figure 3.28: a–e) SAED patterns recorded from the circled areas A–E for the same nanowire presented in Figure 7, showing the different phases along the length of the same nanowire. 120

Figure 3.29: (a) Bright-field and (b) dark-field image to show the antiphase domain boundaries and 120° rotation domain walls in the ε-Fe_2O_3 phased nanowire. 121

Figure 3.30: (a), (d) HRTEM images of the 120° rotation domains as shown in Figure 9. (b), (c) FFT of the domain D1 and D2 in (a). 124

Figure 3.31: HRTEM image of a ε-Fe2O3 phase nanowire, showing the atomic scale structure of an antiphase domain boundary. 125

Figure 4.1: SEM and optical images showing a representative sample of ultralong ZnS-SiO2 nanowires: (a) composite of several SEM images demonstrating nanowires length; (b) optical image taken from above sample, fixed on metal stub; (c) SEM image of the sample's leading edge; (d) SEM image of opposite edge, showing long nanowires reaching past the metal stub. The inset shows corresponding EDS data. 134

Figure 4.2: (a, b) Low-magnification TEM images showing the tip of two ZnS- SiO2 core-shell nanowires, including the terminating metal particle. (c) Low-magnification TEM image of a nanowire center. (d) Electron diffraction pattern and corresponding EDS data from the nanowire illustrating the single-crystalline nature of the core. (e) Electron diffraction pattern and corresponding EDS data from the nanowire shell, showing the shell to be amorphous in nature and consisting of only Si and O. 135

Figure 4.3: Ultralong nanowires as a function of growth time. SEM images show sample characteristics after (a) 15 min, (b) 30 min, (c) 45 min, (d) 60 min, (e) 90 min, and (f) 120 min, at maximum chamber temperature. (g) Plot showing variation in average nanowire core and shell widths as a function of growth time, as determined from TEM analysis. (h) Plot illustrating variation in the core/shell area ratio as a function of growth time. 137

Figure 4.4: (a) Series of XRD patterns from samples with reaction times varying from 30 to 110 min. (b) Plot illustrating the ZnS:SiO2 ratio in nanowire samples as a function of reaction time, derived from XRD pattern semi quantitative phase analysis. 140

Figure 4.5: Composite of photoluminescence data from several ultralong ZnS-SiO2 core-shell nanowire samples. Each pattern corresponds to a unique sample exposed to synthesis conditions for a time interval between 30 and 110 min. The inset illustrates a plot of this data, correlating peak intensities with reaction time. 142

Figure 4.6: Schematic illustrating possible sample formation mechanisms and corresponding TEM images. Here yellow signifies Au, dark blue represents the Si substrate, light blue represents ZnS, and red coloration is used for SiO_2. (a) In this model, ZnS species are preferentially attracted to the Au catalyst particle and migrate to form the nanowire core. SiO_2 species form and migrate up the sides of the ZnS nanowire. (b) This model is similar to (a) except here silica species adsorb as gaseous species rather than migrating up the ZnS nanowire from its base. The final TEM image shows that these mechanisms are unlikely, since examined samples demonstrate uniform shell thickness along their entire length. (c) In this model, the ZnS nanowire forms first and then is completely encased in an amorphous silica coating. If this were the case, the silica coating should be the same thickness for all nanowires in a sample. The included TEM image demonstrates that this condition is not observed. (d) The initially proposed formation mechanism: both ZnS and SiO_2 species travel around the droplet surface to create the amorphous shell. This is the model suggested by our first analysis, but deemed impossible in light of later examinations. 147

Figure 5.1: Au-Si Phase Diagram 158

Figure 5.3: Graphs illustrating influence of temperature on Gibbs Free Energies of four magnetite decomposition reactions (a) demonstrates fluctuations from 0 to 80,000 degrees C (b) shows the area where delta G becomes negative in greater detail. 169

Figure 5.4: SEM image showing ZnSe nanowires grown preferentially on solid Au catalysts 173

Figure 5.4: SEM images demonstrating ZnO nanowires with different growth fronts emanating from the same Sn catalyst particle 178

Figure 5.5: Periodic box of gold atoms (100) packed into Fm-3m space group 182

Figure 5.6: Periodic box of gold atoms (50) packed into Fm-3m space group 182

Figure 5.7: Periodic box with a single Zn2+ ion per unit cell 191

Figure 5.8: Periodic box of Zn ions at a 20% atomic solute concentration before addition of gold solvent 192

Figure 5.9: Periodic box of gold atoms and Zn ions at a 20% atomic concentration 192

Figure 5.10: Periodic box of gold atoms and O^{2-} ions at a 2% atomic concentration 194

Figure 5.11: Periodic box of gold atoms and O^{2-} ions at a 2% atomic concentration after the MD simulation 194

Figure 5.12: Periodic box of gold atoms and O^{2-} ions at a 2% atomic concentration, after the MD simulation and a subsequent re-minimization step 195

Figure 5.14: Periodic box of gold atoms and Si ions at a 10% atomic concentration after MD simulation and subsequent energy minimization 197

Figure 5.15: Periodic box of ZnS molecules at a 2% atomic concentration before addition of gold solvent 198

Figure 5.16: Periodic box of ZnS molecules at a 1% atomic concentration after addition of gold solvent 198

Figure 5.17: Periodic box of ZnS molecules at a 1% atomic concentration after addition of gold solvent and MD simulation 199

Figure 5.17: Gold catalyzed silicon nanowires demonstrating diameter variation during growth directed by the metal particle size. The scale bar is 200nm. 213

Figure 5.18: Cross-sectional SEM image of gallium phosphate nanowires grown from a pattern of gold catalysts with different sizes. Nanowires were grown from 25 nm and 100 nm catalysts with 300 nm spacing. Wires next to a thick wire are taller than the second-nearest wires, which are taller than those in the center. The scale bar is 1 μm. 215

Figure 5.20: Images of three wires grown at 600^{o}C from Au-Si droplets of three different sizes, demonstrating saw tooth faceting at the nanowire edge. Scale Bar is 100nm. 217

Figure 5.21: SEM image of aligned ZnO in three distinct directions, each at a relative 120^{o} displacement, and the corresponding pole figure image (inset) taken from the sample. 219

Figure 6.1: Schematic illustrating basic organization of BCI systems [242] 227

SUMMARY

This work details the synthesis and growth mechanisms of 1D magnetic and semiconducting nanostructures. Specifically, magnetic iron oxide and ZnS-SiO_2 nanowires are examined. These materials are chosen due to their promise for biomedical and electronic applications and the perceived need to both create these structures as tools for these applications and to understand their formation processes so that they can be manufactured at a scale and efficiency suitable for commercialization. The current state and impact of nanotechnology is discussed through the lens of continuing technological advances and environmental factors, and the term is defined according to a specific set of criterion involving size, utility, and uniqueness. Details of synthesis and characterization of Fe_3O_4, ε-Fe_2O_3, and ZnS-SiO_2 core-shell nanowires are presented. Observations regarding the growth of these structures are paired with additional experiments, simple simulations, and other literature to discuss the classical VLS growth process in general, and its applicability to these structures in particular. Finally, some exciting future applications are discussed, with details for initial experimental work presented in the appendix.

CHAPTER 1

INTRODUCTION

1.1 What is Nanotechnology?

The term "nano" derives from the Greek word for dwarf. Today the prefix nano is used to indicate a billionth of a unit. A nanometer is therefore one-billionth of a meter, or approximately 1/10,00th the width of a human hair (on average), and in a material typically comprises the length of a few atoms. If a "nano" is merely a unit of measure, what then is nanotechnology? Wikipedia, a popular open-source based internet site, defines nanotechnology as,

"…a field of applied science and technology whose unifying theme is the control of matter on the atomic and molecular scale, normally 1 to 100 nanometers, and the fabrication of devices with critical dimensions that lie within that size range… Nanotechnology can be seen as an extension of existing sciences into the nanoscale, or as a recasting of existing sciences using a newer, more modern term.[1]"

This definition is surprisingly accurate. However specialists in the field might add more specifically that nanotechnology deals with the creation, engineering, manipulation, and utilization of nanomaterials for systems and devices, and that in order to be classified as a nanomaterial, an object must exhibit at least one dimension in the nanometer range. Nanoscience, a discipline closely related to nanotechnology, could then be defined as the

search to understand the basic principles governing the behavior of these materials and/or application of such information to basic scientific questions.

Yet, nanoscience and nanotechnology imply more than these definitions suggest. According to these descriptions, a study of the nano-sized particulates known as smoke would qualify as nanoscience, yet smoke is not commonly considered a nanomaterial. In order to qualify as a true nanomaterial, something about the dimensions of the material must make it unique. A nanomaterial must behave differently from its bulk counterpart. It must exhibit new properties, challenge concepts, facilitate new devices, or provide new insights into how things work, how they are put together, or how they will perform. Therefore, the best definition of nanotechnology must be one similar to that put forth by the EPA in their 2007 Nanotechnology Whitepaper (based on an earlier definition by the National Nanotechnology Initiative). This text defines nanotechnology as:

"research and technology development at the atomic, molecular, or macromolecular levels using a length scale of approximately one to one hundred nanometers in any dimension; the creation and use of structures, devices and systems that have novel properties and functions because of their small size; and the ability to control or manipulate matter on an atomic scale.[2]"

This document correctly defines nanotechnology according to the three critical elements of scale, utility, and uniqueness.

For several years, many scientists and researchers have professed skepticism regarding the enthusiasm that the nanotechnology and nanoscience fields have generated. Exploitation or misunderstanding of nanotechnology's true meaning is largely to blame.

In a rush to reap nanotech's potential benefits, many technologies were labeled "nano" without meeting the definition's full requirements. Such misuse has led to suspicions that the field is merely one of many scientific fads, and that due to overselling its potential, nanotechnology will fall far short of its hype. Some researchers still maintain this position, but as nanotech begins to emerge from its infancy in the late 20th century and develop now into a more visible and quantifiable domain, its impact has become more easily recognized.

1.2 Why Now?

Nanotechnology is not just a new name for old science. That nanotechnology is drawing so much interest *today* rather than a few decades previously is hardly an accident. The emergence of nanotechnology was initiated and then accelerated by several events combining to create ideal conditions. Among these events, the development of imaging tools, the discovery of novel structures, the observation of surprising new behaviors, the development of mathematical and computational models to understand them, and the commercial need for new engineering paradigms, especially in microelectronics, are the most notable.

Nanomaterials have always been around us. Artisans since the time of the ancient Chinese have been using crushed metal powders, or nanoparticles, in paints, glazes, and glass to create vivid colors. Magnetotactic bacteria, it has been discovered, have evolved an ingenious method of navigation via magnetic nanoparticles lined up inside the organism, acted on by the earth's own magnetic poles. While cells and bacteria are often

relatively large, usually on the order of several microns, viral dimensions are well within the nano-regime, allowing them to easily be transported throughout the body, and even into cell interiors. (See Figure 1.1)

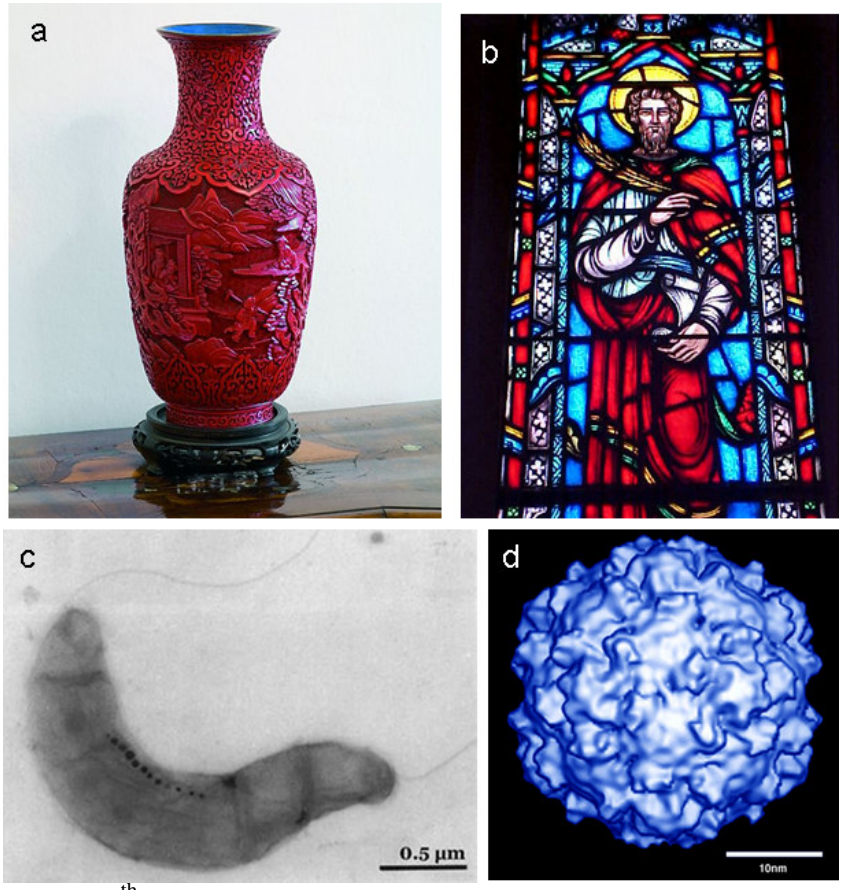

Figure 1.1: (a) an 18th century Chinese vase, demonstrating use of red glaze pigments (b) a medieval stained glass window illustrating use of nanopowders in art glass processing (c) a magnetotatic bacteria, with internal magnetic nanoparticles clearly visible (d) a to-scale computer model of the polio virus

Nanomaterials are not in themselves an original construct. The novelty lies in our ability to understand and engineer these and other truly innovative materials to exploit their unique characteristics in ways that only recent progress has made possible.

The advent of improved imaging properties and a good understanding of quantum mechanics opened the door for the first explorations into the novel properties of

nanomaterials. The development of the requisite tools began early in the 20th century. The first electron microscope prototype, based on fundamental scientific discoveries by physicist Lois de Broglie, was developed in 1931 by Ernst Ruska and colleagues. (For this work, Ruska received the 1987 Nobel Prize in Physics, indicating that the value of his contribution had finally been recognized.) Improvements in both the scanning and transmission electron microscopy followed quickly thereafter, and today the best equipment is capable of imaging materials at resolutions better than 1 angstrom. These developments have provided scientists the ability to probe material composition down to individual atoms. With these powerful tools, scientists found themselves able to investigate structures and identify changes in materials that had been previously impossible. New light was shed on old phenomena, such as precipitation hardening, when scientists were first able to visualize precipitate structures correlating with specific material changes, and defects, when engineers finally could identify specific points in a material leading to failure. Perhaps even more importantly, previously undetectable structures were beginning to be discovered.

The first breakthrough was the discovery of quantum dots. Quantum physicists had long theorized about the ideal case of a single small particle with dimensions similar to the bulk exciton Bohr radius. [3] The Bohr radius is a constant used to describe the size of an electron's orbit around an unexcited hydrogen atom nucleus. Since the hydrogen atom is the simplest atom, its ground state orbit represents the smallest mean radius normally attainable by a neutral atom. The size of this orbit is physically and logically based on the interaction of competing forces in the atom, that is, the attractive Columbic forces between the oppositely charged particles making up the atom, and the repulsive

forces due to the momentum of the electron around the nucleus as described by the Pauli Exclusion Principle. Solutions to the Schrodinger Equation based on the angular momentum of an electron traveling around the nucleus likewise demonstrate that electrons in the ground state can take only certain "quantized" values of energy. As large numbers of atoms are brought together, however, these distinct orbitals overlap into broad "energy bands." Figure 1.2 below illustrates the difference between the narrow quantized energy levels of a single free atom, and the larger energy "bands" observed in molecular clusters and solids.

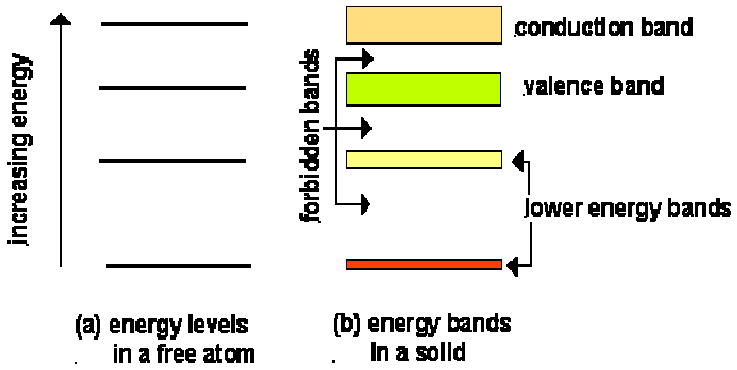

Figure 1.2: (a) A simple energy band diagram of a single free atom showing single potential energy states (b) The corresponding wider energy bands emerging in larger bulk materials in which several states at each level are possible

In large solids, the positions of electrons at these various energies are frequently visualized as "electron clouds" since at any time the position of an electron in each energy band is only known as a statistical average.

Scientists had theorized that if such particles with dimensions on the order of the Bohr radius could be made, atomic effects would again dominate, and the energy bands of the bulk material would reduce to atom-like quantized energy levels. The electrons in

this particle or “quantum dot” could then be envisioned as particles in a theoretical potential well, subject to similar solutions of Schrodinger’s Equation. This effect was confirmed for the first time by researchers at Bell Labs in the course of studying CdSe particles.[4] Quantum mechanics states that as the particle becomes smaller (the quantum well gets deeper) the possible energy levels are shifted upward to higher energies. These energy shifts can be observed as changes in optical emission in a quantum dot, since photons emitted from a material have frequencies directly related to the distance between the material’s electron energy bands.[5] (See figure 1.3)

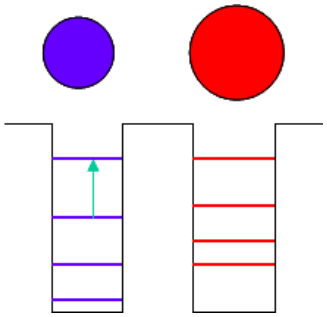

Figure 1.3: Schematic illustrating color change in a quantum dot resulting from a shift in possible energy states corresponding to size change

Quantum confinement in small particles such as CdSe can be easily confirmed, and has been repeated several times, by noting size dependent changes optical emission as observed in Figure 1.4.

Figure 1.4: Vials containing varying sizes of CdSe quantum dots, growing larger from left to right

Without the proper imaging and characterization techniques, scientists would not have been able to successfully identify and measure these first nanomaterials.

After the development of quantum dots, other breakthroughs such as the discovery of the fullerene by Curl, Kroto, and Smalley in 1985, and the carbon nanotube, largely attributed to Sumio Iijima for his 1991 publication (though some suggest that the discovery is actually due to a Russian scientists Radushkevich and Lukyanovich, whose 1954 work went unnoticed due to the political turmoil of the time) provided new and interesting structures for scientific study.[6] Soon thereafter, scientists developed metal and semiconducting nanowires and nanobelts, and later, heterostructures and high complex nanomaterial geometries. The development of these novel structures, made possible by electron microscope imaging techniques, generated new interest in the study of materials at the nanoscale.

As researchers began to examine the properties of these novel structures, they were surprised to find that often properties could not be predicted based on the material's bulk counterparts. Nanobelts composed of metal oxides (or ceramics) for example,

known to engineers as highly brittle materials, were found to be highly flexible. Platinum nanoparticles melted at temperatures far below the melting point of the bulk metal. Carbon nanotubes (CNTs) demonstrated strength and toughness surpassing the strongest diamonds. Further, it was found that depending on the chirality of the atomic arrangements in the carbon nanotube, they could exhibit either semiconducting or metallic electron transport. CNTs in the "zig-zag" conformation, as seen in Figure 1.5 below, demonstrate semiconductor-like electronic conduction in which a band gap must be overcome to free transport electrons, while "armchair" CNTs electronically behave similar to metals. [7]

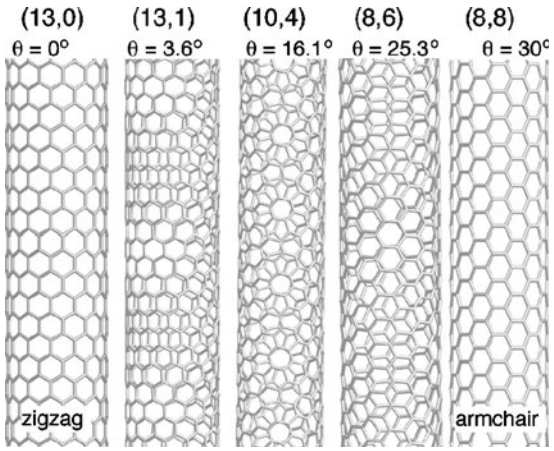

Figure 1.5: Computer generated structures of single-wall carbon nanotubes with different chiral angles between 0° and 30°

Scientists quickly recognized that nanomaterials were not just small, they were different. At nanoscale dimensions, forces and effects normally overwhelmed in bulk materials became dominant. The realization that nanomaterials could provide new insights into fundamental science questions, and that their unique properties could be

exploited for entirely novel applications understandably excited scientists and engineers across many fields, and pushed many researchers to begin their own work in nanoscience and nanotechnology.

Alongside the experimentalists working to develop and use these new materials, theorists were seeking to understand the origins of their surprisingly novel properties. Models were built and simulations were run to probe the physics behind nanomaterials' unique mechanical, chemical, electronic, optical, and many other characteristics. Fortunately for the theorists, both computing power and computer modeling have experienced extraordinary growth in the last few decades. New faster algorithms and user-friendly software have kept pace with the incredible increase in processing power that began in the early 1970s. The calculated results output by nanotechnology theorists have provided experimentalists with informed starting points, and helped to focus their work. Simulations also inspire experimental scientists to test the validity of their computed results, and alert them to new and interesting problems. Rapid growth in intellectual and computational capability has further augmented nanoscience and nanotechnology, at a pace that would not have been possible just a decade previously.

Computer developers have long anticipated the day that current technologies could no longer maintain the current pace of microprocessor improvement. The computer industry has steadily pushed for more devices in ever smaller spaces, increasing computing power and speed while maintaining reasonable price points. However, while manufacturers continue to keep step according to "Moore's Law," – a prediction that the number of transistors on an integrated circuit could grow by a factor of 2 approximately every 18 months – industry leaders have acknowledged that soon the expansion will slow

due to the physical limits of miniaturization. (See figure 1.6) Today, the best microchips contain millions of transistors whose critical dimensions measure only 100 atoms across.[8] Clearly, the Moore's Law paradigm cannot be extended much further if industry maintains reliance on traditional silicon processing technologies.

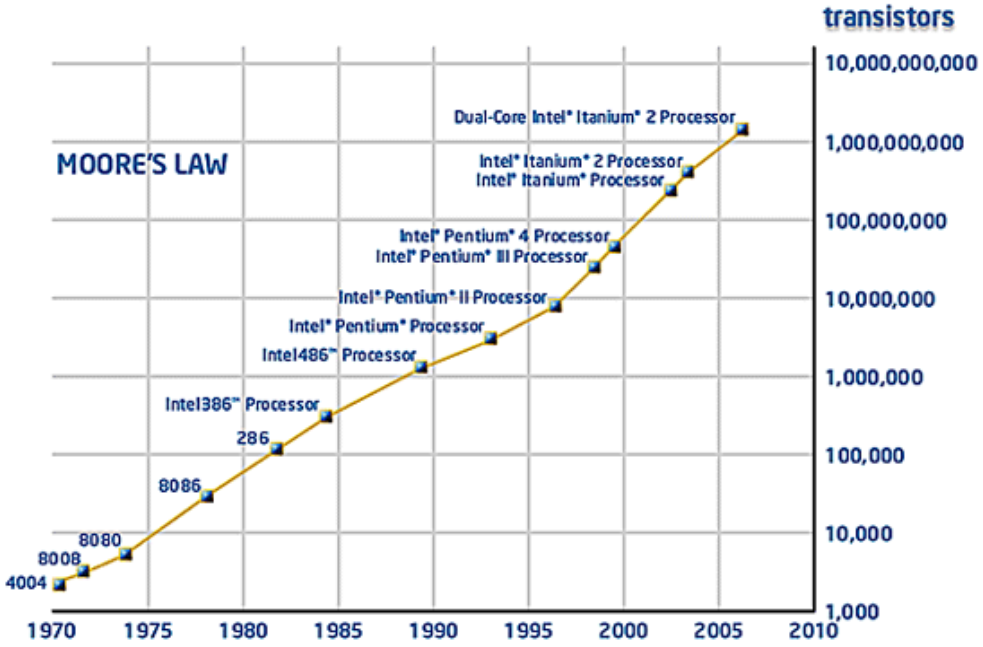

Figure 1.6: Graph illustrating the exponential growth of IC transistors according to Moore's Law from 1971 to 2000.

Just as nanotechnology has heavily benefited from increased computational muscle, computer and component manufacturers have realized the need for reformative technologies to prevent an otherwise inevitable deceleration. Many companies are placing their bets on nanotechnology to overcome the obstacles inherent to traditional device fabrication, and furthermore, are supplying money and people to implement promising nanotech breakthroughs.

1.3 Nanotechnology's Current Impact and Direction

While the largest focus on the nanotechnology and nanoscience fields remains the future, in the last decade advances have led to tangible products with identifiable impact. The first real products of the nanotech revolution have been so-called "passive" nanotechnologies in which nanomaterials play an important but non-elaborate role in enhancing characteristics. Some examples include transparent sun block, tasty low-fat ice cream, tennis balls incorporating CNTs to improve bounce retention, and stain resisting non-wrinkling pants that work by coating the cotton fibers with millions of nanoparticles. The military has reportedly developed self-cleaning underwear for soldiers based on similar technology. Although the biggest hopes lie not with such passive technologies, but the more exciting, and potentially more beneficial "active" applications, these early contributions are non-trivial. A recent survey by the Project on Emerging Nanotechnologies at the Woodrow Wilson International Center for Scholars identified over 300 nanotechnology related products. By the end of 2008, the commercial market for nanotech products is estimated to reach $29 billion. [9]

Still, considering the substantial investment input, the argument could be made that the market should be demonstrating much greater value. This figure is certainly less than those hoped for by many of the first nanotech investors. Business reviews in the first half of this decade placed revenues well below investment in many companies, and some initial startups have already gone bust. The slow start, however, is simply due to the longer term nature of the products nanotech research can produce and the necessary

time to address limiting obstacles. Several indicators are showing that now is the time to begin putting dollars into nanotech-focused companies, not pulling them out.

Early investors in nanoscience research and product development were sometimes surprised to learn that many technologies faced formidable obstacles to commercialization. Commonly these barriers included the ability to efficiently scale up nanomaterial production, the ability to manipulate those materials to precise locations in functional devices, the ability to grow pure, long, or chemically complex nanowires, issues of unknown or low biocompatibility, and insolubility in common liquids. While many of these obstacles still exist, and the billions of dollars invested by government and industry into development of marketable nanomaterials products have taken a few years to yield results, the tides are beginning to change.

Focused efforts on understanding the growth of nanomaterials, improving synthesis and production techniques, and addressing other specific obstacles have produced breakthroughs addressing many previously critical problems. For example, when carbon nanotubes were first predicted as candidates for applications from high strength composites to the space elevator, critics commonly rebutted that CNTs were very short, could not be produced in large quantities, and were completely insoluble in water. Due to plenty of research dollars and a parallel competitive research environment, each of these obstacles has been addressed so that currently companies hoping to use CNTs in their processes can choose from four methods of producing CNTs by the ton, several growth and spinning methods to achieve lengths up to several meters, and a host of processing methods for solubility in almost any environment.[10] Similar advances

have been made in the commercialization of quantum dots (largely for biomedical purposes), semiconducting nanomaterials, catalysts, and others.

Scientists and industry leaders well-connected to ongoing advances, have pointed to the current climate as nanotech's teenage years, i.e. those formative few years leading up to swift maturity. As illustrated in the figure below, commercial nanotechnology seems to be on the cusp of rapid and exiting growth.

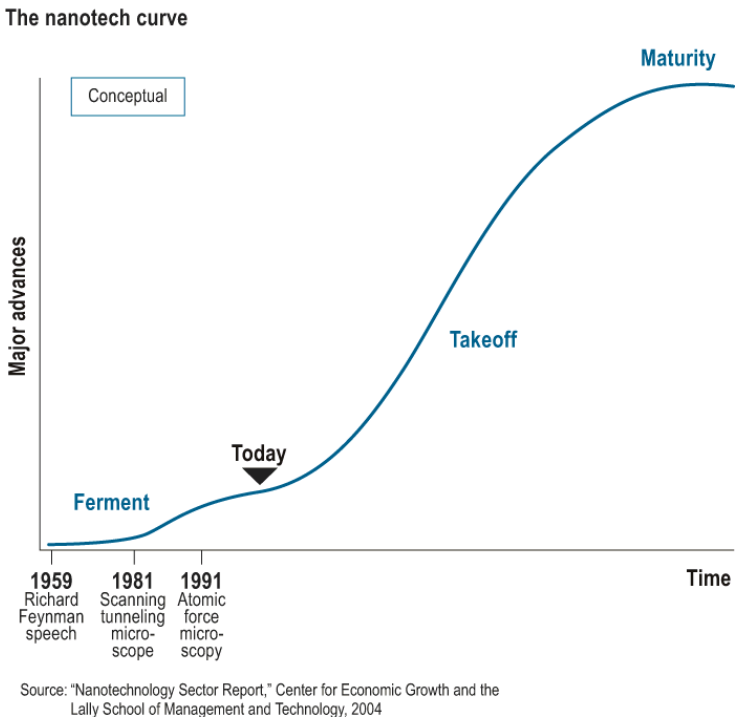

Figure 1.7: Conceptual graph illustrating that nanotech's slow growth period should soon be giving way to rapid development.

A 2007 projection by Cientifica, an EU based market research firm, estimated the market for nanotech enabled products to reach $1.5 trillion by 2015. The National Science Foundation predicts that nanoscience will enable two million new jobs in the next decade.

This growth will be precipitated by a burst of science and engineering breakthroughs occurring most rapidly in the last five years. Nanobot movement, just a few years ago only a computational reality, has been achieved using DNA segments and components. Nanobatteries made from paper or nanowires are promising power necessary for nanomachines derived from solar energy, blood flow, waste vibrations, and even urine.[11, 12] Taking the lead from biology, scientists have married the dry sticking power of gecko feet with that of marine mussels to produce "Geckle" an advanced glue that works well under both wet and dry conditions and remains sticky after hundreds of stick/peel away cycles.

The literature has been filled with nanomaterials based solutions to biomedical, bioengineering, and pharmaceutical problems. Nanowire sensors with single molecule selectivity have been engineered to detect specific chemicals, proteins, and complementary DNA, a critical function for genomics research. [13] Researchers at Harvard University recently used iron oxide containing magnetic nanoparticles to control calcium intake in live cells, demonstrating for the first time a physical rather than chemical means of controlling cellular function. [14] Scaffolds made of biodegradable nanowires have been shown to repair brain damage and repair vision in animals, or coax neurons into forming engineered patterns. [15-17] Neural tissue has been coerced to live happily on computer chips and respond to electrical inputs. The pharmaceutical industry has already released new drugs based on nanotechnologies for slow release and local treatment. [18-21]

The recent acceleration of marketable nanotech products and ideas is made evident through the last decade's surge in nanomaterials patents. As of January 2008, the

US Patent Office had awarded approximately 2800 nanoscience patents. For perspective, consider that the number of patents containing the phrase “nano” numbered only 70 in 1990 and 800 by 2001.[22] Forecasters predict that the next 10 years will experience an even greater boom of nanomaterials enabled products. Commonly, medicine, electronics, energy, and defense are cited as some of the most promising fields for these new technologies. As shown in Figure 1.8, other industries are already benefiting and hoping to gain more from the nanotech revolution include aerospace, laboratory equipment, and chemical manufacturing companies.

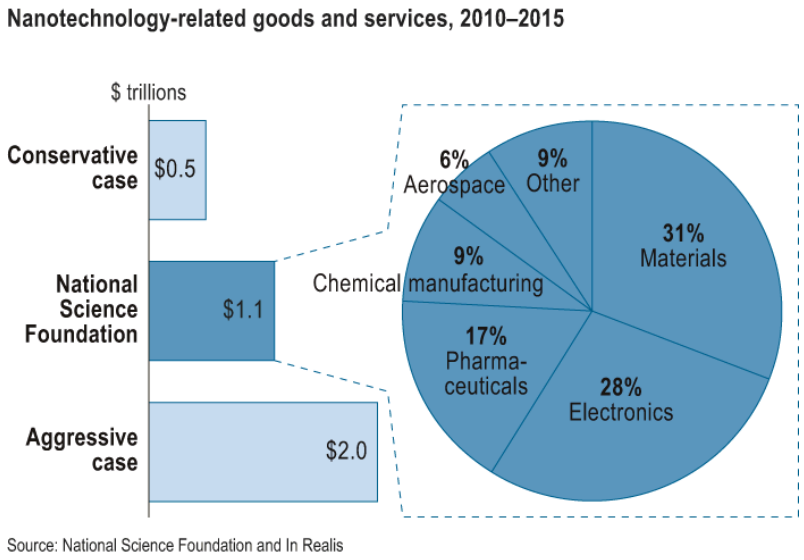

Figure 1.8: Pie chart illustrating predicted importance of nanotechnology in several key industries, according to the National Science Foundation

However, many nanotechnologies still need to overcome formidable hurdles before some of the most exciting potential applications can be realized. While many of the problems holding back commercialization of CNTs have been solved, other materials still want for solutions to both similar and unique barriers. In many cases, synthesis of

nanostructures is not well understood, so that scientists must repeat attempts several times to achieve desired products. Such obstacles make these materials slow to produce, very expensive, and resistant to scale-up processing required for commercial manufacture. Nanomaterial properties are strongly correlated to their geometry and dimensions. Therefore, precise control over synthesis is required to create high quality, consistent products. A lack of understanding regarding the precise processes involved in the synthesis and growth of nanomaterials hinders our ability to gain requisite control over production.

Manipulation of nanomaterials is also still a problem. Nanomaterials are so tiny that conventional tools and methods become clumsy or impossible. Often localization to a certain location in a device requires many trials and high percentages of wasted material. One challenge for application of nanowires to functional devices is the ability to grow the materials long enough to manipulate, while maintaining diameters in the nanometer range for optimal performance.

For medical purposes, researchers must make certain that their nanotech treatments do not cause more harm than good, so biocompatibility, toxicology, and tissue clearance are all vital issues, while our understanding of how nanomaterials interact with biological systems is severely limited. Functionalization may be needed to improve biocompatibility or improve effectiveness of a nanomaterial-based treatment. Functionalization is also commonly required for chemical resistance, sensitivity, or other desired properties for chemical or electronic applications. Additionally, many nano-enabled medical treatments currently require large doses, causing physicians to be

hesitant to prescribe such treatments in all but the most severe cases. Clearly, improvements are still critically needed.

1.4 Thesis Question and Motivation

In an effort to address some of these obstacles, the research described in this thesis focuses on understanding the basic synthesis of metal oxide and semiconductor nanowires of interest for biomedical and electronic applications. The goal was to develop nanostructures relevant to specific medical treatments, and then through careful analysis of these structures, gain new insights into the physical processes governing their nucleation and growth. Other semiconductor materials grown through similar methods were examined to help elucidate which synthesis components may be unique to chemistry, and which are shared in common, due perhaps to processes critical to the synthesis method. In this manner, it was hoped that the dual goals of engineering and creation of important biomedical and electronic tools and progress toward addressing important and relevant scientific questions could be met.

In particular, this work is focused on the synthesis and characterization of novel magnetic iron oxide nanowires and nanorods, with an emphasis on their future use as cancer targeting agents. Iron oxide, specifically the form known as magnetite, was chosen due to preliminary successes in similar applications as nanoparticles and quantum dots, its known biocompatibility, chemical stability, and low price. At the time of this work, solid state synthesis of magnetite nanowires had not been achieved, nor had such a level of synthesis control been reported previously. Observations about the growth of this material were compared with those of ZnS/SiO_2 core-shell nanowires grown through

similar methods, and coupled with experiments to further probe the physical processes involved in nanowire synthesis. These nanowires may be promising future candidates for biomedical applications due to their biocompatible chemistries, but currently are more exciting for electronic sensors and devices. This work is complemented by computer modeling, which is used to explore both the possible scenarios in nanowire synthesis, and the potential effectiveness of these new materials for their intended biomedical applications.

The questions this work seeks to answer are thus: Can high quality magnetite nanowires be grown through solid vapor deposition methods? Can we grow magnetite nanowires with control over alignment, length, and location? How exactly does the growth process work in these and similar nanostructures? How do our observations of these and other nanostructures fit with current understanding of nanowire growth? Can these materials be used to improve current medical treatments?

CHAPTER 2

ONE-DIMENSIONAL NANOSTRUCTURES

2.1 Definition and Types of 1D Nanostructures

Nanomaterials are commonly classified according to their dimensionalities as zero dimensional (dots or mostly spherical nanoparticles) one dimensional (nanowires, nanotubes, and nanobelts) or two-dimensional (thin films). These categories refer to the number of dimensions in which the material is outside the nano regime. A thin film, for example, consists of large expanses of material in both in-plane directions, and is nano-sized only in its thickness; therefore it is termed a two-dimensional (2D) nanomaterial. Due to the effects of size discussed in the previous chapter, the dimensionality of a nanomaterial can alter its properties, such that a thin film may behave very differently from a nanowire with the same chemistry. These distinctions therefore are not arbitrary, but important in distinguishing these materials according to unique characteristics. Figure 2.1 below illustrates the differences between these classes of nanomaterials.

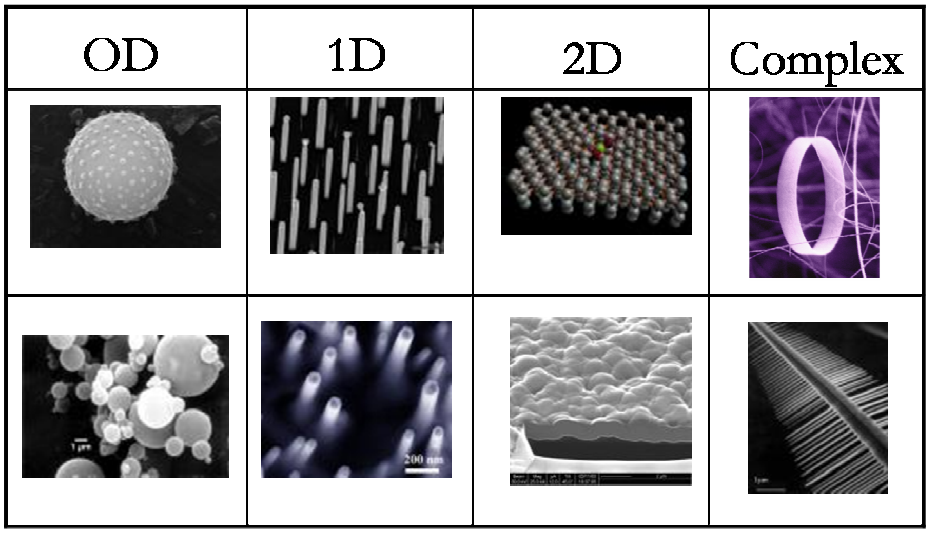

Figure 2.1: Images demonstrating nanomaterial classifications

Much work has been focused on the development and application of two and zero dimensional (0D) nanomaterials, due in part to their relative ease of synthesis compared to similar one dimensional (1D) nanomaterials. The development of molecular beam epitaxy (MBE) techniques, in which a material can be built up in single-atom layers, has allowed extensive research on 2D nanomaterials. Chemical monolayer formation has also been adopted as a reliable means of forming high quality 2D nanomaterials. The formation and properties of thin films are now well-understood, and these materials form the cornerstone of many high-precision products including commercialized lasers, silicon microelectronics, and NASA quality optical components. 0D quantum dots are also easily synthesized through wet chemistry, aerosol spray, and other methods (though uniform size distribution is an issue), and so have been developed in the past few decades into a host of commercial applications. Among these are quantum dot lasers [23] biological fluorescence probes [24], and single electron transistors [25]. Many

researchers traditionally have not pursued research into 1D nanomaterials due to their complex and mysterious formation processes and the corresponding lack of control over their synthesis, difficulties in manipulation, and a lack of standard and verifiable properties observations.

However, as our understanding of these materials has grown and synthesis techniques have been greatly improved, the last five to ten years have demonstrated an explosion in publications focused on 1D nanomaterials. Beginning with carbon nanotubes, the toolbox of 1D nanomaterials has grown to include nanowires and nanobelts of semiconducting materials, complex geometries, and multi-component nanoscale heterostructures. The potential of these for use in structural, commercial, environmental, electronic, and biological applications, to name a few, have lately sparked the interest and imaginations of researchers from almost all science disciplines, and even the general public. Still, our understanding of 1D nanomaterial formation is incomplete, our control limited, and production is still highly costly, even compared to other nanomaterials. While certainly improved synthesis techniques have helped move 1D nanomaterial research forward, the driving force behind their rapid development is a new appreciation for their unique properties, driven by the need to utilize these properties in highly demanding applications.

2.2 Nanowire Synthesis and Theory

Controlled synthesis of nanostructures has attracted much attention, as many exhibit size and dimensionally dependent chemical and physical phenomena which can

be tuned as desired to suit specific applications.[26] 1D nanostructures such as nanowires are of interest for fundamental material studies, and are adaptable to many applications as they can function both as active devices and interconnects.[27] While several methods may be used for nanostructure fabrication, these can be classified as vapor deposition or solution based chemistry techniques, as seen in the table below.

Table 2.1: Classifying nanostructure fabrication techniques

Physical Vapor Deposition (PVD)	Thermal Evaporation *Electron-beam* *RF Induction* *Resistive* Sputtering *Focused Ion Beam* *Radio frequency* *Magnetron* Pulsed Laser Deposition
Chemical Vapor Deposition (CVD)	Thermal CVD Low-pressure CVD (LPCVD) Plasma-enhanced CVD (PECVD) Metal-organic CVD (MOCVD) Molecular Beam Epitaxy (MBE) Atomic Layer Deposition (ALD)
Solution Based Chemistry (SBC)	Hydrothermal Sol-gel

This section discusses general theory and relevant synthesis of nanowires, including vapor synthesis and solution based chemistry techniques. While this dissertation focuses on vapor growth processes, hydrothermal synthesis is also included as an alternative to these methods, and therefore requires a brief discussion as well.

2.2.1 Vapor Synthesis

The majority of nanowires discussed in this work were created through the use of vapor deposition synthesis techniques. Vapor deposition synthesis is generally divided into two categories, physical vapor deposition, or PVD, and chemical vapor deposition,

or CVD. These categories describe differences between processes occurring at the molecular level to create desired nanowires. In PVD, a source material is vaporized and re-assembled into a nanowire without changing the basic chemical components of the starting material. CVD on the other hand involves a chemical change occurring in the vapor phase, whether through re-arrangement of the source material's elements, made possible by excess energy provided to the system, or through reactions of the source vapors with gasses introduced separately into the system. To understand how vapor synthesis techniques work to create nanowires from heated or ablated powders, one must first understand the basics of the processes that work together to form these structures.

2.2.1.1 VLS and VS Processes

Two prominent mechanisms for growth of nanowires under evaporation techniques, with and without catalyst, are vapor-liquid-solid (VLS) and vapor-solid (VS) growth mechanisms, respectively. The figure below shows a schematic diagram depicting the three basic stages attributed to nanowire formation due to VLS growth. [26]

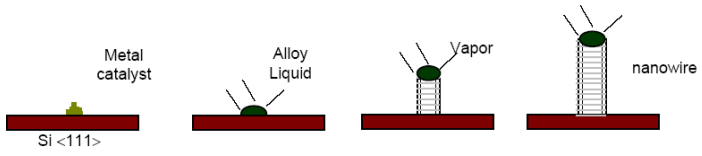

Figure 2.2.: Schematic illustration of proposed VLS nanowire growth mechanism including alloying, nucleation, and axial growth stages

In the first step, metal catalyst is deposited onto a substrate where it forms liquid droplets. Vapor of the desired nanowire species is then introduced to the atmosphere. According to

the generally accepted model, the liquid droplets act as preferential sites for the deposition of the vapor species due to the greater sticking coefficient of liquid relative to solid surfaces. (By definition the sticking coefficient is the ratio of the incorporated vapor flux to the external vapor flux supplied from the source.) It is believed that as the vapor saturates the area around the catalyst, some is dissolved into the metal forming an alloy solution. Recently, scientists have been questioning this part of the model, and experiments are beginning to show that in many cases the vapor species may be transported on the surface of the droplet, rather than diffusing into the liquid. The role and state of the metal catalyst particle in nanowire synthesis will be discussed later in greater detail. Over time, the liquid droplet becomes supersaturated with the vapor compound. If the properties of the catalyst and substrate are such that the metal catalyst is not strongly held to the surface, a precipitate of reactant material, often the same diameter as the metal droplet, is rejected out of the metal droplet onto the substrate. In the case of strong adhesion of catalyst to substrate, the nanowire may grow such that the catalyst remains on the substrate surface, and the wire grows out from the top of the metal droplet. As more reactant is added, more is rejected from the catalyst, causing vertical growth of a column or wire. It is believed that the nanostructure grows vertically due to the kinetic effect of preferred growth of some crystallographic planes relative to others dictating fast growth in one direction with other planes growing more slowly. Occasionally, conditions will allow some transverse growth to occur, increasing the wire diameter beyond that of the catalyst droplet.[27]

Although first developed by Wagner and Ellis in 1964 to describe the growth of silicon whiskers, vapor evaporation growth methods and the VLS mechanism have

experienced renewed interest due to their ability to control size, morphology, and placement of 1D nanostructures and a desire to fully understand the dynamics of their growth.[28] The VLS mechanism was adapted by Morales and Lieber to explain 1D silicon nanostructure growth in 1998. [29] Later, *in-situ* VLS growth of Ge nanowires from Au was observed using a high-temperature TEM.[30] The basic VLS process described above is based on that proposed by Morales and Lieber, however the Fe-Si, Fe-Ge, and Si-Au systems are much simpler than multiple component ferrite systems. The thermodynamics of alloying in these systems is more easily explained.

In addition to parameters such as system temperature, pressure, etc. it is evident that the choice of substrate and catalyst materials is of great importance to successful synthesis of magnetite 1D nanostructures. To choose the most desirable candidate materials one should ideally understand the basic stages of the nanowires' growth mechanism, including characteristics of vapor species, mechanics of adsorption onto the catalyst if this occurs at all, any chemical effects of catalyst or substrate on source species, transportation of the source species to the catalyst/substrate interface, conditions determining species rejection from catalyst particle, role of the catalyst and substrate in determining growth direction, size, and morphology, incorporation of source species into the nanowire structure, radial and transverse growth, and finally termination. Although literature reports many instances of nanostructure synthesis via the VLS method, much is still unknown regarding the details, or if the traditional model truly explains the mechanics of common nanowire growth. This work aims to provide new insights into how the vapor evaporation nanowire synthesis process occurs in the context of the materials examined with an eye toward specific biomedical and electronic applications. A

more detailed analysis of the VLS process is discussed later in Chapter 5 after details regarding nanowire synthesis have been presented.

The VS growth mechanism is not well understood. This process occurs under similar conditions to VLS growth, however, without the aid of a catalyst. Some researchers believe the source of VS nucleation and growth may be high energy defects on the substrate, or grain boundaries formed by epitaxial deposition previous to nanowire growth. Since all nanomaterials created in this work through vapor deposition methods involved the use of catalyst, the VS process will not be examined in detail here.

Beyond the conceptualization of nanomaterials synthesis theory, careful attention must be paid to details of the growth process for any fabrication attempt. Scalability and repeatability are key to real application and commercialization of nanomaterial tools. To understand and repeat favorable results, careful record keeping must parallel a thorough understanding of the synthesis process, and possible weaknesses and variations in both process and synthesis equipment. Experimental variables initially assumed to be constant or negligible may later prove to cause significant impact on the final result. The next section addresses experimental setup and procedures used to create nanomaterials through the physical vapor processes utilized in this work in a general manner, so that variations in conditions specific to each material later can be better highlighted and examined. Information regarding the equipment utilized for synthesis is also presented, as such detail is outside the scope of later chapters.

2.2.1.2 Vapor Synthesis

Synthesis of the ZnS-SiO_2 core-shell nanostructures discussed later in this work was accomplished entirely through chemical vapor synthesis. The major equipment utilized for vapor synthesis consisted of a furnace system for temperature control, a corresponding vacuum system for reaction pressure control, and a carrier gas system, designed to help move vapor species along the tube and purge atmospheric oxygen. A schematic of the equipment setup incorporating each of these modules is provided in Figure 2.3.

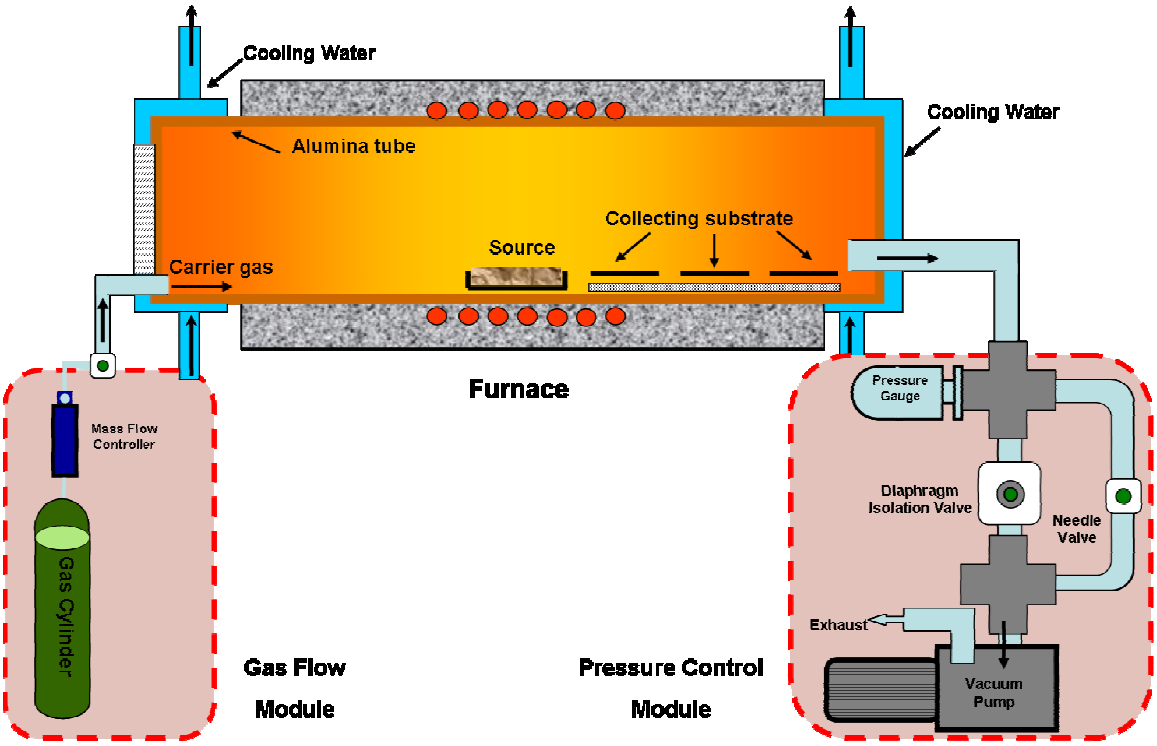

Figure 2.3: Furnace, gas flow, and pressure control systems used for vapor evaporation synthesis of 1D nanomaterials.

The furnace used for these experiments was a Thermolyne 79300 single zone split tube furnace, with a PID (proportional, integral, derivative feedback) temperature control system, capable of achieving up to 1200 degrees C at a rate of 50 degrees per minute. The

furnace and control system allow the user to design a number of programs in which dwell temperature, dwell time, and temperature ramp rate may be varied. A photograph of the Thermolyne 79300 split tube furnace is shown in Figure 2.4.

Figure 2.4: A photograph of a Themolyne 79300 Single Zone Split Tube Furnace

For vapor deposition synthesis without the addition of laser energy, the furnace was fitted with a 99.8% alumina refractory tube to contain and isolate chemical vapors. Alumina was chosen due to its mechanical and chemical stability at high temperatures. The tubes utilized for this work were obtained from Coorstek company and measured 30 inches in length, with a thickness of 0.5 inches. As seen in the diagram, the tube overhangs the furnace (the furnace is only 24 inches long) by three inches on each side, and endcaps are fitted to the tube ends. To support the weight of the tubes and endcaps and prevent tube sag at high temperatures, braces were placed on each side of the furnace to support tube ends. Tubes were cleaned before and after each use.

Prior to a synthesis experiment, source materials (usually powders) are loaded into the center of the furnace. In this way, the designated maximum furnace temperature

is known to correspond to the temperature of the source. Deposition substrates, often pre-coated with catalyst material, are usually placed downstream in the cooler regions. The tube ends are closed via metal endcaps and water-cooled to maintain a uniform thermal gradient, with one end connected to a rotary vacuum pump and the other to a gas supply. To promote an efficient seal between the alumina tube and the endcaps, rubber o-rings treated with vacuum grease are fitted to the tube ends and pressed into the cap creating a compression fitting. Because the temperature can only be controlled in the center of the furnace, a uniform thermal gradient is essential to maintain an accurate and predictable relationship between distance from the tube center and local ambient temperature.

The temperature inside the furnace is monitored by a centrally located thermocouple and displayed digitally on the furnace assembly. Real-time monitoring of the ambient temperature within the tube was not possible due to the risk of an internal thermocouple creating disturbances within the tube, as well as practical considerations such as contamination of the thermocouple itself. To help overcome this obstacle, a representative study of the thermal as a function of various center zone temperatures was conducted, with a graph illustrating the results shown below.

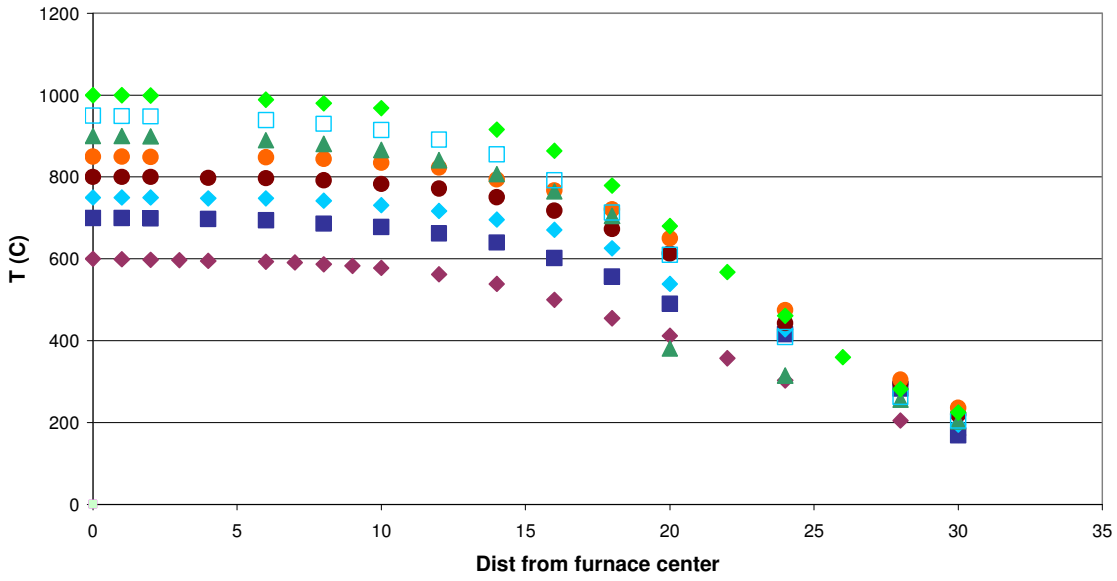

Figure 2.5: Graph illustrating thermal gradient in tube furnace at several maximum center temperatures. Distances are in centimeters.

These measurements were used to estimate temperatures of sources and substrates during synthesis. Though small deviations from these values during experiments due to ramp rate or variance in water cooling temperature may have occurred, the gradual nature of temperature change within the tube indicates that deviations should not have been more than a few degrees, so internal temperatures can be known with a high degree of confidence despite the absence of *in-situ* monitoring.

Chamber pressure is determined by the pressure control and gas application systems. After proper sealing the tube via o-rings, a BOC Edwards RV8 Hydrocarbon Rotary Vacuum Pump connected to the chamber is turned on, and valves are opened to allow the full force of the pump to evacuate the reaction tube and purge the system of residual oxygen. Two valves are incorporated into the system to allow pressure adjustment. A BOC Edwards Diaphragm Isolation Valve aids in coarse adjustments, having

a large orifice to allow rapid pressure variation. For fine adjustments such as those needed to maintain stable pressure during the reaction, the coarse valve is closed, and pressure is controlled via a Cole-Palmer Multi-Turn Needle Valve. The valve system is connected through a series of aluminum tubes and cross-bars joined via aluminum compression clamps. The pumping force also aids in creating a compressive seal between the o-ring and the endcap to ensure isolation of the reaction chamber from the atmosphere. While at one point the system was fitted with a third automatic control valve, it was found that manual monitoring and adjustment provided a more stable reaction pressure. Of course such adjustments necessarily introduce human error into the synthesis process, a topic previously discussed in detail by Dr. Christopher Ma.[31]

Often argon or other inert gasses are flowed through the reaction system to further aid in reduction of contaminants. The gas control module is a simple system incorporating one or more gas tanks, each connected to an Aalborg Mass Flow Controller with an operation range of 0-100 standard cubic centimeters per minute (sccm). Gasses are introduced to the reaction chamber via inlets in the metal end caps. System pressure is measured using gauges connected to the aluminum fitting network. Two gauges are needed to measure lower and higher pressures, since the system ranges beyond the accuracy rating of a single measurement device. A convection gauge (BOC Edwards Analog Pirani Vacuum Gauge) is utilized to monitor lower pressures, as it is more sensitive in this range, while a digital gauge monitors the system at higher pressures. The system pressure is maintained at a minimum level for a duration adequate to reasonably assure significant atmospheric oxygen reduction (usually one hour or more). The pressure control valves are normally then closed to isolate the chamber from the vacuum pump, and the desired reaction pressure is reached. The pressure is continually monitored during

the reaction, and is adjusted up or down via fine adjustments to balance any perturbations away from the desired value. Depending on the nature of the desired synthesis, the pressure may be elevated to its maximum desired level prior to or after elevating the chamber temperature.

Reaction temperature is controlled as previously described according to programmed values. Ramp rates normally vary from 20 to 50 degrees C and can influence the final synthesis product. After the reaction is complete, a vacuum is reestablished, flowing gasses are arrested, and the tube is cooled. Often fans are used to speed up the cooling process.

2.2.1.3 Laser Assisted Vapor Synthesis

Pulsed laser deposition (PLD) coupled with catalyst-assisted vapor evaporation growth is the focus of more complex magnetic 1D nanostructure synthesis efforts due the PLD method's ability to maintain stoichiometry of ablated species to a greater degree than purely thermal evaporation, and the greater control of location and morphology of growing nanostructures the method affords. Though PLD was developed for fabrication of crystalline films, it has been successfully utilized for a variety of 1D nanostructure synthesis as well. PLD utilizes the energy of a focused laser beam on a material target, instead of or in combination with thermal energy, to vaporize the target materials which then re-assemble into new structures in cooler regions. A top-down schematic view of the PLD process is provided in Figure 2.6.

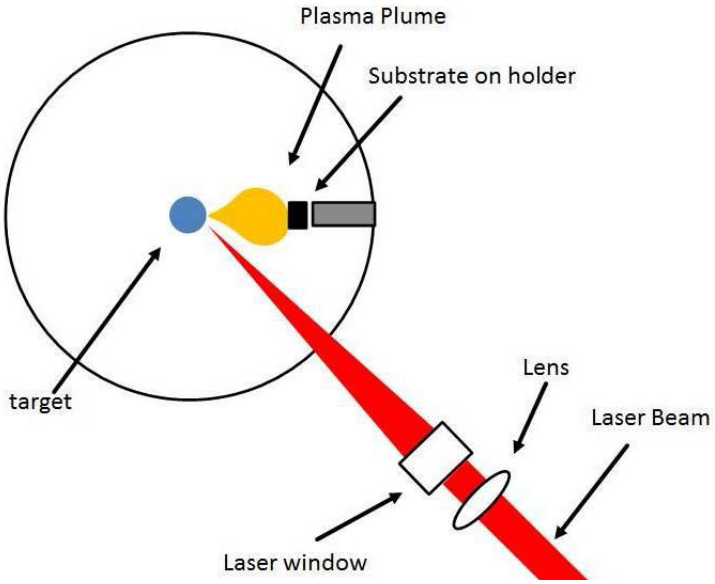

Figure 2.6: Schematic of a PLD System

According to Huntington Mechanical Laboratories, a manufacturing vendor and distributor of Kawasaki Pulse Laser Deposition Systems as well as online information published by NIST, the ability of PLD to retain the stoichiometry of the target in the deposited structure is the result of the extremely high heating rate of the target surface (108 K/s) due to the pulsed laser irradiation. This leads to the congruent evaporation of the target irrespective of the evaporating point of the constituent elements or compounds of the target. Also, because of the high heating rate of the ablated materials, laser deposition demands a much lower substrate temperature than other evaporation growth techniques. Nanostructured oxides of several compounds have been successfully grown by this method.[32] The figure below shows a schematic illustrating the basic PLD setup utilized for synthesis of 1D materials presented here. For these experiments a Compendex Series Excimer 102 Laser was used. The vacuum and gas flow modules are exactly the same as those used for general vapor deposition synthesis without the use of a laser. The furnace is also the same, however with a few modifications such as a laser-

rated end cap viewing glass and a change to a transparent tube material to allow for laser alignment.

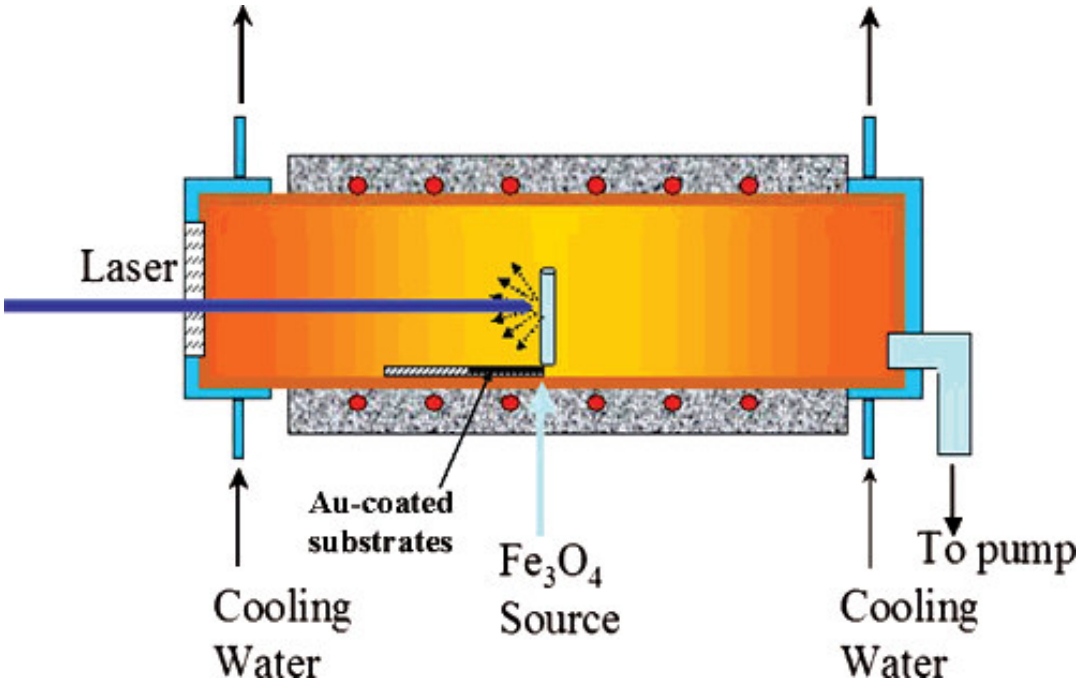

Figure 2.7: Schematic diagram of typical tube furnace PLD apparatus

The PLD apparatus consists primarily of a transparent quartz tube placed horizontally inside the single-zone tube furnace as shown in the diagram. As can be seen in the diagram, the center zone contains the source material. The quartz tube is more fragile than the thicker alumina tube used in thermal-only evaporation synthesis, but is chosen so that the laser can be aligned on the center of the source material prior closing the furnace and applying thermal energy. To minimize residual oxygen, the tube is evacuated to 10^{-2} Torr and held for 1 hour prior to running the experiment.

The furnace is heated to a temperature below the vaporization temperature of the source material to allow melting of the metal catalyst while ensuring that the source

vaporizes only via the energy of the incident laser beam. Pulsed laser energy is then directed through a specially-coated transparent window on one end of the tube toward the source material placed in the beam path. Vapors then condense onto waiting substrate strips pre-seeded with catalyst metal, and over time grow to form nanostructures of varying size, structure, and morphology. As substrate temperature decreases gradually from left to right, it is not uncommon to observe variation in size and morphology of products grown on different substrates in a single experiment.

2.2.2 Solution Based Synthesis

Any chemical formation process requiring solution chemistry is considered a solution based process. Since solution based (SB) processes are generally founded on simple mixing, heating, and separation processes, they have the advantage of generally requiring less sophisticated and therefore less expensive equipment, and tend to be more easily scalable to large volumes. Often materials with complex compositions are more easily synthesized through SB techniques compared to vapor evaporation. Also, since the material synthesis is conducted in solution, water solubility of the final product is usually not an issue.

However, SB synthesis suffers from its own disadvantages. Often synthesized products demonstrate a size distribution, rather than producing highly uniform nanostructures achievable through many evaporation methods. Contamination from residual reaction species can also be a problem. Finally, SB techniques are generally not the best methods to achieve high quality crystalline nanostructures, as synthesized materials are often plagued by many more point, line, and planar defects than vapor deposition fabricated materials.

This work leans heavily on vapor evaporation nanostructure synthesis. This technique allows creation of very high quality crystalline nanomaterials, and can produce complex and interesting nanostructures of extraordinary length. For some applications however, complex or long structures are not needed, and solubility and scalability issues are more important.

CHAPTER 3

MAGNETIC IRON OXIDE NANOWIRES

Advances in growth and characterization techniques have led to the production of modern magnetic materials which reveal a range of fascinating phenomena. These phenomena derive from the fact that magnetic materials take advantage of the spin component of electrons rather than charge, providing an extra level of complexity in physics, and an extra degree of freedom in device design. Magnetic materials allow action at a distance, providing a unique set of abilities to researchers in applying these materials to complex and practical problems.

In the nanoscale, where the influence of surface effects is much greater than in bulk, novel properties such as increased magnetization or superparamagnetism are often observed. Properties often can be tailored to specific needs by varying size, composition, or growth direction of the nanostructures. Nanoscale magnetic ferrites are of particular interest due to their size and chemical compatibility with biological tissues and their unique combination of electronic and magnetic properties. Magnetic nanostructures offer increased functionality for biomedical applications since they allow action from a distance through optically opaque living tissues via external magnetic field manipulation. They may also resonate in response to a time-varying field, transferring energy from the magnetic field to the structures themselves. [33]

Current biomedical uses of ferrite nanoparticles include targeted drug delivery, ultra-sensitive disease detection, gene therapy, hyperthermic cancer treatment, and MRI contrast enhancement. Much work is also focused on developing ferrite nanoparticles for ultra high-density memory storage, antiradar, and advanced communications devices.

Still, many current or proposed applications which utilize ferrite nanoparticles require a set of properties not achievable through available particle sizes and morphologies.

Although much recent work has been focused on synthesis, characterization, and application of ferrite nanoparticle and quantum dot morphologies for various uses, until the last few years, little literature has been published describing research relating to one-dimensional (1D) ferrite nanostructures. Based on experiments showing large variation in magnetic behavior due to size or morphology differences in nanoparticles, 1D ferrites, which confine atoms to nanometer scales in only two dimensions, exhibit properties unlike those of particles of the same phase. For example, published theoretical and some experimental evaluations state that ferrite 1D nanostructures maintain a greater magnetization than particles of similar volume, allowing better control of these structures when directed by a magnetic field.[34-37] However, much is still not known regarding how the properties of these materials respond to reduced dimensionality at the nano-level.

The objective of the work in this chapter was to gain greater understanding of magnetic behavior in 1D nanostructured ferrite materials through synthesis and detailed characterization, and to use this knowledge to work toward developing such structures into novel electronic and biomedical devices. Enhancement of these structures for specific applications can include tailoring of size and morphology, ordering, doping, and functionalization. In particular, 1D structures of magnetite (Fe_3O_4) and epsilon-Fe_2O_3 (ε-Fe_2O_3) were studied. Because magnetite is relatively nontoxic to human tissues, emphasis is placed on biomedical applications of these nanostructures, in particular their potential use as alternatives to spherical magnetic particles for cancer thermotherapy, while the epsilon iron oxide phase is explored with a focus on possible electronic applications such

as magnetic recording, microwave communication, and antiradar devices, as well as the conditions necessary to create this unique and elusive material.

3.1 Background

3.1.1 Magnetic Materials Theory

Any moving charge will produce a magnetic field. The physical source of magnetism in objects, distinct from electrical currents, is the atomic magnetic dipole. Considering the electron as a particle orbiting an atomic nucleus, magnetic dipoles or moments arise principally from two sources of electron movement. The first is the electron's orbital precession around the atomic nucleus, resulting in what is referred to as an orbital dipole magnetic moment directed along the nuclear axis. This effect is much weaker than the magnetic moment arising from the second source, the spin dipole magnetic moment, which originates from individual electron spins. Figure 3.1 provides an image demonstrating the generation of a magnetic moment arising from the spin of a single electron as it also completes its nuclear orbit.

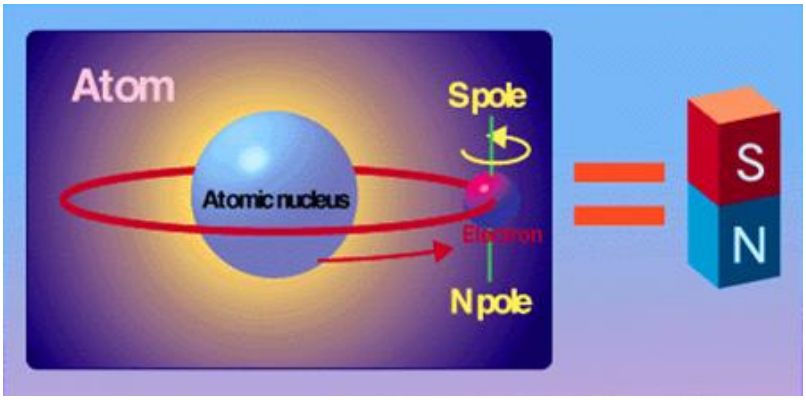

Figure 3.1: A schematic image showing a magnetic moment arising from a single electron's spin and orbital movement.

The overall magnetic moment of the atom is the net sum of moments produced by individual electrons. To reduce the net energy of the atom, electrons occupy first the lowest energy orbitals. Within these orbitals, unpaired electrons reduce Coulombic repulsions by aligning spins parallel while electrons in filled shells must align antiparallel to satisfy the Pauli Exclusion Principle. These effects combine such that often within an atom opposing pairs of magnetic moments will cancel. Thus an atom with a completely paired electron shell will experience no net spin magnetic moment. Only atoms with partially filled electron shells will possess a spin magnetic moment, whose strength depends on the number of unpaired electrons. The differences in configuration of the electrons in various elements thus determine the nature and magnitude of the atomic magnetic moments, which in turn determine the differing magnetic properties of various materials.[38]

All materials are magnetic to some extent, with their response depending on their atomic structure and temperature. They may be classified in terms of their magnetic susceptibility χ, where:

$$M = H \chi \qquad \textbf{(Eq. 3.1)}$$

In the above equation, M is the magnetization of the material, and H is the applied field. The susceptibility therefore is a measure of the material's magnetic response to an applied magnetic field, and as a vector quantity may vary both in magnitude and direction. χ is dimensionless, and M and H can both be expressed in terms of Am^{-1}. In ordered materials, M approaches saturation at large values of H. Coercivity is another measure of a material's magnetic response, and is defined as a measure of the reverse field needed to drive the magnetization back to zero once saturation has been achieved. [33]

General classes of magnetic behavior include diamagnetism, paramagnetism, superparamagnetism, ferrimagnetism, antiferromagnetism, and ferromagnetism. Each of these terms describes magnetic behaviors of materials based on the net strength of the materials' combined magnetic moment vectors. Whereas diamagnetic materials have no unpaired electrons and may weakly oppose magnetic fields due to orbital motion (negative susceptibility), paramagnetic substances contain unpaired electrons whose spin moments tend to align, to some degree, parallel to the applied field direction. However, the magnetic energies involved in this alignment are relatively small and the energy

associated with thermal agitation (kT) tends to work against the alignment, having a randomizing effect.

Unlike paramagnetic materials, ferromagnets retain a component of magnetization in the direction of the applied field after the field is removed.[38, 39] Magnetic moments in ferromagnetic materials are equal in magnitude and aligned parallel relative to each other. Since ferromagnetism results from the interaction of atomic moments in materials, there exists an exchange energy associated with coupling of the spin moments. At room temperature, this exchange energy is much greater than the energy due to randomizing thermal effects. If thermal energy exceeds the exchange energy, the coupling breaks down and the material behaves as a paramagnet. This critical temperature is dependent on the material and is called the Curie temperature (T_c) or, in the case of antiferromagnetic materials, the Neél temperature.[40, 41] Ferromagnetic crystals interact more than a million times more strongly with external magnetic fields than do diamagnetic or paramagnetic materials.[42] Antiferromagnetic and ferrimagnetism are special cases of ferromagnetism in which the strengths or directions of the individual magnetic moments vary, reducing or reversing the material's net attraction to the applied field.

In ferromagnetic and ferrimagnetic materials one often sees hysteresis, which is an irreversibility or energy loss in the magnetization process related to the pinning of magnetic domain walls at defects or grain boundaries in the material, as well as intrinsic effects such as magnetic anisotropy of the crystal lattice. Curves plotting magnetization of the material as a function of applied field (M-H curves) in these materials called hysteresis loops are open and sinusoidal. The area inside the curve is a measure of the irreversible work done by the material. The shape of these loops is determined in part by

particle size. In samples of micron size or larger, the ground state is multi-domain, leading to a narrow loop since it takes little magnetizing field to cause domain wall movement. In smaller particles, there is a single domain ground state which requires large energy to change and leads to a broad hysteresis loop. At even smaller sizes superparamagnetism is observed producing a non-hysteretic but still sinusoidal curve.[33]

Superparamagnetism is a phenomenon primarily observed in magnetic materials of reduced dimensions, on the order of tens of nanometers or less. Like paramagnetic behavior, superparamagnetic materials retain no magnetization upon removal of a magnetic field.[41] According to the Potts model, homogenous systems, where nearest neighbor electron couplings are equivalent, exhibit a single phase transition from ferromagnetic to paramagnetic at the Curie temperature as described previously. Inhomogeneous systems however, in which spins form magnetic "grains" with strong couplings between neighboring grains, but weak interactions between other pairs, show an intermediate superparamagnetic phase transition as the temperature is raised up to T_c. This transition is characterized by a sharp increase in the magnetic susceptibility of the material. The temperature where the superparamagnetic transition is observed is referred to as the Blocking temperature (T_b).[33, 43] This phenomenon is governed by the Neél-Arrhenius equation:

$$\tau = f_o \exp\left(\frac{v M_s H_c}{2kT}\right) \qquad \textbf{(Eq. 3.2)}$$

where
τ = relaxation time
f_o = lattice vibration frequency
υ = grain volume
M_s = spontaneous magnetization
H_c = Coercivity

k = Boltzman's constant
T = temperature
and ($\upsilon M_s H_c$) is the magnetic anisotropy energy.

According to this equation, the relaxation time, or the time the magnetization of the material remains stable after field removal, is exponentially dependent on the temperature and volume of the given sample. For this reason, superparamagnetism does not normally occur in larger particles as the temperature required to significantly reduce the relaxation time is higher than the Curie/Neél temperature.[41] The magnetic anisotropy represents a barrier to switching the magnetization of the sample. In reduced dimension systems, where υ is very small, the anisotropy energy required to achieve the phase transition from disordered (paramagnetic) to ordered (ferromagnetic) is on the order of kT, causing large thermal fluctuations of the magnetization direction between parallel and antiparallel orientations, while individual atomic moments maintain their ordered state relative to each other, significantly increasing the magnetic susceptibility of the material.[44] One cannot assume that the size and morphology dependence of this phenomenon is a simple function of the sample's volume, however, since the magnetic anisotropy energy is also dependent on sample geometry, stress, and crystal structure.[45]

3.1.2 Magnetic Iron Oxide

Magnetite (Fe_3O_4) and Barium hexaferrite ($BaFe_{12}O_{19}$) are two examples of metal oxides which act as strong ferrimagnets in bulk. As seen in the figure below, magnetite has a cubic inverse spinel structure in which oxygen ions form an FCC structure, with

cations occupying tetrahedral and octahedral interstitial sites.

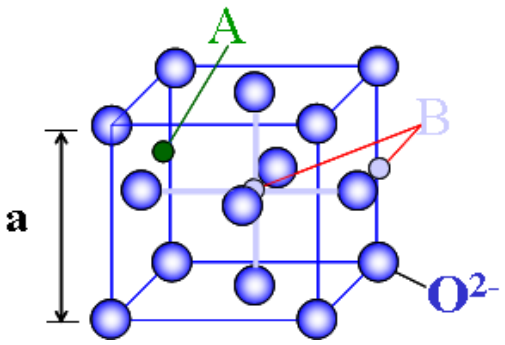

Figure 3.2: A ball and stick diagram of a magnetite unit cell

One tetrahedral site is occupied by a single Fe^{3+} ion, while the remaining Fe^{+3} ion and Fe^{2+} ion occupy two octahedral sites in the cubic unit cell. At room temperature, electrons can hop between the octahedral Fe^{2+} and Fe^{3+} ions,[46] making bulk magnetite not only highly magnetic (T_c = 858K) but electrically conducting as well. Magnetite's "easy" axis of magnetization, that is, the axis where the crystallographic contribution to the anisotropy energy is minimized, has been found to be the [111] direction at room temperature (see Figure 3.3).[42, 47]

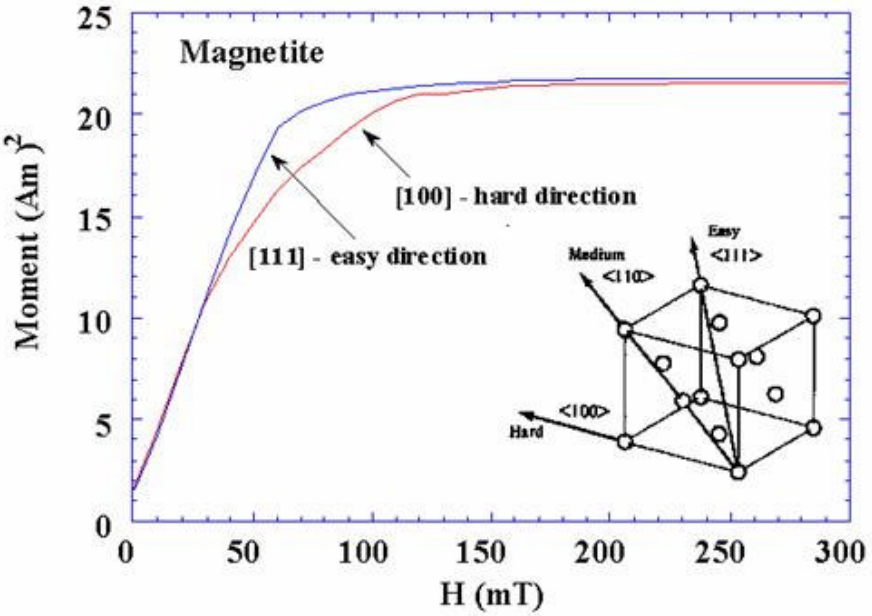

Figure 3.3: Magnetite's "easy" axis of orientation is in the [111] direction.

Unpaired electron spins contributed by Fe ions combine in magnetite such that its net moment is four Bohr magnetons per molecule, a relatively high magnetization.[46] . In bulk, magnetite has a high Curie temperature (T_c ~850 K) and nearly full spin polarization,[48] which make it appealing for giant magnetoresistance and spin valve devices.

The α-Fe_2O_3 phase, commonly known as hematite or rust, is only weakly ferromagnetic above its Morin Transition at 260K. Below this temperature the material is antiferromagnetic. The structure of this phase is similar to that of corundum, and consists essentially of a dense arrangement of Fe^{3+} ions in octahedral coordination with oxygen atoms in hexagonal close-packing arrangements. Hematite's structure can also be described as the stacking of sheets of octahedral (six-fold) coordinated Fe^{3+} ions between

two closed-packed layers of oxygen atoms. Since Fe is in a trivalent state (ferric Fe), each of the oxygen atoms is bonded to only two Fe ions, and therefore, only two out of three available oxygen octahedrons are occupied. This arrangement makes the structure neutral with no charge excess or deficit. The Fe-O sheets are held together by strong covalent bonds and these results in a very hard and dense structure. Hematite is a low energy phase and therefore is thermodynamically stable compared to other phases of iron oxide, such as magnetite. Figure 3.4 and Table 3.1 below show an iron-oxygen phase diagram and a table identifying some other iron oxide phases, respectively.

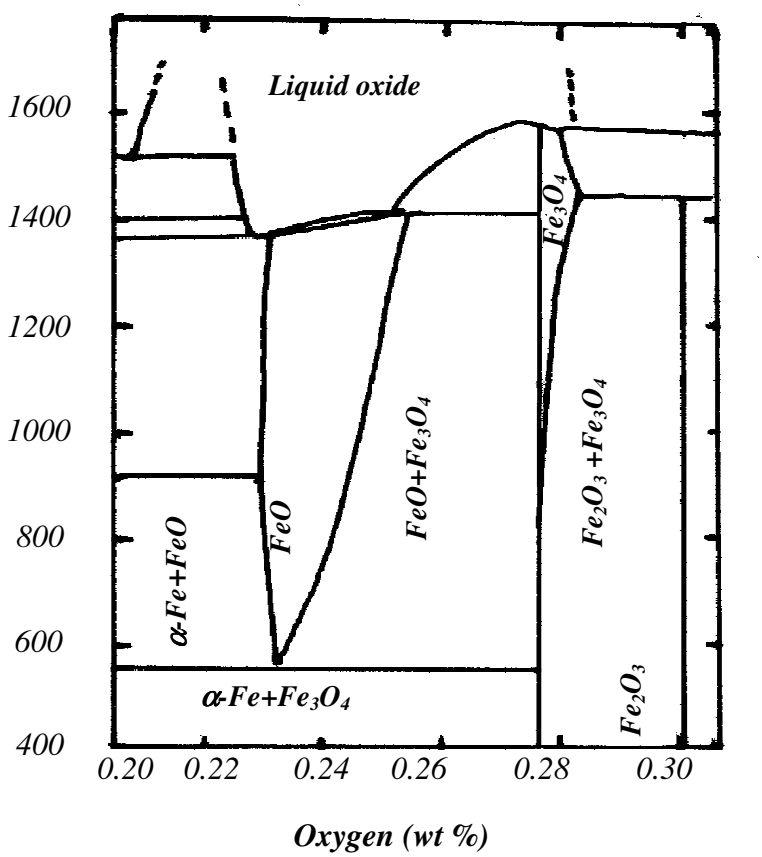

Figure 3.4: Phase diagram illustrating chemical relation between several iron oxide phases.

Table 3.1: Table with properties of some common iron oxide phases

Color	Designation	Name	Structure	Crystal System
Yellow	FeOOH	Goethite	Ramsdellite/ hcp oxygen	Orthorhombic
		Akaganeite	Hollandite/ bcc oxygen	Tetragonal
		Lepidochrocite	Boehmite/ ccp oxygen	Orthorhombic
		–	CdI_2	Hexagonal
Red	Fe_2O_3	Hematite	Corundum	Hexagonal
		Maghemite	Defect spinel	Cubic
Black	Fe_3O_4	Magnetite	Inverse spinel	Cubic

3.1.2.1 Magnetic Iron Oxide Nanostructures

Much is not known regarding magnetic behavior of materials in the nanoscale, where some bulk characteristics are maintained, yet surface and quantum effects are no longer negligible. Reduced dimensions at the nanometer regime push the material to theoretical limits of behavior. One of the most important driving forces in condensed matter physics in the last thirty years has been the controlled growth of layered structures so thin that interface effects dominate bulk properties and quantum size effects can be observed. Structures and properties on the atomic level are determined by complex interactions that require a full quantum-mechanical treatment. At dimensions so small, both experimentalists and theorists have found the task of identifying and organizing material characteristics difficult.

Understanding nanoscale magnetism, arising within the atom at the single-electron level, has proven extremely elusive for scientists, but as the ability to make, manipulate and test magnetic nanomaterials grows, so does insight. Considerable research has been conducted on magnetite thin films (2D) and particles (0D) to try to

understand changes in magnetic behavior at the nanoscale. Magnetite 1D structures have also been studied, including both rod and tube morphologies.[49] Since the theory of magnetic nanomaterials necessarily involves the aid of quantum physics, a realm in itself not wholly complete, the underlying physical nature of these materials' intriguing properties will not be discussed at length here. This work will focus on practical understanding of materials synthesis (examined in relation to known principles) so that these materials may be successfully applied to applications for which their properties are well suited.

Nanoscale magnetic ferrites are of particular interest for use in devices and medicine due to their size and chemical compatibility with biological tissues and their unique combination of electronic and magnetic properties. Current biomedical applications of magnetite nanoparticles include targeted drug delivery,[50, 51] ultra-sensitive bio-agent detection,[52, 53] gene therapy,[50, 54] hyperthermic cancer treatment,[50, 51, 55] and Magnetic Resonance Imaging (MRI) contrast enhancement.[50, 56, 57] The stability and electronic properties of the more common hematite (α-Fe_2O_3) make it an ideal candidate as a photocatalyst and as a photoelectrode in solar energy conversion applications.[58]

Much work is also focused on developing ferrite nanoparticles for ultra high-density memory storage[59, 60] and advanced communications devices.[61] Ferrite nanoscale materials are favored over other rare-earth alloys to aid in addressing the current need to overcome superparamagnetic limits in conventional recording due to their relative low cost, stability, low toxicity, and most importantly, high resistivity, reducing unfavorable eddy current energy loss.[62] ε-Fe_2O_3 is well suited to such applications due

it its very high room temperature coercivity (maximum H_c = 20 kOe).[62, 63] In fact, at low magnetic saturation (M_s), nanorods of ε-Fe_2O_3 exhibit greater coercivity than "model" hard magnetic materials like Barium Hexaferrite and HCP Co.[64] Unlike α-Fe_2O_3, ε-Fe_2O_3 is considered a rare and metastable form of iron oxide,[65] and until now has only been observed in small nanorods or nanoparticles. It is ferrimagnetic at room temperature (T_c ~510K), and due to its magnetic moment coupled with an orthorhombic non-centrosymmetric structure, ε-Fe_2O_3 is expected to also exhibit piezoelectric, magnetoelectric, optical, and pyroelectric behaviors. Such coupling of spontaneous magnetization and electronic polarization promises exciting advances in such areas as electric/magnetic field tunable devices or multiple state memory.[66]

Still, many current or proposed applications that utilize ferrite nanoparticles require a set of properties not achievable through available particle sizes and morphologies.[67, 68] Many current technologies relying on magnetic iron oxide particles or quantum dots could be greatly improved through enhanced magnetic and electronic properties. Based on experiments showing large variation in magnetic behavior due to size or morphology differences in nanoparticles as well as a few recent studies on ferrite nanorods and nanowires, 1D nanostructured ferrites are expected to exhibit many properties unlike those of particles of the same phase. [69-72] Recent research has shown that the high aspect ratio of magnetic nanowires can produce a larger magnetic moment than that observed in particles of the same volume, providing significant benefits in numerous applications.[73] Biomedical applications, for example, could potentially benefit greatly through the use of such nanostructures, allowing advances both in the lab and in the clinical setting. In fields such as local drug delivery, improved magnetic

properties would allow the ability to deliver drugs more quickly and accurately, enabling treatment of smaller areas with lower dosages and decreased side effects. Novel ferrite properties could likewise benefit current communications, defense, memory storage, and energy technologies. The large coercivity (H_c) observed in nanoparticles of ε-Fe_2O_3, for example, is believed to be the result of the material's large magnetocrystalline anisotropy. [62, 63] 1D morphologies provide an additional component of magnetic anisotropy, the shape anisotropy.[74] Often dominant in nanoscale materials, shape anisotropy contributions could produce 1D structures of ε-Fe_2O_3 capable of properties far exceeding those observed in nanoparticle morphologies. 1D nanostructures of magnetite, hematite, and ε-Fe_2O_3 also provide ideal theoretical systems for fundamental studies of electron spin and magnetic behavior of materials near quantum levels. Magnetic characterization of 1D ferrite nanostructures is essential both as a step toward exploitation of desirable properties for new and improved applications, and also as a means to better understand electronic behavior in the nanoscale regime.

This section focuses on ferrite 0D and 1D nanostructures. Much work has been conducted previously on ferrite 2D thin films for recording media and other applications. [75, 76] Due to the wealth of previous work on 2D ferrites and the emphasis of this effort on applications generally requiring 0D or 1D morphologies, 2D nanoscale ferrites will not be discussed at length here.

3.1.2.2 0D Magnetic Iron Oxide Nanostructures

In one representative paper published in 1996, D. T. Marguiles *et al* observe anomalous behavior in magnetite thin films grown on a variety of substrates. They report

that magnetic moments were unexpectedly found to be directed out of the plane of the film, and unlike bulk material, the 2D magnetite would not saturate even at very high magnetic fields. In addition, by testing films of various thickness (10nm-6μm), the authors determined that these behaviors were a volume, not surface, effect and appeared to be intrinsic properties of all Fe_3O_4 films.[77] More recent work finds similar deviations from bulk behavior in 2D magnetite. A few years ago, Moussy et al reported that Fe_3O_4 (111) thin films 5nm to 50nm in thickness exhibited anomalous magnetic properties such as lower magnetic moments than that of bulk and uncharacteristic inability to saturate at high field strengths. These phenomena also varied according to film thickness in good agreement with earlier research. Explanations of these abnormal phenomena vary, and include effects due to phase boundaries, defects, and internal strain among others. [77, 78]

In 0D morphologies, deviations from bulk behavior are even more pronounced. Phase transitions in ultrafine particle systems can take place at significantly lower temperatures as compared to the bulk material.[79] Magnetite nanoparticles from 3 to 300 nm in diameter have been found by many sources to behave as superparamagnets at room temperature, magnetizing strongly under an applied field, but retaining no magnetization once the field is removed.[46, 80-82] Researchers disagree regarding the effect of reduced size on saturation magnetization of Fe_3O_4 nanoparticles, finding in some cases that values decrease as sizes reach 12nm, while others report an increase in saturation magnetization down to 10nm, with a decreasing value as size is reduced beyond this point.[82, 83] Like magnetic thin films, researchers have not reached a consensus on the principle mechanism responsible for such anomalous behaviors.

Possible explanations include irreversible changes due to experimentation, surface layer effects, superparamagnetic relaxation, and others. [82]

Current biomedical applications of magnetic nanoparticles include MRI contrast enhancement (Figure 3.5), cell separation (shown schematically in Figure 3.6 below), hyperthermic cancer treatment, drug targeting, genetic screening, disease detection, and others. [81] Magnetic nanoparticles are also currently being developed into single-molecule biosensors, as illustrated in Figure 3.7.

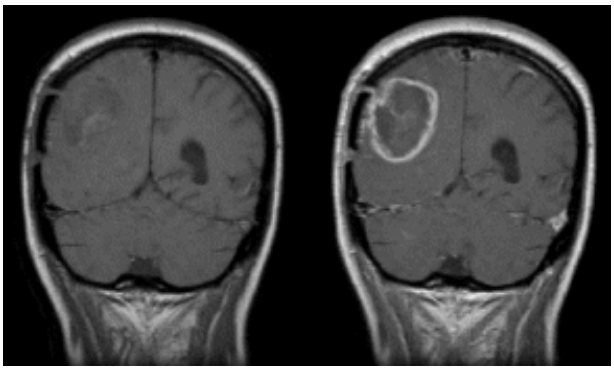

Figure 3.5: An MRI image showing the same location in the brain of a human patient before (left) and after (right) addition of magnetic nanoparticles for MRI contrast enhancement.

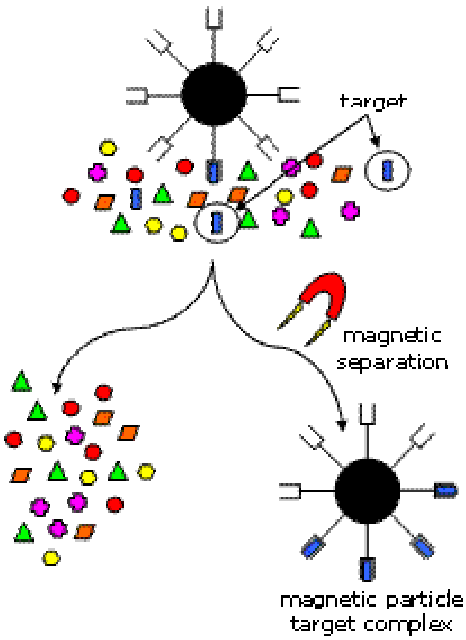

Figure 3.6: A schematic illustrating basic molecular target or cell separations with specially functionalized magnetic nanoparticles.

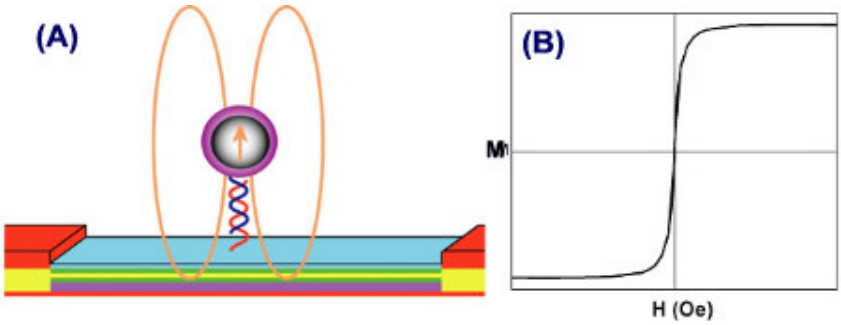

Figure 3.7: (A) Schematic illustration of magnetic nanoparticles as labels for DNA sensing. The particles are attached to a magnetic sensor via DNA hybridization. (B) Hysteresis loop of superparamagnetic particles.

Nanoparticles of Fe_3O_4 are often used for biomedical applications since they are relatively easy to synthesize, chemically stable, superparamagnetic, and are known to be nontoxic.[84] Since many biological systems are designed to process excess iron, iron oxide nanostructures left in the body are eventually broken down to form blood

hemoglobin. Magnetite nanoparticles have been found as naturally occurring compounds in animal species such as trout, ants, mice, and birds, as well as human organs such as the brain, spinal cord, and bone tissue.[42] Other magnetic compounds are also under investigation for biomedical applications; however, so far few have been found to offer a better combination of properties than Fe_3O_4 for its common uses.[81]

In some *in vivo* applications, magnetic nanoparticles are injected intravenously, utilizing blood circulation as transportation, or may be injected directly into the general treatment area. Either of these routes demands that the particles do not aggregate, so superparamagnetic behavior is desirable for such applications. Fortunately there is appreciable intercellular space in the body through which nanoparticles can diffuse, largely between cells. Diffusion of particles less than 50nm in diameter is presumably aided by pressure gradients from blood vessels to the tissue spaces. Experiments have shown that larger particles of 50-100nm diameter are not able to be transported in this manner and remain in circulation or attached to vascular walls, a condition which carries the risk of complicating normal flow and cellular processes. Unfortunately in 0D morphologies such as particles, once the superparamagnetic limit is reached, response to applied magnetic fields may decrease as diameter decreases. [84]

Magnetite nanoparticles are also increasingly being used for hyperthermic cancer treatments in which an alternating magnetic field generates heat in precisely located particles to kill (thermablation) or sensitize (hyperthermia) cancer cells. These treatments are described as “localized” cancer treatments because the disease fighting agents are designed to accumulate locally, around the affected area, rather than the entire body. A schematic describing the general localized treatment process is provided in Figure 3.8.

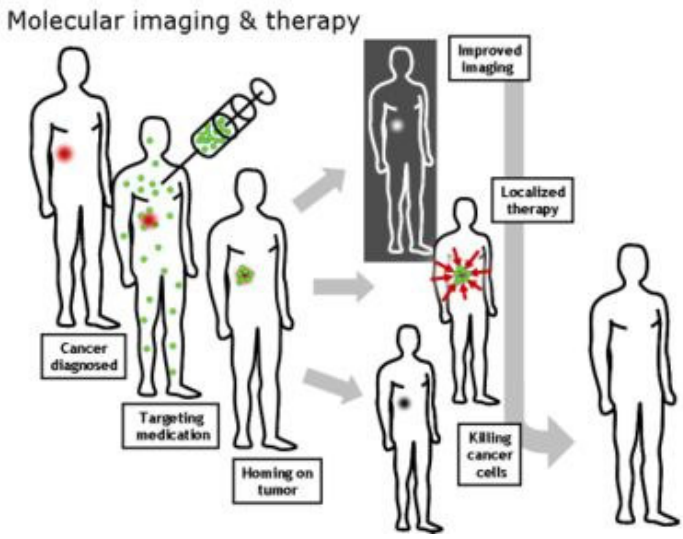

Figure 3.8: Schematic illustrating basic steps in localized cancer treatment process

As the figure shows, disease-fighting agents are localized to a known tumor region where they commonly are imaged and then through external cues are released to kill or weaken cancer cells while maintaining health in normal tissues.

Thermotherapy treatments follow a similar process. First magnetic particles are localized near cancer cells. Magnetic particles are either injected directly into the diseased tissue or allowed to accumulate via transport through vasculature, often under the direction of an applied field. Blood vessels created by cancerous cells rather than healthy tissues often are not well-formed and are described as "leaky." These leaky vessels provide ideal routes for anti-cancer agents to diffuse through the vasculature and agglomerate near diseased tissue. Often the particles are designed to bind specifically to cancer markers via specially designed antibodies. [84] In this way, the surface of the nanoparticle can be functionalized to bind specifically to the targeted tumor tissue, and not to healthy tissues. For this to work, however, the biochemical signature of the cancer must be well known.

Once the magnetic particles are localized near the site of the tumor, they may stick on the outside of the diseased cells, or may be taken in by them, according to the design of the magnetic particle. An MRI can then image the nanoparticles to ensure that they are well-localized, and apply an alternating magnetic field to the targeted area. The energy generated due to the particles inability to keep up with the switching field is lost to the environment as heat. This heating of only a few degrees above normal body temperature ideally affects tumor cells, causing them to weaken or die, while minimally affecting normal tissues. It is still somewhat unclear as to why localized heating works so effectively, though studies have shown that cancer cells are less able to withstand elevated temperatures compared to normal cells due to reduced vasculature in cancerous tissue. Cancer cells' relative inability to resist heat shock proteins generated by the process may also be a factor. [85-87] These treatments are generally referred to as cancer thermotherapies. Literature reports temperatures generated in the tissue must reach 50-55^{o}C to ensure complete cell necrosis, while temperatures as low as 40^{o}C can successfully sensitize cells for further treatment. These therapies offer significant benefits over more common routes such as radiation, chemotherapy, and surgery in that treatment is site-specific and non-invasive. [33]

Magnetic particle heating in the external AC (alternating current) magnetic field is due either to loss processes associated with reversal of coupled spins within the particles or frictional losses caused by viscous interaction of the rotating particles and their tissue medium. Magnetic losses can be further subdivided into two classes, either hysteretic losses of the type discussed previously, or relaxation losses caused by 1) reorientation of the magnetic moment of the particle or 2) Brownian losses due to

reorientation of the magnetic particle itself. Relaxation times depend in part on particle diameter. With the exception of ferromagnetic coupling, similar loss mechanisms apply whether magnetic moments in the material express ferromagnetic or superparamagnetic behavior. However, superparamagnetic particles are usually preferred as they produce more heat per mass, offering better heating at reduced field strengths, and do not pose agglomeration risks.[33, 84] The level of heating is controlled by the material's Curie temperature, above which the particles lose magnetic susceptibility and are no longer able to respond to the AC magnetic field.[88]

For the AC field parameters, the general tendency is that the higher both the amplitude and frequency, the more heating power may be generated in the particles. However, there exists a limitation in that exposed tissues may be unintentionally heated by eddy currents producing harmful side effects. For this reason it is common to require a 1cm buffer safe area around target tissue in case undesired heating of surround regions occurs. Also, parameters that may interfere with the body's normal electromagnetic processes must be avoided. Unfortunately, these effects increase the minimum tumor size available for thermotherapy. It is imperative therefore that particles can be precisely placed and heat efficiently as possible for successful results.

Experiments have shown this technique highly effective in treatment of tumors both in animals and in initial human clinical trials. Studies on rats have shown complete remission of cancer cells following AC magnetic field thermotherapy compared to no remission in animals given up to ten times the dose of particles but with no magnetic targeting. According to clinicaltrials.gov which posts information from the National Cancer Institute, a Duke University study entitled "Hyperthermia, Radiation Therapy,

Surgery, and Optional Chemotherapy in Treating Patients with Soft Tissue Sarcoma of the Limbs" is currently seeking participants to investigate the effects of such thermotherapy treatments when given in parallel with radiation and optional chemotherapy. Magnetic heating has also been employed in a similar fashion as a method of drug delivery for cancer, utilizing the temperature rise to induce drug release into diseased tissue. Other methods of thermotherapy such as induction heating have been explored, but have so far been found to be less effective, as magnetic heating offers a way to ensure that only the intended target tissue is heated.[33] Also, thermotherapy treatments which utilize light energy at frequencies transparent to many tissues to heat up particles such as gold are being investigated for similar applications, and have found some success in *in vivo* studies. [89, 90] Thermotherapy has even been shown as an effective treatment for tumors in the brain, a difficult location to target due to the necessity of the particle to pass through the blood brain barrier (BBB), a kind of biologic guardhouse designed to prevent passage of harmful substances into the body's neurological center.[91]

Even though magnetite nanoparticles are physiologically well tolerated, any biomedical application whether *in vivo* or *ex vivo* requires surface modification to ensure that they are not recognized by biologic defense systems as foreign. Particles with largely hydrophobic surfaces are efficiently coated by the body with plasma components, rendering them recognizable to the body's defenses, thus rapidly removing the particles from the bloodstream. Functionalization with hydrophilic polymer chains is often necessary to resist this coating process and allow particles to be circulated out more slowly [88] PEG (polyethylene glycol) and dextran (a high molecular weight

polysaccharide) are both compounds commonly utilized to reduce uptake and lengthen circulation times *in vivo*.

Nano sized ferrites are also beneficial in electronic applications and devices where ultra small components are necessary. Materials such as ε-Fe_2O_3, with high magnetic anisotropy, coercivity, and mechanical hardness make ideal candidates for magnetic storage media, and in fact ε-Fe_2O_3 is commonly used for this application in thin film morphologies. While bit densities have increased enormously over the last decade, media noise and superparamagnetic effects dictate that the current fabrication processes be revised. Most commercial magnetic recording systems use a 2D medium in which signal-to-noise considerations demand at least 1000 polycrystalline grains per bit. Increasing storage density requires decreasing grain size, however, at very fine grains the superparamagnetic limit is reached, rendering the material useless for storage applications. As shown in Figure 3.9, one possibility to overcome this obstacle is the use of vertically patterned media, in which magnetic moments are aligned perpendicular to the plane of the film, and each bit is stored in an individual single-domain magnetic nanostructure. One-domain structures necessitate the use of nano-sized 0D or 1D nanostructures. [92-95] The benefits of 1D morphologies in magnetic nanostructures for some applications traditionally employing 0D nanoparticles is described below.

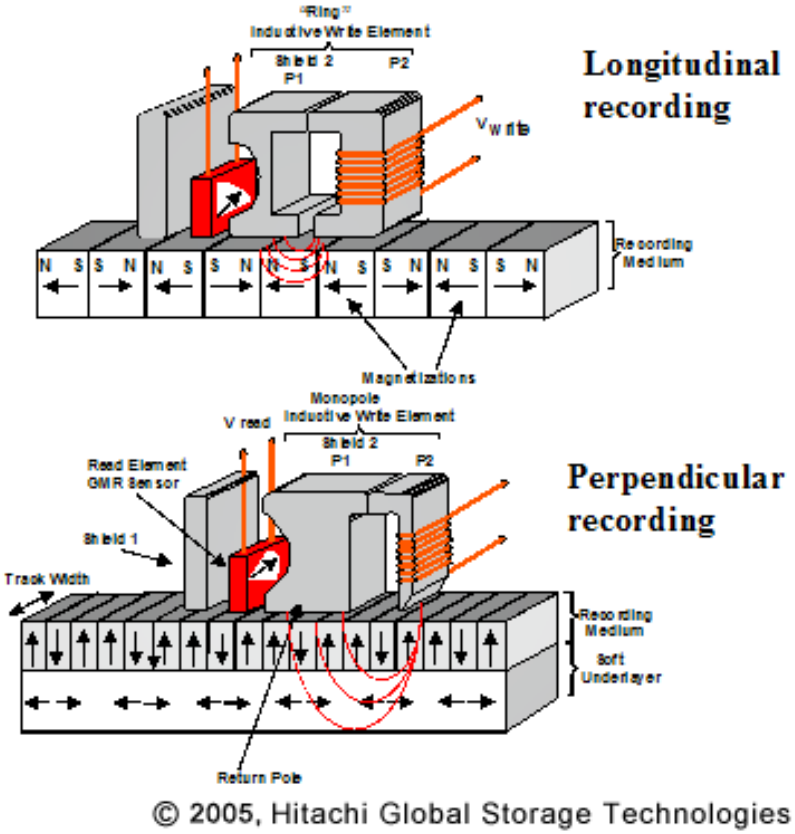

Figure 3.9: Schematic images illustrating traditional recording media (top) and the benefit of smaller bit sizes through perpendicular recording media (bottom)

3.1.2.3 Applications and Motivation for 1D Magnetic Iron Oxide Nanostructures

While magnetic quantum dots and nanoparticles have shown great promise for non-invasive AC magnetic field based tumor thermotherapy treatments, proper location and regulation of generated heat energies within tissues is still critical. Effectiveness of these therapies is dependent on several parameters, including field strength, concentration, volume and magnetic properties of the particles. For magnetite nanoparticles, safety concerns and imperfect delivery limit tumor sizes realistically available for magnetic particle thermablation to over 1 cm in diameter. In easily

accessible areas, efficiency can be improved by increasing nanoparticle concentration through direct injection; however, this approach restricts the therapy's applicability and elicits concerns regarding adequate organ clearance and toxicity. Volumetric augmentation reduces the particles' ability to safely navigate into the tumor region. Some have proposed use of other materials with enhanced magnetic properties; however, magnetite remains the material of choice due to its long history of biologic compatibility.

A focus of this work is an investigation of one-dimensional magnetite nanorods and nanowires as alternatives to spherical particles for non-invasive thermotherapy treatments in an effort to improve both delivery and heating effectiveness. Both literature and computational models predict that due to shape factor effects, magnetite nanorods and nanowires display significantly enhanced magnetic field response compared to spherical magnetite particles of the same volume. This increased response should translate to improved field-directed delivery and greater efficiency in tissue heating. If successful, such advances would allow treatment of smaller tumors in more remote areas, effective use of safer magnetic field strengths, reduced risk of complications due to accumulation or damage to healthy tissue, and increased mortality of targeted cells. In addition, nanorod morphologies provide improved physical surfaces for multiple species functionalization which later on may be exploited for tumor targeting, drug delivery, or clearance.

The shape of nanomaterials can be as vital as the size in determining the novelty of material properties due to the dominating role of anisotropy in magnetism.[96] 1D nanosystems are often the most challenging to prepare due to the highest anisotropy parameters, however high anisotropy is commonly a desired property for functional

magnetic nanomaterials. For example, highly anisotropic magnetic nanowires have been shown to posses ferromagnetic properties at room temperature even at diameters as low as 2nm. Such high remanence magnetization at very small sizes is greatly desired for high density recording media. [97] Unique magnetic properties have been observed in magnetite nanowires such as perpendicular (rather than in-plane) magnetic anisotropy and reduced transition temperatures.[98]

Research has shown that the high aspect ratio of magnetic nanowires can produce a larger moment than that observed in particles of the same volume, providing significant benefits in both biomedical and electronic applications. [81] Competition between shape and crystalline anisotropy is the most common mechanism attributed to deviations from bulk magnetic properties in magnetite nanowires.[96, 98, 99] Quasi-1D wires made up of agglomerations of Fe_3O_4 particles may exhibit properties more common to 0D morphologies such as irregular hysteresis, so high quality single-crystalline nanowires or nanotubes are essential.[99, 100] Magnetite nanostructures in 1D morphologies may provide the perfect balance of magnetic properties for *in vivo* applications, allowing superparamagnetic behavior with enhanced remote manipulation abilities. One study reports use of magnetic nanowires rather than beads of similar diameter in magnetic cell separations increases effectiveness by a factor of four.[88] The increased magnetizations of 1D nanostructures allows for manipulation at lower field strengths and reduced dosages. Varying processing parameters should provide control over nanowire length and aspect ratio, which may allow 1D ferrites to act as ferromagnets for some applications, or superparamagnets for applications where remanence is not desired. Properties can be further engineered through control of growth direction and functionalization. Commonly

performed on nanoparticles, 1D morphologies should make functionalization easier due to increased area, or even allow for attachment of multiple species. [101] Complex functionalization may be key to allowing access of nanostructured devices to areas such as brain and kidneys. For applications relying on heat generation, larger susceptibilities of 1D magnetite nanostructures should increase heating effectiveness in an alternating magnetic field. Studies find even small deviations of particles from spherical morphologies cause magnetic anisotropy exceeding that originating from crystalline effects.

This enhanced magnetic effect is demonstrated in the figures below, which were generated by COMSOL Multiphysics computer simulations software. The COMSOL program uses the finite element method (FEM) to model and solve scientific and engineering problems based on partial differential equations. The red arrows in these images indicate magnetic flux density and direction, while the white to grey color bar and shading indicate quantitative values for magnetic potential. In these examples only quarter sections of the permanent bar magnet and magnetite objects are shown. This is because the symmetrical nature of the problem allows simplification of the model for shorter processing times without compromising results. The table reports quantitative results from the study for a full system. The belt morphology listed in the table is for a 1D structure with rectangular dimensions not shown in the pictorial figures.

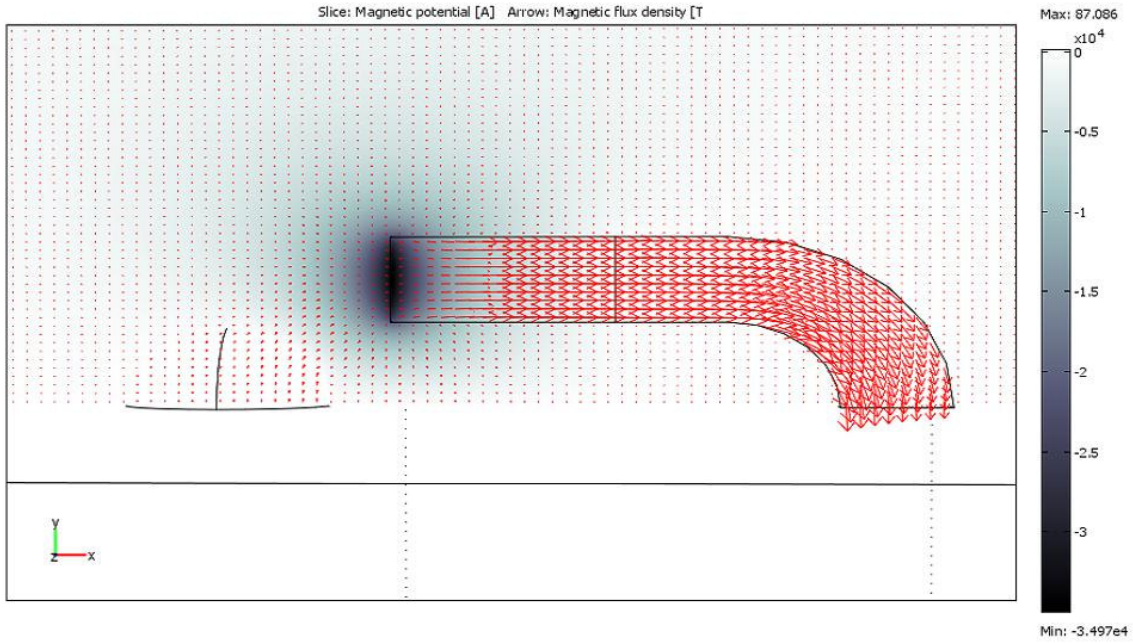

Figure 3.10: Arrow plot of magnetic flux density as it acts upon magnetite material with a spherical geometry. The sidebar indicates the magnetic potential from the applied bar magnet.

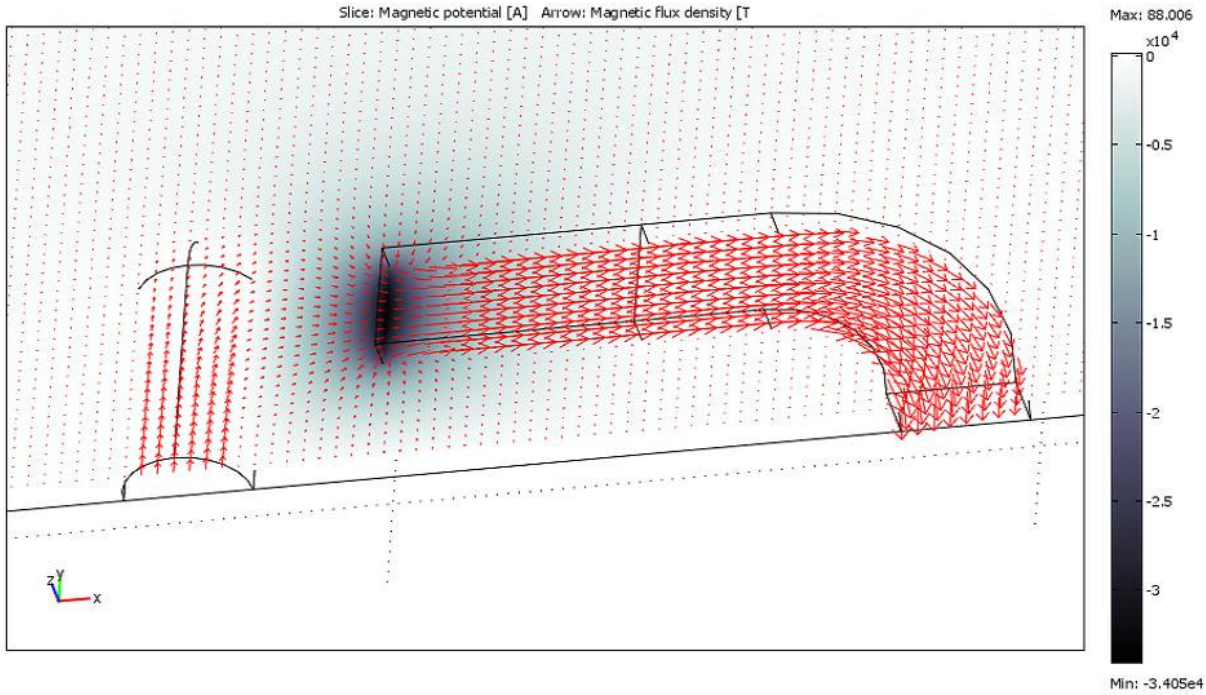

Figure 3.11: Arrow plot of magnetic flux density as it acts upon magnetite material with a rod-like 1D geometry. The sidebar indicates the magnetic potential from the applied bar magnet.

Table 3.2: Quantitative results from COMSOL simulation demonstrating greater magnetic forces in the x and z directions under application of a permanent magnet on a magnetite rod compared to a magnetite sphere of the same volume.

	Radius	volume	Max Mag Permeability*	Force x	Force y	Force z
	(units)	(units^3)		(Newtons)	(Newtons)	(Newtons)
Iron Rod	0.1	0.11728	5000	590.8	62.8	286.28
Iron Sphere	0.1913	0.11728	5000	242	301.88	123.92
Iron Belt		0.11728	5000	525.6	24.8	91.2

In these simulations the initial permeability of Fe_3O_4 is input as 5000 (unitless) with a maximum permeability of 25,000. The magnet's magnetization value is input as 750,000 (A/m). These values are commonly accepted for bulk materials and common permanent magnets. The force on the magnetite materials is calculated by integrating the surface stress tensor over all boundaries of the magnetite geometry. The expression for the stress tensor reads:

$$n_1T_2 = - ½(H \cdot B)n_1 + (n_1 \cdot H)B^T \qquad \textbf{(Eq. 3.3)}$$

where n_1 is the boundary normal pointing out from the rod, T_2 is the stress tensor of air, H is the magnetic field intensity, and B is the magnetic flux density. This integration yields values which correspond to one quarter of the full system, since the model has been reduced to a fourth for increased processing speed. Output values have been multiplied by 4 to find the full-system values reported in the above table. Along the boundaries far from the magnet, the magnetic field is set to be tangential to the boundary, as the flow

lines should (according to physical laws) form closed loops around the magnet. This is done by setting the boundary condition on the potential according to the equation:

$$n \cdot (\mu_0 \nabla V_m - \mu_0 M_0) = n \cdot B = 0 \qquad \textbf{(Eq. 3.4)}$$

where μ_0 is the initial magnetic permeability, V_m is the scalar magnetic potential, M_0 is the initial magnetization, and other variables are consistent with the previous equation. [102]

In the table above, note that the magnet acts with greater force upon the rod geometry in the x and z directions. Only in the y direction is the force on the sphere greater. (The belt morphology is reported as a comparison and is not an ideal geometry for this application.) This finding indicates that for the purposes of magnetic localization, spherical geometries should be non-ideal since the nanorod will need to move in a transverse direction to the applied field, and should demonstrate greater force due to the field in two of the three special dimensions. Note however that this finding should not be extended beyond its immediate implications, since the system does not perfectly describe the phenomena it models. The magnetic force is derived from a non-uniform permanent magnet with a scalar magnetic potential instead of MRI or other alternate sources, likely having different and more complex characteristics. This treatment is for a single magnetite object and does not take into effect the potential complications if many magnetizable objects interacting with the field. Finally, this simulation uses bulk values and mathematical equations which may not be fully accurate for smaller systems.

However, these results are supported by other more rigorous treatments found in the literature. [103]

For thermotherapy application it is highly desirable for dosage to remain as small as possible while still achieving effective heating. One must consider that *in vivo*, less than ideal conduction, binding and accumulation conditions will decrease effectiveness of treatments. [84] For treatment of tumors in areas where health of surrounding tissues is critical, the benefit of more precise location targeting through 1D nanostructures' improved magnetic field response is also very important. Increased magnetization in 1D structures, due to increased crystalline and shape anisotropy, would allow for more precise location targeting, greater heating ability, lower necessary dosage, ability to treat smaller tumors, and less risk of harmful side effects due to eddy currents. In addition to possible benefits provided by larger magnetic moments, 1D nanostructures may also offer greater heating efficiency in thermotherapy treatments due to a possibly narrower size distribution than that of particles. [84]

Of course with any new technology, the benefits must outweigh any additional negative risks. Potential problems with 1D nanostructures compared to nanoparticles may include difficulties in engineering and fabrication, the potential to damage cells if high aspect ratios lead to sharp edges, and the potential for difficulties with flow through vasculature and proper localization. Fabrication issues are addressed elsewhere. The risk of sharp edges damaging tissues can likewise be addressed through careful synthesis or post-synthesis functionalization and should be tested as are all new medical materials for general toxicity. Differential flow, however, is an engineering problem. Some initial reports have found that ellipse-like 1D geometries actually demonstrate improved

vasculature flow and localization compared to spherical particles.[104]The work below provides further evidence through computational modeling that flow should not be a limiting obstacle to the application of nanorod or ellipse-like 1D nanoparticles to localized cancer thermotherapy.

Figures 3.12 and 3.13 below present the results of fluid flow simulations modeled with COMSOL Multiphysics for three different potential obstacles. These models examine unsteady, incompressible flow past an immovable object placed in a long channel with rigid walls. The Reynolds number of the fluid modeled in Figure 3.12 is a low value of 20, while Figure 3.13 demonstrates simulations run with a value of 100. The Reynolds number is a dimensionless quantity in fluid dynamics which describes the ratio of inertial forces to viscous forces. It can also be understood as the ratio the dynamic pressure exerted on a fluid to its shear stress. A general relation for the Reynolds number takes the form:

Reynolds # = (fluid density x fluid velocity x channel length) / fluid viscosity **(Eq 3.5)**

A critical value of the Reynolds number describes a system's transition from lamellar to viscous flow, and as it depends upon the characteristics of the system, usually is determined experimentally, but for a rigid cylindrical tube, this value is generally accepted at around 2000. In this simulation, values below 100 create steady flow, while a Reynolds number of 100 allows the beginning of vortexes without creating full turbulence. Blood flow in the human body is largely lamellar, with the exception of some turbulence in the center of the aorta where flow velocities are very high, or in areas of

very high blood pressure due to unnatural vessel constriction. Capillary flow is considered lamellar. [105-108] Therefore, Reynolds's numbers chosen for the below simulations should be good approximations of the flow profiles occurring in the human body.

The large and small ellipses seen in parts (b) and (c) of the two figures below approximate geometries similar to low aspect ratio 1D magnetite nanorods or nanowires. Parts (a) in these figures model flow around a 2D slice of a perfect sphere, or idealized nanoparticle. The small ellipse in parts (b) maintains the same area as the circle observed in parts (a), while the large ellipse was constructed so that its smaller diameter corresponds to the initial sphere's diameter. In these images, color variation corresponds to variation in fluid velocity. Axes are dimensionless, but quantitative velocities are reported in units of (m/s) and so for quantitative analysis, lengths must be understood in meters. System variations should remain accurate at smaller sizes as long as relative dimensions remain constant. The simulation is run over a period of seven virtual seconds. The red dots observed in Figure 3.13 are the results of particle traces. Dots in these traces follow fluid flow lines; their movements are not based on any further particle-fluid interaction calculations. These are shown for better flow profile visualization only.

A more rigorous treatment would take particle movement into consideration rather than simulating flow past immovable objects, and would also demonstrate any complicating effects of multiple objects within the fluid. Further, for even more accurate results, the model should include a simultaneous nonlinear mechanical analysis of the channel walls to better approximate the rubber-like behavior of vessel walls. However,

such simulations and their equations are quite complex and were determined to be beyond the scope of this work.

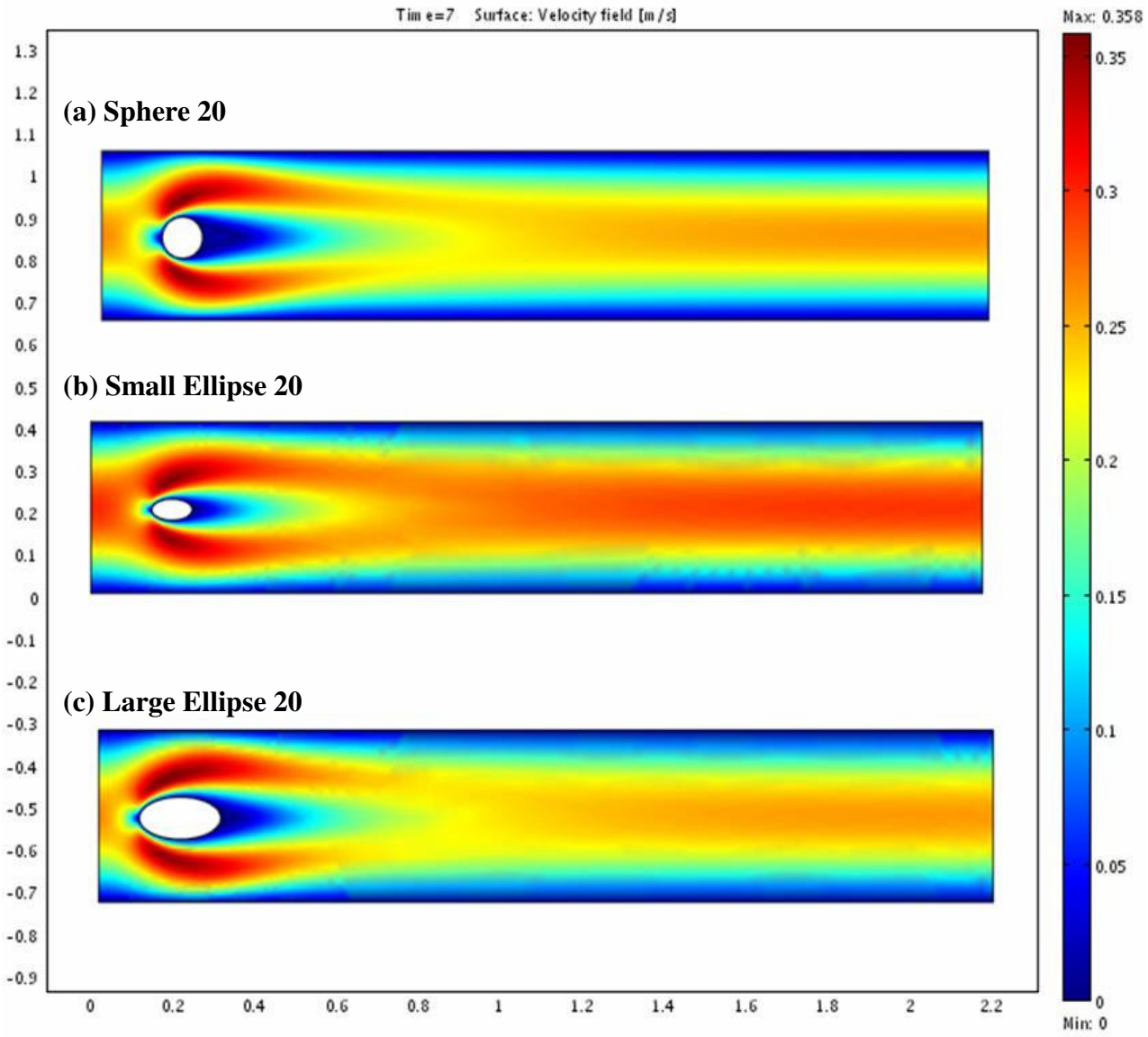

Figure 3.12: Flow profiles for fluid with a Reynolds number of 20. Axes are dimensionless. Coloration shows fluid velocity variation from 0 (blue) to a maximum of 0.358 (m/s)

Observe in Figure 3.12 three fluid flow profiles under similar conditions with varying immovable obstacles. While some fluid velocity variation can be observed, most notably the increased velocity of the fluid beyond the small ellipse in part (b), in general at a low Reynolds value of 20, few differences are notable. This result indicates that where blood pressure and velocity are low, elliptical 1D nanoparticles should not appreciably inhibit normal circulation or create turbulence, and should not demonstrate reduced flow relative to mostly spherical particles

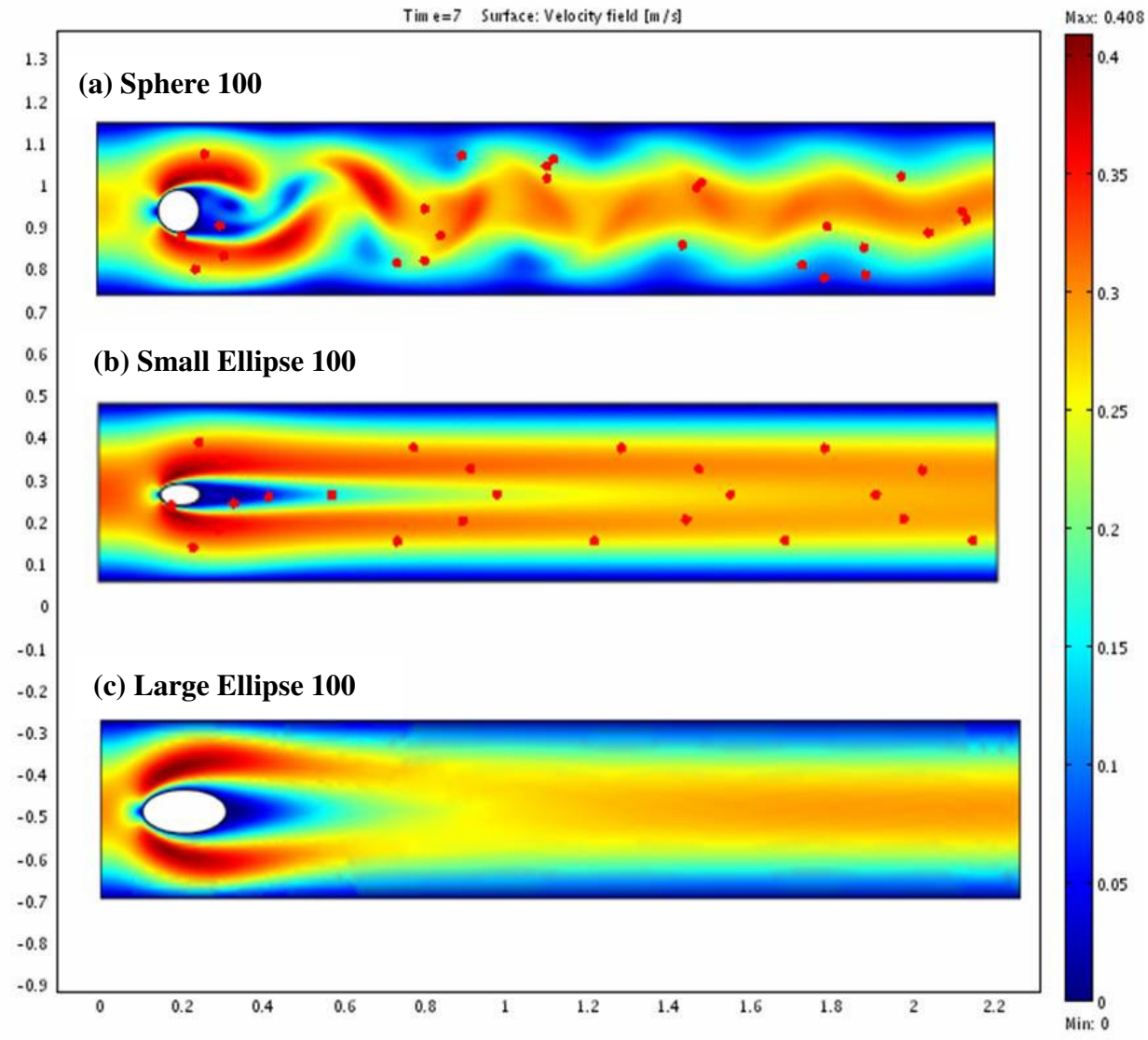

Figure 3.13: Flow profiles for fluid with a Reynolds number of 100. Axes are dimensionless. Coloration shows fluid velocity variation from 0 (blue) to a maximum of 0.358 (m/s)

Figure 3.13 illustrates the results of similar simulations calculated with a Reynolds number of 100. The most dramatic difference is observed in part (a) in which the circular obstruction is causing vortex formation in the fluid. Fluid flow around both large and small ellipses is largely unchanged and maintains a lamellar profile. These effects can be examined more quantitatively in Figure 3.14 and Table 3.3. Figure 3.14 illustrates the dramatic changes in lift forces exerted on the obstacle as a function of time for the models seen in Figure 3.13 (a) and (b). Table 3.3 displays values for the lift and drag coefficients for each simulation shown in Figures 3.12 and 3.13 above. These coefficients are calculated according to

$$\text{Drag Coefficient} = (2F_{Drag}) / (\rho U^2_{mean} D) \quad \textbf{(Eq. 3.6)}$$

$$\text{Lift Coefficient} = (2F_{Lift}) / (\rho U^2_{mean} D) \quad \textbf{(Eq. 3.7)}$$

such that F_{Drag} is the drag force, F_{Lift} is the lift force, ρ is the fluid density, U_{mean} is the mean velocity, and D is the characteristic length, which in this case is the obstacle diameter. Note that for the Reynolds 100 condition even the large ellipse -- having greater area than the circle – experiences small lift and drag forces relative to the circular obstacle.

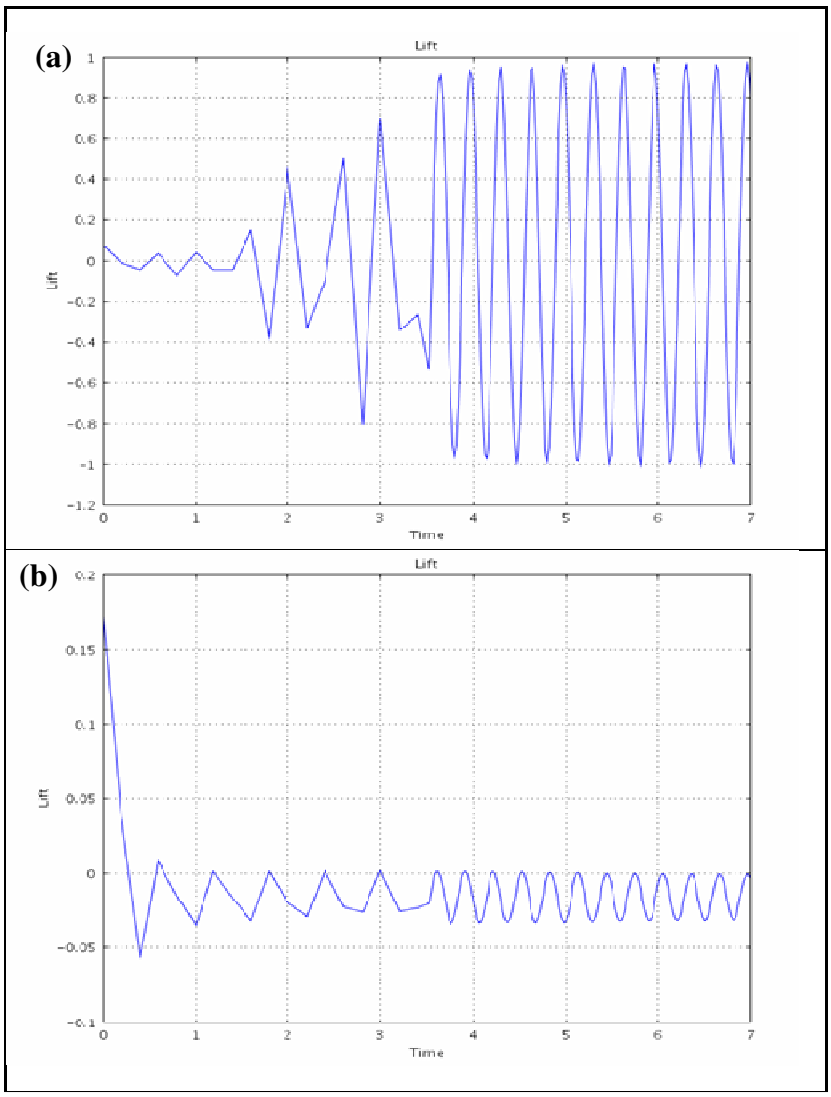

Figure 3.14: Lift force variation in time for Reynolds 100 flow simulations. (a) Lift force plot corresponding to simulation shown in Figure 3.13 part a (b) lift force plot corresponding to the simulation shown in Figure 3.13 part b.

Table 3.3: Values for drag and lift coefficients calculated from the simulations shown pictorially in Figures 3.12 and 3.13. Areas of the immovable obstacles are also given.

Simulation Name	Reynolds #	Drag Coeff.	Lift Coeff.	Obstacle Area
				m^2
Sphere 20	20	5.579	0.011	0.0079
Sphere 100	100	3.210	0.697	0.0079
Small Ellipse 20	20	3.202	0.009	0.0079
Small Ellipse 100	100	1.365	-0.005	0.0079
Large Ellipse 20	20	6.344	0.108	0.0628
Large Ellipse 100	100	2.660	-0.012	0.0628

These results indicate that, at least for the low aspect ratio nanorods and wires likely to be incorporated into biomedical tools, 1D geometries should not demonstrate reduced flow capabilities compared to spherical geometries. In addition, the lamellar nature of blood flow within the body is ideal for incorporation of these geometries, since flow profiles under this state are smoother, and should only be perturbed in the presence of vortexes or turbulence. The risk for tissue damage from sharp ends is greatest in conditions of turbulence, when circular eddies cause particles to move in a direction perpendicular to blood flow, posing a risk of shear and puncture. As long as lamellar flow conditions are maintained and edges are not too sharp, it appears that 1D geometries should not damage tissues or affect blood flow any more than spherical nanoparticles, and may even demonstrate improved performance.

Beyond cancer treatment applications, 1D magnetite nanostructures also seem uniquely suited to the obstacles inherent to bimolecular sensor development. Fe and Co particles are commonly used due to their high magnetization; however their tendency to aggregate can prevent the sensor from working properly. Polymer coated particles are

able to move freely, but they have a reduced magnetic moment. Micron sized particles while more easily manipulated, are too large and can impede bimolecular recognition and interaction.[81] As1D ferrites possessing highly superparamagnetic properties, Fe_3O_4 nanorods or nanowires may provide a practical solution to these problems. 1D ferrite nanostructures may also provide valuable new tools for electronic, recording, and communications devices. Conventional top-down fabrication of magnetic recording media is plagued by difficulties of etching and patterning novel hard magnetic systems, making controlled synthesis of 1D hard magnetic nanomaterials imperative in this industry.[93, 95]

In addition to practical applications, nanowires are also of interest for fundamental materials studies. Nanowires provide a physical manifestation of what once was solely a theoretical construct for physicists to study material behaviors at extremes, assuming quasi-infinite lines or strings. Researchers can now test theoretical predictions and gain new insights into the fundamental nature of these materials. Yet much is not yet known about these structures. Our understanding of electronic and magnetic behaviors is not sufficient to explain many anomalous behaviors in 1D magnetic materials, and researchers still do not fully understand the growth mechanisms responsible for producing these materials. In particular, 1D ferrite structures are of interest for theoretical applications, since these structures reportedly retain more ferromagnetic behavior than particles, yet have a simpler and more easily studied structure than thin films. 1D structures of Fe_3O_4, for example, where magnetic domains are aligned in series, would be ideal to study electron transport behavior and magnetoresistance in nano-sized materials. Despite obvious promise in such applications as magnetic MEMS, so far only a few

publications mention transport studies on this material. [109] Because 1D ferrite nanostructures offer unique and novel properties, they provide both a model to better understand the fundamental principles governing matter at the nanoscale and new tools that can be utilized to develop new applications in a variety of disciplines.

In order to use 1D nanowires for these purposes, one must gather the necessary tools. At the start of this work, synthesis of magnetite nanowires for thermotherapy and other applications was needed to be able to begin testing and device fabrication. However, synthesis of these materials is non-trivial. The magnetite phase is not the most stable form of iron oxide, which tends to oxidize to hematite, and 1D nanostructure formation mechanisms are not well understood. Published literature did not describe means of single-crystalline magnetite nanorod or nanowire fabrication. The next section addresses details regarding synthesis of these structures, with an emphasis on understanding how the details of their structures can provide clues to critical steps in their formation process. Though magnetite is a focus of this work because it is so well suited to biological applications, other phases are also examined in detail so that differences between these similar phases can help to provide additional information.

3.2 PLD Synthesized Iron Oxide Nanowires

For arrays of nanowires, spatial control and alignment with respect to the substrate is critical for integration into electronic and photonic technologies.[110] Single-crystalline structures are also essential, since the presence of grains and grain boundaries will affect magnetic domain structure and electron transport such that a polycrystalline nanowire behaves more like an aggregated chain of particles rather than a true one-

dimensional (1D) nanostructure. Although iron oxide nanowires and nanorods have been fabricated through a variety of methods, such as templating,[71, 111] hydrothermal synthesis,[112] thermal decomposition,[113] and sol-gel[62, 63, 66] techniques, these methods are often plagued by undesired contaminants, lack of control over morphology, size, and orientation, grainy structures, and the need for annealing treatments post-synthesis.[111, 114] Oxidation of iron has been used to produce arrays of α-Fe_2O_3 nanowires,[110] however, this method does not allow for location-specific selection of nanowire growth.

Controllable vapor deposition processes are promising candidates for scalable industrial production in the future, due to their simplicity and low cost, and have been employed to overcome many of these obstacles in simple chemical systems such as ZnO, [115, 116] ZnS, [117, 118] and CdSe,[119, 120] yet evaporative methods in the synthesis of iron oxide 1D nanostructures have produced limited success. Magnetite nanowire fabrication in particular has proven difficult due to the thermodynamic driving force for crystallization of vapors into the more stable α-Fe_2O_3 phase. The PLD method had previously shown some success in magnetite synthesis, however, only with the aid of a template, necessitating fabrication of either core/shell or tube-like structures.[111, 121] In addition, ε-Fe_2O_3 had until this work been observed only in nanoparticle and short nanorod morphologies, regardless of method. PLD assisted vapor deposition growth such as that reported here allows for simple synthesis of hematite and magnetite 1D nanostructure arrays and long ε-Fe_2O_3 nanobelts, lacking many of the problems encountered with other methods, while still granting spatial and size control.

The PLD method allows an additional level of control to the researcher due to the ability to maintain stoichiometry defined by a pre-mixed target material. The ability of PLD to retain the target stoichiometry in the deposited structure is the result of the extremely high heating rate of the target surface (~108 K/s) due to the pulsed laser irradiation. This leads to the congruent evaporation of the target irrespective of the evaporating point of the constituent elements or compounds of the target. Also, because of the high heating rate of the ablated materials, laser deposition demands a much lower substrate temperature than other evaporation growth techniques.[122] Despite the degree of control granted by the PLD method, literature had not previously reported synthesis of single-crystalline magnetite nanowires or nanobelts via evaporation methods without the aid of a template. Environmental XRD experiments in which magnetite nanorods were exposed to elevated temperatures in air produced clear conversion to the hematite phase, with no indication of the epsilon iron oxide phase present. These results also indicate that the PLD method is important to the creation of less traditionally stable phases such as ε-Fe_2O_3.

This section describes successful application of PLD assisted methods for growth of aligned hematite and magnetite nanorods, nanobelts, and nanowires. This work presents the first known synthesis of ε-Fe_2O_3 long nanobelts. Through a series of experiments, a primitive "phase diagram" has been produced for growing these structures based on several designed pressure and temperature parameters. This work is also the first known report of magnetite 1D nanostructure growth via catalyst assisted vapor deposition techniques without using template. The structure of the nanowires is investigated by transmission electron microscopy (TEM) and X-ray diffraction (XRD).

The magnetic properties of the synthesized nanostructures are investigated by Superconducting Quantum Interference Device (SQUID).

3.2.1 Fabrication Method

The iron oxide nanorods, nanowires and nanobelts were synthesized via pulsed laser deposition (PLD), using a pellet of pressed magnetite powder as target. Approximately 5 grams of Fe_3O_4 powder (Alfa Aesar 98%) was pressed in a 9.5 mm. diameter steel die at ~680 kg. pressure to form a cylindrical pellet. The Fe_3O_4 target was placed in a quartz tube in the center of a single-zone horizontal tube furnace. A schematic of the basic apparatus is shown in Figures 2.3 and 2.7. Next to the target was placed a quartz boat containing polycrystalline alumina wafer substrates coated with 2 nm of Au film to form catalyst islands. The tube ends were closed and water-cooled to maintain a uniform thermal gradient, with one end connected to a rotary vacuum pump and the other to a gas supply. To minimize residual oxygen, the tube was evacuated to 10^{-2} mbar and held for 1 hour prior to running the experiment. Argon gas (99.999%) was intermittently added during this time at a flow rate of 50 sccm to facilitate reduction of adsorbed oxygen, and then stopped to allow the system to return to a low pressure of around 0.02 mbar. The furnace was then allowed to heat up at a rate of 20^{o}C per minute to the desired maximum temperature under a well-maintained ambient pressure prescribed according to the chart shown in Figure 3.15(a). Argon flow gas was simultaneously introduced into the system at 50 sccm and was maintained throughout the duration of the synthesis.

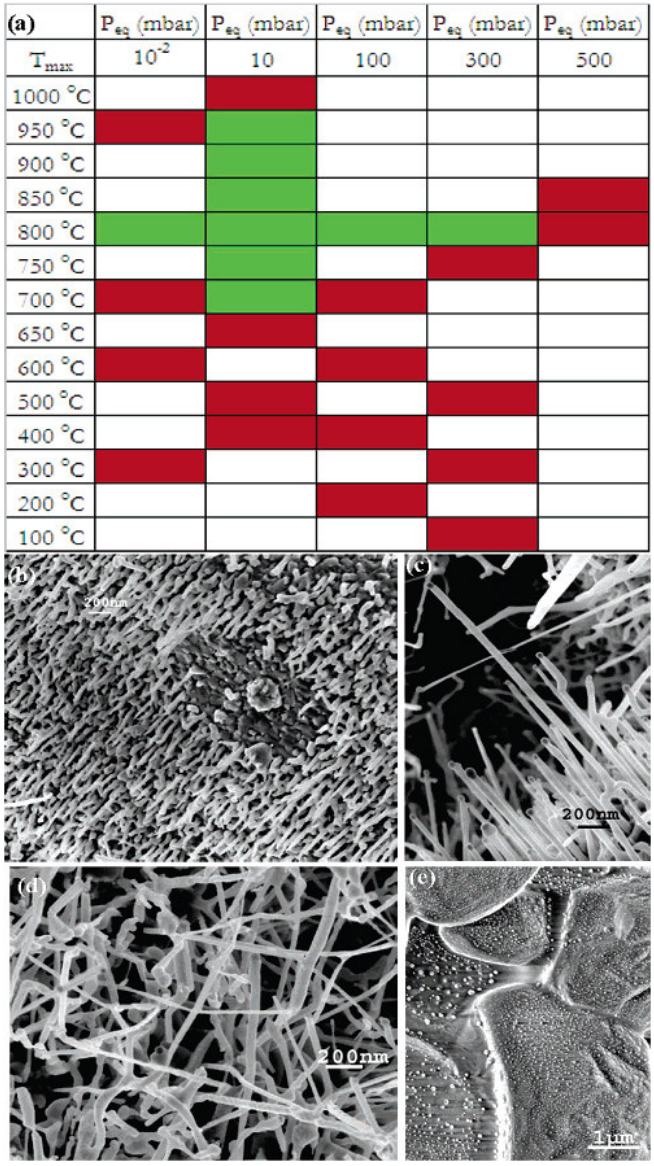

Figure 3.15: (a) Table showing tested pressure/temperature combinations and observed outcomes. Each cell represents a unique experiment. Green cells indicate combinations that produced high-density 1D nanowire growth. Red cells indicate no or very low growth. White cells indicate untested parameter combinations or those in which results were inconclusive. All other parameters were kept constant in these experiments. (b) SEM image showing short rods synthesized at 700°C, 10 mbar. (c) SEM image showing long belts synthesized at 900°C, 10mbar. (d) SEM image displaying greater secondary growth after 120 min of laser energy exposure compared to usual 60 min growth time at 900°C, 10 mbar. (e) SEM image showing no 1D growth at 900°C, 10 mbar, without laser energy.

Once the temperature and pressure had stabilized, pulsed laser energy generated by a Compendex Series Excimer 102 Laser (20 Hz, 30 kV, ~300 mJ) was directed through a transparent window on one end of the tube and focused toward the source material placed in the beam path. The laser spot on the target measured approximately 1mm wide by 5 mm long in most experiments. The laser was then allowed to ablate the target for 60 minutes, while pressure and temperature remained constant. After 60 minutes, the laser, furnace, and flow gas were turned off, and the system was evacuated back down to 0.02 mbar. A fan was placed near the tube to ensure rapid cooling. After the system reached room temperature, nitrogen gas was pumped into the tube to equilibrate the pressure, the tube was opened, and the substrate with the deposited sample was carefully collected and loaded onto an SEM stub for analysis. It was noted that most samples appeared red/orange to grey in color with rainbow-like fringes on the substrate radiating away from the leading edge.

To better understand the conditions necessary for 1D nanostructure growth using the catalyst assisted PLD method, we undertook a series of experiments in which nanostructure growth was correlated to systematic variations in experimental parameters. As Figure 3.15(a) shows, the parameters most explored were the maximum ambient temperature (T_{max}) inside the tube, and the controlled equilibrium pressure (P_{eq}) during laser ablation. Each cell in the table represents a possible unique experiment keeping all other variables, such as substrate type, catalyst density, target species, Ar flow rate, temperature ramp rate, ablation time, laser energy, and laser frequency, constant. After each experiment was complete, samples were examined in the SEM to determine the ability of the chosen parameters to sustain growth of 1D ferrite nanostructures. In the

figure, red cells correspond to experiments in which nanowire growth was unsuccessful, green cells correspond to parameters yielding successful growth, and white cells correspond to untested parameter combinations, or those in which results were inconclusive.

Since the ferrite nanostructures grew only on catalyst particles, successful growth was measured primarily according to nanostructure length rather than density. For the purposes of this study, a successful experiment was defined as one showing uniform high-density growth of nanostructures with length dimensions at least three times that of the catalyst particle diameter. In fact, the smallest nanorods found in these experiments displayed lengths far greater than the minimum described. The best 1D ferrite nanostructure growth was reliably found to occur from 700-950^{o}C at 10 mbar pressure. Experiments utilizing these parameters were repeated several times with consistent results. Figures 3.15(b) and 3.15(c) show length variation of nanostructures according to chamber temperature (T_{max}) at time of synthesis. Nanorods grown at 700^{o}C as shown in Figure 3.15(b) were aligned, and single-crystalline just like those shown in Figure 3.15(c) grown at 900^{o}C, with the only difference being nanostructure length. This result illustrates our ability to control ferrite nanostructure size, simply by varying reaction chamber temperature.

Although P_{eq} and T_{max} were the primary parameters investigated in this study, we also examined the effect of laser ablation time on 1D nanoferrite growth. Results of experiments carried out at 900^{o}C and 10 mbar showed that increasing ablation time from 60 minutes to 90 or 120 minutes did not significantly increase mean nanostructure length, but instead increased branching and secondary growth in the sample. Figure 3.15(d)

demonstrates this finding with an SEM image taken from a sample ablated for 120 minutes at 900°C, 10 mbar, the same P_{eq} and T_{max} combination shown in Figure 3.15(c) after the normal 60 minute ablation time. We were also curious to test our hypothesis that the laser energy is the primary energy source for nanowire growth, and whether instead T_{max} was producing growth before or in addition to the target's exposure to laser energy. To answer this question we conducted an experiment in which the procedure was followed exactly as in other runs, however, the target was not exposed to laser energy. This experiment was conducted at 10 mbar, 900°C, a parameter combination previously shown to produce very high density ferrite nanostructures when laser energy was applied. The results of this test are shown in Figure 3.15(e). Clearly, there is no growth at all on the substrate, confirming our hypothesis that the laser irradiation is the principle energy source responsible for target vaporization and resulting nanostructure growth. This result also indicates the ability for greater control over growth time in the PLD process relative to thermally driven vapor evaporation growth techniques in which critical growth initiation temperature is often unknown.

3.2.2 Characterization

The as-synthesized sample was directly imaged using a LEO 1530 field emission scanning electron microscope (SEM) with a resolution of 1nm. The accelerating beam voltage was limited to 3 kV to reduce sample charging and potential damage. Some nanobelts were observed to interact with the electron beam, occasionally vibrating and later breaking if under beam focus. Several images as well as EDS data on the sample were collected.

Grazing incidence X-ray diffraction measurements were performed on each sample using a PANalytical X-Pert Pro MRD with Copper K-alpha radiation. A 1 degree grazing angle was used to minimize substrate signal noise, along with a parabolic mirror, 0.27 degree parallel plate collimator with a flat graphite crystal diffracted beam monochromator. The monochromator was utilized to reduce iron fluorescence under Cu radiation. Measurements were taken with a tube power of 45 kV and 40 mA, from 28-60^{o} 2θ, with a 0.04 ^{o} 2θ step size and a 100 second count time.

For detailed local structural analysis, a carbon film coated copper grid was swept over the sample and loaded into an JEOL 4000EX high-resolution transmission electron microscope (TEM) operating at 400 kV. Electron diffraction patterns as well as high resolution images of several nanostructures were recorded and developed on film. EDS coupled with a Hitachi HF-2000 (FEG) TEM provided further evidence for chemical identification of the sample.

Figure 3.16 shows typical SEM images recorded from an as-synthesized sample with the inset containing EDS data gathered from TEM.

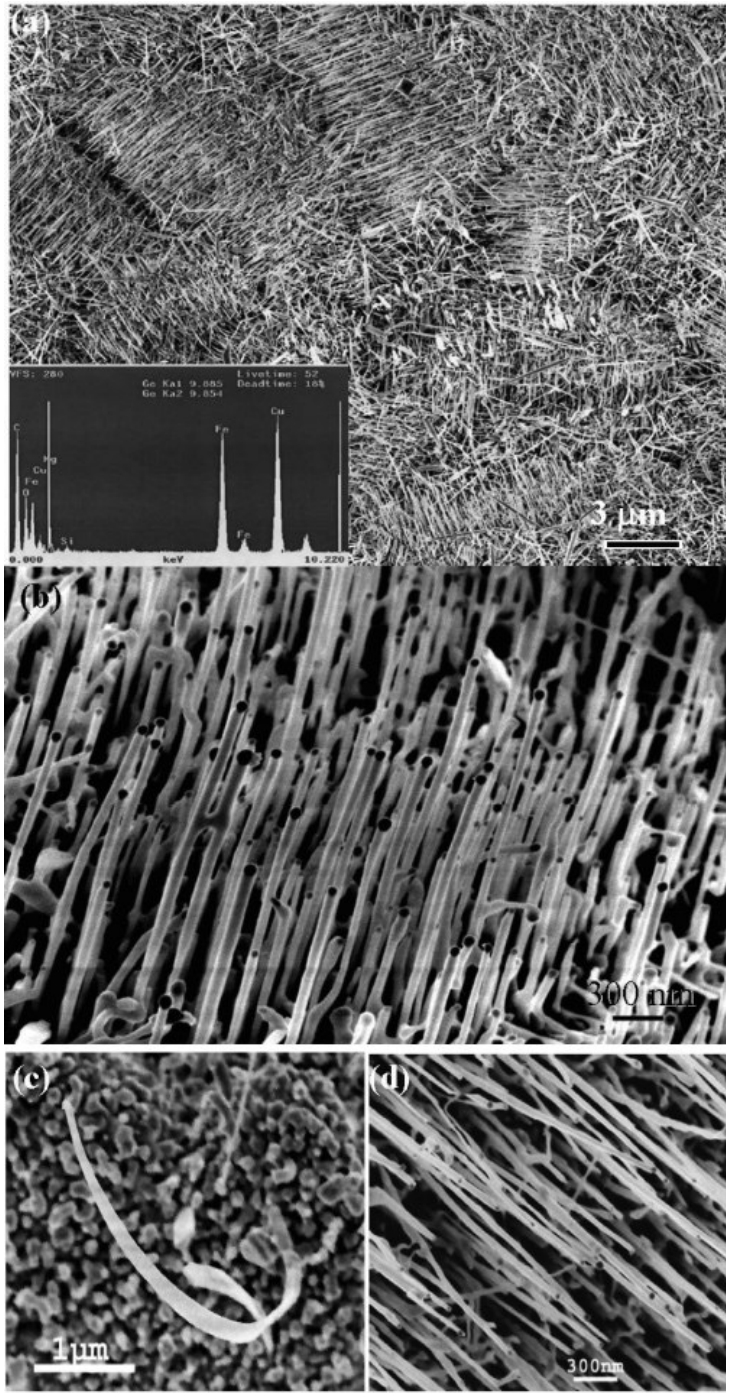

Figure 3.16: SEM images of Mg-doped and pure iron oxide 1D nanostructures. (a) Low-magnification SEM image of aligned iron oxide nanowires doped with Mg showing local alignment along alumina crystallites. Inset shows EDS chemical signature. (b) Higher magnification SEM image showing aligned Mg-doped iron oxide nanorods. (c) SEM image showing long nanobelt structure most likely having ε-Fe2O3 microstructure, without presence of Mg. (d) SEM image showing group of aligned iron oxide nanowires with Mg absent.

The EDS data taken from TEM analysis indicates presence of Fe, Mg and O, with Cu and C radiation originating from the sample grid, and Si peaks due to the signature of the detector. We were able to grow both Mg-doped and pure ferrite nanostructures via this method. Images in figures 3.16(a-b) illustrate ferrite nanowires including some nanobelts with approximately 6 atomic% Mg present, while figures 3.16(c-d) show pure iron oxide nanostructures. As these images demonstrate, both pure and Mg-doped 1D ferrites are of high quality single-crystalline nanostructures. Mg incorporation seems to occur almost exclusively in the longest nanobelts. Nanowires and nanobelts in Figure 3 were grown at a maximum ambient temperature of 900^{o}C. Although nanostructure dimensions varied greatly within samples, nanowires and nanobelts grown at 900^{o}C were generally highly dense, and on the order of 1μm long x 30 nm wide with the longest nanowires growing up to approximately 5 μm. Most long structures appeared to possess a rectangular cross-section, giving them a belt-like morphology, however those with more circular cross-section were observed as well, especially at the higher temperatures. Under the 700^{o}C condition, nanorods were the prevalent morphology with typical dimensions 500 nm long x 30 nm wide. Long nanobelts up to 7 microns in length and averaging around 100 nm in width were observed under both temperature conditions and appeared to grow in random orientations in or near grain boundaries. Density of these structures likewise increased at elevated temperature.

Note the uniform length and alignment of the nanorods localized on different alumina grains as seen at low magnification in Figure 3.16(a). Interestingly, each grain promoted aligned growth in a specific direction relative to the plane of the substrate. It appears that some grain faces are more favorable and initiated growth earlier, as

nanostructures are longer in some orientations relative to others. This effect is not due to simple vapor flow variation, as evidenced by observation that nanostructures growing on adjacent grains commonly exhibited significant length differences. The nanostructures' preference to grow at specific orientations and according to substrate crystallography indicates that researchers should be able to exactly control the angle of growing nanostructures relative to the substrate by carefully engineering surface orientation on single-crystalline substrates. Indeed, later synthesis on *c*-plane and *a*-plane sapphire (single crystalline Al_2O_3) produced high density arrays with perpendicular and in-plane growth, respectively. Figure 3.16(b) also clearly shows each nanowire tip terminated with a spherical gold particle. The ability to determine nanowire location though precise placement of catalyst material provides further spatial control over the nanowire synthesis.

Figure 3.16(c) is a typical image of the frequently observed long nanobelts found in our samples. Electron diffraction analysis (not shown) as well as XRD data indicate that these long nanobelts exhibit a ε-Fe_2O_3 phase of iron oxide. Some were shown in EDS to contain a small amount of Mg species as mentioned previously. Mg incorporation into these nanobelts is not surprising given reports that addition of column II cations like Sr^{2+} or Ba^{2+} to ε-Fe_2O_3 stabilized the phase and allowed for growth of larger nanocrystals.[62, 63] In our samples EDS analysis did not reveal Mg in all long ε-Fe_2O_3 nanobelts, indicating that its presence is not necessary for ε-Fe_2O_3 nanobelt formation using this method.

Figure 3.17(a-e) shows TEM data of magnetite and hematite nanowires, respectively.

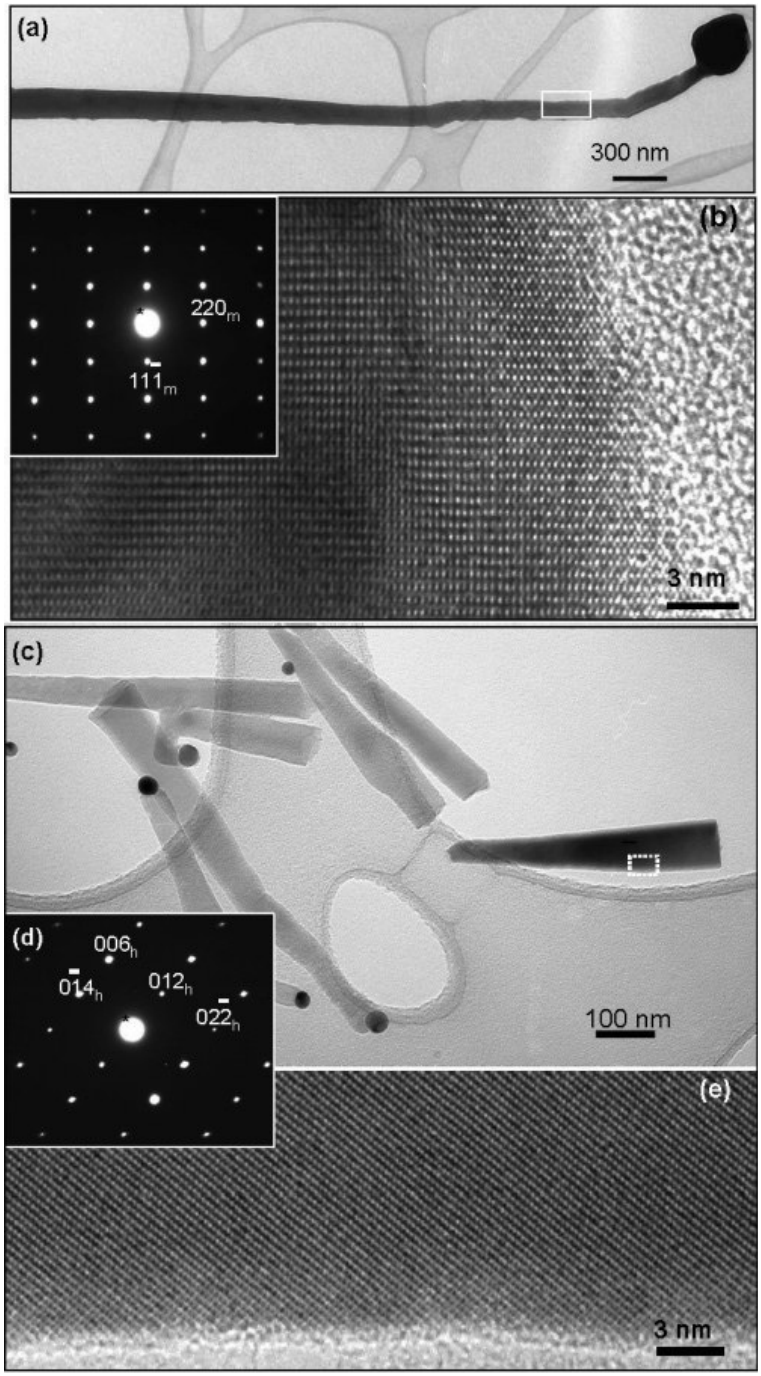

Figure 3.17: TEM data on magnetite and hematite nanostructures. (a) Low-magnification bright field TEM image of magnetite nanowire. (b) High-resolution TEM image of nanowire taken from the side edge of the wire in (a), illustrating high-quality single-crystalline nature of the wire. (c) Low-magnification bright field TEM image of hematite nanorods with Au particle tips. (d) Electron diffraction image taken from dark rod in previous image shows single-crystalline nature of the rod. (e) High-magnification TEM image of the section outlined in (c), showing well ordered structure and very little amorphous material on the nanorod surface.

Both hematite and magnetite nanostructures were found within the same sample, with no observable local phase domains. Although early samples were shown to contain a majority of hematite structures, predominantly magnetite samples were later synthesized by flowing Ar (50 sccm) for 10-20 minute intervals during initial tube evacuation to better eliminate residual oxygen in the system. Adding a piece of iron foil to the chamber to act as an oxygen "getter" was also helpful in increasing the relative magnetite yield. This finding indicates that phase can be controlled through careful variation of oxygen partial pressure within the tube. In Figure 3.17(a) one can see a bright field image of a magnetite nanowire with the spherical gold catalyst particle visible at the tip. The high resolution TEM image of this structure seen in Figure 3.17(b) illustrates the near perfect single-crystalline arrangement of atoms in the nanowire. Very little amorphous material is present on the surface. The electron diffraction pattern in the inset provides further evidence for the single-crystalline nature of this nanowire, and shows that the wire grew along the $[1\bar{1}1]$ direction. This is not the sole growth direction of magnetite nanowires in the sample, as others characterized by TEM (not shown) were found to grow along the <110> directions.

Presence of magnetite rather than maghemite (γ-Fe_2O_3 defect spinel) in the samples was confirmed through careful determination of lattice parameters from TEM diffraction data as well as XRD phase analysis. Both electron diffraction and XRD can distinguish the structures based on differences in the space groups, with Fe_3O_4 and γ-Fe_2O_3 corresponding to Fd3m (227) and $P4_232$ (208) respectively. The d-spacing of Fe_3O_4 is about 0.48 nm while that of γ-Fe_2O_3 should be 0.59 nm.

Figure 3.17(c) shows a bright field TEM image of several hematite nanorods.

Again, Au catalyst particles are observed at the tips, indicating the gold catalyst's role in synthesis. The high resolution image in Figure 3.17(e) clearly shows the ordered arrangement of atoms and the lack of a significant amorphous layer at the surface. The nanorod in this figure grew along the $[01\bar{1}]$ direction as seen in the electron diffraction pattern shown in Figure 3.17(d).X-ray diffraction characterization of several samples is given in Figure 3.18.

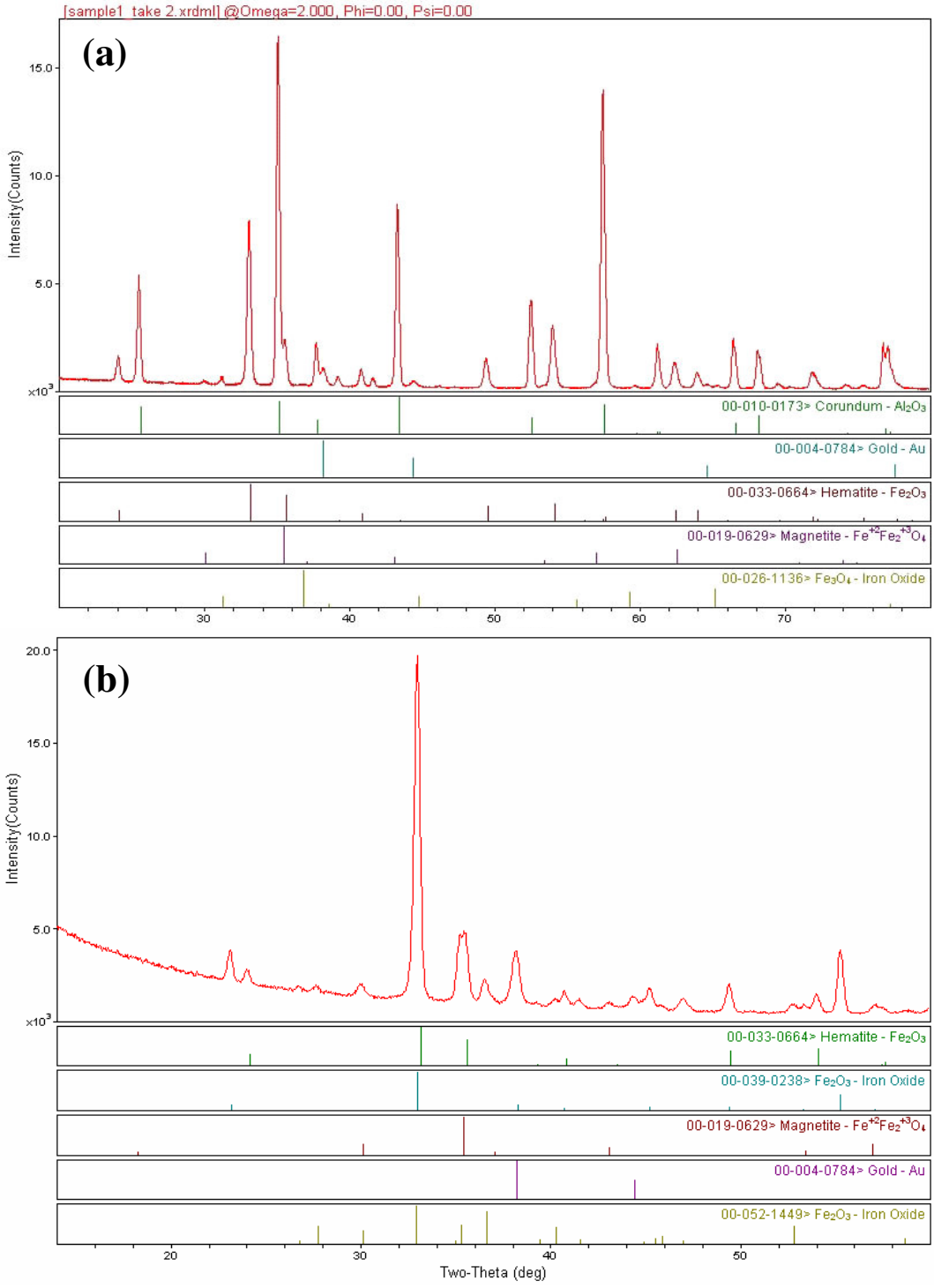

Figure 3.18: XRD data taken from samples grown at 800°C, 10 mbar, and 750°C 10 mbar, respectively. (a) XRD signal from grazing incidence measurements of iron oxide nanobelts and nanowires grown on polycrystalline alumina. (b) Similar measurements on iron oxide nanostructures grown on a *c*-plane sapphire substrate.

The image in Fig. 3.18(a) shows XRD data from a sample grown at 700°C, 10 mbar, on a polycrystalline alumina substrate. The diffraction pattern was analyzed with Jade software. Although the polycrystalline alumina peaks are predictably the strongest, the pattern clearly shows presence of gold, magnetite and hematite, confirming our assessment though electron diffraction studies. Figure 3.18(b) shows a similar pattern performed on an iron oxide nanowire sample grown at 750°C, 10 mbar, on c-plane sapphire substrate. Sapphire was used in this example to eliminate the influence of the substrate on the XRD diffraction pattern. The structures in this sample grew primarily perpendicular to the substrate in a high density nanowire array tipped with gold particles. Phase identification of the diffraction pattern in Figure 3.18(b) using MDI Jade7.5 yields five known phases: Au (PDF#4-784) hematite (Fe_2O_3 PDF#33-664), a magnetite-like phase (closest match PDF#19-629), an orthorhombic iron oxide (Fe_2O_3 PDF#52-1449) found to correspond to ε-Fe_2O_3, and a cubic iron oxide (Fe_2O_3 PDF#39-238). The cubic iron oxide phase has been identified as a BCC phase. Since the current paper focuses on the physical chemistry involved in the synthesis, detailed structure analysis of the new phase will not be discussed here.

Quantitative analysis performed using the reference intensity ratio (RIR) method on a similar sample yields a weight fraction ratio of 0.57 hematite to magnetite. It should be noted that previous XRD analysis of the clean alumina substrate (not shown) indicates small amounts of a spinel aluminum oxide phase within the corundum Al_2O_3 wafer. Most

likely this is a $MgAl_2O_4$ phase added to aid in sintering, and is the source of the Mg seen in some of our long nanobelt structures.

3.2.3 Properties

SQUID (superconducting quantum interference device) measurements on samples created at 700^{o}C, 10 mbar, and 900^{o}C, 10 mbar, are shown in Figures 3.19. Figure 3.19 demonstrates magnetic hysteresis behaviors of these samples at 300K (room temperature) and 5K.

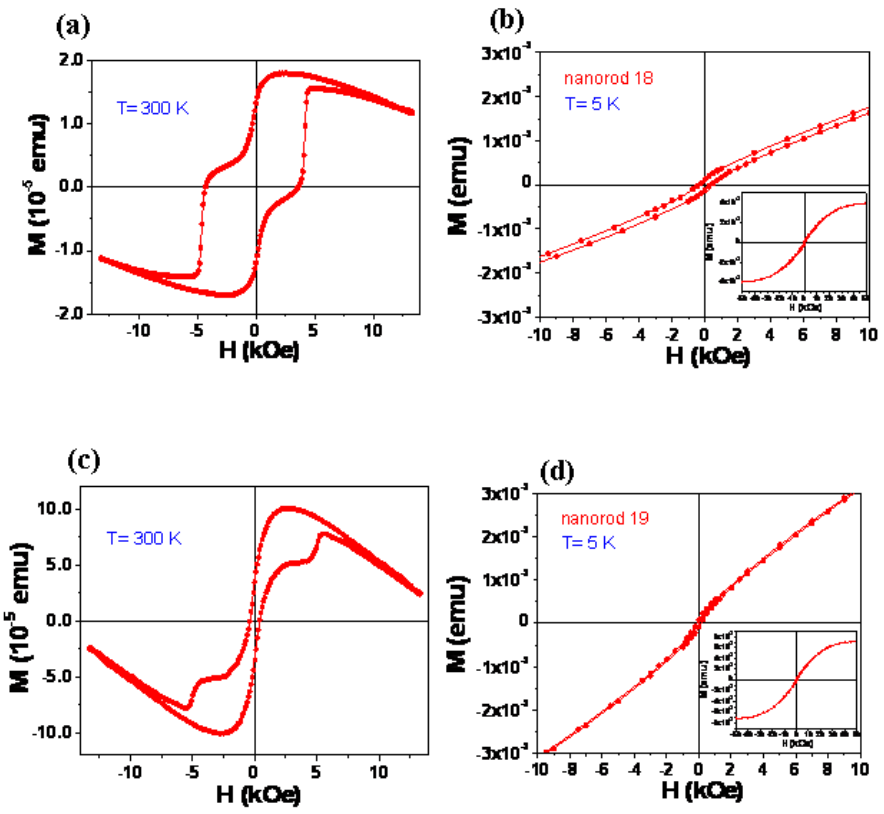

Figure 3.19: Magnetic hysteresis behavior of iron oxide nanostructures grown at 700oC, measured with SQUID. (a) M-H loop at 300K showing ferromagnetic behavior and wasp-waist shape most likely derived from multi-phase nature of sample. (b) M-H loop at 5K with low-field region expanded, showing soft magnetic behavior with a saturation magnetization around 5 Tesla. Right inset: M-H loop from -5 to 5 T. (c) and (d) show similar results in a sample prepared at 900C. In (c) the presence of the soft phase is more pronounced, consistent with observations of increased hematite concentration in this sample.

Data for nanostructures created under the 700^{o}C condition is shown in Figure 3.19(a-b), with 3.19(c-d) correlating to the 900^{o}C synthesized sample. As shown in Figure 3.19(a), the nanostructures grown at 700^{o}C exhibit strong ferromagnetic behavior at room temperature. The kink, or “wasp waist” shown at approximately 4 kOe in the curve indicates presence of two compatible magnetic phases. The diamagnetic nature of the alumina substrate is most likely the cause of the curve’s decay at high field strengths.

While ferromagnetic behavior of the kind shown here is expected for the magnetite 1D nanostructures, above the Morin Temperature of hematite (~263K bulk) magnetic moments are canted slightly away from the antiferromagnetic axis, resulting only in a very small net positive magnetization. This effect should not be diminished by the small size of the nanowires studied here. In fact, the Morin Temperature has been found to decrease as particle size decreases in hematite samples, depressing this transition further away from the temperature shown in this figure. Publications reporting magnetic characterization of hematite nanowires and nanoparticles show only very weak ferromagnetic or paramagnetic behavior at room temperature, quite unlike our sample's hysteresis behavior.[69, 123] Therefore, it is possible that the two compatible magnetic phases displayed in the graph shown in Fig. 3.19(a) are not magnetite and hematite, but rather magnetite and the nanobelts of the ferrimagnetic ε-Fe_2O_3 phase. The figure shows an H_c value of about 4 kOe for this sample. This value is much less than the maximum reported room temperature coercivity of 20kOe for ε-Fe_2O_3 nanoparticles. The decrease in coercivity may be due to interactions with the magnetite and hematite phases, and the relatively low yield of ε-Fe_2O_3 compared to other phases in this sample. Since the reported 20 kOe value was obtained in samples containing IIA metal ions with much lower values reported for pure phase samples,[62] the absence of Mg may also provide some explanation for the lower coercivity demonstrated by this sample.

Figure 3.19(b) shows the M-H behavior of this sample at 5K. It is clear that at this low temperature, the hysteresis behavior disappears, producing a curve that looks much like a soft magnetic material. At 5K, the magnetic response from the hard phase seen at room temperature disappears, so that the kinks seen earlier disappear. This result

indicates the presence of two phases with different temperature-dependent magnetic behaviors. This figure provides further evidence for the presence of magnetite and ε-Fe_2O_3 as magnetic phases in the sample. Previous reports on ε-Fe_2O_3 observe an unusual temperature dependence in which the coercivity decreases significantly below 100K. This effect is described by Gich *et al* to be due the Arrhenius nature of domain wall motion. The critical magnetic domain size may reduce to a value below the size of the nanostructure as T and therefore K (the reaction rate constant) decrease, causing an inhomogeneous state, and loss of single-domain character.[64] The inset shows the expanded M-H loop indicating magnetic saturation around 50 kOe.

Figures 3.19(c) and 3.19(d) show similar data for the 900^{o}C sample. In this sample, the magnetic response from the softer phase has a greater influence on the overall hysteresis curve. Quantitative XRD measurements show that the hematite concentration in this sample is greater than that in the previous one, indicating that hematite nanostructures may be contributing to the change in magnetic response. Long nanobelts were also observed in large density on this sample, however, indicating that the influence of the ε-Fe_2O_3 phase cannot be ignored. The stronger soft magnetic response is further evident in Figure 3.19(d) in which the area contained within the loop is observed to be smaller than that in the other sample.

It should be noted that further SQUID studies on small portions of samples shown in Figure 6 demonstrate typical hysteresis behavior like that of a soft magnetic material with small remnant magnetizations. It is very likely that these small portions contain a local phase domain such that the magnetic behavior again appears like that of a

homogenous group of ferrite nanowires. In these samples, SQUID measurements revealed saturation around 15kOe when exposed to temperatures from 5 – 300 K.

The temperature dependence of the magnetization under ZFC-FC (zero field cooling – field cooling) conditions at 1000 Oe is shown in Figure 3.20(a-b). The same sample shown in Figure 3.20(a) is measured again at 100 Oe and the result is shown in Fig. 3.20(c). These figures show significant irreversibility from room temperature, with FC curves demonstrating Curie-like increasing. In Figure 3.20(c) it is evident that the irreversibility occurs at 250 K. The magnetic field application direction should have little effect on these results, since the nanowires are aligned only locally according to each grain, but globally should appear as in random orientations. Strangely, these curves appear quite unlike those for other iron oxide nanostructures published in the literature [48, 64, 71, 112, 114, 123] and no Verwey transition point can be observed. Magnetic Force Microscopy was also conducted on these samples, but due to the relatively low resolution, yielded no informative data.

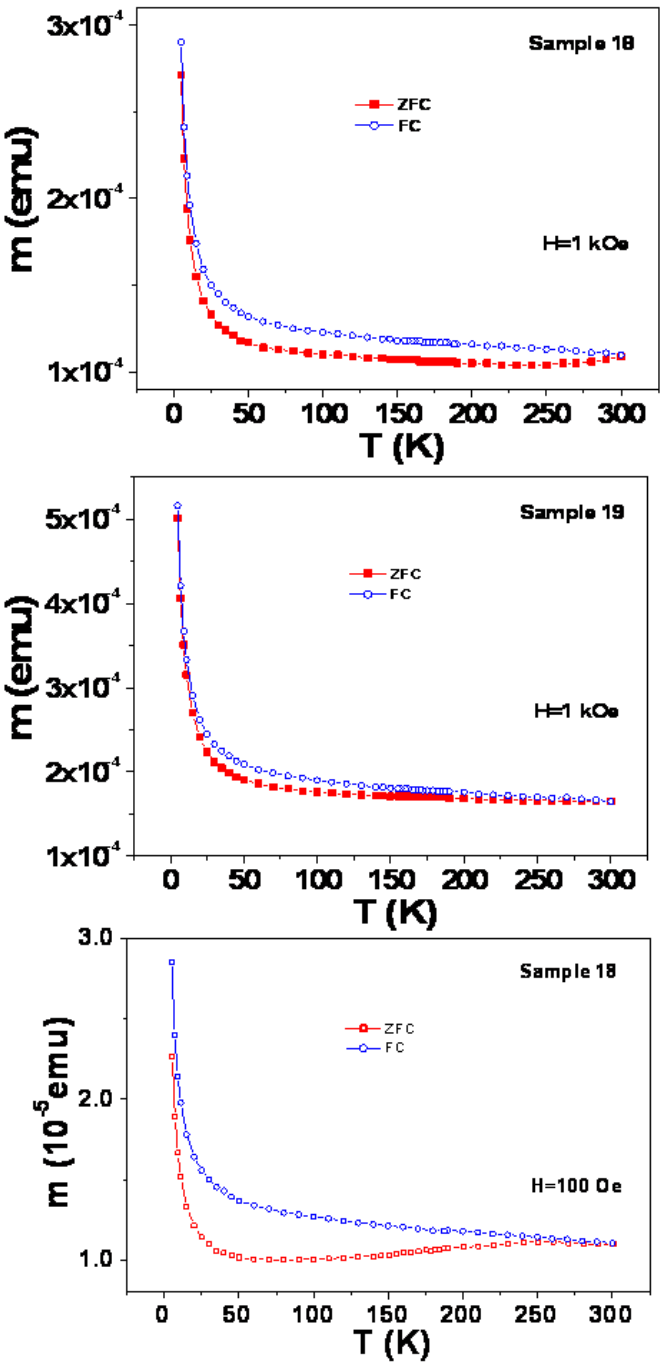

Figure 3.20: Temperature-dependent magnetization under ZFC-FC (zero field cooling-field cooling) conditions at applied field of 100-1000 Oe. (a) Effect of temperature on magnetization for iron oxide nanowire sample on alumina substrate prepared at 700 °C at 1000 Oe field strength. (b) Effect of temperature on magnetization for iron oxide nanowire sample on alumina prepared at 900 °C under 1000 Oe. (c) ZFC-FC curve for same sample as (a) under 100 Oe field strength.

This work reports the first known PLD assisted template free growth of single-crystalline magnetite and hematite nanowires and nanobelts. It further demonstrates the success of the PLD method in the first known synthesis of long ε-Fe_2O_3 and Mg stabilized ε-Fe_2O_3 nanowires and nanobelts. This technique offers many benefits over previous synthesis methods, including higher quality structures, higher density structures, greater spatial and size control, ability to grow complex structures, and no need for a template. In addition the PLD method should allow synthesis of even more complex chemistries due to its ability to maintain the stoichiometry of the target material in the growing nanostructure. The work includes a primitive phase diagram for the synthesis of these structures and shows how different variables affect the size, morphology, and phase of the grown product. This information should be helpful both for those interested in utilizing this technique, as well as those hoping to further elucidate the underlying mechanisms behind catalyst-assisted vapor evaporation nanowire growth. High density aligned growth on polycrystalline alumina is demonstrated. It is also shown that growth direction of the iron oxide nanowires can be controlled through use of different planes in single-crystalline substrates. SQUID measurements on these samples indicate novel and interesting magnetic properties which could be beneficial to many current and future technologies based on ferrite and magnetic materials.

3.3 Epsilon – A Novel Iron Oxide Nanowire Phase

During the characterization of the iron oxide nanowires samples examined in the previous section, the nanowires of the epsilon iron oxide (ε-Fe_2O_3) phase were

discovered. As this is a very rare form of iron oxide, and one not well understood, it was determined that a study in greater depth was warranted. The results of this study are presented in this section. Understanding the structure and formation of this unusual iron oxide phase provides rich information to help understand the formation of iron oxide nanowires with the aid of metal catalysts, and catalyst assisted vapor deposition growth of nanowires in general. Much thanks goes to Dr. Yong Ding for the substantial contribution he made to this section in the form of detailed TEM and structural analysis of the epsilon phase, and writing collaboration.[124]

The ε-Fe_2O_3 phase is commonly considered an intermediate phase during thermal treatment of maghemite, γ-Fe_2O_3, to hematite, α-Fe_2O_3. The routine method of synthesis for ε-Fe_2O_3 crystals uses γ-Fe_2O_3 as source material and requires dispersion of γ-Fe_2O_3 into silica, with the obtained ε-Fe_2O_3 particle size limited, normally under 200nm. By using pulsed laser deposition (PLD) method and Fe_3O_4 powder as source material, synthesis not only of one-dimensional Fe_3O_4 nanowires but also high-yield ε-Fe_2O_3 nanowires was achieved. Detailed transmission electron microscopy (TEM) study shows that nanowires of *pure* magnetite grow along [111] and [211] directions, although some stacking faults and twins exist. However, magnetite nanowires growing along [110] were found in every instance to accompany a new phase, ε-Fe_2O_3, with some micron-sized wires even fully transferring to ε-Fe_2O_3 along the fixed structural relationship, $[001]_{\varepsilon-Fe_2O_3} \| [111]_{Fe_3O_4}$, $[010]_{\varepsilon-Fe_2O_3} \| <111>_{Fe_3O_4}$. Contradictory to generally accepted ideas regarding epsilon phase formation, there is no indication of γ-Fe_2O_3 formation during the synthesis process; the phase transition may be described as from Fe_3O_4 to ε-Fe_2O_3, then

to α-Fe_2O_3, as indicated by systematic TEM study. 120°rotation domain boundaries and antiphase boundaries are frequently observed in the ε-Fe_2O_3 nanowires.

3.3.1 Epsilon Iron Oxide Background

Among the polymorphs of ferric oxides, maghemite, γ-Fe_2O_3, and hematite, α-Fe_2O_3, are well-known, [125-129]however, knowledge of ε-Fe_2O_3, considered an intermediate phase between maghemite and hematite, is relatively limited. The disparity is most likely due to difficulties in synthesizing pure and sufficiently large ε-Fe_2O_3 crystals. The earliest known report on the existence of ε-Fe_2O_3 was published in 1934 by Forestier and Guillain.[130] However, detailed structural characterization of this phase was not published until 1998 by Tronc *et. al.*, [65]and was later refined in 2005 by Kelm and Mader.[113] R. Zboril *et al* observed the transformation of γ-Fe_2O_3->εFe_2O_3->α-Fe_2O_3 in small particles through Mossbauer Spectroscopy in 2002, noting that most likely the formation of ε-Fe_2O_3 as an intermediate was related to the degree of agglomeration in precursor powders, with those more loosely packed tending to form the intermediate, and those with heavy agglomeration tending to lead straight to the more stable alpha phase. [131-133]When considered in the framework of nanomaterials, this finding is interesting, perhaps indicating the role of high surface energy, a characteristic of most nanostructures, as a key component in the formation of the epsilon phase.

Until now, the γ-Fe_2O_3->εFe_2O_3->α-Fe_2O_3 pathway was the only known route to synthesis of ε-Fe_2O_3, however, our work indicates a completely novel synthesis path, one involving magnetite, or Fe_3O_4 , rather than maghemite as the precursor phase. In hindsight, it is perhaps not surprising that if maghemite can give rise to the epsilon phase,

magnetite can do so as well. Both magnetite and maghemite phases share the same basic structure, with close-packed oxygen atoms resting in alternating ABCABC formations along the [111] direction, and Fe occupying octahedral or tetragonal lattice sites. The distinguishing feature of the gamma phase is that some Fe positions are left unoccupied as random vacancies, reducing the order in the crystal. In the TEM, this loss of symmetry corresponds to the appearance of diffraction spots that should be forbidden in a more perfect lattice. Most likely, previous observations of ε-Fe_2O_3 described the phase as an intermediate of γ-Fe_2O_3 and not Fe_3O_4 because of the additional complication of stoichiometry. The conversion from Fe_3O_4 to ε-Fe_2O_3 implies, equivalently, an overabundance of iron or an oxygen deficiency in the starting phase. Therefore, the forming material (ε-Fe_2O_3) must either get rid of the excess iron or adsorb additional oxygen atoms. For our high surface area nanowires grown via solid state physical evaporation, oxygen adsorption would not have been problematic. Likewise, at low pressures, it is possible that iron desorbed from the lattice. If oxygen had adsorbed into the lattice (or iron desorbed from the lattice) randomly, such that Fe site occupation was no longer periodic, the maghemite phase would have been observed. Our investigation shows a direct transition from Fe_3O_4 to ε-Fe_2O_3 without evidence of other intermediate phases, indicating that the formation of the epsilon phase was accompanied by perfectly ordered species evolution.

Pure iron oxides including maghemite and magnetite have been widely used in many fields, from magnetic recording, storage, and magnetizable printing to medical applications, such as cell separation and MRI imaging.[134, 135] For future technological advances, further improvements of their magnetic properties are necessary.[136,

137]While many applications require soft magnetic properties, large coercivities are required in applications such as high density magnetic recording, where the magnetic domain needs to be stable, and desire for ever smaller pixel sizes has pushed some traditional materials to the superparamagnetic limit. Researchers are currently working to maximize the coercivity in materials employed in these technologies. Ferric oxides like magnetite and maghemite are attractive choices for several reasons, including their low toxicity, low cost, availability, stability, high corrosion resistance, and high resistivity, which correlates to low eddy current energy loss.[137] However, their *fcc* crystal structure leads to a low magnetocrystalline anisotropy constant, therefore, augmentation of the coercive field (H_c) is difficult. Remarkably, the ε-Fe_2O_3 phase takes the orthorhombic crystal structure, producing a room temperature H_c as large as 20kOe.[138, 139] As a comparison, the highly anisotropic magnetoplumbite Barium Hexaferrite ($BaFe_{12}O_{19}$), commonly utilized for magnetic recording, can only produce a coercive field as large as about 7.5kOe.[140] In addition, this magnetic behavior is stable at elevated temperatures in the epsilon phase, which has a reported Curie temperature of ~510 K. [138, 139]Crystals of ε-Fe_2O_3 larger in size, yet still retaining the favorable characteristics observed at the nanoscale would prove ideal candidates for most any technology requiring hard magnetic materials, and could provide the additional benefits of low toxicity, high corrosion resistance, etc. inherent to ferric oxide materials. Furthermore, long nanowires of this material are ideal morphologies for many current and future electronic, storage, and printing technologies. With further understanding of the phase stability and exploring new synthesis methods, ε-Fe_2O_3 may prove a sound

replacement for maghemite and magnetite in many of their current applications as well as those of more complex and expensive hard magnetic materials.

Added to its high coercivity, the epsilon phase of iron oxide also may host several other interesting and desirable properties. The non-centrosymmetric structure of this material indicates the existence of permanent electric dipole moments within the crystal, granting it both spontaneous magnetization and electric polarization. The coupling of these attributes promises the occurrence of physical effects such as optical activity, pyroelectricity, piezoelectricity, magnetocapacitance, and second harmonic generation, with possible applications including motion detection, bone and tendon biomimetic devices, electric (magnetic) field tunable magnetic (electric) field devices, or multiple state memory, among many others. Indeed, Gich *et al* recently reported observations of abrupt changes in the dielectric properties of ε-Fe_2O_3 nanoparticles at temperatures near the magnetic transition, with further experiments on the material's electric properties confirming magnetoelectric coupling.[66] These findings provide strong evidence that such exciting properties originating from electronic and magnetic coupling in this material are more than mere theoretical prediction.

A standard synthesis method for ε-Fe_2O_3 nanocrystals presented in the literature is the heat treatment of γ-Fe_2O_3 nanoparticles dispersed in silica xerogels. [63, 65] Drawbacks of this method include the existence of silica impurities and small grain size, which normally falls under 200nm. For many potential applications, pure crystals of ε-Fe_2O_3 are required. Impurities can alter the performance of devices based on ε-Fe_2O_3 materials, and create obstacles in further refining or treatment. In addition, small particle sizes severely limit the applicability of these materials due to in part to practical

complications regarding maneuverability and processing, as well as integration into larger systems. Other reported synthesis methods such as thermal decomposition, and previously reported high energy deposition syntheses likewise produced products of mixed phase or other impurities, and often with low yield.[66] It is likely for these reasons that ε-Fe_2O_3 has not been more fully exploited in novel technologies.

Section 3.3.2 describes synthesis of not only one-dimensional Fe_3O_4 nanowires, but also high-yield ε-Fe_2O_3 nanowires by applying the pulsed laser deposition (PLD) method and Fe_3O_4 powder as precursor. Specifics regarding synthesis parameters, nanowire alignment, and magnetic properties of these materials, as well as brief structural characterization information have been presented elsewhere.[141]The next section contains a much deeper and more detailed description of the structural evolution of three iron oxide phases found to exist in nanowires grown by this method. The findings demonstrate both a novel practical synthesis route for ε-Fe_2O_3 and, through detailed TEM investigation involving high resolution images, systematic diffraction, and simulated models, the complete structural evolution process as observed within the nanowires themselves.

3.3.2 Epsilon Iron Oxide Nanowires Characterization

The iron oxide nanowires were synthesized via pulsed laser deposition (PLD) process, using a target of pressed magnetite powder as source material. The detailed experimental setup has been presented previously. The structural analysis was carried out using a JEOL 4000EX high-resolution transmission electron microscope (HRTEM) operating at 400 kV. Electron diffraction patterns as well as high resolution images of

several nanostructures were recorded and developed on film. The HRTEM image simulations were performed using *Cerius2* commercial software.[142, 143]

The synthesized Fe_3O_4 nanowires can be classified according to growth direction into three categories, as those growing along the $[111]_M$, the $[211]_M$ and the $[110]_M$ directions, which are displayed separately in Figures 1, 2, and 3 respectively. (Note our notation convention of using M, ε and H subscripts to denote the plane and orientation indices in Fe_3O_4 (magnetite), ε-Fe_2O_3 and α-Fe_2O_3 (hematite) phases, respectively. Also, though many of our examples appear to posses rectangular geometries, for simplicity, we will refer to all examined structures using the term "nanowire." Figure 3.21(a) and (b) are the bright-field and dark-field TEM images of a Fe_3O_4 nanowire grown along the $[111]_M$ direction. The select-area electron diffraction (SAED) pattern in Figure 3.21(c) can be uniquely indexed using cubic phase magnetite. Although some stacking faults can be identified in the dark-field image in Fig. 3.21(b), the entire wire is single crystalline and is well described as a pure magnetite structure. The HRTEM image in Fig. 3.21(d) confirms the $[111]_M$ growth direction of the nanowire.

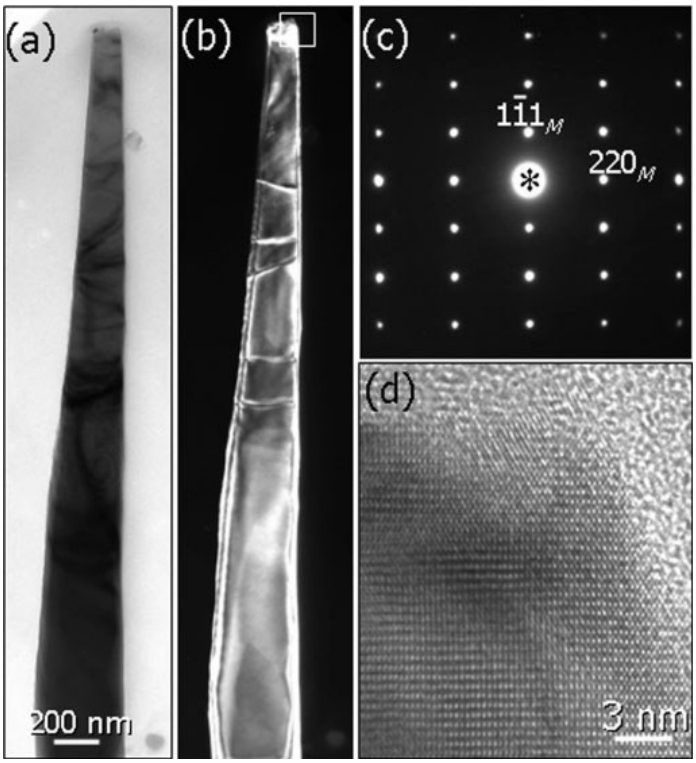

Figure 3.21: General morphology of the nanowires. TEM (a) bright-field and (b) dark-field images of the [111] growth magnetite nanowire. (c) SAED pattern of the wire. (d) HRTEM image recorded from the white rectangular area in (b).

The nanowire displayed in Fig. 3.22(a) takes the $[211]_M$ growth direction. Twin boundaries and stacking faults can be seen in the image. Further, the existence of twin structures also can be seen in the SAED pattern in Fig. 3.22(b). Without exception, all diffraction spots in Fig. 3.22(b) can be indexed using the twinned magnetite structure, taking $(111)_M$ as the twin plane. Although the planar defects exist within the wire, it is still best described as a phase of pure magnetite.

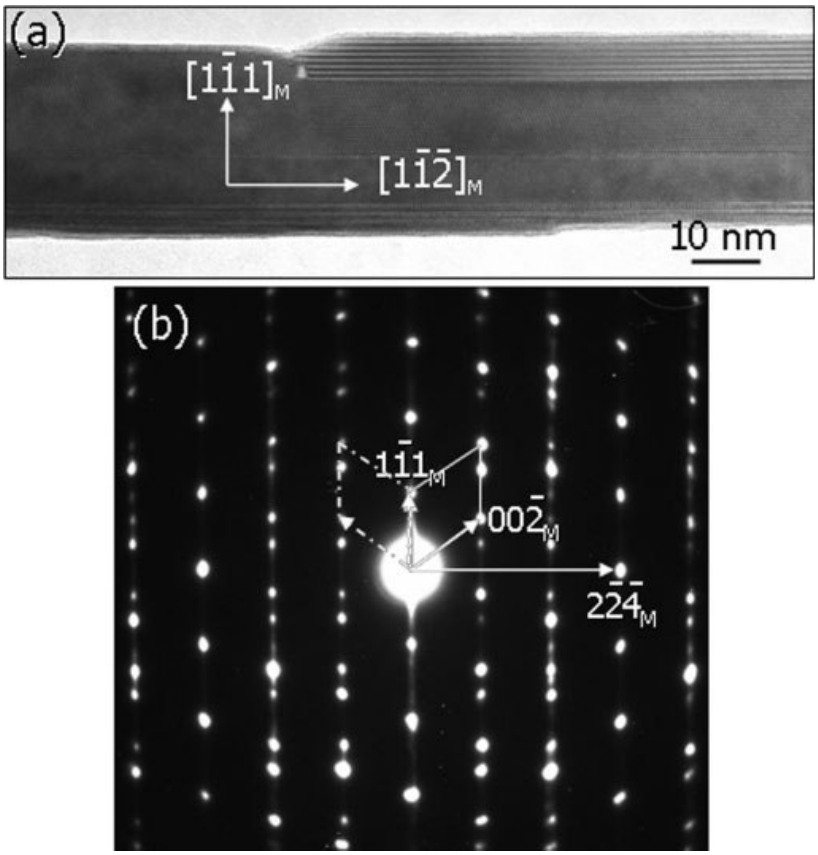

Figure 3.22: (a) HRTEM image and (b) SAED pattern of a magnetite nanowire grown along the <211> direction. Stacking faults and (111) twins can be observed in the HRTEM image.

While the nanowire shown in Fig. 3.23(a) grew along the $[110]_M$ direction, there are extra diffraction spots in the SAED pattern recorded from the whole nanowire as shown in Figure 3.23(b), which could not be fully indexed by the magnetite phase. Changing to a small select-area aperture, the SAED patterns seen in Figure 3.23(c) and (d) were created, recorded from the circled areas "C" and "D" in Figure 3.23(a). The pattern in Figure 3.23(c) can be indexed as the lattice projection expected when the electron beam is parallel to $[\bar{1}\,12]_M$, while the SAED pattern in Figure 3.23(d) is indexed as the projected ε-Fe_2O_3 structure with the electron beam along $[100]_\varepsilon$.

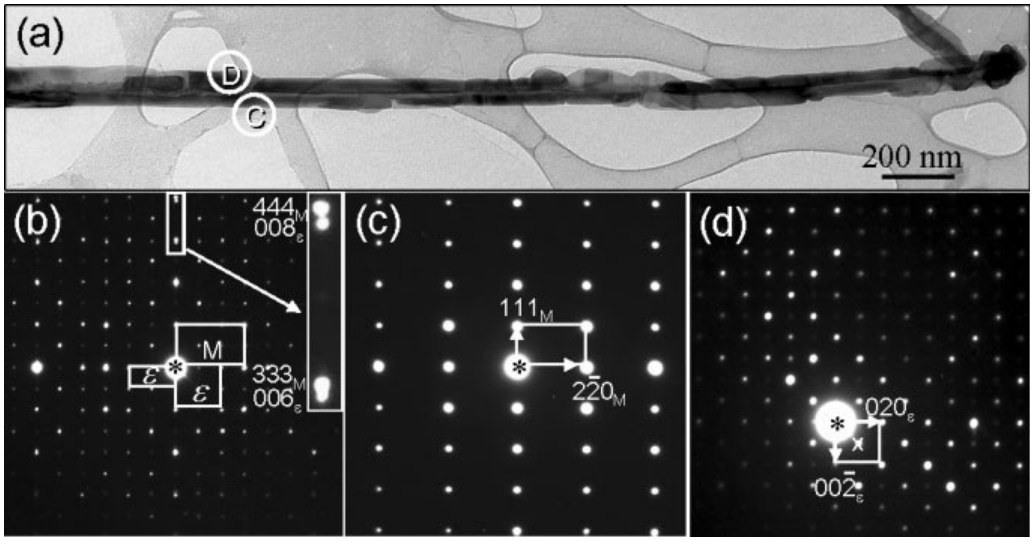

Figure 3.23: (a) Low-magnification TEM image of a [110] growth magnetite nanowire. The SAED patterns from the whole wire, and circled areas "C" and "D" are displayed in (b), (c), and (d), respectively.

In order to confirm and clarify the presence of the ε-Fe_2O_3 phase, a systematic procedure involving construction of the lattice based on varying geometric projections observed in electron diffraction patterns was used. Based on the series of electron diffraction patterns shown in Figure 3.24, in which the sample was rotated along a fixed axis so that the electron beam would project atomic positions at known angles, the reciprocal space lattice shown in Figure 3.24(f) was constructed. Each diffraction pattern in Figure 3.24 (a-e) corresponds to a slice through this reciprocal lattice at a unique orientation, identified by the matching letter label. This reciprocal space lattice was found to correspond to a real space orthorhombic unit cell, with a ~ 5.11Å, b ~8.72Å and c ~9.42Å, parameters which well match the ε-Fe_2O_3 phase. Looking back to the SAED pattern in Figure 3.22(b), the 333_M and 444_M diffraction spots are not single points, but are separated into pairs, with the additional spots corresponding to 006_ε and 008_ε as

shown in the inset. This effect is due to the small difference between the planar distance of magnetite (111) and ε-Fe_2O_3 (001). There is no splitting of the 333_M and 444_M diffraction spots in Figure 3.21(c) and Figure 3.22(b), indicating the absence of ε-Fe_2O_3 phase in these nanowires. Besides the $[\bar{1}\,12]_M$ pattern, two sets of ε-Fe_2O_3 patterns can be distinguished in Figure 3.23(b). The structural relationship between magnetite and ε-Fe_2O_3 phase can be described as, 1. $[001]_\varepsilon \parallel [111]_M$, $[010]_\varepsilon \parallel \langle 110\rangle_M$, and 2. $(001)_\varepsilon \parallel (111)_M$, $[1\,\bar{1}\,0]_\varepsilon \parallel \langle 110\rangle_M$. The two different structural relationships are due to the existence of 120° rotation domains in the ε-Fe_2O_3 section, which will be discussed later.

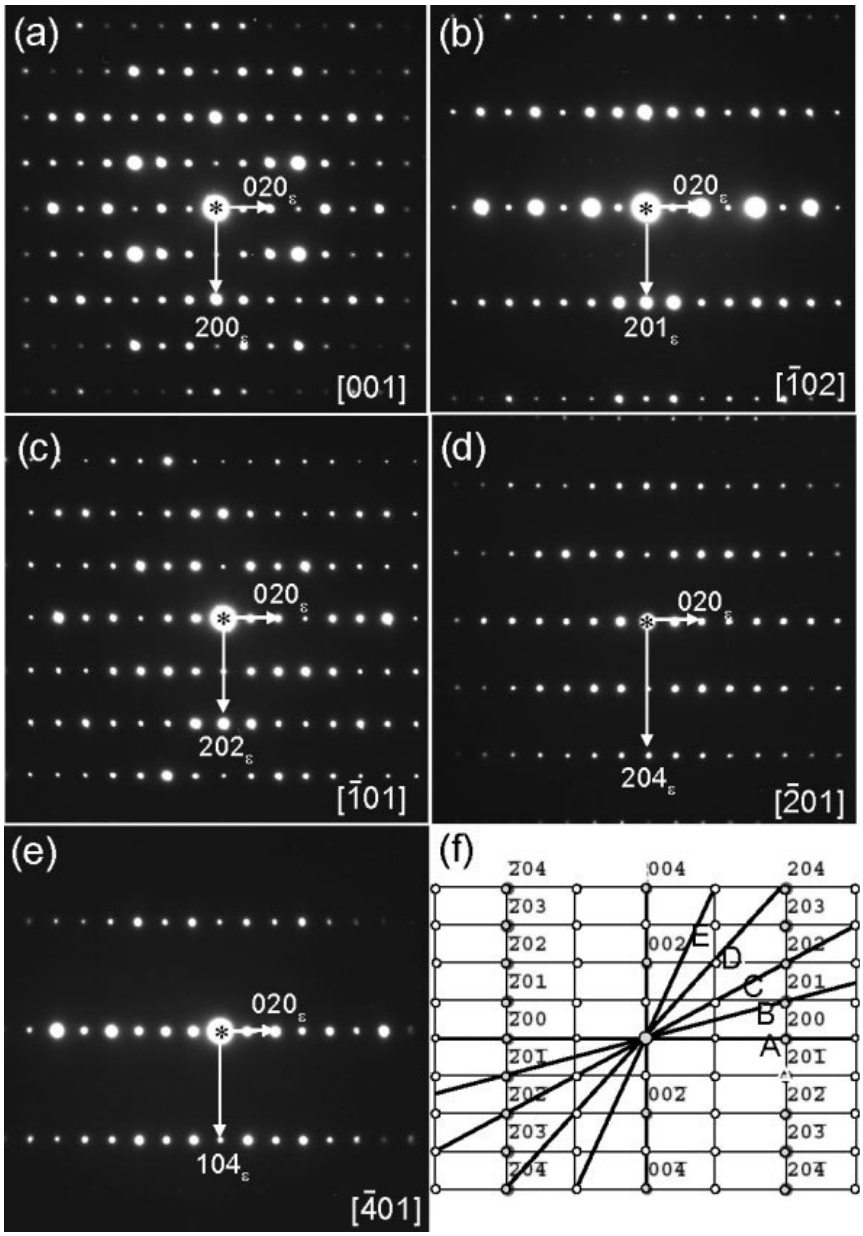

Figure 3.24: Multiple directional examination of the diffraction behavior of the ε-Fe_2O_3 nanowires. (a–e) A series of zone-axis diffraction patterns of the ε-Fe_2O_3 phased wire with beam directions along the [001], [1¯02] [1¯01], [2¯01], and [–401] directions, respectively. These diffraction patterns provide a systematic expression about the 3D structure of the ε-Fe_2O_3 phase. (f) Schematic of the reciprocal space lattice built up from these patterns, where the reciprocal planes corresponding to the patterns displayed in (A–E) are marked.

The HRTEM images in Fig. 3.25(a) and (b) were recorded from the nanowire previously shown in Fig. 3.23(a). The fast Fourier transforms (FFT) areas 1, 2, 3, and 4

are displayed in Fig. 3.25(c), (d), (e) and (f), respectively. After indexing these FFT patterns, we can find that area 1 corresponds to the magnetite phase, while areas 2 and 4 correspond to the ε-Fe_2O_3 phase, and area 3 is best described by two ε-Fe_2O_3 phase domains overlapped. The two individual structural relationships between magnetite and the ε-Fe_2O_3 phase can be confirmed in the HRTEM images.

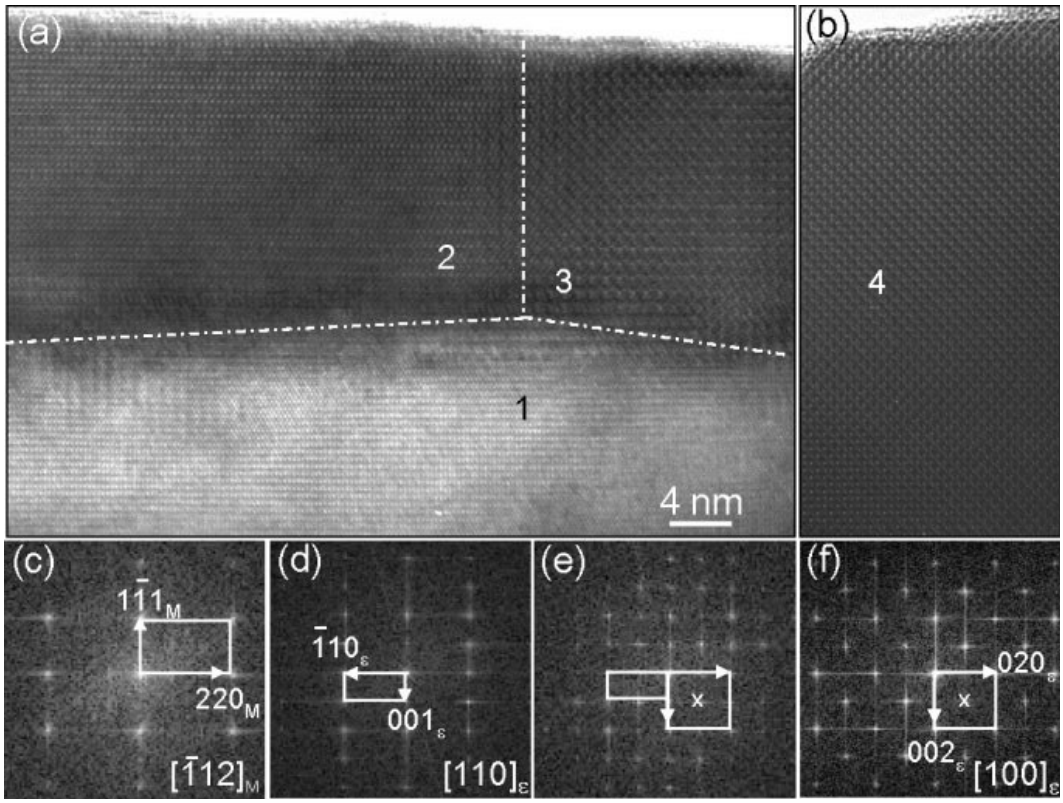

Figure 3.25: Domain structure in a single nanowire. a, b) HRTEM images recorded from the wire shown in Figure 3a. c–f) FFT patterns from the 1–4 areas shown in (a) and (b).

From the crystallographic point of view, both magnetite and ε-Fe_2O_3 are composed of close-packed oxygen layers with Fe ions occupy the interstitial oxygen octahedral or tetragonal sites.[144, 145] The close-packed oxygen layers in magnetite stack in the …ABCABC… sequence along $[111]_M$ direction, whilst the stacking

sequence in ε-Fe_2O_3 changes to …ABACABAC…along the $[001]_\varepsilon$ direction. Figure 3.26 (a) shows a schematic ball and stick model of the magnetite structure, and Fig. 3.26 (b) and (c) show similar models for the ε-Fe_2O_3, phase. The two ε-Fe_2O_3 models, I and II in Figure 3.26, are based on the two structural characterizations reported in the literature. [65, 113] Model I is the ideal structure, while II is the refined structure. By tilting the nanowire, HRTEM images with the electron beam along $[\bar{1}01]_\varepsilon$ and $[001]_\varepsilon$ were recorded in Figure 3.26 (d) and (e), respectively. Taking into account a sample thickness of ~ 3nm and Scherer defocus effects, simulated images based on models I and II were created. The simulated patterns are seen in the small squares superimposed on the actual high resolution images seen in Figure 3.26 (d) and (e). Comparing the two sets of simulated images, model II demonstrates a better match with the experimental data in both cases.

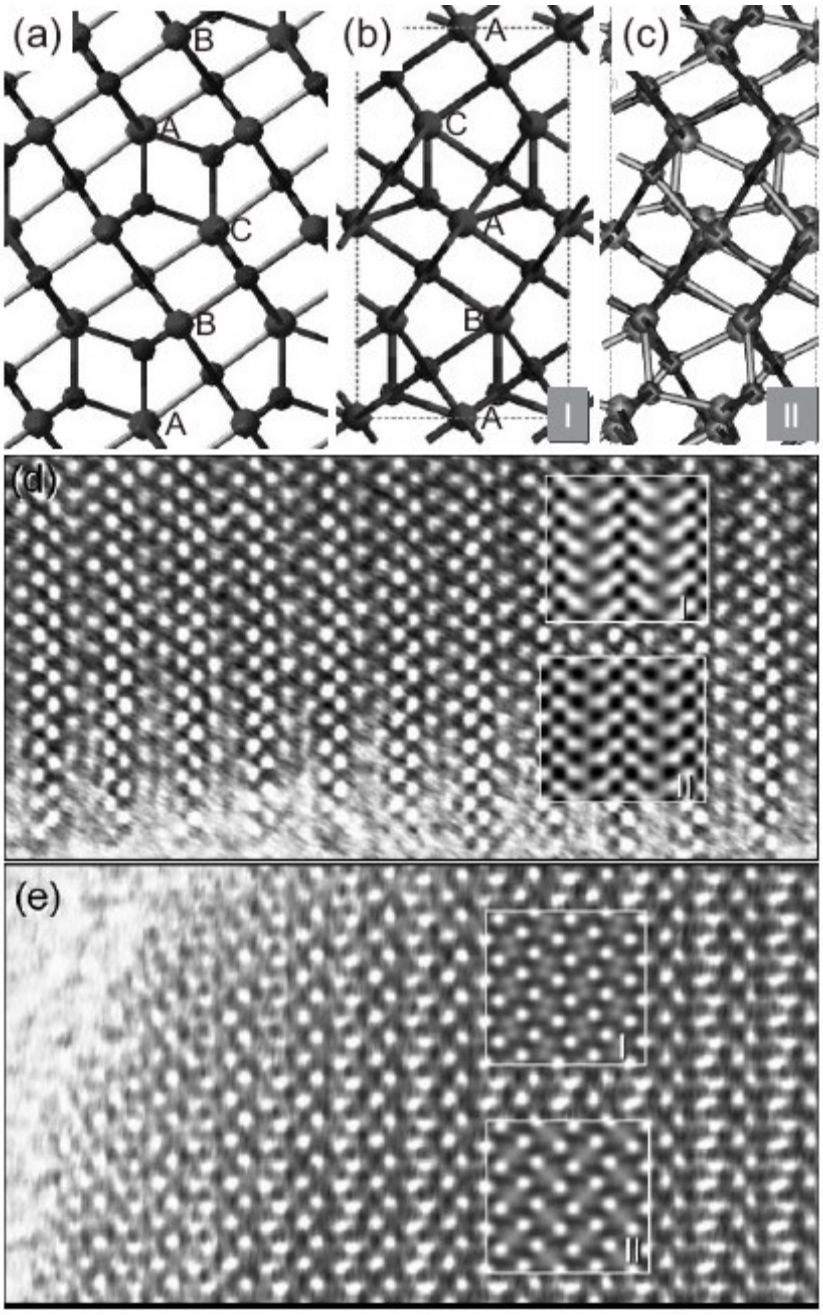

Figure 3.26: Atomic models of a) magnetite, b) ε-Fe_2O_3, and c) ε-Fe_2O_3 d, e) Experimental and simulated (inset) HRTEM images of the ε-Fe_2O_3 phase with the beam along the [1¯01] and [001] directions, respectively. The insets are the simulated images based on model I and model II as displayed in (b) and (c), respectively, for the ε-Fe_2O_3 phase.

According to the literature, it is generally accepted that ε-Fe_2O_3 is well described as an intermediate phase between γ-Fe_2O_3 and α-Fe_2O_3. [65] In analysis of these

experiments, we found that magnetite and ε-Fe_2O_3 phases coexist without the presence of γ-Fe_2O_3. It is therefore worthwhile to clarify the phase transition process during the synthesis. It seems that the images in Figure 3.27 of a long wire and its SAED patterns seen in Figure 3.28 provide some hints regarding this issue. The existence of the Au catalyst at the tip of the wire suggests the synthesis process follows a catalyst-assisted vapor growth mechanism. [146-148] Figures 3.27(a) and (b) show the low-magnification TEM images from two connected parts of the same nanowire.

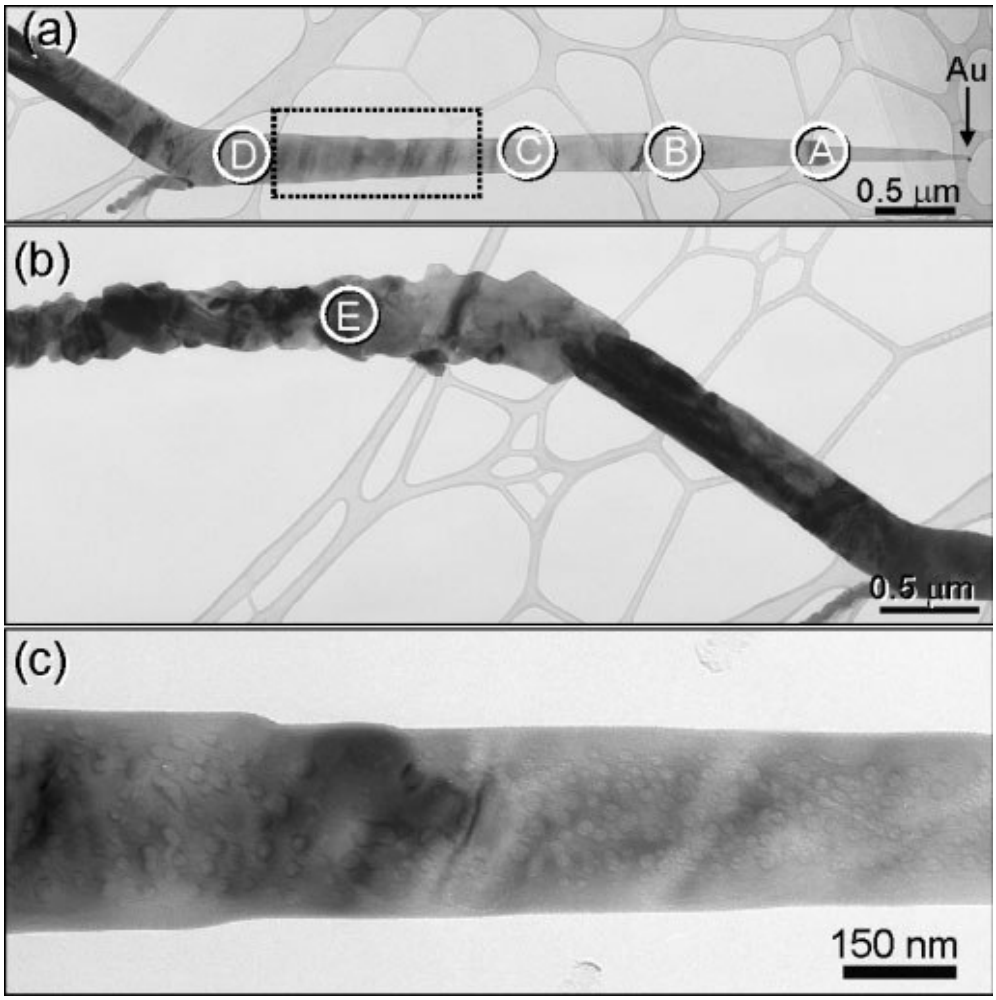

Figure 3.27: Structural evolution among the three phases along a single nanowire. a,b) Low-magnification TEM images showing different parts of the same nanowire. c) Enlarged image of the enclosed rectangular area in (a).

The SAED patterns in Figure 3.28(a)-(e) were recorded from the circled areas "A"-"E" in Figure 3.27. The SAED pattern in Figure 3.28(a) shows that the area "A" close to the Au catalyst is composed of the pure magnetite phase. Area "B" is composed of two phases, magnetite and ε-Fe_2O_3, with a fixed orientation relationship between them. Based on the SAED pattern shown in Figure 3.28(b), this orientation relationship can be described as $[001]_\varepsilon \parallel [111]_M$, $[010]_\varepsilon \parallel \langle 110 \rangle_M$, which is the same as that shown in Figure 3.23. Progressing to area "C", the nanowire here fully changes the to ε-Fe_2O_3 phase. At area "D", the diffraction pattern in Figure 3.28(d) is composed of three $[001]_\varepsilon$ patterns. By rotating 120ºclockwise or anti-clockwise around $[001]_\varepsilon$ axis, each of these $[001]_\varepsilon$ patterns can be superimposed onto any of the other two $[001]_\varepsilon$ patterns.

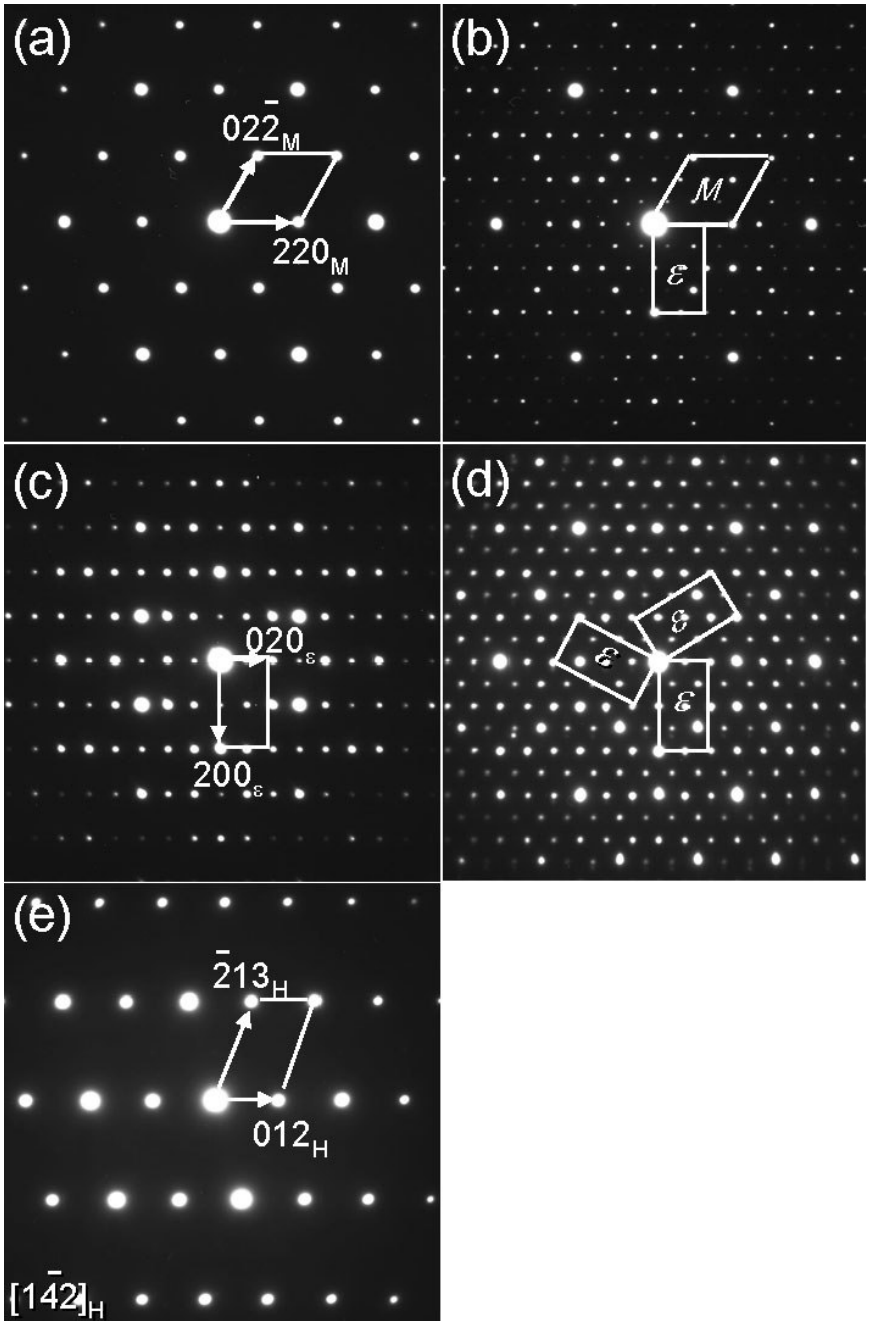

Figure 3.28: a–e) SAED patterns recorded from the circled areas A–E for the same nanowire presented in Figure 7, showing the different phases along the length of the same nanowire.

Relating this diffraction phenomenon back to a real space structure, the diffraction pattern in Figure 3.28(d) signifies the formation of rotation domains, discussed later in

more detail. There is some misalignment between the structure in areas “E” and in “A”-“D”. We have to tilt the wire to get the right zone-axis SAED pattern as shown in Figure 3.28(e). Neither magnetite nor the ε-Fe_2O_3 phase can be used to index the pattern displayed in Figure 3.28(e). Indeed, it belongs to the hematite phase, with the electron beam along the $[1\,\bar{4}\,2]_H$ direction. Although we cannot find the orientation relationship between the connected ε-Fe_2O_3 and α-Fe_2O_3 regions due to the wire bending, the confirmation of the existence of ε-Fe_2O_3 phase is sufficient to understand the phase transition process.

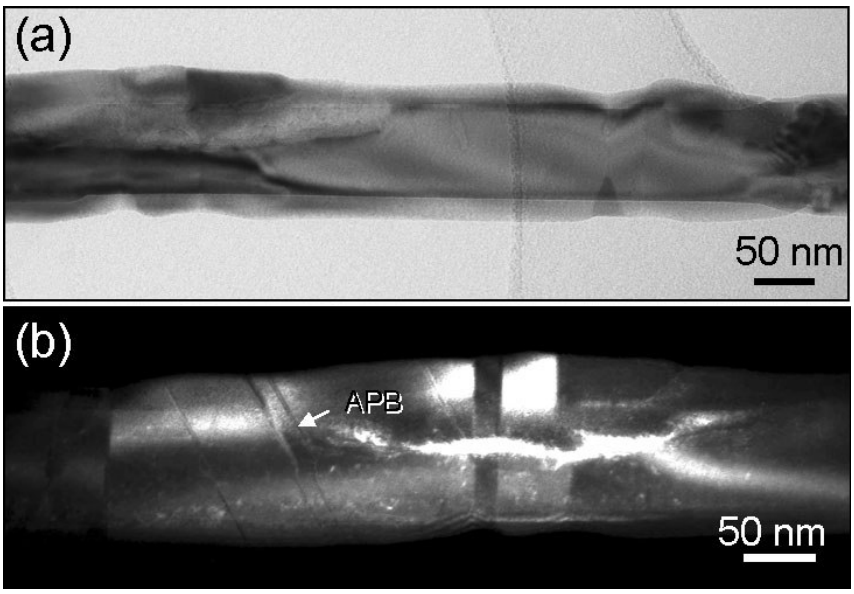

Figure 3.29: (a) Bright-field and (b) dark-field image to show the antiphase domain boundaries and 120° rotation domain walls in the ε-Fe_2O_3 phased nanowire.

In summary, the phase structure from the tip to the end of the nanowire changes continuously, from magnetite to ε-Fe_2O_3, then to α-Fe_2O_3. There is no evidence of the γ-Fe_2O_3 phase at any point. If it did exist, the diffraction pattern could unambiguously separate it from the above three phases. Keeping in mind that the earliest formed portion

of the wire should be the furthest away from the catalyst, with the latter or freshest growth occurring closest to the catalyst, we can assume that the as-deposited nanowires form the magnetite phase, and with time, oxidize into ε-Fe_2O_3, and later into α-Fe_2O_3. Figure 3.27(c) provides an enlarged image of the rectangle enclosed area in Figure 3.27(a). The bubble-like contrast in the TEM image might be regarded as evidence of oxidization after the wire's initial formation.

Based on the above TEM analysis, another phenomenon needs to be emphasized. While some magnetite nanowires grew along $[111]_M$ and $[211]_M$ directions, we never observe ε-Fe_2O_3 phase in these structures. However, in all examined Fe_3O_4 nanowires grown along $[110]_M$, without exception, we found presence of the ε-Fe_2O_3 phase. It also should be noted that nanowires grown along $[110]_M$ have the longest length (normally >2μm) compared to those found to grow along $[111]_M$ and $[211]_M$. Therefore, the fast growth direction of Fe_3O_4 nanowires should be $[110]_M$. Possibly, the magnetite nanowires growing along the $[110]_M$ direction formed earliest, giving these sufficient time to oxidize to the ε-Fe_2O_3 phase, while the nanowires growing along the $[111]_M$ and $[211]_M$ directions formed too late to undergo the transition. Still, more work is needed to fully understand this phenomenon.

The SAED patterns in Figure 3.23(b) and Figure 3.28(d) reveal the existence of 120º rotation domains. These can be seen more clearly in the bright-field and dark-field images shown in Figure 3.29(a) and (b). Based on the contrast in Figure 3.29(b), besides the 120º rotation domain walls (the interfaces between bright and dark domains), another type of planar defect, anti-phase boundaries (APB), also exist as the white arrowhead indicates.

The HRTEM image in Figure 3.30(a) shows three separated 120° domains. The FFTs of domains “D1”and “D2” are displayed in Figure 3.30(b) and (c). After indexing the FFT patterns, the identified *b* axes of each domain have been marked in Figure 3.30(a). The flat 120° rotation domain walls lie in (010) or (110) planes. Irregular domain walls were also observed as shown in Figure 3.30(d). The formation of these rotation domain walls is related simply to the redistribution of Fe ions in the oxygen interstitial sites from one domain to another. The stacking of the closed packed oxygen ions, which serve as the framework of the structure, remains intact. Therefore, the formation of the irregular shaped domain walls is energetically reasonable.

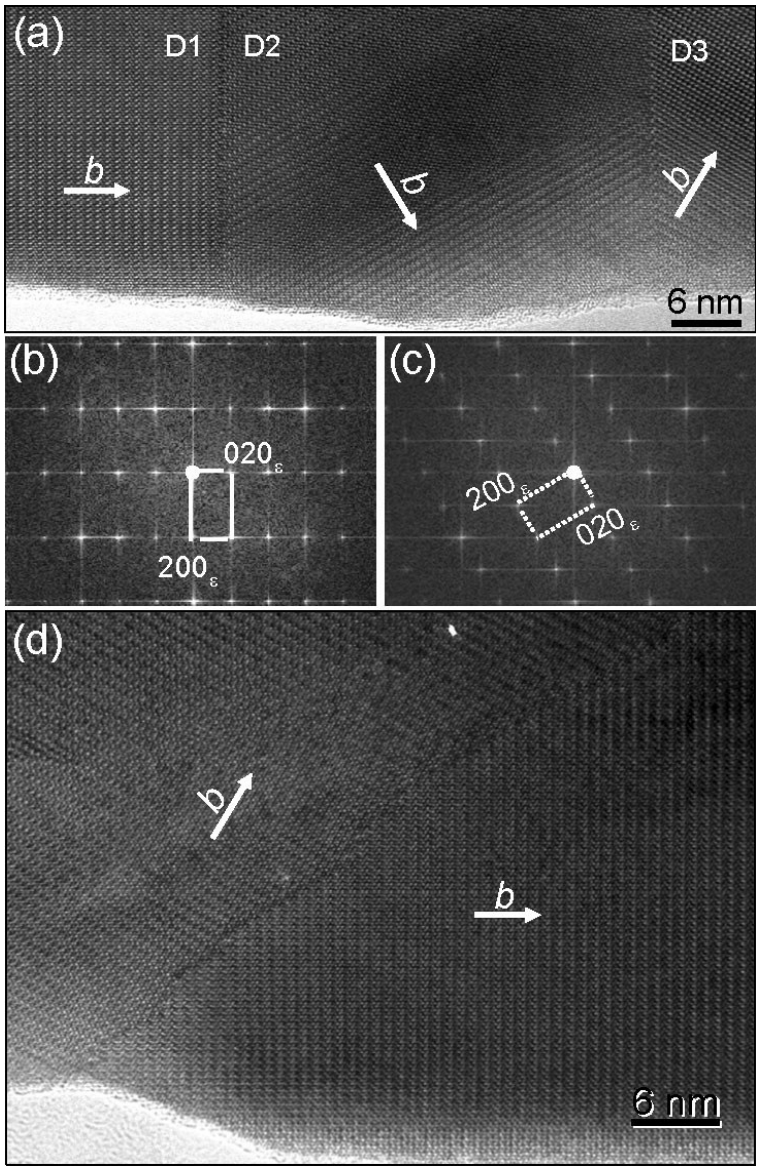

Figure 3.30: (a), (d) HRTEM images of the 120° rotation domains as shown in Figure 9. (b), (c) FFT of the domain D1 and D2 in (a).

The HRTEM image of an APB is shown in Figure 3.31. The boundary plane normally takes the (100) plane. The displacement across the defect is on the order of 1/3 b ~ 2.9Å. Similarly to the case of the 120° rotation domain walls, the framework of close-packed oxygen remains intact; only the cations readjust positions across the defect. In such κ-alumina crystal structures, the displacement of the elementary APB corresponds to

a cation shift of half the O-O distance along the *b* axis, which is around 1.45Å in the ε-Fe_2O_3 crystal. The observed APBs in Figure 3.31 can be considered as two elementary APBs combined together.

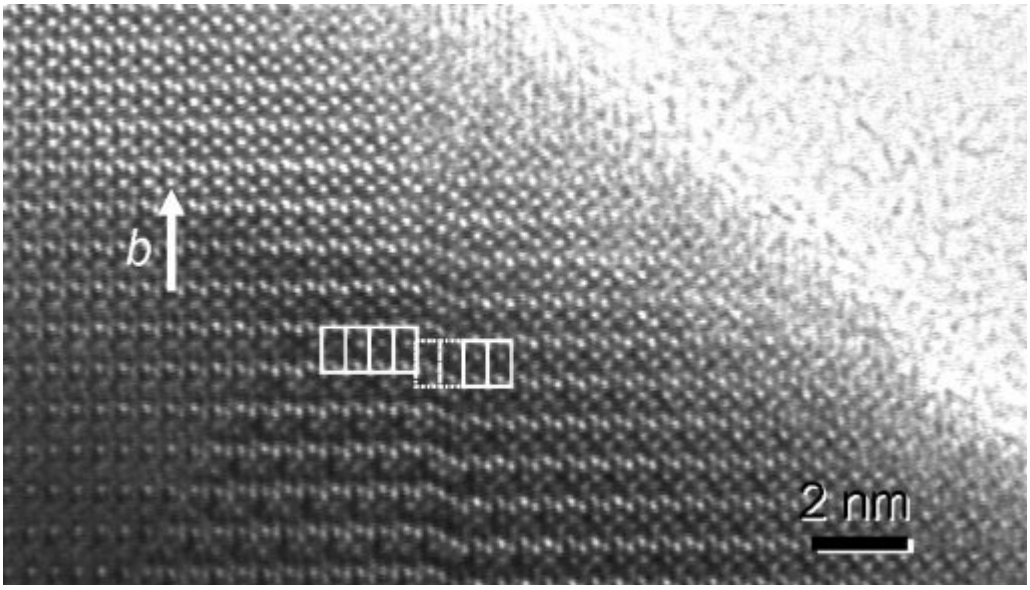

Figure 3.31: HRTEM image of a ε-Fe2O3 phase nanowire, showing the atomic scale structure of an antiphase domain boundary.

By using pulsed laser deposition (PLD) method and Fe_3O_4 powder as precursor, we synthesized not only one-dimensional Fe_3O_4 nanowires but also high yield ε-Fe_2O_3 nanowires. The crystal structure of these nanowires and the structural relationship between magnetite and ε-Fe_2O_3 phases have been characterized by systematic transmission electron microscopy (TEM) study. The pure magnetite nanowires were found to grow along $[111]_M$ and $[211]_M$ directions. Nanowires which grew along $[110]_M$ were found in every instance to contain the ε-Fe_2O_3 phase, with the fixed structural relationship of $[001]_{\varepsilon-Fe_2O_3} \parallel [111]_{Fe_3O_4}$, $[010]_{\varepsilon-Fe_2O_3} \parallel <111>_{Fe_3O_4}$. Remarkably, we found no indication of the existence of γ-Fe_2O_3 during the synthesis process. Therefore, the

phase transition may be described as from magnetite to ε-Fe_2O_3, then to hematite, a novel structural evolution route in iron oxide. High resolution TEM images and electron diffraction enabled us to observe this entire structural transformation within a single nanowire. Also, the 120ºrotation domain boundaries and antiphase boundaries found in our ε-Fe_2O_3 nanowires have been characterized. We believe this to be the first report of ε-Fe_2O_3 transition from magnetite, rather than the γ-Fe_2O_3 phase. The novel fabrication route reported here should provide researchers with another tool toward practical synthesis of the epsilon phase, a promising and exciting material for many future applications.

CHAPTER 4

CORE-SHELL ZINC OXIDE–SILICON DIOXIDE NANOWIRES

This chapter examines the growth and characteristics of very long zinc oxide-silicon dioxide core-shell nanowires. While these materials are not ideal for the biomedical application examined in the last chapter, they are useful tools for bio-sensing luminescent devices, or lasing, and could be used for non-magnetic *in vivo* applications. [149] The emphasis of this chapter, however, is understanding the growth mechanism of these unusually long wires. This is done to provide a broader context for understanding nanowire growth in general, which appears to vary considerably according to chemistry and structure. Detailed analysis of these nanowires helps place the previous observations relating to iron oxide in perspective and provides some new clues to the catalyst assisted vapor deposition nanowire growth process. Much thanks is deserved by Dr. Daniel Moore who was responsible for the initial interest and synthesis of these wires, as well as SEM, EDS and some TEM characterization.

This work represents a novel synthesis of ZnS-SiO_2 core-shell nanowires exhibiting both dense and well-aligned organization while maintaining high aspect ratios. These nanowires, with lengths on the order of mm to cm, are long enough for simple manipulation into devices, addressing an essential need. The single-crystalline nature of the ZnS core ensures high quality semiconductor materials characteristics, while the amorphous silica shell should help to prevent mechanical or radiation damage and suppress chemical reactivity, which often leads to oxidation and contamination in bare ZnS nanomaterials. For bio-related applications, the low toxicity of both ZnS and silica is

highly desired. In fact, some researchers have found that amorphous SiO_2 demonstrates low toxicity even in systems that do not respond well to its crystalline form. [150]

Nanowires of up to centimeter in length and approximately 30 nm in diameter were synthesized through a simple chemical vapor deposition process. Scanning electron microscopy (SEM) data showed that these nanowires were well-aligned and grew in the direction along the flow of the carrier gas. Through transmission electron microscopy (TEM) and x-ray diffraction (XRD) analysis, the nanowires were found to be composed of a single-crystalline ZnS core and amorphous SiO_2 shell. Gold catalyst particles were found at the tips of the nanowires and completely encased by a silica shell. Photoluminescence (PL) measurements were performed on nanowire samples in which the synthesis time was systematically varied to provide information regarding growth dynamics.

A series of systematic experiments coupled with careful analysis provided the ability to examine how variations in synthesis time affected nanowire growth. These experimental measurements were used to help formulate a proposed growth mechanism. A novel dual-diffusion process is initially suggested, in which ZnS atoms migrate to the growing nanowire core via bulk diffusion through the gold catalyst particle, while the SiO_2 species migrate around the particle surface before becoming incorporated into the amorphous nanowire shell. The theoretical feasibility of this model is tested through diffusion calculations, and the results are found support the proposed process. Later work described in Chapter 5, however, demonstrates that such a bulk transport mechanism could not have occurred for these nanowires, so alternate pathways for growth are explored.

4.1 Background

One dimensional nanostructures such as nanowires and nanobelts have been suggested as ideal candidates for many electrical and optical applications, and several groups have reported successful synthesis in recent years. [29, 117, 151-161] In particular, semiconducting and II-VI nanowires have drawn large interest because of the ability to synthesize them in diverse configurations, and under varying conditions, in addition to their potential use in numerous electronic and optical devices.[117, 151, 155] Zinc sulfide (ZnS), a member of the wurtzite family, is a direct wide band gap (3.91 eV) II-VI semiconductor, and a vital material in the field of photonics. ZnS is also an important phosphor host lattice material used in electroluminescent devices (ELD), due to its large band gap, which enables emission of visible light without absorption, and efficient electron transport. Furthermore, single ZnS nanobelts have been shown to facilitate optically pumped lasing.[151] The successful application of ZnS quantum dots in several biological studies indicates that nanowires and nanobelts of this material may also find practical use in areas such as bio-sensors, multiple cell or protein tagging, and even *in vivo* imaging and therapeutics. [149, 162-166]

Still, the extensive reports of one-dimensional nanostructure growth have revealed several challenges that remain before these tools may practically be applied to commercial or industrial needs. One of these challenges arises from difficulty in producing very long nanowires that can be easily integrated and manipulated post-synthesis through simple methods. Another challenge is the need to organize such long

nanostructures in ordered or aligned patterns, and in high densities, further augmenting ease of use and scaling.[117] Meeting both of these obstacles would significantly advance the development of one-dimensional nanostructures toward commercial and industrial utilization.

In addition, since the discovery of 1D nanostructures grown via catalyst-assisted vapor deposition processes, researchers have been troubled to identify precise formation mechanisms, especially regarding the role of the metal catalyst particle. In a much earlier work, Wagner and Ellis outlined for the Au-Si system what is generally regarded today as the classic vapor-liquid-solid (VLS) nanowire growth mechanism, in which a diffusing species is transmitted through the bulk of a metal catalyst in liquid phase before incorporating into the growing nanowire.[167] Such a process is often applied to other dual component systems,[168] which often, [26, 169] but not always,[170] appear to mimic the Au-Si model system. Growth mechanisms in multiple component systems, however, have proved much more difficult to conclusively identify, as in many cases the final product is not well-explained by this VLS process. In addition, these complex systems often lack experimental phase diagrams necessary to determine solubilities of diffusing species in the catalyst material, preventing easy identification of the conditions necessary for true VLS growth.

Several alternative mechanisms have been proposed for catalyst assisted nanowire growth, often varying according to experimental parameters and growth species. The most applicable for our system, those in which ZnS or SiO_2 1D nanostructures grow via Au catalysis, vary across the literature, and include several atomic transport schemes.[155, 158-160, 171-173] Such variance reveals a lack of consensus regarding the

phase condition of the metal catalyst particle at elevated temperature, the diffusion mechanism in the metal catalyst, the role of transverse growth, and the state of the arriving gas species, among other issues. One source of discrepancy may be that growth mechanisms may vary according to the growth chemistry and parameters, and may utilize not just one, but a combination of processes. Additionally, formation mechanisms may appear similar to VLS growth, yet without demonstrating key components such as alloying in the catalyst particle. We examine previous investigations into the growth of 1D ZnS and SiO_2 nanowires, and compare these findings to our own experimental evidence. Early observations led to the proposal of a dual-diffusion mechanism for our core-shell nanowire samples, in which both surface and bulk diffusion occur simultaneously. Further experiments described later in Chapter 5 however, point to the possibility of a mechanism in which both forming species are diffusing on the catalyst surface.

4.2 Fabricated Core-Shell ZnO-SiO2 Nanowires

4.2.1 Fabrication Method

Synthesis of the ZnS/SiO_2 nanowires was carried out via a simple vapor deposition process as shown in Figure 2.3. Commercially available ZnS powder (Alfa Aesar, 99.99% purity, metal basis) was placed in the center of a single-zone horizontal tube furnace (Thermolyne 79300), where the atmosphere, evaporation time, pressure, and temperature were controlled. Single-crystal silicon substrates with 20 nm of gold deposited by thermal evaporation were placed “downstream” at a lower temperature

region in the furnace. Using a rotary vacuum pump, a vacuum was pulled in the tube for several hours to purge oxygen from the chamber. After evacuation to a pressure of about 2×10^{-3} torr, the temperature in the center of the tube was elevated to 1000 °C at a rate of 50 °C/min. N_2 gas flow was introduced into the system at a rate of 50 standard cubic centimeters per minute (sccm). The pressure in the system was allowed to increase to a value of 20 torr (~0.03 standard atmospheres) and was held at that level through the duration of the synthesis. The silicon substrates reached a temperature of about 750 °C, as determined through prior thermocouple studies. After maintaining these conditions for between one and two hours, the N_2 gas flow was turned off and a vacuum with a pressure around 2×10^{-3} torr was again achieved. At this time, the furnace was allowed to cool to room temperature.

4.2.2 Characterization

Optically, each sample appeared as a thick deposition of white powder or fluffy white fibrous material covering the silicon substrate. Samples growing for longer times showed increased deposition density on the substrates, with some deposition masking the silicon wafer completely. Some samples exhibited deposition product several millimeters past the silicon substrate. Care was taken when preparing samples for analysis not to destroy or contaminate the as-grown nanowires. Samples were analyzed initially using XRD and SEM. Initial XRD scans were fast scans (~10 min per sample) performed to determine basic phase information. Longer subsequent scans were then taken to gather more in-depth information from the samples. The SEM used for our analysis was a LEO

1530, operated at 5 kV. The samples were also examined using TEM (Hitachi HF-2000 operated at 200 kV).

X-ray diffraction measurements were performed on each sample using a PANalytical X-Pert Pro MRD X-ray machine with Copper K-alpha radiation. As-grown samples previously affixed to aluminum SEM stubs with carbon tape were loaded into the Sample Holder for Solid Samples affixed to the MRD Cradle. Alignment was then performed via manual scans to check the sample position with respect to the 2theta, Z, and Omega axes. Sample offsets were input into the system to calibrate zero positions for each axis. In this way, the sample was aligned parallel to the beam without the necessity to perform otherwise potentially destructive sample preparation.

For the measurements, the radiation beam emitted from a x-ray tube set to line focus, coupled with a parabolic mirror and $1/8^{o}$ fixed divergence slits was directed toward the unmodified nanowire coated substrate. After interacting with the sample, a 0.27 degree parallel plate collimator with a flat graphite crystal diffracted beam monochromator helped refine the signal before reaching the Miniprop large window point detector. 2theta-omega measurements were taken with a tube power of 45 kV and 40 mA, from $5\text{-}120^{o}$ 2θ with a 0.01^{o} step size and a 2 hour and 23 minute total scan time.

SEM images like those illustrated in Figures 4.1 and 4.3 identified the synthesis product as nanowires aligned laterally to the substrate and in the direction of the N_2 gas flow in the tube furnace. Additionally, these images show that the aligned nanowires on the top layer of the substrate are fine and very long. Figure 4.1 (a-d) reveals several images of a single representative nanowire sample.

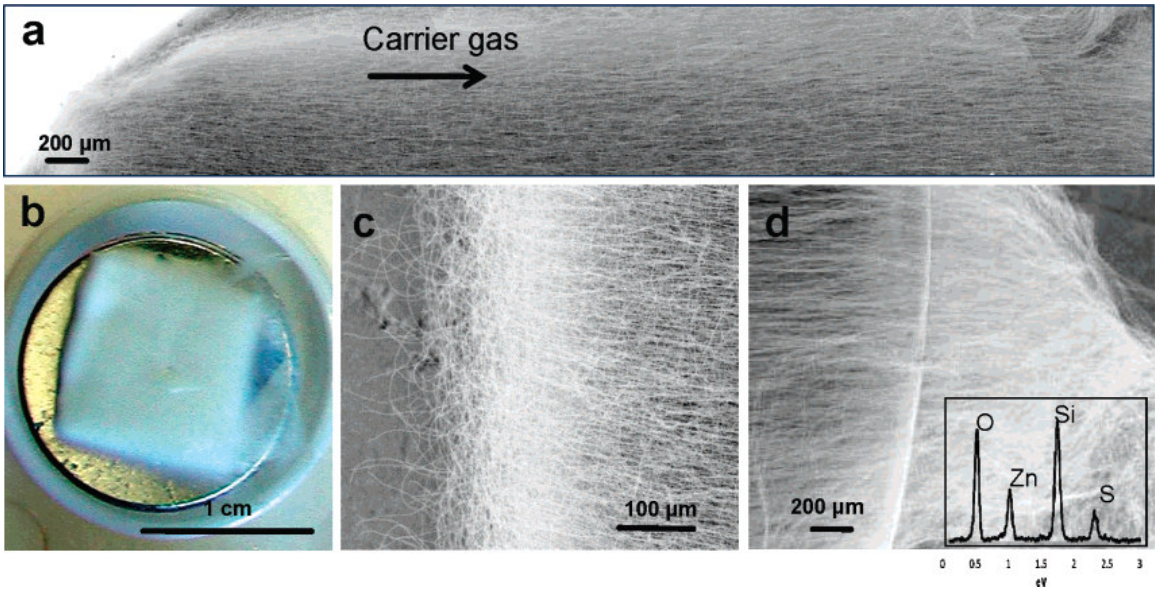

Figure 4.1: SEM and optical images showing a representative sample of ultralong ZnS-SiO2 nanowires: (a) composite of several SEM images demonstrating nanowires length; (b) optical image taken from above sample, fixed on metal stub; (c) SEM image of the sample's leading edge; (d) SEM image of opposite edge, showing long nanowires reaching past the metal stub. The inset shows corresponding EDS data.

Figure 4.1 (a) shows a composite SEM image taken across the ~1 cm deposition substrate. As shown in this figure, the nanowires are aligned along the flowing direction of the carrier gas. It appears that some nanowires begin at the leading edge of the substrate and continue well past substrate edge, making these nanowires approximately 1.5 cm in length. It was attempted to follow an individual nanowire by microscopy along the entire length of the substrate; however, in every attempt, the nanowire was lost about two-thirds of the way due to SEM image shift. Figure 4.1(b) contains an optical image of this sample, illustrating the length and density of the nanowires at low magnification. Note that the silicon substrate is completely masked by the nanowire sample. Figure 4.1(c) illustrates an SEM image of the substrate's leading edge. Figures 4.1(b) and 4.1(d)

confirm that the nanowires grew beyond the substrate. Note that the boundary observed in Figure 4.1(d) corresponds to the edge of the sample stub, seen at the far right of Figure 4.1(b), rather than the edge of the silicon substrate. The EDS profile taken in the SEM, seen in the inset, reveals presence of Zn, S, Si, and O in the sample.

TEM images and electron diffraction patterns are presented in Figure 4.2. Several nanowires were imaged using low-resolution TEM, as shown in Figure 4.2(a-c). The images shown in Figure 4.2(a) and 4.2(b) show the tip of the nanowire, including the terminating metal catalyst particle. EDS scans across the area of the particle (not shown) indicated the presence of Zn, S, Si, O, and Au.

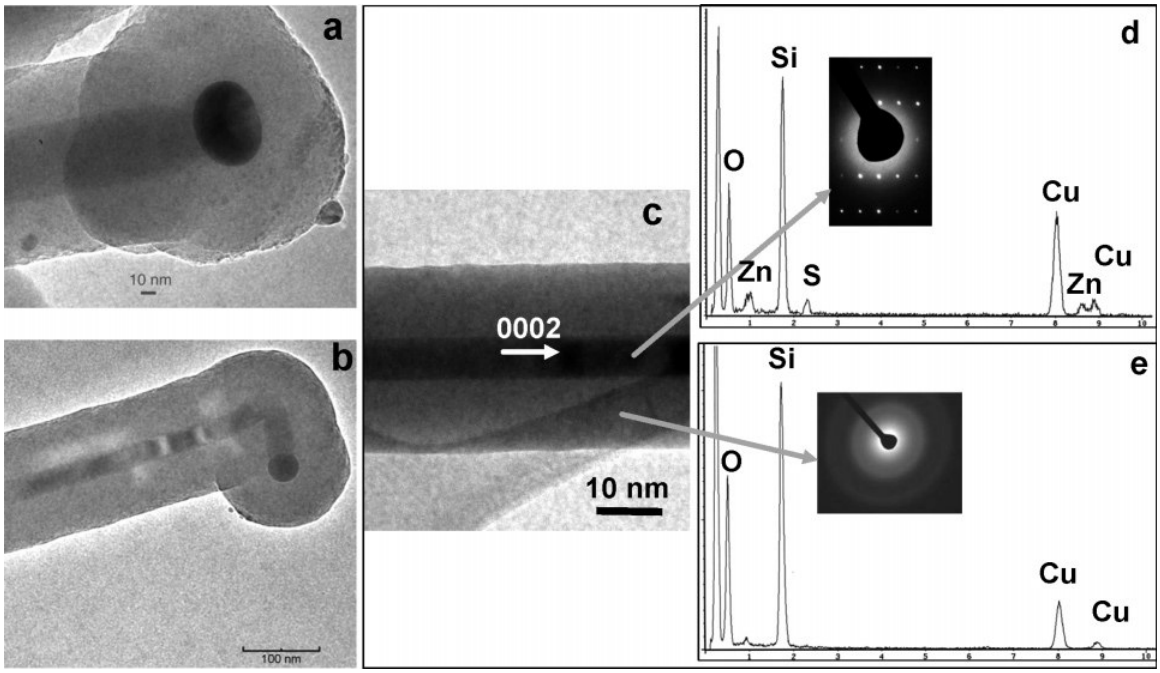

Figure 4.2: (a, b) Low-magnification TEM images showing the tip of two ZnS- SiO2 core-shell nanowires, including the terminating metal particle. (c) Low-magnification TEM image of a nanowire center. (d) Electron diffraction pattern and corresponding EDS data from the nanowire illustrating the single-crystalline nature of the core. (e) Electron diffraction pattern and corresponding EDS data from the nanowire shell, showing the shell to be amorphous in nature and consisting of only Si and O.

Note the contrast change seen in the amorphous shell layer at the tips of these nanowires. This contrast change in the 2D TEM projection seems to indicate the presence of a sphere or half-sphere of amorphous material surrounding the metal particle. The "neck" region of the nanowire just below the particle in Figure 4.2(a) is also of interest. Figure 4.2(c) shows a slightly higher magnification image of a nanowire center. Electron diffraction patterns were taken of the core and shell areas of this nanowire and are presented in Figures 4.2(d) and 4.2(e), respectively. The electron diffraction pattern shown in Figure 4.2(d), together with the EDS data also taken in the TEM, reveal that the nanowire core consists of a Wurtzite structured ZnS. The presence of Cu seen in the EDS spectrum is likely due to the Cu TEM grid used to affix the sample. Using analysis of the electron diffraction pattern, it was also determined that the ZnS core of the nanowire grew along the [0001] direction, the fast growth direction of wurtzite ZnS. Figure 4.2(e) shows TEM and EDS information corresponding to the shell of the nanowire sample. The electron diffraction pattern indicates that the shell is made up of an amorphous material, while the EDS graph shows presence of Si and O, but not Zn or S. These results indicate that the nanowire is composed of a crystalline ZnS core and an amorphous SiO_2 shell.

4.2.3 Growth Mechanism

To gain insight regarding the growth mechanism of these core-shell nanowires, synthesis at different time periods was conducted in an effort to observe their growth evolution. Synthesis runs were performed in which the maximum reaction chamber temperature was maintained for 15 minutes, 30 minutes, 45 minutes, 60 minutes, 90

minutes, and 110 minutes. To ensure that results were consistent and reproducible, at least three experiments were run for each set of parameters. The uniformity of the results observed in these experiments suggests a high degree of repeatability in the growth process. SEM images corresponding to each of these synthesis times are shown in Figure 4.3.

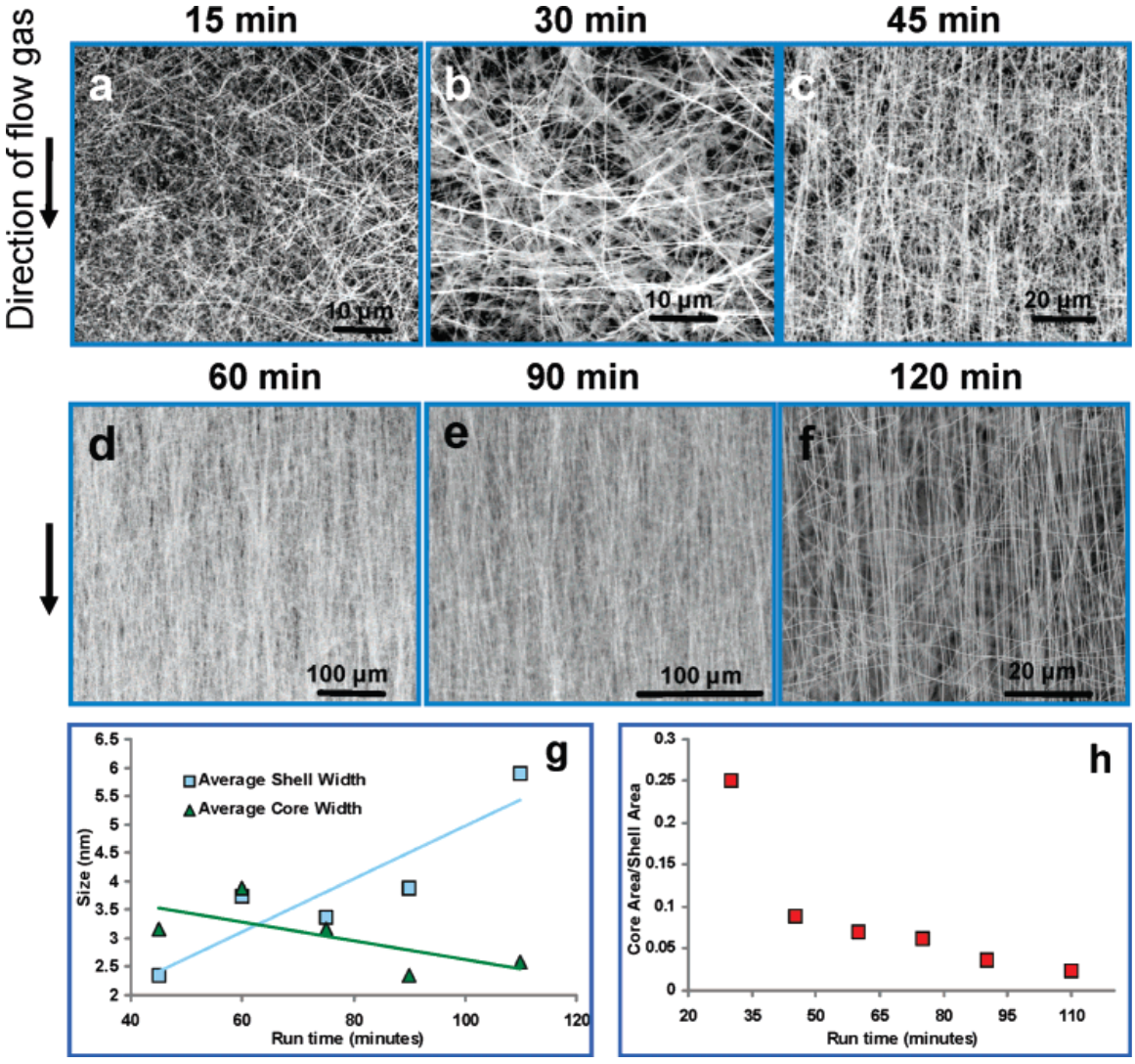

Figure 4.3: Ultralong nanowires as a function of growth time. SEM images show sample characteristics after (a) 15 min, (b) 30 min, (c) 45 min, (d) 60 min, (e) 90 min, and (f) 120 min, at maximum chamber temperature. (g) Plot showing variation in average nanowire core and shell widths as a function of growth time, as determined from TEM analysis. (h) Plot illustrating variation in the core/shell area ratio as a function of growth time.

Although ZnS/SiO_2 nanowires were synthesized with growth times as short as 15 minutes, nanowire alignment was not observed in growth times shorter than 45 minutes. Longer synthesis times corresponded in general to longer and denser growth product. Although Figure 4.3(f) appears to show a lower density of nanowires compared to previous images, this is not the case, as this image is taken at higher magnification to show greater sample detail. Note that the images in Figure 4.3 are rotated 90^o relative to those in Figure 4.1, such that the flow gas here is indicated to be in the vertical direction.

Several analysis techniques were performed to compare samples of varying synthesis times. First, a TEM-based study of the various widths of the ZnS core and the SiO_2 shell was conducted. This consisted of measuring, via TEM images, the widths of both the core and the shell, and comparing them according to synthesis time. Measuring over 30 nanowires from each of the six time intervals, the average (mean) widths of core and shell for nanowires in each section were determined. While core widths were measured directly, shell widths were determined by subtracting the core size from the total width of the nanowire. A graph of this data is shown in Figure 4.3(g). Not included on this graph are measurements for the 30-minute synthesis time interval. These values were omitted as outliers, determined initially by distortion of the graphs, and then confirmed via a standard statistical analysis technique in which the values were found to lay more than one standard deviation away from the next closest data point. For completeness, it should be noted that measurements on samples run in the 30-minute interval confirmed the overall trend observed in other samples, showing an average ZnS core size of 13.84 nm and a silica shell width average of 1.59 nm. As can be seen in the

graph, the ZnS core tends to become smaller over time (although only by a maximum of a few nm) while the SiO_2 shell grows larger with longer synthesis times.

While core and shell width values differ between samples according to time interval, we observed that each nanowire maintains a constant width along its entire length, without the presence of dips or tapering. Therefore the nanowires' relative volumes should be able to be determined from their respective widths according to the following equation:

$$\frac{\textit{Core Volume}}{\textit{Shell Volume}} = \frac{r_c^{\,2}}{[(r_c+w_s)^2 - r_c^{\,2}]} \qquad \textbf{(Eq. 4.1)}$$

where $r_c = w_c/2$ is the radius of the ZnS core and w_s is the thickness of the SiO_2 shell. Results of this analysis for nanowires in each time interval are shown in Figure 4.3(h). As seen in this figure, we found that the core volume relative to the shell volume decreases over time.

While TEM analysis supplied detailed information regarding the nature of a small subset of nanowires in each sample, X-ray diffraction (XRD) techniques were utilized to provide a better understanding of the global nature of the nanowires. In particular, we sought to investigate the overall changes in relative core and shell thickness with respect to synthesis time, for an area of nanowires measuring a few square millimeters. Six samples were examined, each differing only according to experimental reaction time, as in the quantitative TEM analysis. These times were: 30, 45, 60, 75, 90, and 110 minutes. The results of scans from each sample are shown in Figure 4.4(a).

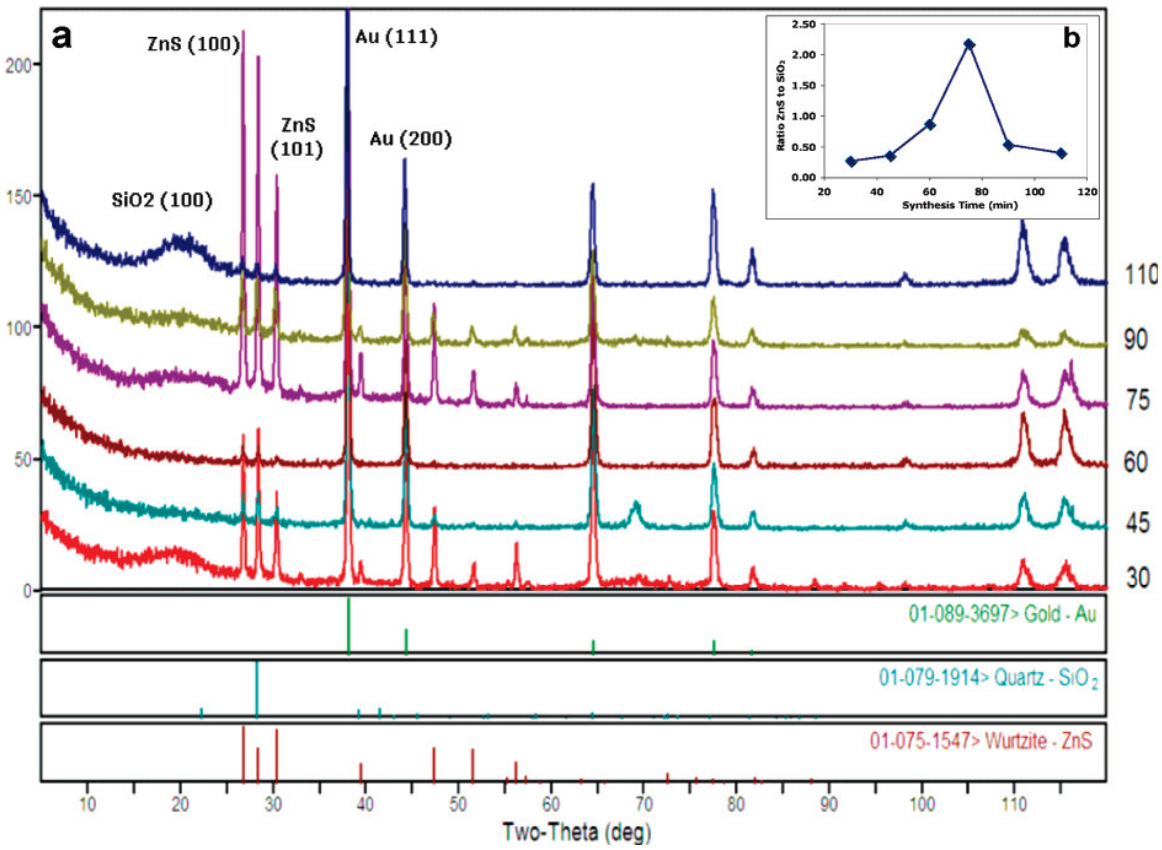

Figure 4.4: (a) Series of XRD patterns from samples with reaction times varying from 30 to 110 min. (b) Plot illustrating the ZnS:SiO2 ratio in nanowire samples as a function of reaction time, derived from XRD pattern semi quantitative phase analysis.

Note that while intensities vary, scans show similar peak profiles for each sample. This result confirms that the experimental design and sample preparation were such that phases remained consistent, and no contamination occurred. Variations in intensity may occur for many reasons, including instrumental effects, sample alignment, nanowire density, relative phase concentration, crystallite size, and preferred sample orientation, among others. Phase identification of the diffraction pattern in Figure 4.4(a) using PANalytical X-Pert HighScore Plus software yielded three known phases: Au (PDF#89-3697,) the Wurtzite phase of ZnS (PDF#75-1547) and SiO_2 (PDF#82-0512). MDI Jade7.5 software was later used to confirm phase results**.** To determine relative ZnS and

SiO_2 core and shell thickness from the XRD data, semi-quantitative phase analysis was utilized for the ZnS phase. HighScore and Jade software were employed to perform the XRD analysis.

The semi-quantitative analysis in X'Pert HighScore works on the basis of reference intensity ratio (RIR) values, which divide the intensity of the pure phase to be determined by the intensity of a standard material, often corundum (Al_2O_3). To perform analysis on a sample containing multiple phases, the Normalized RIR Method developed and published by Chung was used.[174] The normalization used in this method assumes that the sum of all identified phases is 100%. This means that unidentified or amorphous phases will reduce the meaning and accuracy of this analysis. In the case of these samples, TEM found the SiO_2 shell to be mostly amorphous in nature, which was validated through broad peak signatures in the XRD pattern. In such cases, the result is still a good estimate of the relative mass fractions of the identified phases. Since this investigation seeks simply to find the relative differences between ZnS and SiO_2 in the sample, rather than actual empirical values for these, this method was deemed reasonable. Figure 4.4(b) shows a graph illustrating the relative concentration of ZnS versus SiO_2 for each sample, as reaction time increases. Note again that due to the presence of some amorphous SiO_2 in the sample and the possibility of an oxidation layer on the silica substrate surface, these values must be regarded as indicative of a trend, rather than as stand-alone empirical values.

Through the use of semi-quantitative phase analysis on XRD diffraction patterns produced by samples created at varying reaction times, this work has shown a clear trend in the variation of core size in the ZnS/SiO_2 core-shell ultra-long nanowires as reaction

time progressed in the experiments, illustrated in Figure 4.4, part (b). At short reaction times, both the relative percentage of ZnS in the nanowires and the average size of the ZnS Wurtzite crystal begin at a low base value. As the reaction progresses, the ZnS core grows larger, and a larger proportion of ZnS is present in the nanowires, relative to the SiO_2 amorphous shell. As the reaction continues, however, the size of the core appears to reach a maximum value, and then the ZnS again decreases, both in size and concentration.

Lastly, the photoluminescence spectra are compared for the samples grown at different time periods. The resulting graphs are shown overlaid in Figure 4.5.

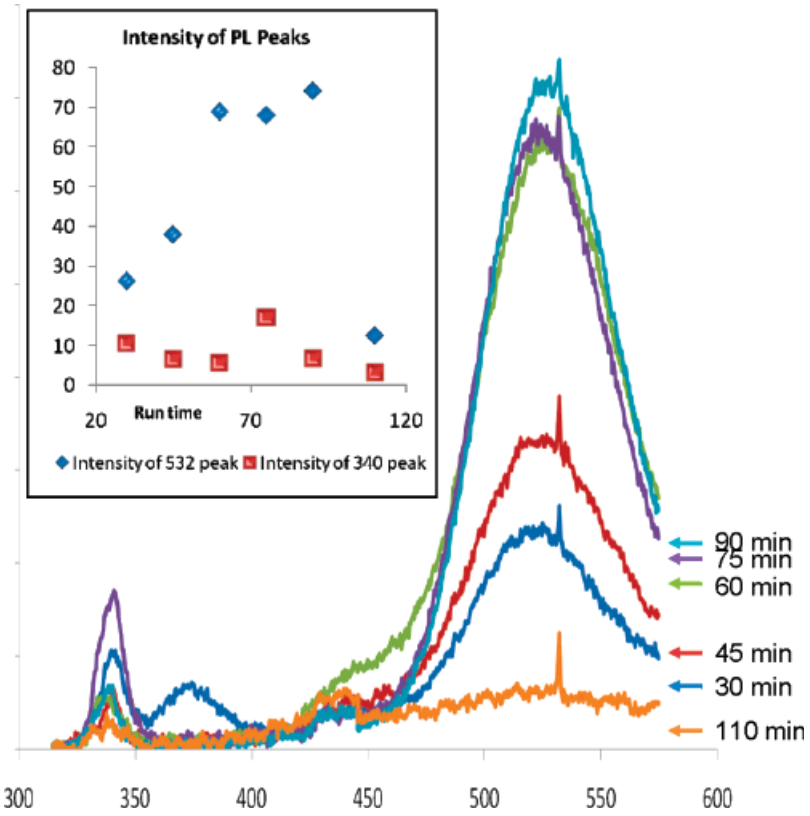

Figure 4.5: Composite of photoluminescence data from several ultralong ZnS-SiO2 core-shell nanowire samples. Each pattern corresponds to a unique sample exposed to synthesis conditions for a time interval between 30 and 110 min. The inset illustrates a plot of this data, correlating peak intensities with reaction time.

All of the spectra show at least two distinct peaks. One peak appears at 340 nm and the other around 532 nm. The lower wavelength peak is well explained as a pure ZnS PL peak. This peak is associated with a material band gap of about 3.65 eV, a good match with the theoretical wurtzite value of 3.91 eV. Because ZnS with very few defects, vacancies, or interstitials is conventionally difficult to find, in the literature it is rare to see the 340 nm ZnS peak. However, for nanostructures such as these, which are well-structured and contain few defects compared to bulk materials, the presence of this peak is not surprising. The 532 nm peak is significantly more common. It is associated with Zn defects, vacancies, and interstitials in the ZnS crystal. This peak translates into a band gap of 2.33 eV. [160, 175] The sharp peak that appears to be convoluted with the much broader signature around 540 nm is due to an instrumental effect, and is present in all profiles originating from the PL equipment used for this analysis.

In the lowest growth time measured, that of 30 minutes, a broad peak can also be observed at 375 nm, which corresponds to a band gap of 3.30 eV. This peak has been shown to exist in studies of pure silica. [176] This result indicates the possible presence of a silica layer on the substrate surface, exhibiting observable luminescence only in the sample with the lowest density of nanowires. It is important to compare the intensities of the peaks and how they change with longer synthesis times. This is shown more clearly in the inset of Figure 4.5. Focusing on the 532 nm peak, one can observe an interesting phenomenon. The intensity of the peak increases with increasing synthesis times from 30 up to 90 minutes. However, for nanowires allowed to grow for 110 minutes, the peak disappears. Also, the ratio between the two major peaks increases with longer synthesis

times from 30 to 90 minutes. Again, at the 110 minute measurement, the ratio drops dramatically.

Since the first observations of catalyst assisted vapor deposition nanowire synthesis, researchers have sought to identify underlying growth mechanisms governing the production of these materials. Although much progress has been made, in many cases 1D vapor deposition synthesis remains as a kind of "black box" in which parameters are set, experiments are run, and a final product is achieved, without a full understanding of the processes combining to deliver the result. Observation of a metal catalyst particle at the nanowire tip is no longer considered sufficient evidence to support the classic VLS formation process in whole or in part, especially in light of studies with GaAs and InAs structures and other metal catalysts, which seem to indicate that nanowires can be grown by particles remaining in the solid state throughout the synthesis process. [170, 177] Studies on Sn catalyzed ZnO 1D nanostructures indicate that the crystalline and electronic structures of the substrate, nanostructure and catalyst particle can all play a role in determining the nature of the final growth product. [178, 179] In the case of gold catalyzed ZnS, Si, and SiO_2 1D nanostructures, much has been written regarding possible formation mechanisms specific to synthesized products. In examining the wealth of literature on these structures, some general trends can be identified.

Silicon appears most often to form nanostructures via bulk diffusion through the Au catalyst particle. Rarely is silicon observed as a tube or shell structure. A recent publication in which successful synthesis of ZnS-Si core-shell nanowires was achieved, reports this result through templating of the silicon onto a previously grown ZnS nanowire, and not direct vapor deposition growth.[155] The work by Wagner on this

topic has been previously mentioned**,** and other papers report *in-situ* observation of the classic VLS process in Si nanowire systems. [180] The literature also suggests that ZnS nanostructures may form primarily by bulk transport means, as 1D nanostructures of this material also tend toward formation of solid products and core, rather than shell, components. Further evidence has been supplied through EDS analysis, as in the case of one recent study reporting that an EDS detector fit to a TEM revealed traces of Zn and S as well as Au when focused on the terminating Au particle of a ZnS nanowire.[181] Another publication has presented AFM data indicating that Au catalyst islands grew in volume just prior to growth of ZnS nanowires, suggesting that arriving species were diffusing into the catalyst material. [182]

However, these studies may be misleading. Bulk diffusion through the catalyst particle is difficult to justify thermodynamically, and much data in the literature citing VLS growth of nanostructures can also be explained via surface diffusion mechanisms. The EDS data cited above did not include a careful TEM study to determine if the Zn and S were actually present within the gold particle, or if the data was generated by these species laying on the surface. Swelling of Au catalyst islands uncovered through AFM could likewise be due to the adsorption of surface species. While most steps in the classical VLS model are most likely occurring, the phase of the catalyst particle during growth is difficult if not impossible to determine simply from observation post growth.

Conversely, SiO_2 commonly appears as a shell or as a tubular structure, frequently forming coating layers over other growth products, and in some cases even capping the metal particle. [183] Such behavior is not surprising when considered in light of silica's reduced solubility in gold compared to elemental Si. It is not uncommon to observe areas

of increased gold mobility on silicon substrates with localized oxidation, as demonstrated in earlier reports, in which low Si nanowire growth and high Au mobility were correlated to locally oxygen rich regions on a Si substrate. [183, 184] This phenomenon has even been demonstrated as an effective technique for patterning of gold particles on selectively etched Si-SiO_2 wafers.[185] In this case, the Si substrates were the only source of silicon, while oxygen species likely originated from residues left in the reaction chamber, or even from slight oxidation of the substrate surface. Additionally, SiO, a common vapor, may have acted as an intermediate in the process.

Exactly how these processes occur remains a source of debate. Mass diffusion through the metal particle, surface diffusion around the metal particle, selective incorporation entirely at the particle-nanowire interface, transport up the sides of the growing nanowire, and direct adsorption onto the nanowire, have all been identified as possible formation mechanisms in ZnS and SiO_2 1D nanostructures**.**[186] To help identify the mechanism responsible for the growth of the nanostructures described here, each of these possible mechanisms was examined with regard to observations of the final ZnS-SiO_2 nanowire growth product. It was initially determined that any of four distinct growth processes could reasonably be suggested for the growth of these ZnS-SiO_2 nanowire structures. Each of these is examined schematically in Figure 4.6.

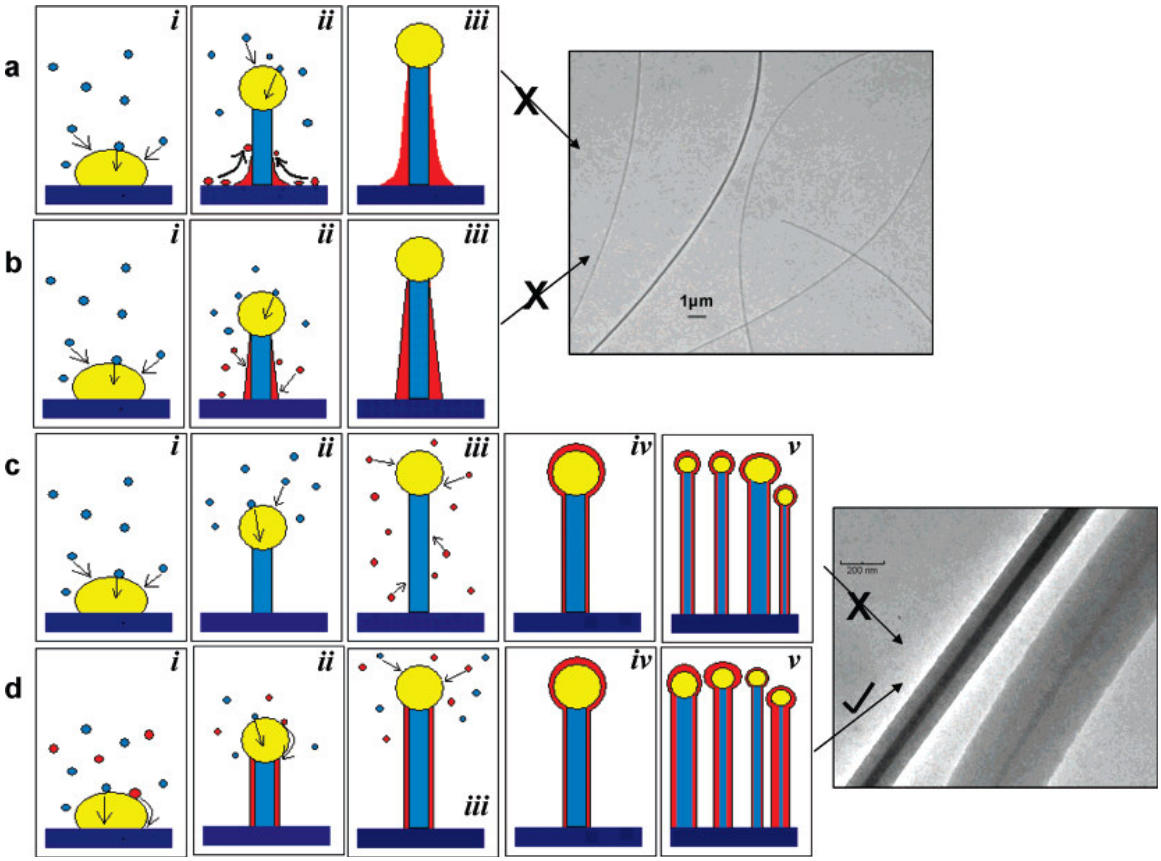

Figure 4.6: Schematic illustrating possible sample formation mechanisms and corresponding TEM images. Here yellow signifies Au, dark blue represents the Si substrate, light blue represents ZnS, and red coloration is used for SiO_2. (a) In this model, ZnS species are preferentially attracted to the Au catalyst particle and migrate to form the nanowire core. SiO_2 species form and migrate up the sides of the ZnS nanowire. (b) This model is similar to (a) except here silica species adsorb as gaseous species rather than migrating up the ZnS nanowire from its base. The final TEM image shows that these mechanisms are unlikely, since examined samples demonstrate uniform shell thickness along their entire length. (c) In this model, the ZnS nanowire forms first and then is completely encased in an amorphous silica coating. If this were the case, the silica coating should be the same thickness for all nanowires in a sample. The included TEM image demonstrates that this condition is not observed. (d) The initially proposed formation mechanism: both ZnS and SiO_2 species travel around the droplet surface to create the amorphous shell. This is the model suggested by our first analysis, but deemed impossible in light of later examinations.

Figure 4.6(a) illustrates a growth process in which ZnS molecules diffuse through or around the gold catalyst particle, with silica species originating on the substrate surface, and moving up the sides of the growing nanowire. A similar process is

illustrated in Figure 4.6(b); however, here the shell is formed via direct adsorption of silica species from the gas phase. For very long nanostructures containing an amorphous silica shell, synthesis via these processes is likely to produce structures that vary in thickness along the length.[168, 187] In short, one would expect to find variations in silica shell thickness along a single nanowire. In the first case, this phenomenon would likely occur due to the increasing distance that the silica species would have to travel up the nanowire to reach close to the tip. In the latter case, the portion of the nanowire forming earliest, or that at the bottom, would be exposed to the silica (or SiO) vapor for a longer period, and therefore should form a thicker shell. An amorphous silica layer like that observed in the samples examined here would likely not experience a strong enough driving force to promote the silicon oxide species up the nanowire such that newly formed ZnS core material at the top would maintain exactly the same shell thickness as earlier areas near the substrate surface. As can be shown in the last image of these figures, nanowires in our samples demonstrate uniform thickness along their entire length, sometimes of several hundred microns, suggesting that neither of these mechanisms is applicable for their formation.

Another possible synthesis route is presented in Figure 4.6(c). The process depicted here can be considered as similar to an atomic layer deposition (ALD) process in two steps, in which the ZnS nanowire forms first, and then is uniformly coated with an amorphous silica shell. Previous reports have cited this process as a possible formation mechanism for silica nanotubes in which the metal catalyst particle becomes completely encased. [186] However, as shown in part *v* of this figure, such a mechanism would yield nanowires with completely uniform shell thickness, despite any variations in core size or

structure. Much as in a conventional ALD process, we would expect to observe similar shell thickness among *different* nanowires in a single sample, since at the time of silica deposition the ZnS core would not be exhibiting dynamic growth. The image shown in conjunction with Fig. 4.6(c), which illustrates significant variation in shell thickness between nanowires from the same sample, indicates that for our synthesis, such a result is not observed.

Therefore we initially described growth these structures as occurring according to that illustrated in Figure 4.6(d). This series of images describes a process in which ZnS diffuses through the Au particle to form the nanowire core, and SiO_2 (or SiO) travels on the surface of the Au particle to the nanowire interface in a simultaneous and dynamic growth process. Variations in particle size and surface contact angle, among other factors we believed, could lead to observed thickness variations in the core and shell portions of these ultralong nanowires.

Later experiments have demonstrated that this mechanism could not have occurred, due to the absence of alloying species in the gold particle. We determined that a previously unexamined fifth growth mechanism could be responsible for the growth of these nanowires. In such a process, both species are transported to the nanowire interface through surface diffusion, and yet grow the resulting core and shell portions of the nanowire due to differences in surface and interfacial energy between the arriving molecules. Details of the evidence supporting the surface role of the catalyst particle, rather than bulk diffusion or alloying will be discussed later. The previously discussed mechanisms also must be re-examined in light of this new evidence. One obstacle to understanding the growth mechanism of these wires is their unusually long length.

Though we could find no variation in the thickness of the amorphous silica layer in a single nanowire, very small and gradual thickness variations could have been overlooked.

Based on the originally proposed growth model, the results of the systematic analysis were examined. TEM studies indicated that the size of the silica shell increased over time, while the ZnS core remained relatively the same, with a slight decrease in size. XRD analysis likewise suggested an initial increase in the ZnS core material with increase in reaction time, however, this increase peaked near 60-75 minutes and then declined. It is interesting that the description offered in the XRD data differs somewhat from the trend revealed through TEM analysis. Each technique contains inherent sources of error. TEM analysis provides useful information regarding a small subset which may not be typical of a much larger sample. Sources of error in the XRD techniques employed here have been described previously. It is also possible that what appears as a disparity is in fact simply differences due to analysis methods. Since the XRD techniques plotted ZnS core *ratio,* if after the peak synthesis time the silica shell thickness increased, or the ZnS core incorporated more defects, the XRD signatures could report a ZnS size decrease while the actual ZnS size remained constant.

Photoluminescence data was likewise employed to explore the development of the ultralong nanowires at each time interval. Some studies have shown that SiO_2 passivation layers on Si have the effect of increasing the intensity of measured photoluminescence peaks. In fact, the intensity of the emission has been shown to correlate to the degree of surface passivation on the films. The SiO_2 shell could have the same effect on the ZnS core's luminescence. This, along with the XRD suggesting that the ZnS core is initially increasing, would explain the increase in intensity of the 532 nm

peak. What remains unexplained is the complete disappearance of this peak at very long synthesis run times. Several explanations are plausible. The ZnS core may be so reduced that the intensity of the 532 nm peak greatly diminishes. Because this peak is associated with defects in the crystal structure, it could be that the defects are too energetic to remain in the ZnS core as the annealing time (growth time) being long. This explanation, however, is not supported by other data. It is also possible that the SiO_2 shell is so large that it eclipses the effective luminescence of the much smaller ZnS core

Based on the trends revealed in the semi-quantitative XRD analysis, the nanowire growth process as it evolved in time can begin to be described. Most data suggests that as synthesis time increased, the silica shell thickness also increased. The shell thickness increase is easily explained as a function of increased number of available species in a very fast and efficient surface diffusion growth process. The size variation of the ZnS core is somewhat under debate; however, both the PL and XRD data support an initial increase and then decrease of the ZnS core size *relative* to the silica shell. Because we know the shell thickness increases as time evolves, the indication of a decrease in these analyses could be due simply to the role of a thicker SiO_2 layer, with the ZnS core size remaining the same. Whether the ZnS grew to a maximum size and then decreased, or whether the average core size remained mostly unchanged after this period, such a peak in core thickness suggests that at 60-75 minutes there existed a set of conditions producing ideal growth of these structures, i.e. high quality aligned nanowires of greatest length and density.

Interestingly, when experimental conditions were kept consistent for producing the ultralong core-shell nanowires, but the thickness of the gold catalyst layer was

reduced (below 20nm), the synthesized product changed dramatically, producing short, unaligned, low density structures. Therefore, the gold catalyst layer must be a key component in the formation of these ultralong nanowires. Several prior publications cite the critical influence of the Au-Si alloy in formation of Si nanowires, and the Au-Si phase diagram shows that such an alloy allows for a dramatically reduced temperature at which the material exhibits a liquid phase. If alloying occurred in the gold substrate particles, the presence of a thick gold layer coupled with the elevated chamber temperature could have facilitated a formation of a Au-Si eutectic alloy on the substrate surface which would have aided in a rich source of SiO vapor after oxidation. *In-situ* analyses have shown that in the case of Au on Si, an alloy layer is formed on the substrate surface which then quickly nucleates spherical Au particles. These would then have continued to agglomerate until large enough to sustain nanowire growth. In the absence of alloying, as we have determined through further examinations, the role of the thick gold layer could have been to prevent poisoning of the catalyst particle surface, or to provide so many nanowire nucleation sites that almost all arriving species were able to adsorb and contribute to growth in a synergistic fashion. Thinner gold layers do not appear to sustain high-density production of these small yet growth sustaining Au catalysts needed for the formation of such fine, dense, and ultralong nanowires.

Such a result explains the role of the thick gold layer, but not the observed maximum in ZnS core thickness occurring at intermediate synthesis times. SEM observation of a 20 nm gold-coated substrate imaged prior to and after exposure to the same experimental conditions, but without the presence of ZnS powder provides some clues. This sample indicates that while the surface initially appears like a rough film, after

just 15 minutes at elevated temperature before cooling, the gold on the surface migrated to form regions of large islands and small particles. Prior publications have established that similarly to very small gold particles, those above a certain size also do not promote as efficient nanowire growth as those with higher surface contact angles. It is likely that at short synthesis times, only the smaller more ideal catalyst sites initiated nanowire growth, while longer synthesis times allowed the larger less efficient sites to begin to nucleate ZnS nanowires. Therefore, we find that the growth of ultralong ZnS-SiO_2 core-shell nanowires depends upon the presence of gold catalyst particles of a size within an ideal range. Above or below a critical size, gold islands do not support nanowire growth, leading to a peak in ZnS core size at around 60-75 minutes growth time, and only with a sufficiently thick substrate surface gold layer. As discussed previously, the crystalline ZnS nanowire core formation is critically dependant on the size and condition of the catalyst particle. The Si species, however, most likely combines with residual oxygen in the chamber before diffusing around the catalyst particle (or adhering to the nanowire surface) to form an amorphous silica coating, and is much less critically dependent on Au particle size.

Finally, theoretical calculations were performed to determine the feasibility of the dual diffusion (both bulk and surface diffusion) growth model. The goal was to determine if the dual diffusion model could be reasonably predicted according to general diffusion relations. For this analysis it was decided to assume the case of bulk diffusion for ZnS, and then find the resulting diffusion constant for SiO_2. Absorption operations involve contact of a gas mixture with a liquid and preferential dissolution of a component in the contacting liquid. Depending on the chemical nature of the involved molecules, the

absorption may or may not involve chemical reaction. This calculation was based on the expression for adsorption of a gas in a liquid with a chemical reaction at the interface:

$$N_A\Big|_{Z=0} = \frac{D_{AB} C_{A0}}{\delta}\left[\frac{\sqrt{k/D_{AB}}\ \delta}{\tan h\left(\sqrt{k/D_{AB}}\ \delta\right)}\right] \qquad \textbf{(Eq. 4.2)}$$

where N_A is the flux of species A through the liquid, D_{AB} is the diffusivity of species A in B, C_{AO} is the maximum concentration of arriving species at the liquid surface, and δ is the distance that the diffusing species must travel, here taken to be the diameter of the catalyst particle. This equation assumes a constant diffusivity and a low concentration of A in the liquid such that the liquid interface contains plenty of adsorption sites. The constants of this equation can be evaluated from the boundary conditions:

$$\text{at} \quad Z = 0: \quad C_A = C_{A0}$$

$$\text{And} \quad \text{at} \quad Z = \delta: \quad C_A = 0. \qquad \textbf{(Eq. 4.3)}$$

With careful evaluation of equation (2) it is apparent that the term

$$\left[\sqrt{k/D_{AB}}\,\delta \Big/ \left(\tan h\left(\sqrt{k/D_{AB}}\,\delta\right)\right)\right] \qquad \textbf{(Eq. 4.4)}$$

describes the influence of the chemical reactions at the liquid interface. This term is a dimensionless quantity, often termed the Hatta Number. If the chemical reaction at the interface is neglected, (a reasonable assumption due to the unchanged state of the ZnS precursor in the final nanowire chemistry) the simplified expression correlating flux and diffusivity is,

$$N_A \approx (D_{AB})(C_{AO})/\delta \qquad \textbf{(Eq. 4.5)}$$

which is the equation used for final calculations. Here, the diameter of the catalyst particle, δ, was approximated at 40 nm. To find the concentration of each gaseous species an ideal-like behavior was assumed and it was noted that the evaporation temperature of Si (and SiO_2) is approximately twice that of ZnS. In this case, the total pressure is taken to be a simple sum of the partial pressure contributed by each species. Since the relative thicknesses of the core and shell did not fluctuate or taper, the flux of ZnS molecules was constrained to be equivalent to that of SiO_2 species at the nanowire-gold interface. The diffusivity of ZnS was found by observing the average experimental nanowire growth rate and applying this to the molecular system. For ZnS, the diffusivity, D_{AB}, was found to be ~8 x 10^{-6} cm^2/s. This value is well within the range of bulk diffusion through a liquid. Equation 4.5 was then used to find the flux for ZnS. This value was then fixed for the case of SiO_2, and the diffusivity was calculated. This value was found to be 0.16 cm^2/s, a much high diffusivity, best explained by a surface diffusion mechanism.

Therefore, the calculations seem to attest to the theoretical feasibility of the initially proposed growth model, in which the ZnS core was formed by volume diffusion across the catalyst particle, while the silica shell was formed by surface diffusion on the catalyst particle. Yet, as mentioned previously, further experimental evidence has shown that bulk diffusion of species into the gold particle did not occur. While the observations and calculations support a liquid gold VLS model, surface diffusion of both species is the most likely mechanism. The above calculations therefore while reasonable, must not accurately describe behavior in this system. Simple equations, while elegant, are sometimes not sufficient to correctly describe complex physical processes. In this case, the initial diffusion rate assumptions are most likely the cause of the error.

Core-shell ZnS-SiO_2 nanowires with widths on the order 30nm and up to 1cm in length were synthesized through a simple vapor deposition process. The nanowires were aligned as-synthesized along the direction of the gas flow in the system. All nanowires in grown samples were shown to contain a crystalline ZnS core surrounded by an amorphous SiO_2 shell. Their growth was analyzed experimentally, comparing varying synthesis time and subsequent product using SEM, TEM, XRD, and PL techniques. The growth mechanism of these core-shell nanowires was investigated utilizing literature, calculation, and detailed analysis.

CHAPTER 5

FUNDAMENTAL UNDERSTANDING OF NANOWIRE SYNTHESIS

To reliably integrate 1D nanomaterials into their many promising applications, their growth processes and growth-property relationships must be understood to a degree that synthesis can be performed reliably, and properties can be precisely engineered to create optimum performance. This chapter contains an examination of the vapor-liquid-solid (VLS) nanowire growth process (as it is generally understood), viewed through scientific literature, experimental observation, and computational modeling. Specifically, the systems examined in previous chapters, Fe_3O_4, ZnS, and SiO_2 nanowires catalyzed by gold, are the focus of the succeeding discussion. Each component of the VLS processes briefly mentioned in previous chapters is considered in detail; observations and simulation results are explored in parallel with relevant information found in peer-reviewed publications.

Vapor deposition processes are commonly employed in the synthesis of semiconductor nanostructures. These methods frequently involve sublimation of a powder precursor in a horizontal tube furnace, with subsequent deposition of these species onto metal catalyst particles in cooler regions, precipitating continuous growth of semiconductor nanowires. Since the discovery of 1D nanostructures grown via catalyst-assisted vapor deposition processes, researchers have been troubled to identify precise formation mechanisms, especially regarding the role of the metal catalyst particle. The VLS method was first described in the 1960s, but the growth of nanowires via vapor deposition has renewed interest in this still not fully understood phenomenon. Almost a decade ago, Dr. Charles Lieber outlined for the Au-Si system what is generally regarded

today as the classic VLS nanowire growth mechanism [29], in which a diffusing species is transmitted through the bulk of a metal catalyst in liquid phase before incorporating into the growing nanowire. The Au-Si phase diagram, seen in Figure 5.1, is regularly used to explain how such a VLS process could occur for this system, especially in light of the deep eutectic point, which allows for the alloy to reach a liquid phase at temperatures well below the normal melting point of gold (1337K).

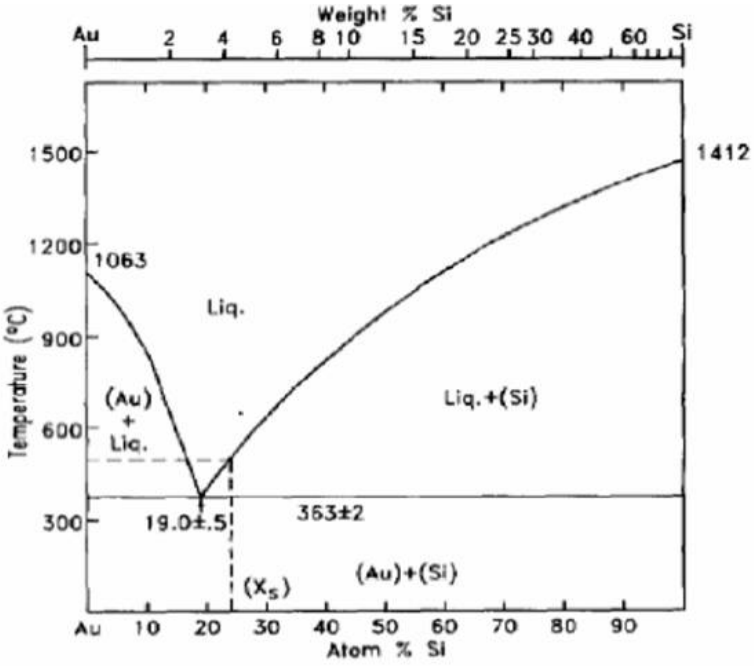

Figure 5.1: Au-Si Phase Diagram

Such a process is frequently applied to other dual component systems, which often (but not always) appear to mimic Lieber's Au-Si model. Growth mechanisms in other chemistries, or multiple component systems, however, have proved much more difficult to conclusively identify, as in many cases the final product is not well-explained by the traditional VLS process. In addition, these complex systems often lack

experimental phase diagrams necessary to determine solubilities of diffusing species in the catalyst material, preventing easy identification of the conditions necessary for true VLS growth. In particular, researchers continue to debate the role of the metal particle, i.e. if species arrive as ions or small molecules, and if these are transported through the bulk of the "catalyst", or on the surface. Many researchers even question the necessity of the metal particle in the liquid phase, and have provided evidence to show that nanowire growth can occur even with the particle remains in the solid state.[188]

Several alternative mechanisms have been proposed for catalyst assisted nanowire growth, often varying according to experimental parameters and growth species. Those investigated for this model, ZnS or SiO_2 (here, SiO is substituted) nanostructures grown via Au catalysis, vary across the literature, and include several atomic transport schemes. [3-8] Such variance reveals a lack of consensus regarding the phase condition of the metal catalyst particle at elevated temperature, the diffusion mechanism in the metal catalyst, the role of transverse growth, and the state of the arriving gas species, among other issues. One source of discrepancy may be that growth mechanisms may vary according to the growth chemistry and parameters, and may utilize not just one, but a combination of processes.

Ideally, synthesized nanostructures are pure single crystals of correct stoichiometry in nanowire or nanobelt morphologies. The purpose of detailed synthesis studies is not only to obtain sufficient quantities of sample material. This research should also provide valuable information regarding thermodynamic and kinetic formation processes of these structures and 1D nanomaterials in general. Vapor deposition processes are promising candidates for scalable industrial production in the future, due to

their simplicity and low cost.[189] While VLS growth of simple systems such as Ge or Si nanowires with Au catalyst have been reported many times in the literature[168, 190, 191] and even in some cases observed *in-situ*, [190] recent evidence suggests alloying in multi-component eutectics is far from clear, and there are many inconsistencies and unexplained phenomena in current theory. Three recent papers cite failure of the VLS mechanism in catalyst-assisted GaAs, InAs, and ZnSe nanowires, with growth occurring only when the Au catalyst is in the solid phase, well below the eutectic point.[170, 177] An earlier paper describes similar phenomena in Ti catalyzed silicon nanowires.[170] XRD analysis has shown that for Au catalyzed ZnO nanowires, alloying of the gold particle could not have occurred, as the lattice parameters of the gold that precipitated the nanowires matched those of similar gold particles never exposed to ZnO vapor. Findings also suggest that the gold particle is not in the liquid phase during growth of the ZnO nanowires.[188]

This chapter revisits each component of the VLS growth mechanism described below, and examines it in reference to current literature and synthesis of the nanowire systems of interest here in particular.

1. In the first step, metal catalyst is deposited onto a substrate where it forms nano-sized liquid droplets.
2. Vapor of the desired nanowire species is then introduced into the atmosphere.
3. The liquid droplets act as preferential sites for the deposition of the vapor species due to the greater sticking coefficient of liquid relative to solid surfaces.

4. It is believed that as the vapor saturates the area around the catalyst, some is dissolved into the metal forming an alloy solution

5. If the properties of the catalyst and substrate are such that the metal catalyst is not strongly held to the surface, a precipitate of reactant material is rejected out of the metal droplet onto the substrate. The nanowire diameter is dictated by the circumference at the interface of the metal droplet on the substrate. In the case of strong adhesion of catalyst to substrate, the nanowire may grow such that the catalyst remains on the substrate surface, and the wire grows out from the top of the metal droplet.

6. As more reactant is added, more is rejected from the catalyst, causing vertical growth of a column or wire. It is believed that the nanostructure grows vertically due to the kinetic effect of preferred growth of some crystallographic planes relative to others, dictating fast growth in one direction with other planes growing more slowly.

7. Conditions allowing some transverse growth may occur, increasing the wire diameter beyond that of the catalyst droplet.[27, 192]

1)Metal catalyst is deposited onto a substrate where it forms nano-sized liquid droplets.

To grow the iron oxide nanowires presented previously in this work, the gold metal catalyst was deposited onto the substrate via thermal evaporation of a very thin layer, approximately 2nm. (It should be noted that the term “catalyst” does not necessarily indicate a chemical reaction with surrounding molecular species, but instead indicates that the metal particle facilitates and often speeds nanowire growth.) The layer

is often kept thin to ensure dispersion of the metal as discrete islands rather than a continuous film. VLS theory states that these islands of metal form the small droplets at elevated temperature essential to nanowire growth. Other means of catalyst deposition are possible, such as dusting the substrate with a fine powder of metal; however it may be more difficult to achieve very small droplet sizes utilizing this method. For a 2nm gold layer deposited via thermal evaporation, these islands appear in the SEM at room temperature as spheres with a diameter of approximately 10-50 nm.

According to VLS theory [27, 159, 168], the catalyst must be selected to ensure it will exist in the liquid phase above the vapor/metal eutectic point at the experimental temperature and pressure parameters. This ideal catalyst, then, should not chemically react with the vapor species, yet should allow diffusion into the droplet and physical alloying of source vapors with the metal liquid. Au is a commonly chosen catalyst in semiconductor and oxide nanowire synthesis due to its low melting point, tendency to form spherical droplets on common substrates, and noble chemical nature in bulk.[193] (Although gold may be noble in bulk form, molecules and even nanoparticles of gold are actually far from noble as will be discussed later.) Other low melting point metals such as gallium and tin have also been successfully utilized for similar nanowire growth processes. In the case of magnetite nanowire synthesis, Au was the chosen catalyst due to its relatively high solubility with Fe, [193] (the common occurrence of magnetite and gold found in geological rock formations testifying to solubility of these species in absence of a representative phase diagram[194]), and the reported successful growth of other nanowire species such as GaAs, InAs, Ge, ZnS (sublimation point before melting at around 1800^{o}C), SiO_2, Si, CdSe, ZnO and others using Au.[170, 171, 195, 196] Gold's

relatively low melting point of 1064^{o}C at 1atm (magnetite's melting temperature – 1591-1650^{o}C in air, 1583^{o}C in O_2 at 1atm)[193] makes it a common candidate for use as a catalyst in synthesis like that conducted, and for testing for possible differences when maintained in the solid phase. Though as mentioned previously, evidence is mounting that gold alloying is not necessary to nanowire growth in many chemistries, low melting point metals continue to be successfully utilized as a nucleation hosts for a variety of nanostructure chemistries and morphologies.

Vapor evaporation growth without the aid of a catalyst is another common 1D nanostructure growth process. Similar to VLS, this process is often termed VS, for vapor-solid growth. VS growth will frequently occur in systems where metal catalysts have been employed successfully, however nanowire synthesis often takes longer time or higher temperatures, and may produce nanowires of lower aspect ratio, and of lesser crystallographic purity. It is believed that a "seed" of the original material coalesces to begin growth in this case, the accumulation and location of which is somewhat haphazard.

In previous experiments in which ZnS 1D nanostructures were grown on catalyst coated and uncoated areas of the same substrate, distinct differences in sample characteristics were noted. Nanowires grown on the Au deposited area were observed to grow with higher densities. It was also noted that while the catalyst coated side consistently produced nanobelts, each ending with a single catalyst particle, the uncoated side produce many geometries, with several structures originating from a single ZnS "seed." Clearly, the catalyst plays an important role in regulating the growth of these

nanostructures. It is this higher degree of control granted by the catalyst assisted process that has contributed to its popularity.

Substrates are often chosen to minimize lattice strain between the substrate and growing nanomaterial. Experiments conducted with iron oxide nanowire growth demonstrated that while alumina and sapphire substrates yielded high density nanowire growth, little to no iron oxide nanowires could be grown on silicon substrates. Listed below are lattice parameters (a_0) for relevant bulk materials, reported in angstroms.

Si = 5.43

Au = 4.08

Fe_3O_4 = 8.39

α-Fe_2O_3 = 5.04

ZnS = 5.41

Al_2O_3 (alumina or sapphire) = 4.75

While lattice parameters do vary somewhat from bulk values for nanomaterials, studies have shown that gold nanoparticles demonstrate reduction in lattice constant as size decreases, most likely due to increasing surface and internal bond strain, providing potentially even greater lattice mismatch while in solid form. This analysis predicts that at least for the ZnS nanowires examined in our system, the gold particle most likely promotes growth in a semi-liquid phase or a mostly solid phase with high surface atom mobility. In the iron oxide system, the solid gold lattice parameter is roughly half that of magnetite, while the hematite parameter is similar to the alumina structure. Such an

analysis therefore cannot provide as much information regarding VLS growth in this system.

The state of the catalyst particle during this growth process remains a debated question. While many scientists believe that the classical VLS process is still valid, others doubt the necessity of the metal particle's liquid state. In some systems, the ability of the particle to grow aligned nanowires in an apparently solid or semi-solid state has been demonstrated through *in-situ* TEM study. If alloying in the gold particle is not a necessary requirement for vapor evaporation nanowire growth, the liquid phase of the gold particle is likewise non-critical. Conversely, if the metal particle never achieves a liquid state, then the VLS process can not occur, and researchers must look to another mechanism to describe nanostructure growth. Buffat and Borel demonstrated in 1976 through careful experimentation that melting point depression in pure gold nanoparticles is not significant above 7nm in atmosphere. [197] A graph demonstrating the effect of size on gold particle melting point can be see in Figure 5.2.

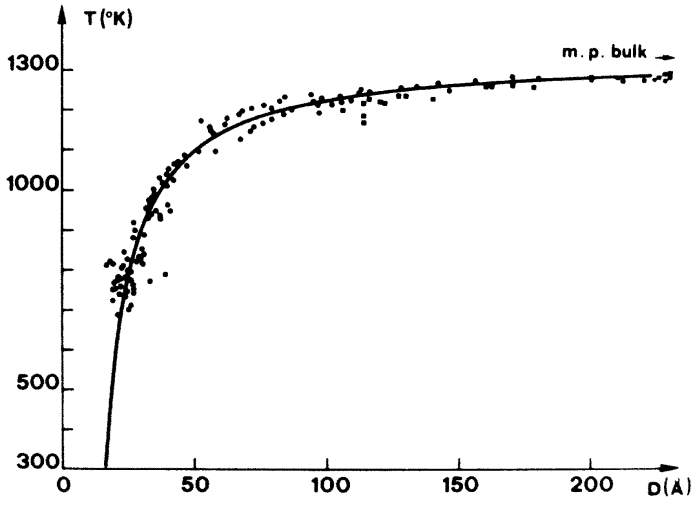

Figure 5.2: Graph taken from Buffat and Borel demonstrating influence of particle size on the melting point of gold nanoparticles.

Unfortunately, there is little published data of these trends at lower pressures near 0.01 standard atmospheres, similar to the conditions used for the experiments described in this work. Lower system pressures could increase the equilibrium vapor pressure of the metal particle and depress the melting point beyond that measured at atmosphere; however, we have no evidence to demonstrate the influence of decreased pressure on the state of our gold particles. The catalyst particles assisting growth of the iron oxide and ZnS-SiO_2 nanowires varied greatly in size, but averaged between 10-50 nm, indicating that they did not melt at synthesis temperatures (750-1000^{o}C). Most likely the gold particles maintained a high surface mobility allowing transport of arriving species around the outside to a low energy site at the growing nanowire interface.

2)Vapor of the desired nanowire species is then introduced to the atmosphere.

Here we must consider the nature of our vapor species. For synthesis of magnetite nanostructures, a pressed disk of 98% Fe_3O_4 powder purchased from Alfa Aesar was used as source. A PLD device was chosen for its ability to ablate the material according to correct stoichiometry creating a dense vapor plume. The two graphs in Figure 5.3 below shows Gibbs Free Energy value changes in relation to reaction temperature for four Fe_3O_4 decomposition reactions:

$2Fe_3O_4 = 6FeO(g) + O_2(g)$ (dark blue)

$Fe_3O_4 = 3Fe(g) + 2O_2(g)$ (pink)

$Fe_3O_4 = 4O^{2-}(g) + 3Fe^{+3}(g) + e^{-}$ (yellow)

$Fe_3O_4 = 4O^-(g) + 3Fe^{+2}(g) + 2e^-$ (light blue)

It is unlikely that the vapor contained large Fe_3O_4 molecules, due to the large driving force for decomposition into the more stable FeO vapor species at higher temperatures as shown in the graphs below. Since the temperature created by the laser beam incident on the source has been roughly calculated as ~68,000^{o}C under adiabatic conditions, the vapor is likely to decompose further into charged ions as shown in the graph. Of course, following the laser pulse, the vapor should experience rapid cooling as it expands outward and may re-condense into larger and more stable species. As FeO is the primary stable vapor species in this reaction at lower temperatures, one may reasonably assume that the majority of vapor species arriving at the substrate particle are FeO gas. However as these graphs show, ionic species are also thermodynamically stable over a range of temperatures, so depending on the degree of cooling, impinging molecular species may also be significant in nanowire growth. It should also be noted that the reported melting temperatures for these materials are based on bulk values under atmospheric pressure. Magnetite (Fe_3O_4) in powdered form has been found to sublimate at much lower temperatures (~700^{o}C) at 1 atmosphere and most certainly dissociates even earlier at lower pressures. This result is corroborated by the experiments described in earlier chapters. Unfortunately, a similar graphical examination for the ZnS material system has not been conducted, but it can be reasonably assumed that results should be similar, based on similar ZnS nanowire synthesis parameters and the similar sublimation temperatures of these materials. Let us now examine the theoretical basis of the vapor species as it

relates to our system. System parameters and details of experimental setup can be found elsewhere.

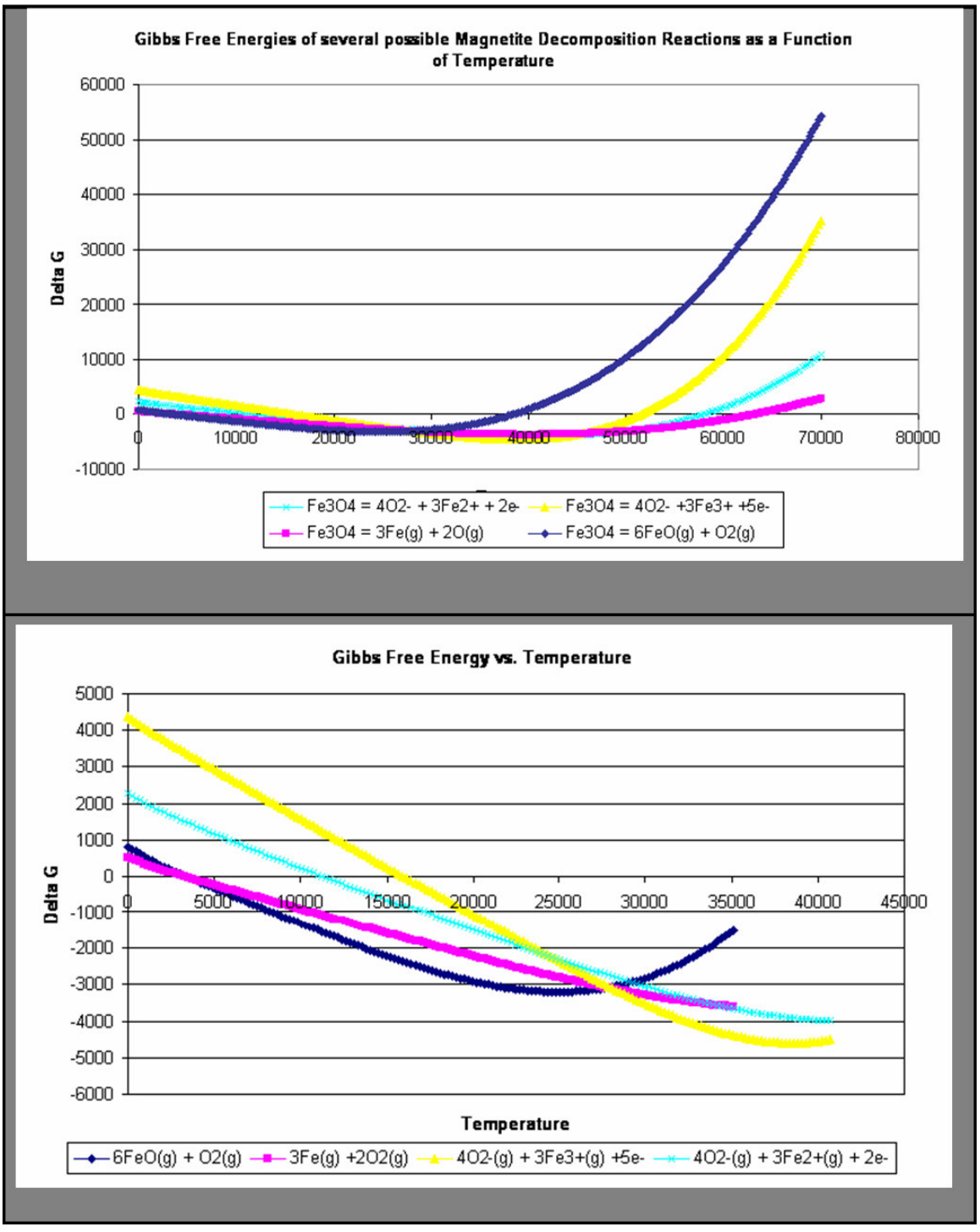

Figure 5.3: Graphs illustrating influence of temperature on Gibbs Free Energies of four magnetite decomposition reactions (a) demonstrates fluctuations from 0 to 80,000 degrees C (b) shows the area where delta G becomes negative in greater detail.

Most physical vapor deposition (PVD) theory is based on a system with a pressure on the order of 1 or less Pascal. The system used for this research is on the order of 10,000 to 50,000 Pascal. For a typical high vacuum pressure of 10^{-4} Pa, we can calculate the mean free path of the vapor atoms using the equation

$$\lambda = kT / (\sqrt{2} * \pi * P * d^2) \qquad \textbf{(Eq. 5.1)}$$

where d is the diameter of the gas molecule and is in the range of 2 to 5 angstroms. This gives a mean free path of approximately 60 m for a 4 angstrom atom. Since the distance between the source and the deposition substrate is significantly less than this, PVD is usually treated as a line-of-sight process with little scattering of the evaporated atoms and with little loss of energy. [198]

A similar calculation with a pressure of 30,000 Pa and a temperature of 1323 K gives a mean free path of about 3.5 µm. Because the travel distance of the species in this system is much greater than 3.5 µm, this has a large impact on the deposition. A material being deposited in the system tends to scatter often with the flowing argon atoms and arrives at the deposition substrate from a somewhat random direction. We say only "somewhat random" because the carrier gas has a flow direction to it (i.e. it is not ambient) and the material deposits, generally, in the “downstream” direction. However for PLD growth, the greatest deposit of material was found slightly upstream and in front

of the target, due most likely to scatter backward from the source.

Currently, we have no equipment to identify or characterize vapor species downstream of the reaction. Mass spectroscopy would be very helpful in providing more information as to the nature of the reactions occurring within the tube chamber, however low pressures required by these devices necessitate gas sampling in these experiments. Gases physically removed from the furnace are likely to condense into forms uncharacteristic of the actual reaction species unless the temperature can be maintained. Also, because of imperfect vacuum levels, one cannot ignore the potential of chamber contamination from air leaks, as well as the presence of adsorbed species lingering on the tube's surface. In any case, vapor species are likely to be ionic or small gas molecules. In the case of our SiO_2 shell synthesis, Si originates from the substrate.

3) The liquid droplets act as preferential sites for the deposition of the vapor species due to the greater sticking coefficient of liquid relative to solid surfaces.

The earliest model of gas adsorption was suggested by Langmuir in 1916. The classical Langmuir model is limited to monolayer adsorption. It is assumed that gas molecules striking the surface have a given probability of adsorbing. Molecules already adsorbed similarly have a given probability of desorbing. According to the IUPAC (International Union of Pure and Applied Chemistry) Compendium of Chemical Terminology, the "sticking coefficient" is the ratio of the rate of adsorption to the rate at which the adsorptive strikes. Thermodynamically speaking, this value is a measure of the efficiency of energy transfer each time a gas molecule encounters a surface. At equilibrium, equal numbers of molecules desorb and adsorb at any time. The probabilities

are related to the strength of the interaction between the adsorbent surface and the adsorbate gas. It is usually a function of surface coverage, temperature, and the details of the surface structure, with loosely bound atoms in liquids or semi-liquids having much greater values. Nanoparticle surfaces can be likened to semi-liquids, as the high surface energy, especially at elevated temperatures, make surface atoms highly mobile as compared to bulk solids. The Langmuir model is applicable at isothermal conditions when there is a strong specific interaction between the surface and the adsorbate so that a single adsorbed layer forms and no multi-layer adsorption occurs. [199] This model can be considered a good first approximation for a nanowire growth system. The Langmuir model is usually expressed as:

$$\frac{V}{V_m} = \frac{Cx}{1+Cx} \qquad \textbf{(Eq. 5.2)}$$

where:

V= volume of gas adsorbed at pressure P; V_m = volume of gas which could cover the entire adsorbing surface with a monomolecular layer; P_0 = saturation pressure of the gas, *i.e.,* the pressure of the gas in an equilibrium with bulk liquid at the temperature of the measurement; $x = P/P_0$ = relative pressure; and C = a constant for the gas/solid combination.

The sticking coefficient, also known as the accommodation coefficient, can then also be defined as the fraction of the impinging growth species that is accommodated on the growing surface. It is a *surface* specific (not a *material* specific) property. Because it is surface specific, it is likely that it has a significant impact on faceted growth and on preferred growth directions of nanostructures. Ideally, the growth of a crystallographic

face is linearly dependent on the accommodation coefficient, which being surface specific, is anisotropic. A surface with a higher accommodation coefficient will have a higher growth rate than other surfaces, and significant difference in the coefficients between different facets would result in the anisotropic growth seen in nanowires and nanobelts. The sticking coefficient of the nanowire growth site is especially important in systems where the source concentration is low and vapor species are limited.

The mean diffusion distance of an impinging gas molecule ($\lambda \approx \sqrt{\ } Dt$) is interesting to note because if it is far longer than the distance between two growth sites on the nanostructure such as a defect or a ledge, then the adsorbed growth species will be incorporated into the nanostructure and the accommodation coefficient discussed above approaches 1. However, if lambda is much smaller than the distance between two growth sites, then the adsorbed species escapes back to the vapor and the accommodation coefficient approaches zero. The accommodation coefficient therefore is dependent on the desorption energy, the activation energy of surface diffusion, and the density of the growth sites.[199]

The average sticking or accommodation coefficient of a liquid relative to purely crystalline solid surfaces is on the order of 50 times greater when comparing pure substances just above and below the melting point. It is commonly accepted that because the catalyst particles act as preferential deposition sites for source vapor, the catalyst assisted vapor growth processes allow control over nanowire location on the substrate limited only to the ability to position catalyst material prior to the synthesis process. It is interesting to note therefore, that even in reported instances where Au catalysts remained in the solid state, highly preferential growth along the catalyst was observed, as seen in

the image below (Figure 5.4) showing ZnSe nanowires.[200] The gold surface must present a low-energy interface to vapor species even in solid form, providing a suitably rough surface with many more defects and attachment sites than substrate material, often single-crystalline. Wagner and Ellis, the first VLS pioneers found through careful experimentation that the "condensation coefficient" is about 10^{-3} for the VLS process and 10^{-5} for the VS (vapor-solid) process, and that the liquid phase as such rather than the chemical nature of the catalyst particle was responsible for accelerated axial growth in nanowires. [168] It is possible that in cases where the catalyst is believed to be solid, the surface atoms are still in a disordered state whether through partial melting common in small particles or other surface effects, allowing greater accommodation. The role of lattice mismatch between the arriving materials and alternate deposition locations may also be significant.

Figure 5.4: SEM image showing ZnSe nanowires grown preferentially on solid Au catalysts

In the systems examined for this research, it was noted that growth only occurred on substrates containing metal catalyst particles. Even within a single substrate, areas devoid of metal catalyst islands, sometimes occurring in the middle of a high growth area, demonstrated little or no nanowire growth. These results indicate the critical importance of the metal catalyst particle to vapor deposition nanowire growth.

4) It is believed that as the vapor saturates the area around the catalyst, some is dissolved into the metal forming an alloy solution.

The location and movement of arriving gas species in or around the catalyst particle is a much debated issue. These alloying and saturation processes depend on the mutual solubilities of vapor species and catalyst, traditionally found according to equilibrium phase diagrams. Classical VLS theory states the optimum temperature and pressure combination for VLS nanowire growth occurs in a region just above the eutectic, where the liquid phase of the catalyst and the solid phase of the desired nanowire material exist in equilibrium. The ideal relationship would include a wide range of parameters where this equilibrium state could be maintained. According to this model, the metal particle should have a low melting point, and solve the diffusing species at a wide range of temperatures. If the liquid phase of the catalyst is not required, then this criterion is no longer valid, and the experimentalist is instead free to choose catalyst based on other contributing properties such as adhesion coefficient, reactivity with adsorbing species, lattice match with substrate, etc.

For several years, researchers have been gathering information about the VLS process through careful variation of experimental parameters, and later, *in-situ* TEM studies. Most of this early work focused on nanowire growth as a function of the system temperature. The first real-time observation of catalyst assisted vapor deposition semiconductor nanowire growth was demonstrated and recorded in an *in-situ* high temperature TEM for a germanium (Ge) nanowire catalyzed with Au. The classical VLS growth mechanism was observed and confirmed in this work, and selective growth of Si

nanowires of varying diameter were synthesized based on the information gleaned from this mechanistic study. In addition to meticulous TEM observations and calculations confirming the supersaturated state of the alloy liquid, analysis of the droplet post cooling found that the weight percentage of Ge matched qualitatively with the estimated alloy composition at which the first Ge nanocrystal nucleates. [190] Several later works have utilized *in-situ* TEM videos to prove the liquid state of the metal catalyst during nanowire growth in other systems at temperatures similar to those used for nanowire synthesis. Ga, Au, Sn, and other catalysts have been demonstrated to form liquid alloys in the growth of other nanowire chemistries. Growth rate measurements in varying conditions to determining rate-limiting reactions further confirm the VLS model of nanowire growth in many systems. [201]

Variables besides temperature must also be considered when examining the transport of the arriving species into the growing nanowire. The catalyst droplet size is an important aspect, as it has been shown in several systems that catalyst size reduction can depress the melting temperature relative to bulk. Further complicating the issue, alloying and supersaturation in the liquid can also affect the behavior of the system. An *in-situ* TEM study published in 2005 demonstrated that for growth of In nanowires with Sn catalyst, a reduction of the catalyst diameter to 7nm decreased the eutectic temperature of the alloy by more than 100K, a value greater than that expected due merely to particle size reduction. It is believed that this effect is due to the increased contribution of interfacial energy between the two phases to the total free energy of the particle. The interfacial energy is changed to such a degree that the eutectic temperature

of the alloy is depressed even faster than the increased surface area of a similarly sized particle of either pure phase reduces the melting temperature. [202]

System pressure also plays an important role in nanowire growth dynamics. Therefore, an immediate concern regarding *in-situ* TEM analysis is the ultra high vacuum necessary for such work, which may skew results toward growth at temperatures lower than those necessary at pressures closer to atmosphere. To address this issue, some researchers have begun working with environmental scanning transmission electron microscopy, or E-STEM, which allows scientists to use gas pressures up to 40 mbar in the sample region. *In-situ* E-STEM studies have demonstrated a linear relationship between the depressed melting temperature $(T_0\text{-}T)/T_0$ and the inverse local diameter of many metal particles even at such higher pressures. [203] These results have been used to help explain formation of nanowires via the VLS process at temperatures well below the bulk melting temperature of the catalyst metal, at pressures more similar to those commonly used in actual synthesis.

Several recent E-STEM papers have found nanowire growth to occur at temperatures both well below the eutectic points of the considered reactions, as well as at temperatures below the melting point of the catalyst particle. A recent paper in *Science*, reported that, "for the classic Ge/Au system, nanowire growth can occur below the eutectic temperature with either liquid or solid catalysts at the same temperature." Rather than merely a function of temperature and size, the catalyst state depended as well on growth pressure and thermal history. Below the eutectic temperature, the liquid Au is stabilized by the supersaturation of Ge in the droplet. [204] It appears that at least for the Ge/Au system, both VLS and growth without the catalyst achieving a liquid state, or VSS

(vapor-solid-solid) growth modes are possible at identical temperatures. [201]Other works have noted that local pressures and concentrations of the arriving vapor species independent of total local pressure can also influence the reaction dynamics. These observations likewise indicate that transport of the vapor species to the growing nanowire may vary based on local availability, and that transport dynamics may change in response to history or variations in local environment. [205] Notably, each of these are simple systems in which a single element is transported through the catalyst. Similar studies with identical results have yet to be published for more complex systems.

For other systems, evidence shows that the alloying step of the VLS process is not necessary. Numerous publications report growth of ZnO nanowires, SnO_2 nanowires, and those of other chemistries without the presence of metal catalyst particles. [192, 206, 207]Other recent work utilizes careful XRD analysis to determine that even when Au particles are present, ZnO nanowire growth appears to occur before the Au particle reaches the liquid state and lattice parameter measurements confirm that the lattice of the gold is not changed post growth. These results indicate that alloying did not occur in this system. [188] In the case of Sn catalyzed ZnO nanobelts, researchers found that contrary to traditional VLS theory, the interface between the ZnO nanostructure and the catalyst particle influenced the growing nanowire's crystal structure. [208] Such nanowires are illustrated in the figure below.

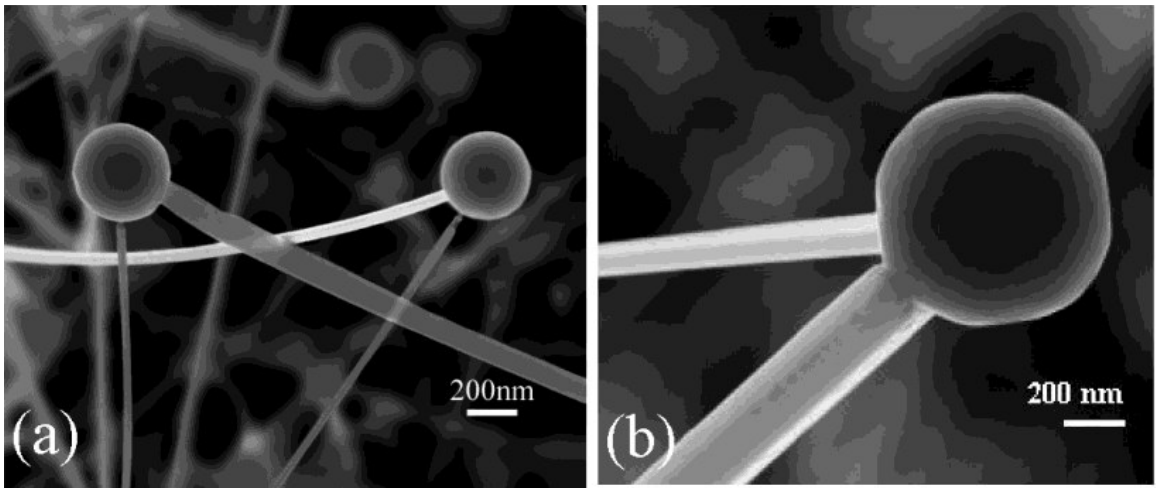

Figure 5.4: SEM images demonstrating ZnO nanowires with different growth fronts emanating from the same Sn catalyst particle.

One journal article maintains that growth of nanowires occurred for the authors *only* under conditions where the gold particle remained in the solid state and that growth terminated once the catalyst particles melted. In fact, for these cases the entire mechanism must be re-considered as a VSS process, involving either surface or bulk solid state diffusion of the adsorbing species. [170, 177, 200] Similar results have been found for other Au catalyzed GaAs and InAs nanowire systems as observed through *in-situ* TEM analysis and careful synthesis evaluation. [177] In these examples, liquid alloying can no longer be considered a viable mechanism, and instead solid or surface diffusion of species must be the primary means of transport to the catalyst/nanowire interface. In such instances, the Au particle appears to provide a low energy interface at which the precursor materials are accumulated such that epitaxial growth occurs at a rate higher than elsewhere in the region.

Due to the ambiguous and apparently system-dependent nature of the metal particle's role in nanowire formation, it was determined that a molecular simulation

would be helpful as a complement to experiment and literature for the Au catalyzed nanowires of interest here. One important issue is the ability of the gold particle in the liquid state to accommodate precursor ions and small molecular species into its bulk. If the increase in system energy is too high, the gold particle is unlikely to incorporate arriving species, and would likely instead serve as a vehicle for surface diffusion to the nanowire interface. While the model here is somewhat primitive and specific free energy decreases due to complex alloying phenomena are not considered, this study serves well as a first approximation to describe both the most likely diffusing species, and the ability of gold to accommodate nanowire vapors within the metal particle. The simulation described in the next section focuses on ZnS and SiO_2 dispersion in gold in order to better understand the growth process of the core-shell nanowires synthesized in this work. This system was chosen based on the wealth of experimentally gleaned information regarding the growth dynamics of these nanowires.

The work described below aims to investigate the nature and behavior of small inorganic molecules and ions surrounded by gold atoms to provide insight into a common semiconductor nanowire synthesis process. This simulation attempts to provide some insight into these questions by investigating the relative energies of ZnS, SiO and their ions surrounded by gold, a common catalyst material in VLS nanowire growth. A periodic box of 50-100 gold atoms is used to approximate local conditions within a gold droplet. The density of atoms in the box is varied to reflect common bulk gold densities in the solid and liquid state, though true droplets of only a few nanometers may demonstrate reduced density due to relaxation effects. Molecular dynamics (MD) simulations are run on several inorganic species to determine relative energies for each

system and parameters. Much time is also spent identifying a reasonable force field for the gold solvent and collecting baseline information with which to compare the behavior of solute species dispersed in the gold medium. SiO is tested, rather than SiO_2, as larger molecules are less likely to dissolve into the gold intact, and even the SiO system frequently produced enough strain energy as to overload the simulation. This model aims to answer the following questions:

1. Can gold systems be reasonably modeled through simple Leonard-Jones interaction potentials?
2. How do the force fields differ for this system?
3. Are ZnS and SiO more likely to diffuse into gold as ions or as small molecules?
4. Are ZnS and its ions (together and separately) more likely to diffuse into gold than silica and related species?
5. How does temperature affect these results?
6. How does concentration affect these results?
7. Does the simulation predict precipitation?

The Molecular Operating Environment (MOE) software from the Chemical Computing Group was used to carry out all simulations. The gold system was tested with both the MMFF94 force field (MMFF94.ff) and the empirical default force field provided by MOE (empirical.ff), modified to better represent gold-specific properties. Although MMFF94 was called to run energy minimizations, examination of the code text indicated that gold was not parameterized for this force field. Therefore, the minimizations listed

as MMFF94 were most likely parameterized according to MOE's Leonard-Jones default force field. Molecular dynamics simulations were first run according to MOE's own MD simulation algorithm, and later using a program written by Dr. Pete Ludovice, and Andrew Swann (md2006-NOLRC.svl). (In the tables below, this program is recorded as "SwannMD.") This program uses a modified Nose-Hoover (integral controller) algorithm for parameter control and dynamic iteration. Unless otherwise stated, simulations were run for 500 picoseconds with a time step of .002 picoseconds. Periodic conditions were enabled, and a spline of 2 angstroms was used for the cutoff. For NVT (constant number, volume, and temperature) simulations, Q values (false discovery rate) were maintained at a value of 1. All systems were minimized prior to running MD simulations, and were done so again after the simulation, with energies recorded at each point.

The periodic box of gold solvent was created via the "Soak" program (soak2007.svl), which incorporates a Monte-Carlo like algorithm to define a periodic box and solvate an existing solute. Initially, the Soak program had difficulty filling the periodic box to the required density (19.3 g/ccm for solid and 17.31 g/ccm for liquid) so the maximum energy to fill was increased from 10 to 1000 kcal. This change allowed almost any attempt to place a gold molecule to be successful. However, most gold atoms were found outside the box at the completion of the program. To pack all the gold atoms in the box, the crystal parameters were changed such that the box was packed according to the space group for FCC solid gold, Fm-3m. Figures 5.5 and 5.6 below illustrate how these gold-only systems appear prior to simulation. Figure 5.5 was created to contain 100 gold atoms, while Figure 5.6 was created to contain 50. There are obviously more gold

atoms in each box than 100 and 50, respectively. From the simulation results it appears that the program created the box such that it contains not one unit cell of 50 (or 100) atoms, but a large super cell containing 8 such primary unit cells.

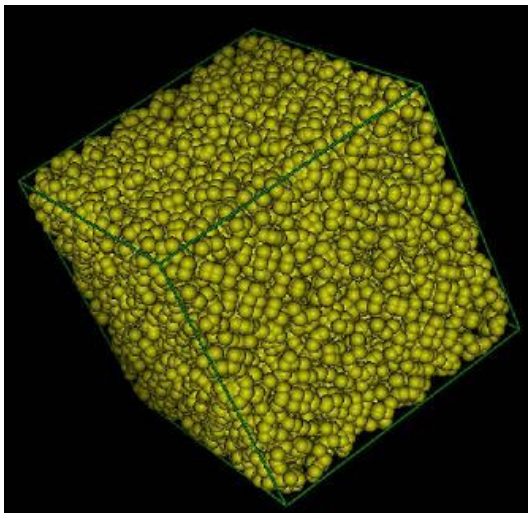

Figure 5.5: Periodic box of gold atoms (100) packed into Fm-3m space group

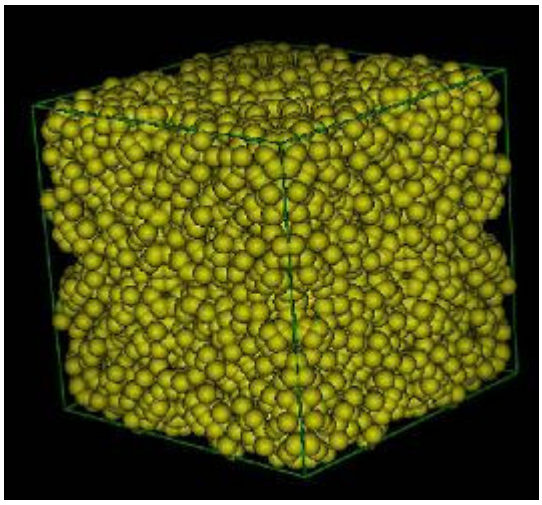

Figure 5.6: Periodic box of gold atoms (50) packed into Fm-3m space group

Several simulations were run on the pure gold system, eleven of which are recorded in the tables below. Information colored in pink indicates conditions that were

intentionally changed from the previous simulation. Series of boxes filled only with “x” indicates either that the simulation was manually stopped, or could not be run with the designated set of parameters due to very high internal strain in the system. In many such cases, some parameters were tweaked to allow the system to run so that a maximum number of simulations could be reported. Those systems demonstrating “x” were not able to be run with only small parameter adjustments. Unless otherwise stated, all length measurements are in angstroms, pressures are in kPa, energies are in kcals (or kcal/mol), and time is in picoseconds. Entries in red are highlighted as being unexpected or anomalous. Note for these simulations, the mean energy values (mean U), and potential energy after minimization (under MD parameters) provided in the tables, indicating the resulting energies under the prescribed conditions.

Table 5.1: Tests on gold-only systems using MMFF94 and MOE's MD software. The first column contains information on the system illustrated in Figure 5.4, while the second column contains information based on the gold box illustrated in Figure 5.5.

Basic parameters		
density (g/cm3)	19.3	19.3
box size (ang)	11.9224	9.46285
Force field	MMFF94	MMFF94
PE before min	-12.499	-3.709
PE after min	-12.499	-3.709
atom number	100	50
MD parameters		
program used	MOE MD	MOE MD
MD alorithm		
ensemble	NPT	NVT
cutoff	6	4.73
Temp (K)	300	300
Pressure (kPa)	101	101
constraints	none	none
time (ps)	100	500
time step	NA	NA
Q	NA	NA
PE after MD	0.739	32.303
new cell size (ang)	101.8	NA
new density		NA
mean sq K fluc	2528.66	25.6437
mean sq U fluc	1.11104	16.6166
Mean U (kcal)	-0.187	32.4091
Mean K (kcal)	88.173	43.7899
Mean P (Kpa)	5460	1.72E+06
Mean V (ang3)	573938	847.356
mean T (K)		299.8
new E min (kcal)	-0.065	-2.55

Table 5.2: Tests on gold-only systems using MMFF94 for minimization and provided software for MD simulations. These tests were all run on the "50 atom" gold box illustrated in Figure 5.5.

Basic parameters					
density (g/cm3)	19.3	19.3	19.3	19.3	19.3
box size (ang)	9.46285	9.46285	9.46285	9.46285	9.46285
Force field	MMFF94	MMFF94	MMFF94	MMFF94	MMFF94
PE before min	3.204	3.204	3.204	3.204	3.204
PE after min	3.204	3.204	3.204	3.204	3.204
atom number	50	50	50	50	50
MD parameters					
program used	Swann MD	Swann MD	Swann MD	Swann MD	Swann MD
MD alorithm	Nose -Hoover	Nose -Hoover	Nose -Hoover	Nose -Hoover	Nose -Hoover
ensemble	NVT	NVT	NVT	NPT	NVT
cutoff	4.73	4.73	4.73	4.73	4.73
Temp (K)	300	0	2400	2400	973
Pressure (kPa)	101	101	101	101	101
constraints	none	none	none	none	none
time (ps)	500	500	500	500	500
time step	0.002	0.002	0.002	0.002	0.002
Q	1	1	1	1	1
PE after MD	39.972	3.198	148.62	x	86.567
new cell size (ang)	NA	NA	NA	18465.5586	NA
new density	NA	NA	NA	0.355 g/(cm3)	NA
mean sq K fluc	26.9624	1.12E+06	1630.68	x	282.586
mean sq U fluc	19.3871	1.12E+06	406.558	x	109.636
Mean U (kcal)	41.1441	3.196	150.089	x	87.3686
Mean K (kcal)	44.1187	0.00548	350.936	x	142.533
Mean P (Kpa)	1.77E+06	687368	5.41E+06	x	3.19E+06
Mean V (ang3)	847.356	847.356		x	847.356
mean T (K)	302.058	0.037503	2402.68	x	975.8
new E min (kcal)	3.507	3.198	4.248	x	3.032

As can be seen in these tables, a few (constant number, pressure, and time) NPT simulations were initially run and recorded. These were tested in an attempt to allow the simulation to more accurately reflect real experimental conditions, in which pressures are be held constant and gold droplet volumes allowed to fluctuate. Also, in the case of NPT simulations, the calculated constant pressure heat capacity (Cp) could be compared with known values to determine the fit of the system. Constant volume heat capacity (Cv) values for gold could not be found in the literature. However, since the density of these

packed solid systems was very high, the result of the NPT simulation was consistently a continuous box volume increase. Temperatures and pressures also fluctuated widely, often rising sharply to values well above the stated initial conditions. The NPT simulation demonstrating several "x" values was manually stopped after several times illustrating this behavior. It was determined from these analyses that the NVT ensemble would be best for the purposes of this project. In retrospect, such behavior might provide some useful insight. For the purposes of the solid simulation at low T, certainly the box size increase does not match well with real behaviors, but at higher temperatures, this behavior could be likened to a melting process. Although gold should not "melt" at 300K, the final calculated density for the first NPT simulation is off by only an order of 10 g/ccm too high for liquid gold. Perhaps a longer simulation would have allowed the gold box to relax further to a more realistic liquid gold density.

Table 5.4 illustrates values collected when the modified empirical force field was used for system energy minimization. Like those shown previously, this table also illustrates tests on a gold-only system. To modify the default empirical force field, which uses a simple Leonard-Jones interaction potential to determine atomic energy minimization, known values for gold were input where the default force field provided nil values. These values are shown in Table 5.3. In this way, the program was modified to more accurately represent gold interactions, without changing the basic operating method. Values input into the program were found online and later verified with the CRC Handbook of Chemistry and Physics. Modified values were input as shown in Table 5.3:

Table 5.3: Values representing gold interaction parameters input into modeling program

```
#type   radius  well    apol    Neff    mass    DA      q0      fcadj   pbci
#----   -------  -------  -------  -------  -------  -------  -------  -------  -------
Au      1.35    -       -       -       197.00 -        0.0000          0.0000  -

[vdw] # ------------------- van der waals parameters -------------------------

#type   type    R       eps             m       n
#---    ----     ------  -------- --      --

Au      Au       1.66      -             12      6
```

Here, "radius" signifies the atomic radius, and "R" indicates the Leonard-Jones radius for gold. The Leonard Jones (L-J) interaction potentials are based on the well-known Leonard-Jones 6-12 interaction equation:

$$V(r) = 4\epsilon \left[\left(\frac{\sigma}{r} \right)^{12} - \left(\frac{\sigma}{r} \right)^{6} \right] \qquad \textbf{(Eq. 5.3)}$$

where ϵ is the depth of the potential well and $\sigma$is the (finite) distance at which the potential is zero. These parameters can be fitted to reproduce experimental data or deduced from results of accurate quantum chemistry calculations. The (1/r)^12 term describes repulsion and the (1/r)^6 term describes attraction. Leonard-Jones equation coefficients and epsilon values were not changed in the force field to eliminate any potential discrepancies with the MOE MD simulation program. A better fitting of these parameters to the gold system would most likely make the force field better at simulating gold systems. Although the L-J interaction potential is commonly used for ideal systems such as Ar gas, it should a reasonably good estimate for gold. While gold is a metal, it

does not often interact strongly with other elements as do other metals, and it is considered relatively "noble." Of course any favorable (or non-favorable) interactions with other atoms or molecules in the simulations are neglected. It is assumed that such interactions are not large enough to significantly affect the behavior of these solutes in the gold medium. This may or may not be an accurate assumption.

Table 5.4: Gold-only NVT simulations using the modified empirical force field for energy minimization

				Basic parameters
19.3	19.3	19.3	17.31	density (g/cm3)
9.46285	9.46285	9.46285	9.813	box size (ang)
modified	modified	modified	modified	Force field
-4.401	-4.401	-4.401	-4.401	PE before min
-4.401	-4.401	-4.401	-43.163	
50	50	50	50	atom number
				MD parameters
Swann MD	Swann MD	Swann MD	Swann MD	program used
Nose -Hoover	Nose -Hoover	Nose -Hoover	Nose -Hoover	MD alorithm
NVT	NVT	NVT	NVT	ensemble
4.73	4.73	4.73	4.73	cutoff
300	0	973	973	Temp (K)
101	101	101	101	Pressure (kPa)
none	none	none	none	constraints
500	500	500	500	time (ps)
0.002	0.002	0.002	0.002	time step
1	1	1	1	Q
-9.997				PE after MD
NA	NA	NA	NA	new cell size
NA	NA	NA	NA	new density
23.9496	3.18816	192.252	243.707	mean sq K fluc
1.84296	3.18821	10.5692	10.377	mean sq U fluc
-9.799	-17.0516	-5.387	-5.29053	Mean U (kcal)
43.7139	12.6509	142.129	142.422	Mean K (kcal)
254262	8291.57	975135	840846	Mean P (Kpa)
847.356	847.356	847.356	944.928	Mean V (ang)
299.287	86.61	973.087	975.087	mean T (K)
-42.415	-43.533	-44.417	-42.031	new E min (kcal)

Since Cv values could not be used to test the accuracy of each force field on the gold system, potential energies were instead used. Other values were used to test how well the system maintained set parameters, and to identify any problems. The last line in these tables lists the system potential energy (U) after the MD simulation and another energy minimization process. It was noted that the modified empirical force field in all cases allowed the system to reach a lower relative U than the other force field. It was

determined that the modified force field was superior, and this program was subsequently used for all solute-solvent simulations. Also of note are the anomalous mean pressures found in these simulations. Very high P values were reported for all simulations, indicating that pressures were not well-maintained. Anomalous pressure values were expected in light of previous MD results, however, these values appear very high.

Below are tables for each of the solutes tested, along with representative graphical images. Note that for the cases of the ZnS and SiO molecules the program required addition of some hydrogen atoms in order to maintain the bonds. Also, the SiO_2 molecule was very difficult to simulate; only SiO ion species would run without generating an error. Light grey regions denote hydrogen species. Si ions were created by ionizing the atoms to +2 and then selectively removing hydrogens. Gold atoms appear in the figures as yellow and contrast with solute species. The number of gold solvent atoms was modified for each simulation to maintain accurate concentration of solute. In some cases, a 100 atom box was utilized to produce concentrations below 2% because richer mixtures would not run. In other cases, 50 atom boxes were preferentially used to limit computation time.

Table 5.5: NVT simulations with Zn ions as solute, with varying solvent density and solute concentration

Zn 2+			
	Zn #1	**Zn#2**	**Zn#3**
Basic parameters			
density (g/cm3)	19.3	17.31	17.31
box size (ang)	9.46285	9.813	9.813
Force field	modified	modified	modified
PE before min	-43.908	-43.161	-21.223
atom number	50	50	50
atomic volume	0.02	0.02	0.2
MD parameters			
program used	Swann MD	Swann MD	Swann MD
MD alorithm	Nose-Hoover	Nose-Hoover	Nose-Hoover
ensemble	NVT	NVT	NVT
cutoff	4.73	4.73	4.73
Temp (K)	973	973	973
Pressure (kPa)	101	101	101
constraints	none	none	none
time (ps)	500	500	500
time step	0.002	0.002	0.002
Q	1	1	1
PE after MD	0.925	-1.907	30.361
mean sq K fluc	210.069	177.609	274.829
mean sq U fluc	12.5966	10.8185	65.8055
Mean U (kcal)	-5.571	-5.2536	30.4812
Mean K (kcal)	142.095	142.198	142.087
Mean P (Kpa)	967114	844033	4.19E+06
Mean V (ang3)	847.356	944.943	944.943
mean T (K)	972.849	973.555	972.798
new E min (kcal)	-43.949	-42.964	-25.719

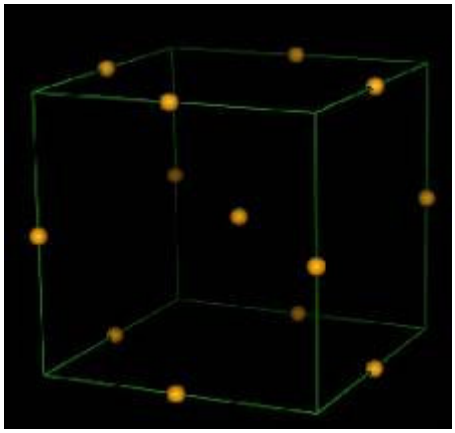

Figure 5.7: Periodic box with a single Zn2+ ion per unit cell

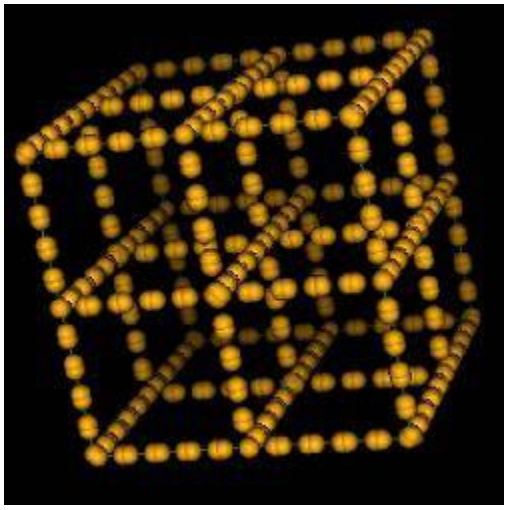

Figure 5.8: Periodic box of Zn ions at a 20% atomic solute concentration before addition of gold solvent

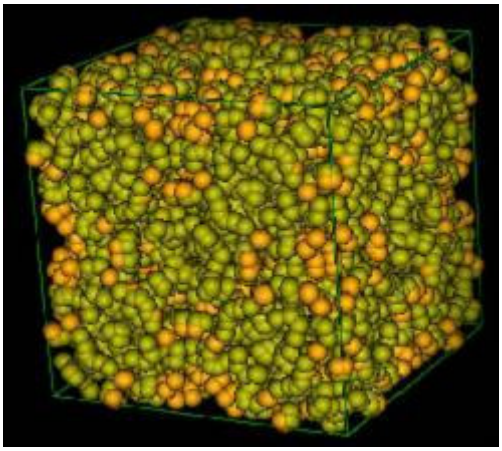

Figure 5.9: Periodic box of gold atoms and Zn ions at a 20% atomic concentration

Table 5.6: NVT simulations with O^{2-} ions as solute, with varying solvent density and solute concentration

O 2-				
	O#1	**O#2**	**O#3**	**O#4**
Basic parameters				
density (g/cm3)	19.3	17.31	17.31	17.31
box size (ang)	9.46285	9.813	9.813	9.813
Force field	modified	modified	modified	modified
PE before min	-43.751	-46.611	-28.501	-45.3
atom number	50	50	50	50
atomic volume	0.02	0.02	0.2	0.1
MD parameters				
program used	Swann MD	Swann MD	Swann MD	Swann MD
MD alorithm	Nose-Hoover	Nose-Hoover	Nose-Hoover	Nose-Hoover
ensemble	NVT	NVT	NVT	NVT
cutoff	4.73	4.73	4.73	4.73
Temp (K)	973	973	973	973
Pressure (kPa)	101	101	101	101
constraints	none	none	none	none
time (ps)	500	500	500	500
time step	0.002	0.002	0.002	0.002
Q	1	1	1	1
PE after MD	-6.035	-5.753	151971	17189
mean sq K fluc	300.155	304.721	x	x
mean sq U fluc	11.3791	10.4639	x	x
Mean U (kcal)	-6.128	-5.759	x	x
Mean K (kcal)	139.427	139.367	x	x
Mean P (Kpa)	940261	817513	x	x
Mean V (ang3)	847.356	944.943	x	x
mean T (K)	974.471	974.052	x	x
new E min (kcal)	-43.97	-43.014	x	x

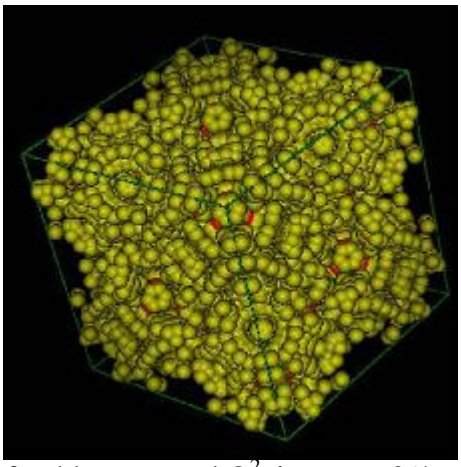

Figure 5.10: Periodic box of gold atoms and O^{2-} ions at a 2% atomic concentration

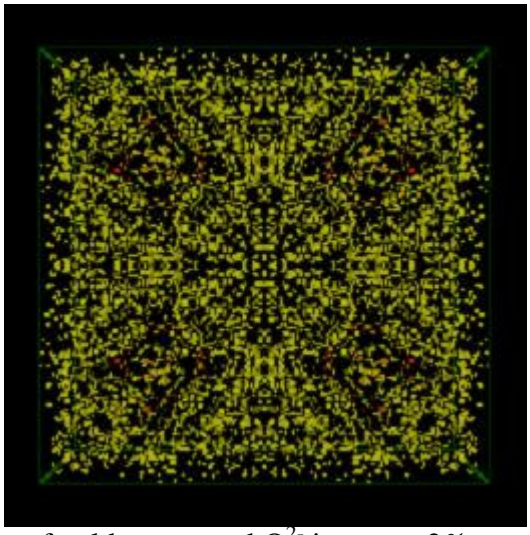

Figure 5.11: Periodic box of gold atoms and O^{2-} ions at a 2% atomic concentration after the MD simulation

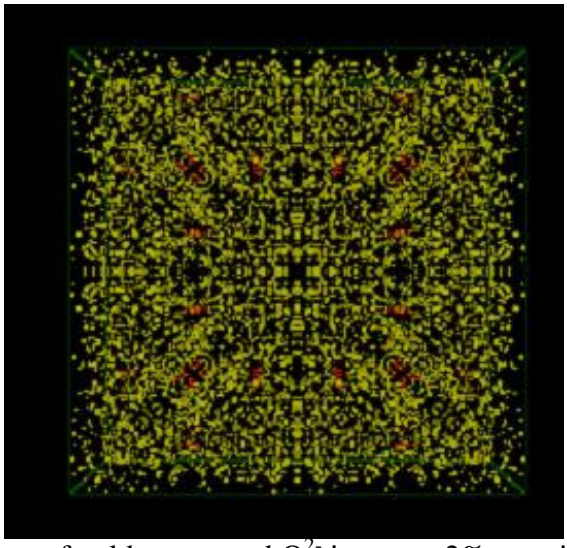

Figure 5.12: Periodic box of gold atoms and O^{2-} ions at a 2% atomic concentration, after the MD simulation and a subsequent re-minimization step

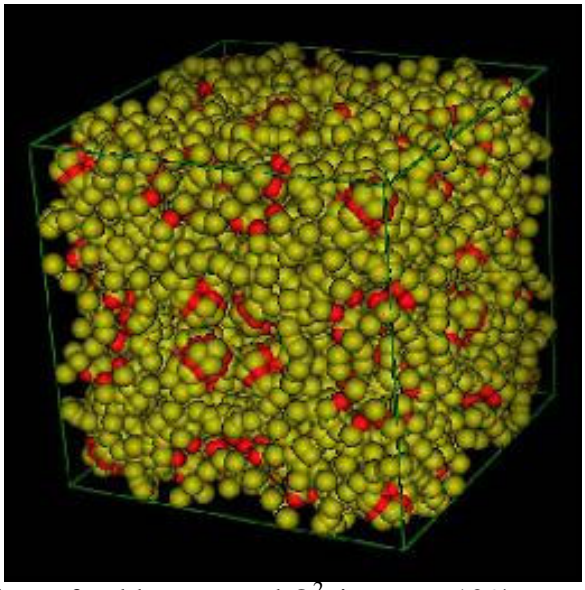

Figure 5.13: Periodic box of gold atoms and O^{2-} ions at a 10% atomic concentration

Table 5.7: NVT simulations with Si ions as solute, with varying solvent density and solute concentration

Si 4+			
	Si #1	**Si #2**	**Si #3**
Basic parameters			
density (g/cm3)	17.31	17.31	17.31
box size (ang)	9.813	9.813	9.813
Force field	modified	modified	modified
PE before min	-47.945	-158.763	
atom number (tot)	50	50	50
atomic volume (ang3)	0.02	0.2	0.1
MD parameters			
program used	Swann MD	Swann MD	Swann MD
MD alorithm	Nose-Hoover	Nose-Hoover	Nose-Hoover
ensemble	NVT	NVT	NVT
cutoff	4.73	4.73	4.73
Temp (K)	973	973	973
Pressure (kPa)	101	101	101
constraints	none	none	none
time (ps)	500	500	500
time step (ps)	0.002	0.002	0.002
Q	1	1	1
PE after MD	-7.612	-24.841	-8.261
mean sq K fluc	775.215	816.513	270.376
mean sq U fluc	14.3702	205.513	19.8717
Mean U (kcal)	-6.115	-9.46	-8.21
Mean K (kcal)	142.288	362.791	141.937
Mean P (Kpa)	859677	7.40E+06	1.00E+06
Mean V (ang3)	944.943	944.943	944.943
mean T (K)	974.175	973.665	971.773
new E min (kcal)	-43.164	-153.755	-53.932

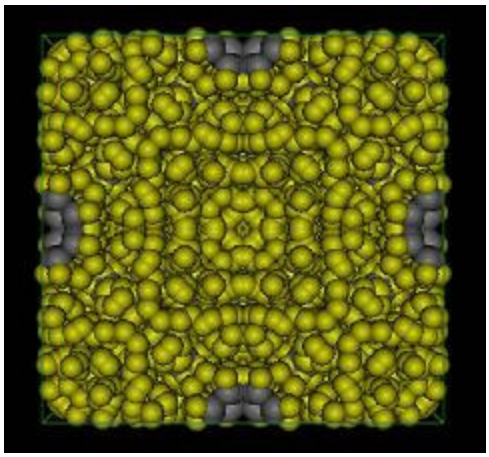

Figure 5.14: Periodic box of gold atoms and Si ions at a 10% atomic concentration after MD simulation and subsequent energy minimization

Table 5.8: NVT simulations with ZnS molecules and stoichiometric ions as solute, with varying solvent density and solute concentration

ZnS			
	ZnS #1	**ZnS #2**	**Zn ions + S ions**
Basic parameters			
density (g/cm3)	19.3	19.3	17.31
box size (ang)	9.46285	11.9224	9.813
Force field	modified	modified	modified
PE after min	-50.767	-111.044	-261.109
atom number	50	100	50
atomic volume	0.02	0.01	0.02
MD parameters			
program used	Swann MD	Swann MD	Swann MD
MD alorithm	Nose-Hoover	Nose-Hoover	Nose-Hoover
ensemble	NVT	NVT	NVT
cutoff	4.73	4.73	4.73
Temp (K)	973	973	973
Pressure (kPa)	101	101	101
constraints	none	none	none
time (ps)	500	100	500
time step	0.002	0.002	0.002
Q	1	1	1
PE after MD	4.19E+03	556794.1	-221.04
mean sq K fluc	1.52E+06	7.36E+72	327.758
mean sq U fluc	2.73E+10	2.89E+10	14.3153
Mean U (kcal)	1.00E+06	558328	-218.764
Mean K (kcal)	1.38E+30	2.86E+36	145.182
Mean P (Kpa)	7.55E+33	8.31E+37	858349
Mean V (ang3)	847.356	1694.69	944.943
mean T (K)	8.91E+30	9.42E+36	974.105
new E min (kcal)	x	-107.73	-262.575

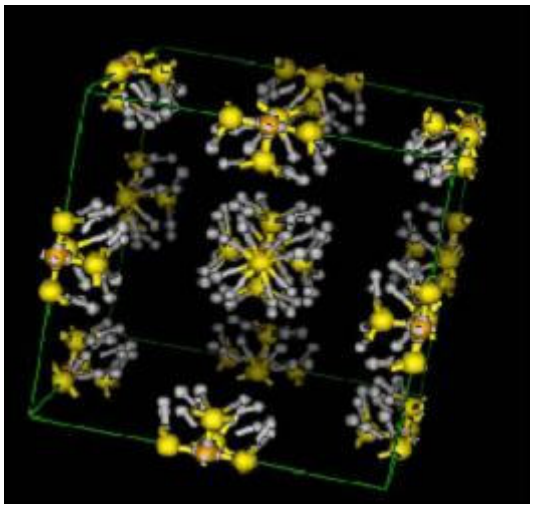

Figure 5.15: Periodic box of ZnS molecules at a 2% atomic concentration before addition of gold solvent

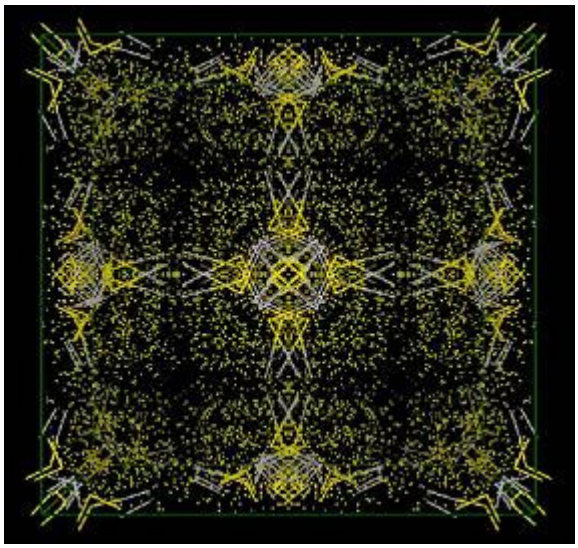

Figure 5.16: Periodic box of ZnS molecules at a 1% atomic concentration after addition of gold solvent

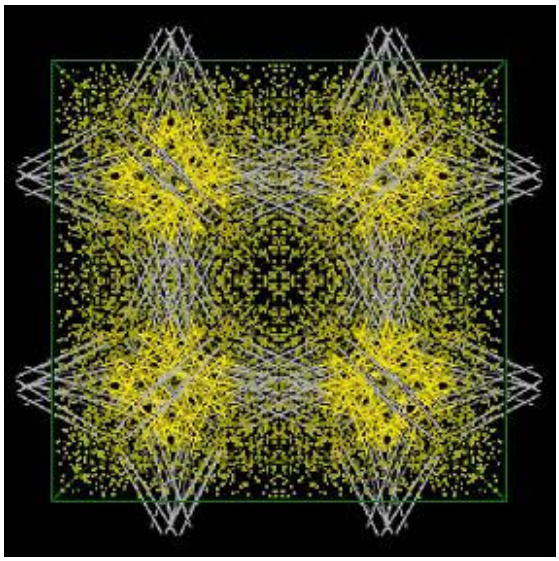

Figure 5.17: Periodic box of ZnS molecules at a 1% atomic concentration after addition of gold solvent and MD simulation

Table 5.9: NVT simulations with SiO molecules and stoichiometric ions as solute, with varying solvent density and solute concentration

SiO 2-			Si + O
	SiO#1	**SiO#2**	**SiO#3**
Basic parameters			
box file	SiO#1.moe	SiO#2_2.moe	SiO#3.moe
density (g/cm3)	17.31	17.31	17.31
box size (ang)	9.813	12.2806	9.813
Force field	modified	modified	modified
PE before min	-214.768	4844571 (no Au)	
PE after min	-214.768	-101.294	-43.359
atom number	50	100	50
atomic volume	0.02	0.01	0.02
MD parameters			
program used	Swann MD	Swann MD	Swann MD
MD alorithm	Nose-Hoover	Nose-Hoover	Nose-Hoover
database name	SiO#1.mdb	SiO#3.mdb	SiO#4.mdb
ensemble	NVT	NVT	NVT
cutoff	4.73	4.73	4.73
Temp (K)	973	973	973
Pressure (kPa)	101	101	101
constraints	none	none	none
time (ps)	500	100	500
time step	0.002	0.002	0.002
Q	1	1	1
PE after MD	x	x	-5.129
mean sq K fluc	x	x	215.951
mean sq U fluc	x	x	12.2487
Mean U (kcal)	x	x	-6.44
Mean K (kcal)	x	x	139.11
Mean P (Kpa)	x	x	846419
Mean V (ang3)	x	x	944.943
mean T (K)	x	x	972.259
new E min (kcal)	x	x	-43.954

Although the L-J potential may not be the best method for simulation of gold solvent, it appears to do well for these simulations, reliably minimizing the energy of the system and producing some expected system results. Constant volume heat capacities calculated for the gold system do not appear unreasonable, though they could not be compared to experimental or empirical data. Other gold models in the literature focus

mainly on just a few gold atoms, or on gold's crystallization and melting behavior (for small particles) and so also could not provide a reasonable method to determine force field accuracy. Perhaps the most noticeable problem in these simulations is the consistently high mean pressures, but these could be the result of the MD simulation as well as the force field. Some MD simulation methods cited in the literature are listed below:

- Glue Model (Potential) of liquid gold
- Embedded Atom method (EAM) (Potential) – used for MD simulation of gold nanowires, Johnson's potential, Voter and Chen version, Daw and Baskes
- RGL many-body potentials - Au is modeled by many-body potentials as developed by Rosato, Guillope´ and Legrand (RGL) on the basis of the second moment approximation to the tight-binding model.
- Effective Medium Theory
- Tight binding potential (TB-MD)
- Modified Embedded Atom Method (MEAM)
- ReaxFF – force field developed for hydrocarbons
- DFT – SIESTA method

These methods are certainly more sophisticated, but the L-J potential seems to work well as a first approximation. Unfortunately, it is difficult to compare the empirical modified force field with MMFF94, since it appears that gold was not parameterized for this program, and MOE most likely defaulted to an unmodified L-J.

It is evident from these simulation results that both the ZnS and SiO molecules created systems of very high energy. In one SiO simulation, the energy minimization left the oxygen species ripped away from the rest of the molecule. SiO as a molecule could not be run under any tested combination of parameters, due to extremely high system strain energy. Comparing similar parameters for SiO and ZnS, it appears that ZnS (ions) incorporate more readily into the gold solvent than the SiO (ions), though energies remain high. This result indicates that incorporation of these species into the gold particle is energetically unfavorable, and would therefore require extreme conditions to create a sufficient driving force for this process to be thermodynamically possible. Though this project only yielded a single data point for the SiO due to the extremely high strain energy, these results generate doubts as to the thermodynamic possibility of classical VLS growth in these systems.

Temperature effects on the gold solvent were small, so all solute-solvent simulations were run at a single temperature. 973K was chosen to emulate common temperature conditions encountered in the VLS synthesis of ZnS and SiO_2 nanostructures. As expected, lower solute concentrations produced systems of lower energy. It appeared that at all concentrations tested, solute atoms and molecules tended to aggregate together. This result was expected for higher concentrations, but not for concentrations as low as 1 atomic%. Perhaps a more homogenous mixture would appear at even lower solute concentrations. In this way the simulation does not realistically predict precipitation limits, since at such high temperatures, there should be a marked difference between 1 and 20 atomic percent solute.

In conclusion, this work provided some interesting information on the nature of semiconductor ions and molecules in solid and liquid gold solvent. A L-J interaction potential was used as the force field for energy minimization. The utilized force field provided a reasonable first estimation for the purposes of understanding how species interact with gold catalysts during VLS nanowire growth. NVT MD simulations were carried out on several systems at several conditions, varying mainly solute concentration. Some results, such as those demonstrating that diffusing species most likely do not enter the solvent as molecules, and those indicating greater tendency for Zn and S to dissolve were expected. Although incorporation of ions and molecules was expected to increase the system energies, the scale of the energy increase, to the point that the small molecules would not even remain within the bounds of the simulation was a surprise. Still, these simulations were based on the most basic inter-atomic interactions. To make such a simulation more vigorous, a more accurate force field should be used, and more parameters should be tested. It would be interesting to investigate the influence of temperature and concentration more thoroughly, perhaps using very low concentrations of solute. MD simulation time should also be increased to ensure that proper minima are reached. Also, replication of the Au-Si phase diagram through computational analysis would be a good way to test the accuracy of the model and the solute-solvent interactions. This model also could be coupled with QSPR methods. Finally, given more time, testing of other small molecules and ions would be interesting and useful.

To further probe the role of the gold catalyst particle in nanowire growth, we designed and performed a series of experiments similar to those published by Kirkham *et. al.*[188] for Au catalyzed ZnO, in which XRD analysis is used to determine gold lattice

parameters before and after nanowire growth. Gold lattice parameters were determined for both ZnS-SiO_2 and iron oxide nanowire samples described in this work via similar XRD analysis. These values were then compared with gold coated substrates exposed to similar conditions to those used to prepare the nanowire samples, but without presence of the nanowire forming species. The results of these experiments can be seen in the tables and figures below. Note that in these figures grey vertical lines correspond to reference gold peak positions, while the red peaks correspond to measured gold XRD data in the specified planes. Light green and light blue peaks correspond to other phases in the sample. The tables provide quantitative data derived from peak fitting and analysis. This work was done with the MRD X-ray Diffractometer, with similar settings as those outlined for XRD analysis in Chapter 4. Calibrations were performed before each run to ensure accurate results.

In the case of the iron oxide system, a sample of previously synthesized iron oxide nanowires was examined to determine the lattice parameters of gold particles on the tips of the nanowires. This value was compared against a polycrystalline alumina substrate coated with 2nm of gold, heated to 900^{o}C for one hour; these are the same substrate material, temperature conditions, and gold deposition thickness as those used to synthesize the nanowire sample. Pressure conditions were not duplicated, however, with the substrate pressures being maintained at atmosphere. A similar study was conducted for the ZnS-SiO_2 core-shell nanowire system. In this case, a control Si substrate was coated with 20nm of gold and heated to 1000^{o}C for 90 minutes to duplicate characteristics of the tested nanowire sample. The gold lattice parameters in all of these four tested samples were found to be within 0.1% (the threshold of experimental error) of

the published bulk value of 0.40786 nm. Data for the control samples is not shown in the figures below to reduce redundancy.

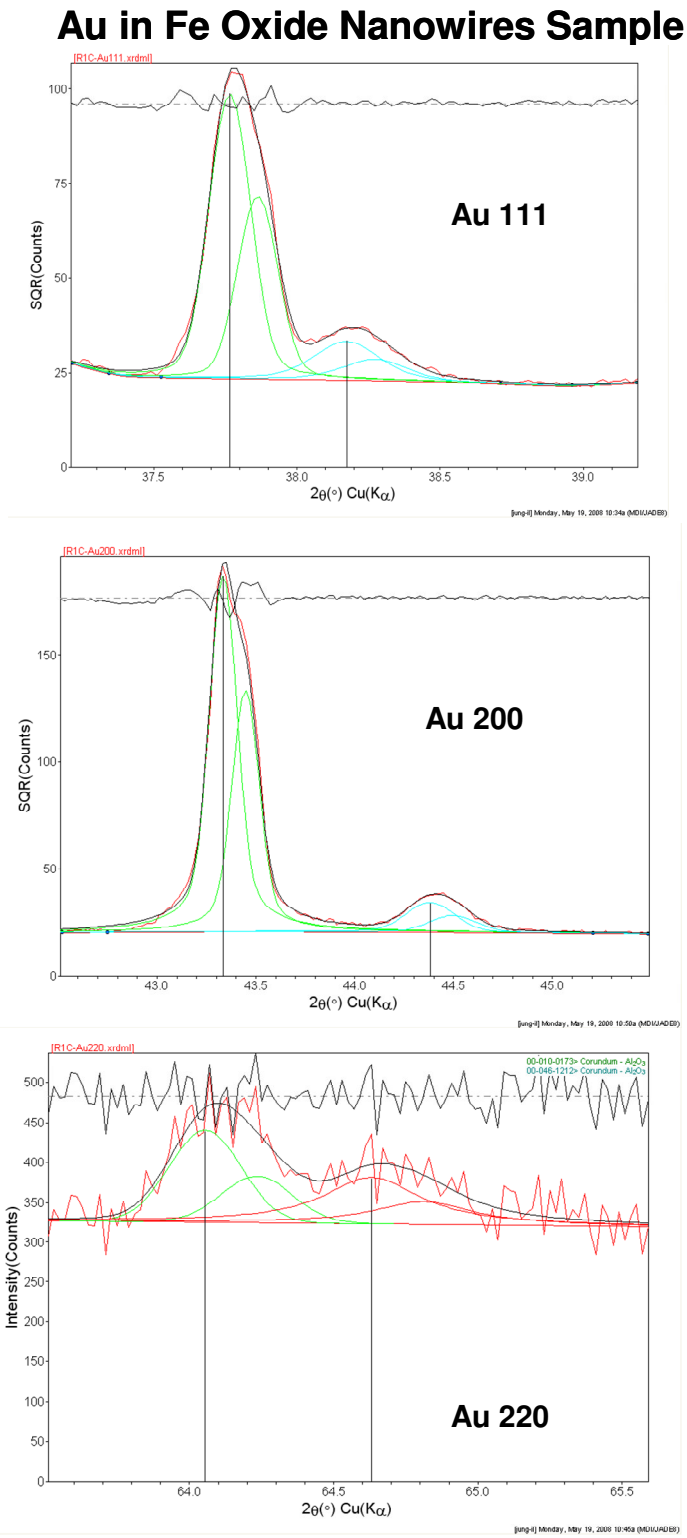

Figure 5.18: XRD peak profiles of Au planes in iron oxide nanowires sample

Table 5.11: Quantitative data derived from iron oxide nanowires sample showing peak profile fitting and lattice constants.

	Profile Fitting Report			
	@ 2-Theta	d(nm)	FWHM	XS(nm)
111	38.174 (0.008)	0.23556 (0.00010)	0.252 (0.021)	43 (5)
200	44.382 (0.011)	0.20395 (0.00009)	0.263 (0.028)	42 (6)
220	64.631 (0.042)	0.14409 (0.00017)	0.412 (0.159)	26 (11)

Lattice Constants from Peak Locations and Miller Indices

2-Theta	d(nm)	H	k	l	a-Axis (nm)
38.174	0.23556	1	1	1	0.408
44.382	0.20395	2	0	0	0.40789
64.631	0.14409	2	2	0	0.40756
				Average Lattice Constants =	0.40782

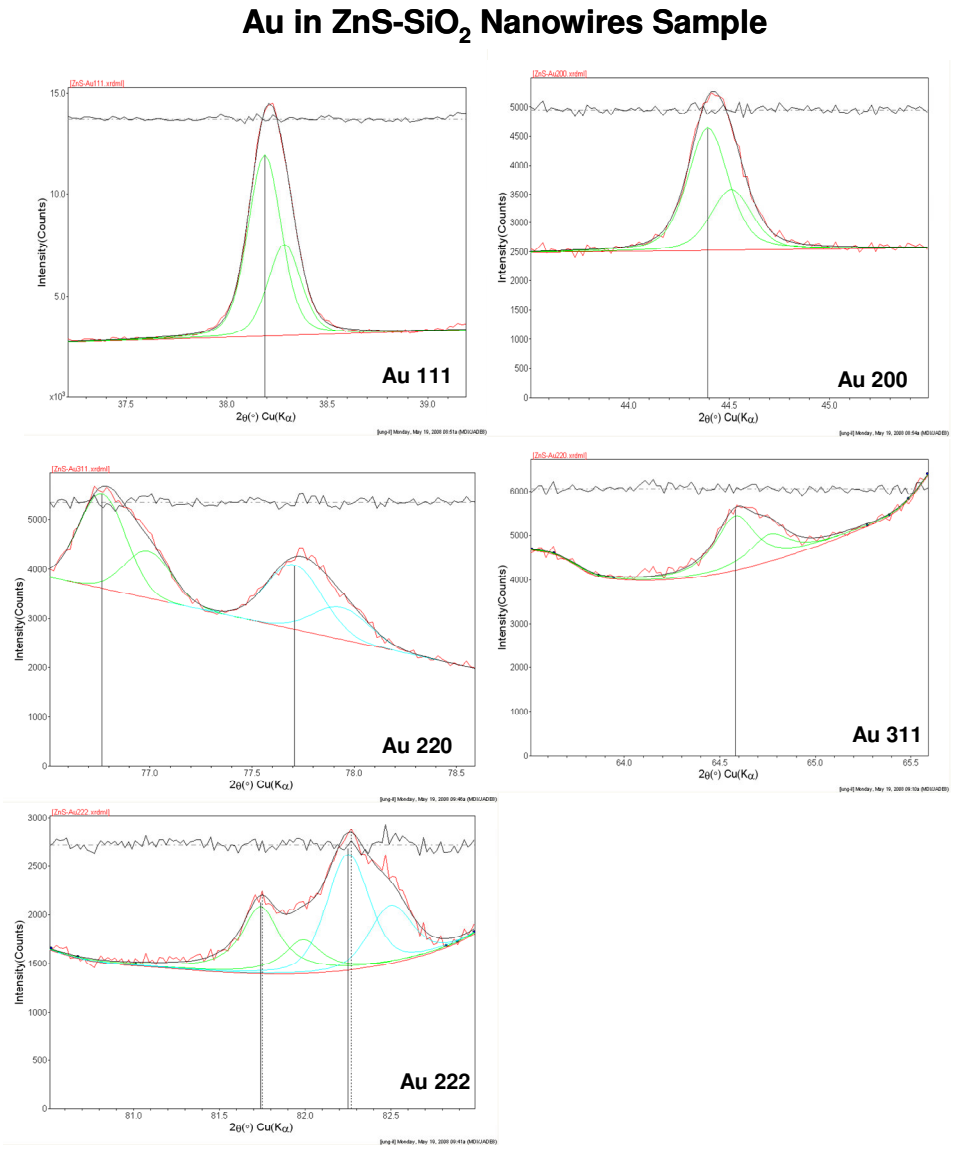

Figure 5.19: XRD peak profiles of Au planes in ZnS-SiO_2 core-shell nanowires sample

Table 5.12: Quantitative data derived from ZnS-SiO_2 core-shell nanowires sample showing peak profile fitting and lattice constants

	@ 2-Theta	d(nm)	FWHM	XS(nm)
111	38.189 (0.001)	0.23547 (0.00001)	0.195 (0.003)	65 (2)
200	44.394 (0.002)	0.20390 (0.00002)	0.239 (0.006)	48 (2)
220	64.582 (0.004)	0.14419 (0.00002)	0.246 (0.016)	50 (4)
311	77.707 (0.004)	0.12279 (0.00001)	0.325 (0.013)	37 (3)
222	81.741 (0.005)	0.11772 (0.00001)	0.265 (0.017)	51 (4)

Lattice Constants from Peak Locations and Miller Indices

2-Theta	d(nm)	h	k	l	a-Axis (nm)
38.189	0.23547	1	1	1	0.40785
44.394	0.20389	2	0	0	0.40779
64.582	0.14419	2	2	0	0.40783
77.707	0.12279	3	1	1	0.40725
81.741	0.11772	2	2	2	0.40779
				Average Lattice Constants =	0.4077 (0.000254)

These results indicate that there was no significant difference between the gold lattice spacing of nanowire samples and those never exposed to the nanowire vapor species. If alloying had occurred, as described in the classical VLS model, small traces of these species should be left to distort the gold lattice. Since bulk values for the Au lattice parameter were found for all samples, these experiments show that for the systems of interest in this work, the VLS mechanism cannot accurately describe the nanowire growth. Most likely growth occurred via a VSS type of mechanism, in which species were transported around the surface of the gold particle. Both the simulations and these experimental results show that the VLS growth mechanism needs to be reevaluated for multi-component systems.

5) If the properties of the catalyst and substrate are such that the metal catalyst is not strongly held to the surface, a precipitate of reactant material is rejected out of the metal droplet onto the substrate. The nanowire diameter is dictated by the circumference at the interface of the metal droplet on the substrate. In the case of strong adhesion of catalyst to substrate, the nanowire may grow such that the catalyst remains on the substrate surface, and the wire grows out from the top of the metal droplet.

The interplay between catalyst, substrate, and growing nanowire is nontrivial. Although traditional VLS theory maintains that the nanowire diameter is primarily determined by the liquid diameter at the solid interface, several groups have published results in which a single catalyst droplet grows up to several hundreds of nanowires, and other contradictory reports have been published on the relationship between catalyst size and nanowire diameter. [209]Another publication found that increasing the metal droplet size induced multiple nanowire nucleation, whereas in the same system less available metal leading to smaller catalyst sizes resulted in single 1D nanostructure growth. [210] For such cases, scientists suggest that in large enough droplets the surface energy can support numerous nucleation events. Here, short-range ordering in the particle allows nucleation at several sites on the surface, often producing growth of nanowires in different crystallographic orientations on the same catalyst. In another paper describing growth of ZnO assisted by tin catalyst, two nanostructures with different growth directions are observed to emerge from the same particle. An SEM image of this phenomenon has been presented previously in Figure 5.4. The authors' analysis finds that the interfacial region between the ZnO nanowire and the metal must be partially crystalline or atomically ordered during growth, although the local growth temperature is

much higher than the melting point of tin, and may play a key role in initiating the 1D nanostructure. They further conclude that the interface prefers in this case to take the least lattice mismatch, and therefore that the crystallographic orientation of the tin particle determines the growth direction and the side surfaces of the nanowires and nanobelts. [208] Literature also reports observations of metal diffusion from smaller catalyst drops to larger ones nearby, leading to changes in nanowire diameter during growth. [211] The metal catalyst particle clearly is misinterpreted as purely static, though we have shown that bulk diffusion is not necessary for metal catalyst assisted nanowire formation.

Publications at the beginning of this decade and earlier attempt to use equilibrium thermodynamics to define nanowire growth behavior based on catalyst properties, such as the minimum radius for a liquid metal droplet to be able to nucleate and sustain nanowire growth, or r_{min}. This value is defined as:

$$r_{min} = 2\,\sigma_{LV}\,V_L / R\,T\,\ln\alpha \qquad \textbf{(Eq. 5.4)}$$

where σ_{LV} is the liquid-vapor surface free energy, V_L is the molar volume, R is the gas constant, T is temperature, and α is the vapor phase supersaturation. Researchers state that typical values (presumably for Si-Fe systems) place this lower radius around 200 nm, and that these results are confirmed by the literature available at the time. Certainly the $\leq$100nm diameter iron oxide nanowires discussed previously contradict this result as applied to PLD iron oxide nanowire growth, but laser ablation techniques are mentioned as a means to overcome equilibrium restraints. However, the ZnS-SiO_2 core-shell

nanowires also discussed in this work demonstrate diameters as small as tens of nanometers, though the energy input is merely temperature elevation. ZnO nanowires have also been grown via thermal evaporation methods to diameters as small as 6nm. [212] Clearly, such treatments of nanowire growth cannot be confidently applied in all cases. The inability to fully describe nanowire evolution with equilibrium thermodynamics is mirrored in researcher's difficulties in explaining what should otherwise be familiar phenomena.

The relationship between substrate and the growing nanostructure likewise cannot be ignored. As described above, the alumina substrate employed for magnetite nanowires clearly affected their growth, as each grain on the polycrystalline surface produced an array of nanowires at an angle to those on other grains, and single-crystalline sapphire substrates yielded fully perpendicular or in-plane arrays according to surface orientation. Adhesion of the metal particle to the substrate surface depends on many factors including the electronic and chemical affinity for each species to the other, the roughness of the surfaces, and the relative lattice mismatch. The lattice parameter of gold is approximately 4.09 angstroms and alumina is 4.75 angstroms, while that of magnetite crystals is 8.389 angstroms, ensuring that the lattice mismatch of the two species should be alike enough to achieve growth from the nanowire tip, but stemming from the alumina substrate. Therefore, it makes sense that in this case (and also the case of the core-shell nanowires) the substrate crystallography plays a role in directing the nanowire growth direction.

To complicate matters further, it is possible that the Au catalyst may play a much more active role in the growth process than the VLS mechanism suggests. In 2006 a detailed investigation of silicon nanowire growth found that the diffusion of gold from one growing nanowire to another induced coarsening or shrinking of the Au droplet, and corresponding diameter changes in single nanowires. [211]These nanowires can be seen in Figure 5.17.

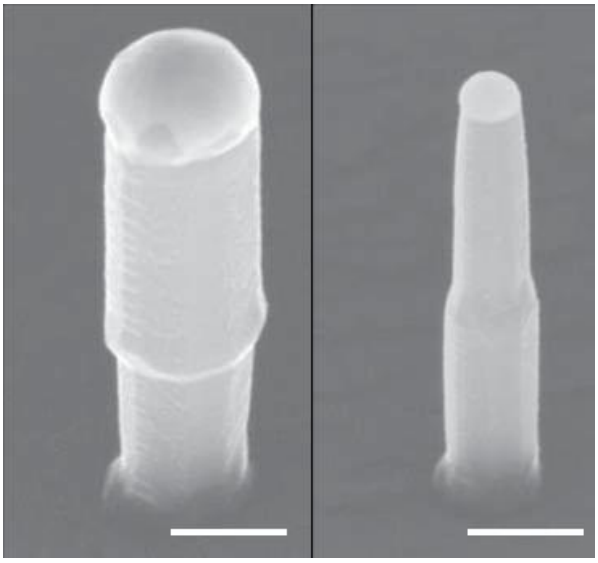

Figure 5.17: Gold catalyzed silicon nanowires demonstrating diameter variation during growth directed by the metal particle size. The scale bar is 200nm.

This finding indicates that the gold particle is not static during the reaction, but may gain or lose volume to other areas throughout the synthesis process. Though bulk Au is considered non-reactive, nanoscale Au particles have been found to be far from noble. *In-situ* TEM observations have shown that when heated, Au metal particles on Si can fully wet the surface and cause reversible surface reconstruction and removal of the native oxide layer.[203] In this case the substrate must be considered as a significant

reactant. Gold nanoparticles are currently under much investigation for use as active catalysts for CO oxidation, and literature reports efficiency of gold in these reactions exceeds even commonly used Pt. Many mechanisms for the reaction are proposed, but none so far have gained greater evidence relative to the others. These proposed mechanisms commonly employ electron transfer from the substrate in the process, due to evidence citing varying ability of gold to catalyze the oxidation reaction depending on its substrate support. [213-215] In 2008 STEM was used to identify the presence of single gold atoms in Si nanowires synthesized via vapor evaporation processes. Earlier publications report gold migration up and down silicon nanowire sidewalls. [211]

Though it is not emphasized in early VLS theory, desorption plays a key role in nanowire growth dynamics. This phenomenon must be taken into account when describing growth mechanisms for many systems. Neither thermodynamics based Gibbs Thomson treatments, which predict lower growth rates for smaller wires (with smaller catalysts) due to requisite nucleation energies, nor ordinary mass transport explanations, in which thinner wires should be longer than thicker wires due to more efficient transport of incoming vapors, could explain observations of GaP nanowires grown through vapor based metal-oxide vapor-phase epitaxy (MOCVD). The *Nature* letter published in 2007 found that desorption and readsorption of vapor species from one nanowire's gold catalyst to another strongly influenced growth rates. In fact, as shown in the figure below, authors identified three distinct growth regimes --competitive, synergistic, and independent --based on relative nanowire spacing and catalyst size. They determined that nanowires with the same catalyst size grew faster when located next to larger diameter

nanowires compared to those located near smaller diameter nanowires, with smaller catalysts. [209]

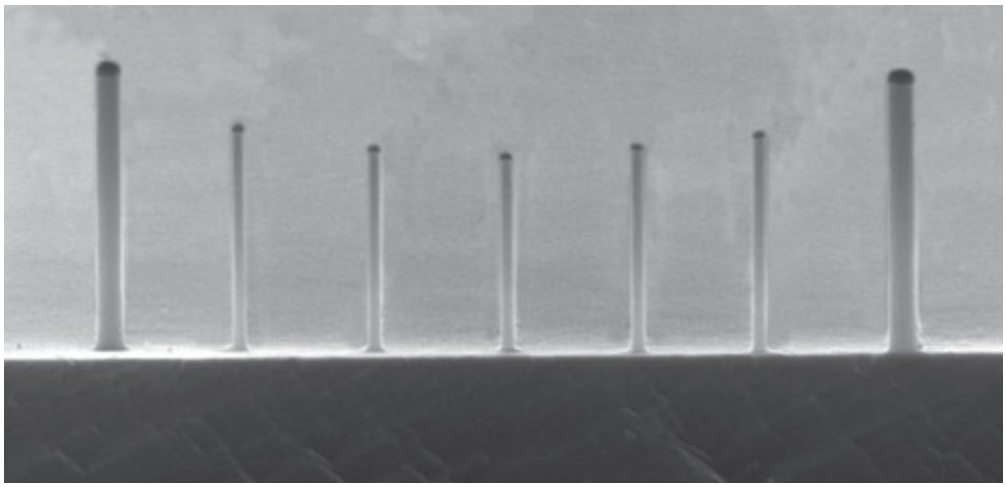

Figure 5.18: Cross-sectional SEM image of gallium phosphate nanowires grown from a pattern of gold catalysts with different sizes. Nanowires were grown from 25 nm and 100 nm catalysts with 300 nm spacing. Wires next to a thick wire are taller than the second-nearest wires, which are taller than those in the center. The scale bar is 1 μm.

In the two systems examined at detail in this work, the traditional view of the metal catalyst particle directing the nanowire diameter from the top, and away from the substrate appears to be appropriate. Nanowires grew within a narrow size range, with diameters mirroring metal particles found on the tips. The silica shell of the core-shell nanowires often extended well past the gold particle, and surrounded the particle terminating the nanostructure

6) As more reactant is added, more is rejected from the catalyst, causing vertical growth of a column or wire. It is believed that the nanostructure grows vertically due to the kinetic effect of preferred growth of some crystallographic planes relative to others dictating fast growth in one direction with other planes growing more slowly.

The rejection of material from the supersaturated metal droplet still appears to be valid for many simple systems in which the catalyst is liquid, and diffusing species are transported through the bulk of the alloy. Solid and liquid catalysts that transport species via surface diffusion clearly do not operate in exactly the same form, however it is believed that the nanowire growth occurs in a similar fashion at the nanowire-catalyst interface. Deposition at the interface in this case is likely due to the greater energy reduction that occurs at that region relative to other possible deposition sites, or re-evaporation. Because one-dimensional nanostructures are a form of anisotropic growth, it is useful to note common mechanisms that result in anisotropic growth:

1. *Imperfections such as defects or dislocations in certain crystallographic directions can cause preferred growth in those directions.* Since such imperfections are rarely seen in nanowires or nanobelts, this is probably not a major cause of their anisotropic growth.
2. *Impurities and other species may preferentially accumulate on specific crystallographic facets.* Because such impurities are rarely observed, this is not considered a major cause of the growth of nanobelts or nanowires.
3. *Different crystallographic directions in a given crystal have different growth rates.* This is frequently due to the differences in the surface energy of the surface, but can also result from different chemical potentials of the different faces and other factors. Different crystallographic facets have significantly different surface energies. As such, this is considered a major cause of the anisotropic growth of

nanobelts and nanowires.

It has been shown that the diffusion distance for a (100) plane in a FCC crystal is about 1 order of magnitude higher than for the (111) plane in the same crystal.[45] Furthermore, the dislocation (and growth site) density on the surface of the low-index planes will be lower. The conclusion is that the higher the free energy of the plane, the faster the growth velocity of the plane. Near equilibrium, growth occurs along the side that best minimizes the crystal's surface free energy. One would predict therefore that nanowires made up of materials in which several crystallographic planes contain similar surface energies should grow along many directions in similar conditions, and may even show oscillatory behavior. These effects are in fact demonstrated often in the literature, including several instances of unusual nanostructure growth in the ZnO system, and an observation of saw tooth faceting in silicon nanowires grown under UHV conditions, shown in Figure 5.20. [216]

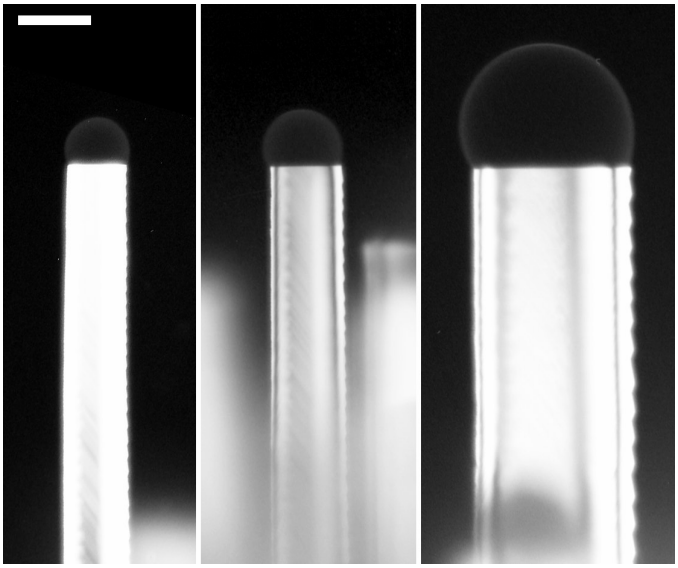

Figure 5.20: Images of three wires grown at 600^{o}C from Au-Si droplets of three different sizes, demonstrating saw tooth faceting at the nanowire edge. Scale Bar is 100nm.

Further, E-STEM reports have observed that nanowires grown through the faster catalyst assisted process exhibit much smoother more perfectly crystalline nanowires compared to nanowires grown by VS or other mechanisms. [201]

The general relationship between the nanowire growth direction, the catalyst crystal structure, and the substrate can be investigated via XRD analysis of nanowire samples. XRD analysis allows a broader view of the growth relationships than TEM analysis where a few samples may not provide a sufficiently representative sampling to formulate accurate conclusions regarding growth of the sample. Also, because XRD analysis is non-destructive, the relationship between nanowire and substrate can be better maintained for examination. Such studies have recently been conducted to investigate oriented ZnO growth on sapphire substrate. Pole figures like those in Figure 5.21 below can identify the average growth direction of wires relative to the substrate as well as catalyst crystal orientation.

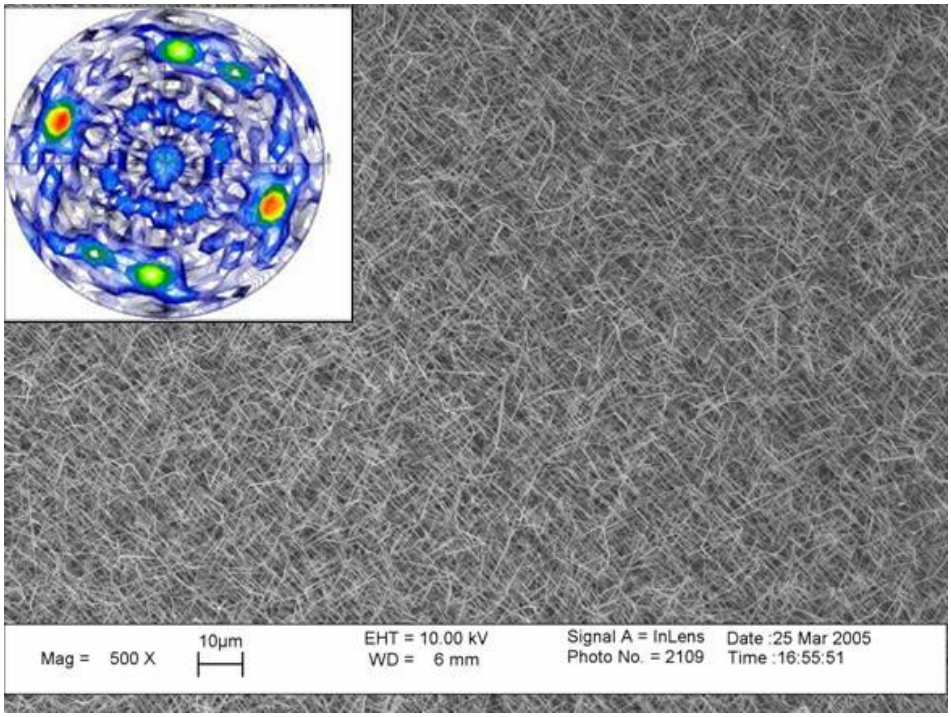

Figure 5.21: SEM image of aligned ZnO in three distinct directions, each at a relative 120^{o} displacement, and the corresponding pole figure image (inset) taken from the sample.

In the case of the magnetite experiments, where Au droplets are used as catalyst on a polycrystalline alumina substrate, several crystallographic faces were available on the surface for wire growth. Both [111] and [100] nanowire growth directions were observed. XRD analysis on magnetite nanowires grown on single crystal substrates demonstrated a preference for [111] growth, a logical result considering that the [111] direction is both the easy axis of magnetization and a smaller diffusion distance in the magnetite unit cell. Likewise, the ZnS nanowires discussed here were found to grow along the [0001] direction, the fast growth direction for Wurtzite ZnS. These data suggest that energetically favorable growth in certain directions relative to others, as described by

the classical VLS mechanism, is the probable reason for 1D growth in the systems of interest here.

7) Conditions allowing some transverse growth may occur, increasing the wire diameter beyond that of the catalyst droplet.

Both triangular-shaped and perfectly cylindrical 1D nanostructure morphologies have been observed in similar chemical systems. Transverse growth most likely depends on the interplay between differences in surface energy of the side facets and that of the growing interface. Temperature also plays a key role in allowing mobility of the moving species to reach lowest energy configurations. One study of growth of InAs with Au catalyst shows wires forming highly tapered morphologies at low temperatures and becoming increasingly rod-like as temperature is increased. These results imply transverse growth due to species movement up the sides of the growing nanowire. As temperature is decreased, the atomic mobility decreases, causing a more pyramid-like morphology as species accumulate further from the nanowire tip. As temperatures increase, more atoms are able to move up the nanowire and attach closer to the interface. In this study, all wires exhibited an untapered top region which authors attribute to the supersaturation gradient along the wire, with the particle acting as a material sink. [177] Surface effects are also possible.

Some theoretical evaluations of the VLS process find a critical radius at certain catalyst saturation such that the nanowire grows thicker or thinner to than its initial diameter until the critical value is achieved. [217] However, results found in this work indicate that nanowires of varying thickness can grow very long while maintaining a very

uniform diameter. More commonly, as long as catalyst droplets are present during growth, nanowire sidewalls remain smooth, but once the metal is consumed through migration or poisioning, fast growth terminates and is overcome by direct transverse growth on sidewalls, often dramatically altering nanowire geometry.

The analysis presented in this chapter indicates that the VLS process may be valid for catalyst assisted vapor evaporation nanowire growth in some systems, but needs to be carefully evaluated for proof of bulk transport, especially in multiple component systems. Depending on experimental and chemical specifics, the metal particle may promote growth through surface diffusion in a semi-liquid or even fully solid state. While presence of a metal particle at the end of a grown nanowire does not guarantee growth via VLS, the inability of this mechanism to describe some systems does not necessarily invalidate it for others. These systems should be carefully tested to determine state of the catalyst particle and any changes in the particle lattice due to diffusing species. Understanding the complex nature of this much disputed processes is key to gaining the control over 1D nanostructure formation needed for their application to the next generation of biological and electronic tools.

CHAPTER 6

FUTURE WORK

6.1 Engineering and Testing for *In Vivo* Application

As described previously, much exciting work has been produced by medically and biologically minded researchers with the aid of nanotechnology. For most of these, scientists have utilized nanoparticles as the carriers, heaters, probes, sensors, or markers needed for each application. New accomplishments in areas such as localized cancer treatment, single-molecule pathogen detection, and gene therapy, made possible through use of nanoparticles or quantum dots (QDs) continue to be reported daily.[218-223] However, QDs need not be the only tools available for us to apply to important biomedical problems.[224] Indeed, reviews of the current state of nanoparticle-assisted biomedicine observe several areas in which QDs cannot perform ideally, and often call for much needed improvements in these fields. In cancer thermotherapy treatments, for instance, those based on magnetic Fe_3O_4 quantum dots have been shown highly effective in reduction of tumors in animal models, and to the author's knowledge are currently being tested in clinical trials; still, scientists point to several obstacles to widespread success of this technology in humans, including poor targeting in deep tissue (i.e. >2cm), poor retention of particles after magnetic field removal, and high required dosages.[225] In addition, due to the shape and size of the particles, these QDs are only effective in thermablation of tumors equal to or greater than one square centimeter.[51] It is evident that new and better tools are needed.

Most likely interest in carbon nanotube (CNT) biocompatibility has arisen out of this observed need to investigate other materials, as well as to open doors for new biomedical uses. Recent publications cite work to establish cytotoxicity, blood clearance, solubility, protein binding, and new CNT based architectures for bioprosthetics, to name a few.[226-234] Although some early work found unmodified CNTs highly toxic[230, 235], later studies have found the materials to be well tolerated[231], especially after functionalization with a variety of active biomolecules. CNTs are appealing in that they have been previously well characterized chemically and physically, and they often exhibit interesting electronic and mechanical properties.[234] One of the key advantages of CNTs is that as 1D materials they have an elongated morphology that allows for functionalization of multiple species, and provides an ideal vehicle for directed electron transport. As a further example, theory predicts that by increasing the aspect ratio of Fe_3O_4 nanostructures, magnetization will be significantly enhanced compared to nanoparticles of the same volume.[50] Such improvement could address current limitations of QD based thermotherapy cancer treatments, including improved sensitivity, lower dosages, and fewer side effects from stimulation sources.

Curiously, despite numerous advantages, 1D nanostructures other than CNTs have until now been largely ignored with regard to development of *in vivo* nanoscale therapies and devices. Researchers responsible for the discovery and synthesis of new nanostructure chemistries and morphologies often cite possible biomedical application in their reports, yet few have taken the next steps toward integrating these materials into biological systems. In addition to Fe_3O_4, ZnO 1D nanostructures are also potentially ideal materials for *in vivo* biomedical applications due to their unique piezoelectric and

mechanical properties, coupled with known bio-tolerance of their chemistries.[116] Yet to the author's knowledge there currently exist no publications reporting *in vitro* or *in vivo* biocompatibility testing of nanobelts or nanowires in either of these chemistries. This omission represents a significant lack of vital knowledge in the bio-nano field. The work proposed in this section, and elaborated upon in Appendix A, would address this deficit.

In conceptualizing such research, the scientist should consider the primary requirements devices based on these materials would need to meet. The first applications of magnetic nanorod and nanobelt materials will likely be in simple, injectable devices, designed to localize to and affect specific biological targets. Each concrete goal should be designed to address one major potential obstacle in the implementation of such devices. Additionally, in each test Fe_3O_4 nanostructures should be compared against CNTs and Fe_3O_4 quantum dots. The purpose in this is twofold; one, to help establish a suitably objective baseline by using more well-studied nanomaterials as controls, and two, to take advantage of any found correlations between these and novel nanostructure behavior so that later researchers will be able to utilize studies on Fe_3O_4 QDs or CNTs to indicate expected outcomes in other structures. Tests also should be conducted on both modified and unmodified versions of each nanostructure. Here the aim is likewise to provide baseline controls, but also to take first steps toward not only assessing biocompatibility of 1D nanostructures, but also their improvement.

Some nanowire-based devices may require introduction into the biological system via intravenous injection. However, it is likely that after injection, opsonization will render the particles recognizable to the body's major defense system, the reticulo-

endothelial system, or RES. For devices requiring longer circulation times, uptake into the RES must be prolonged. Sterically stabilizing the nanobelts with hydrophilic polymer chains may resist the opsonization process and allow structures to circulate longer. Coating Fe_3O_4 nanowires and nanorods with polyethylene glycol (PEG) or dextran, two common polymer chemistries used for non-fouling biomedical applications, should help reduce early uptake. Functionalized 1D nanostructures could then be administered *in vivo* to determine if such modifications slow clearance. While in the body, nanodevices must interface with desired tissues and must not cause significant harm to healthy and peripheral cells. Fibroblasts and neuronal cells could be well utilized as model systems to evaluate general toxicity of tested 1D nanomaterials.

In addition to affecting blood clearance, adsorbed proteins may quickly foul a device rendering it nonfunctional. To address this possibility, an adsorption study of streptavidin and fibrinogen on the nanostructured materials could be conducted. Besides being chosen as two common and well-studied fouling proteins, literature reports that these affect CNTs differently, so by choosing these particular proteins, one should achieve a suitable early representation of protein adsorption on each surface.[236-241]

Last is the issue of degradation. Degradation can be considered positive in situations where the device is not desired to remain in the system long term, or after its function is complete. Too efficient degradation can cause failure of the device. An early study may only consider a small part of the degradation picture; however, this information would serve as a crucial first step in determining corrosive effects of biological agents on these nanomaterials.

A detailed proposal regarding how these tests might take place has been drafted. This detail was determined to be outside the scope of body of work contained in this dissertation, but is available in Appendix A.

6.2 Far Future 1D Magnetic Nanostructure Application: BCI

The discipline of brain-device signaling may provide another perhaps more ambitious application of 1D magnetic nanostructures. Brain-computer interface (BCI) technology aims to provide severely physically disabled, yet cognitively intact individuals the ability to communicate and control their environment through interpretation of signals produced in the brain. [242] BCI systems are composed of several integrated components that must work in concert to accomplish the final goal. Basic components include brain-device signaling, retrieval of signal, amplification, interpretation, and finally actuation of the end device. The figure below shows an organizational schematic, illustrating the steps required to convert a basic neural signal to an external device command. [243] As seen in the diagram in Figure 6.1, brain-device signaling is the first and most fundamental step of a BCI system.

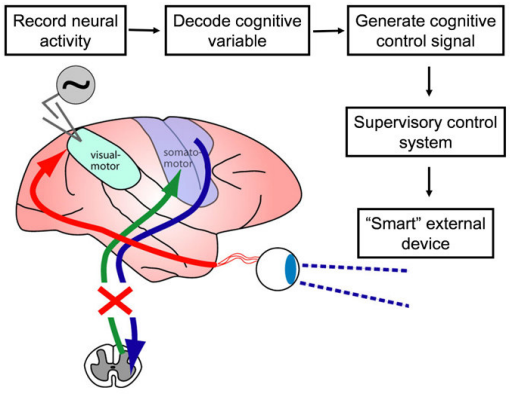

Figure 6.1: Schematic illustrating basic organization of BCI systems [243]

There are currently two basic technologies used to record neural activity in the brain: electroencephalography (EEG) and inserted electrodes. EEG is the method and science of recording and interpreting traces of brain electrical activity as recorded from the skull surface. EEG activity is produced both by random spontaneous activity of the cerebral network and by consistent cortical responses to specific events. These cortical responses are frequently referred to as event related potentials. The amplitude of these potentials is usually smaller than that of the random spontaneous activity, [244] therefore, potentials must be averaged over millions of neurons to separate the target signal from the background noise. [245] To receive the signal, electrodes are commonly placed on the scalp surface after addition of a conductive gel to reduce impedance. This method has the benefit of being painless and non-invasive, eliminating the risk of infection. The electrodes can also be easily replaced or refitted should they malfunction or move. This method has been successfully used to allow patients to move cursors via thought processes.[245, 246]

The problems with EEG information signaling, however, are numerous. Because the signal must be averaged over millions of neurons, resolution is low, and response time often restricts users to a spelling rate of a mere 2-3 letters per minute. Also, many systems require the user to undergo extensive training to learn how to control their signal to produce the desired response. Outside factors such as memory, concentration, attention, and cognitive load have been shown to affect changes in EEG signals. Even the gender and emotional state of the subject have been reported as significant variables in performance of cognitive tasks. Finally, the device itself is vulnerable to sources of outside electromagnetic radiation, making usability in real-world environments a challenge. [247]

The current alternative to EEG recording is to insert electrodes directly into the brain of the patient. At the most basic level, electrodes are passed through skull openings and implanted in specific brain areas near target neurons. Depending on the size and location of the electrode, electrical signals of only one or a few neurons are detected and sent to the waiting receiver. [245] Electrode signaling has several benefits over EEG technologies. Such techniques allow for higher resolution and faster response times. Unlike EEG, response times derived from electrode recording are on the order of normal cortical response and therefore can be more easily used for motor control applications. Less subject training is required since the stimulus-response route is more direct and therefore easier to control. The depreciative effects of outside variables are also reduced for this reason. [248]

Still, electrode recording devices also present several problems for real world application. Surgery is necessarily required, opening up the brain and tissues to possible

infection. It is not uncommon for patients who receive this treatment to experience complications due to surgery.[244] Studies with rats indicate that any device anchored to the skull and in chronic contact with meninges experiences greater tissue reactivity than the same material completely implanted within the brain tissue, providing argument for the use of completely contained devices.[249] Gaining access to the action potentials of individual neurons is a particularly challenging task, because electrode tips require close proximity to the signal source. [250] Implanted electrodes are usually only able to sense consistent signals for a little more than a few months. This sensitivity loss may have several causes, including electrode shift caused by movement of the person or small changes in blood pressure, scar tissue growth on and around the electrode, or necrosis of the emitting neurons. [251]

Due to the complications and limitations of technologies listed above, it is apparent that a brain-computer signaling device incorporating high resolution, speed, and sensitivity while eliminating the necessity for surgery is currently needed. A system based on direct incorporation of magnetic nanowires into specific regions of the brain which act as single-neuron signaling devices may prove ideal. Such a device would eliminate many of the issues inherent to EEG and electrode technologies, and would potentially provide a new route to both understanding and utilizing brain function. Because of the novel nature of such a device, however, several complicating issues must be addressed before a real prototype can be developed. The basic idea would be to introduce nanowires into the bloodstream that would then be directed to specific and localized areas of the brain. There, these materials would form connections with neurons whose electrical activity would produce changes in the materials detectible to an outside

source, converting the brain's own electrical signals into information that could then be used to direct BCI system devices.

Obviously such a scheme is highly complex and requires realization of successive steps including incorporation into the body and brain, localization within the brain, location monitoring and adjustment, neuron interfacing, signaling, reception by an outside device, and low error interpretation. In addition, the device must meet the requirements mentioned previously in regard to current signaling technologies. 1D magnetite nanowires may be well suited to this application for the reasons discussed above in regard to other biomedical applications. It must be shown, however, that these nanowires can pass through the BBB, be successfully incorporated into precise locations in brain tissue, interface with neurons, and successfully respond to neural signals before utilizing such a structure for brain-device signaling can be considered a viable alternative to current methods.

CHAPTER 7

CONCLUSION

While some may still harbor doubts as to the commercial applicability of nanotechnologies, recent trends demonstrate that continued interest in nanomaterials and their unique behaviors is well founded. Still, many of the most exciting potential new applications require that researchers gain greater understanding and control of the nanostructure tools necessary to implement them. The focus of this work was to understand the fundamentals of magnetic and semiconductor nanowire synthesis and properties so that these materials could be realistically applied to exciting new biomedical and electronic applications. Two systems were examined in detail through fabrication and experiment, theoretical calculations and simulations, and investigations into published literature.

Synthesis and properties measurements demonstrated proven routes to create high quality materials as well as provided test systems for understanding basic growth mechanisms. Iron oxide nanowires and nanorods were synthesized through PLD assisted vapor deposition with the aid of a gold particle as catalyst. It was found that PLD is an efficient means to synthesize high quality, aligned iron oxide nanowires, including both hematite and magnetite phases. Epsilon iron oxide, a novel nanowire phase, was also created via this method. The epsilon phase has received little recent attention due to its difficult synthesis in any form despite its interesting properties such as pyroelectricity and very high remnant magnetization. The size of the aligned nanowires can be varied by adjusting reaction parameters and/or metal catalyst particle size. Nanowire growth angle

relative to the substrate is easily tuned by varying the exposed substrate crystallographic plane, with c-plane sapphire producing perpendicular nanowires, a-plane sapphire producing in-plane growth, and off-angle planes producing aligned nanowires at various intermediate angles. Systematic synthesis experiments demonstrated that nanowire growth occurred in a range from 700-950^{o}C and 10^{-2} to 300 mbar, with the best growth occurring around 900^{o}C and 10mbar. These nanostructures exhibit interesting magnetic characteristics, with some remanence at room temperature. The individual magnetic contributions of each phase, however, could not be distinguished, since as grown samples contained multiple phases. Simple flow models found that low aspect ratio nanorods should be able to move through blood vessels as well as or better than spherical particles. These nanowires should provide new and interesting tools, and may be useful for cancer therapy treatments

ZnS/SiO_2 core-shell nanowires were also investigated, both as materials potentially useful in devices, and as an alternate system to gain greater understanding of catalyst assisted growth mechanisms. These wires, containing a highly crystalline ZnS core, and an amorphous silica shell, were synthesized through thermal CVD methods, also employing a gold catalyst particle. SEM characterization showed the wires to be of extraordinary length, up to 1cm, while maintaining nanoscale diameter. Due to their length and aligned growth, these nanowires should be applicable for integration into electronic devices.

The VLS mechanism was then viewed through the lens of these structures, as basic growth processes must be understood for efficient application. Several aspects of the VLS mechanism are currently under debate. Recent research has cast doubt on the

role of the metal “catalyst” particle, specifically the necessity of the liquid state and the traditional model of alloying and bulk diffusion through the particle to create the growing nanowire. For the systems examined here, liquid formation in the gold particle was determined to be possible, but unlikely. Molecular dynamics simulations demonstrated that bulk diffusion of small atomic species into gold raised system energies, with larger diffusing species creating scenarios so excessive that the model could not run to completion. XRD analysis of the gold particle lattice parameters before and after nanowire synthesis showed that lattices did not deviate from bulk values, proving the nanostructures detailed here did not form via bulk diffusion. The VLS mechanism therefore cannot accurately describe growth in these systems. The more likely mechanism was determined to be a VSS-like mechanism in which arriving species are transported around the particle surface. This information casts doubt on the traditional VLS processes as an accurate description of vapor evaporation nanowire growth in other systems, and indicates that careful and conclusive analysis needs to be conducted before bulk diffusion to the growing nanowire interface can be confidently proposed.

Finally, future work and applications based on this research were discussed, including further steps toward integrating inorganic nanowires into biological systems. Both safety and efficacy of these tools need to be established before they can be used to improve currently available technologies. The use of magnetic nanowires and nanowires in brain computer interface devices was also discussed, though much additional work would be required before such a scheme could be realistically applied in human subjects.

APPENDIX A

BASELINE STUDIES OF IRON OXIDE 1D NANOSTRUCTURES FOR CANCER TREATMENTS IN BIOLOGICAL SYSTEMS

Envisioning Tests

Although many researchers propose application of inorganic nanostructures such as nanowires or nanorods of Fe_3O_4 in biological systems, little work has shown the viability of these structures in biological mediums. Of special interest are injectable nanobelt based probes, vehicles, or devices engineered to interface with and affect specific targets. Critical issues to the success of such devices include complex functionality, ability to evade immune defenses, tissue targeting, toxicity, and biodegradability or other means for retrieval. Fortunately, the wealth of recent work on biocompatibility and bio-functionality of carbon nanotubes (CNTs) provides an excellent model to begin studies of other one-dimensional (1D) inorganic nanomaterials. Common obstacles such as non-specific protein binding, cytotoxicity, early uptake into the reticulo-endothelial system (RES) and complex device design have been met with success and continue to be investigated, providing a starting place for promising testing methodologies and surface modifications. Successful early clinical tests of inorganic quantum dots (QD) such as those based on Fe_3O_4 provides encouragement that 1D inorganic nanomaterials may soon be added to the diagnostic and therapeutic toolbox. 1D nanostructures such as nanowires are unique in that their high aspect ratio allows for spatially controlled binding of multiple species, as well as possible enhanced mechanical, electronic, and magnetic properties compared to QDs and CNTs. Research is needed to

test 1D magnetite nanostructures against both of these standards to catch risks, and identify if potential problems are the result of the nanowire chemistry or geometry.

Before these iron oxide 1D nanostructures can be added to the cancer treatment toolbox, much more refinement and study is needed. These will need to be functionalized to evade recognition from the RES system (the gatekeepers of the body) before their job is done, just as quantum dots have been modified for the same purposes. We would need to know how and if this functionalization allows them to be cleared. However, the first task is to make certain that the 1D nature of these devices do not make them any more harmful (relative to their benefits) than earlier QD and CNT technologies.

The objective then should be to investigate cytotoxicity, non-specific protein binding, RES uptake, and degradation Fe_3O_4 nanorods and nanowires, and to identify strategies to improve the performance of devices based on these materials in biological systems. The rationale for this work is that it would establish a baseline of knowledge on biocompatibility of a promising new set of diagnostic and therapeutic tools, and would test strategies for improving basic performance and tolerability of these structures in the body. The central hypothesis then is that studies of CNTs and Fe_3O_4 QDs will provide meaningful models to study the biocompatibility of Fe_3O_4 1D nanostructures, and that the latter may be modified to allow successful insertion and functionality in the body. Single wall CNTs and QDs could be tested in parallel with Fe_3O_4 nanorods and nanowires in all but RES uptake tests to serve as a control and reference for nanobelt performance. Specifically, this hypothesis this work would be based upon attests:

1. Fe_3O_4 nanorods and nanowires will prove nontoxic to cells.

2. RES uptake and non-specific protein binding of Fe_3O_4 1D nanostructures will mimic that previously observed in CNTs and that strategies to reduce these effects in CNTs will likewise prove successful for these other chemistries.
3. Fe_3O_4 1D nanostructures will not quickly degrade in blood or serum.

Possible specific goals for the proposed hypothesis would include:

1. ***Analysis of toxicity effects of unmodified and surface modified Fe_3O_4 nanorods and nanowires on fibroblasts and neuronal cells in vitro as compared to single wall CNTs and Fe_3O_4 QDs***

   Cells would be incubated by administering unmodified nanobelt solution, CNT solution, and Fe_3O_4 QD solution, asbestos fiber solution, or cell culture medium alone to seeded cells in Petri dishes. Live/dead and Trypan Blue exclusion assays could be used to asses cell viability. Tests should be repeated for nanobelts and CNTs with surface modifications designed to reduce RES uptake and nonspecific protein binding. Concentrations of nanobelt and CNT solutions relative to cell density might also be varied to determine possible cytotoxicity thresholds.

2. ***Investigations into non-specific protein binding on Fe_3O_4 nanostructures before and after surface modification in vitro***. Nanorods, nanowires, QDs, and single wall CNTs may be exposed to fibrinogen and streptavidin as model proteins for absorption studies. It has been shown that streptavidin readily absorbs onto CNT surfaces, while fibrinogen is not easily absorbed. Surface modification will include coating the nanobelts, QDs and CNTs with dextran and PEG.

3. ***Investigation of RES uptake and biodistribution of Fe_3O_4 nanostructures before and after surface modification via in vivo and ex vivo testing.*** RES uptake would be measured after intravenous tail injection in murine models. MRI could be used to track magnetic Fe_3O_4 nanobelts. Biodistribution in several organs would ideally be examined after animal sacrifice.
4. ***Investigation of degradation times of Fe_3O_4 1D nanostructures in blood and serum before and after surface modification.*** Nanobelts and nanotubes dispersed on Si substrates may be immersed in blood, serum, DI water, and ethanol, for up to four weeks to determine degradation. Degradation could be determined with SEM, and TEM imaging. DI water and ethanol immersion would act as a control to ensure that the cleaning process does not adversely affect degradation results. Tests should be repeated on surface modified nanostructures.

Fe_3O_4 1D nanostructures could be synthesized via thermal evaporation and pulsed laser deposition (PLD) methods described in the body of this work.[116, 173, 252, 253] All required nanobelt materials should be synthesized prior to biological testing within a span of twelve weeks to help ensure structural consistency. Prior to any modification, nanowire and nanorod samples would be imaged in SEM and TEM, including detailed TEM diffraction analysis to confirm uniform synthesis results. Silicon (100) and alumina substrates would be sterilized and tested for endotoxin via LDL Gel Blot test prior to nanobelt synthesis. All samples should be stored in a desiccator until needed. Nanobelt samples would then be scraped off substrates with a new sterilized razor blade and

dispersed as needed. Highly purified QDs and CNTs can be purchased from one of several commercial suppliers. For consistency and lack of contamination all nanotubes used for these experiments should be highly pure with single walled morphologies. Solutions should be ultrasonicated prior to application to reduce clumping, and measured for pH levels prior to administering the experiments. A portion of nanowire, nanorod, QD, and CNT samples should be separated and tested for endotoxin contamination via the LDL Gel Blot test prior to each experiment.

This work should produce the following outcomes. First, the general cytotoxicity of Fe_3O_4 1D nanostructures of common dimensions for two important cell types would be established, and the results would indicate whether these results are more heavily dependent on the chemical or morphological characteristics of the nanostructure. A critical concentration threshold of Fe_3O_4 nanowires and nanorods below which cytotoxicity is sufficiently low may be determined. Secondly, these experiments should establish the RES uptake of these structures in modified and unmodified forms as compared to published data for CNTs and QDs and possibly identify useful strategies to allow longer circulation times. The studies on non-specific protein binding should elucidate basic information on host responses to these materials, and identify whether in this respect they are analogous to CNT-host responses. This would provide one test CNTs as a model system for other one-dimensional nanostructures. Surface modification with PEG and Dextran, well-tested biomaterials, is considered a first step toward reducing undesired host responses. Finally, degradation studies would take first steps toward engineering strategies for removal of foreign devices based on these materials from the human body.

The proposed work would provide a body of knowledge on biocompatibility of Fe_3O_4 1D nanostructures where currently very little information exists. This information is critical in developing the next generation of diagnostic and therapeutic devices based on our newest and best materials technologies, enabling the possibility of improved sensitivity, faster response times, lower required dosages, and novel functionalities in diagnosis and treatment of disease.

Research Design Rationale

This research is designed to provide preliminary information regarding biological response to Fe_3O_4 1D nanostructures with the expectation that future devices based on these materials may be successfully integrated into the human body. Successful operation of devices based on these materials will critically depend on many issues, among them the requirements to cause minimal harm to healthy tissues, to work properly for the desired time, to localize and remain in desired locations, and possibly to be removed once the function is complete. This proposed work aims to address one critical component of each of these issues, keeping in mind that this work should provide a baseline for further studies. Fibroblasts are chosen for their role in the formation of tissues which such devices may contact as well as their popularity in biomaterials research. The wealth of information regarding fibroblast response to various biomaterials should provide a strong basis for evaluating nanobelt performance. Neuronal cells are chosen due to the exciting potential for use of nanobelt devices in the brain and other neuronal tissues. In addition, several studies show data in which CNT-based surfaces have no or positive impact on neuronal growth. Non-specific protein absorption of two common proteins, RES uptake

and biodistribution in murine models, and device degradation in common biological fluids provide obvious indicators of success in each of the last three listed criteria respectively.

Due to the lack of previous reports regarding biological response to Fe_3O_4 nanowires and nanorods, better-evaluated materials like CNTs and Fe_3O_4 QDs could provide convenient analogues; however, the validity of such comparisons is currently unknown. Two fundamental characteristics of the materials under investigation are chemistry and morphology. Although successful clinical implementation of Fe_3O_4 QDs has shown this chemistry to be compatible with some biological tissues, the morphological consequences of these nanobelts must be critically examined, especially in light of known deleterious effects of other high aspect ratio materials such as asbestos fibers and some reports on CNTs. In addition to collecting basic information on the behavior of critical nanomaterials relevant to device integration, and possible methods to modify these, conducting parallel experiments on CNTs and Fe_3O_4 QDs is intended to probe the usefulness of these materials as chemical and morphological analogues and provide comparative controls for data evaluation.

In this proposed future research, biocompatibility of Fe_3O_4 nanorods and nanowires is investigated as measured by cytotoxicity, protein absorption, RES uptake, and degradation. This work would provide a small subset of information in each of these categories: post exposure viability of two cell types, adsorption of two common proteins, clearance in murine models, and extent of degradation in bodily fluids. The proposed work is meant to provide a base of information where currently none exists, and to enable future researchers to work to increase this knowledge with the aim of engineering new

tools and devices for improved nanomaterial-based diagnosis and therapy. Its significance cannot be underestimated, as research like this will be critical in developing the next generation biomedical tools.

Ultimate Goals: Introducing Magnetite Nanowires into Human Trials.

When transferring from mice to human models for treatment testing, there are two important issues a researcher must consider; these are 1) the inherent biological differences between the two models that may affect the success of the treatment, and 2) the increased need to ensure safety of the individual. Common safety concerns in administering new agents to patients are the often unknown chronic and long term effects. Unfortunately, little is known about the mechanism of metabolism or clearance of QD probes injected into living animals. A systematic study on the clearance pathways of these probes in mice and others, and observations on their degree of degradation post-elimination, would be a next step on the path toward human studies. Longer term toxicity studies of these particles would also be useful to help ensure patient safety. Often, patients chosen for initial clinical trials are those most in need of new treatments. Research showing effective location *and* treatment of cancer cells, and of numerous cancer types, in animal models should add significant evidence that these devices should move quickly toward use in human patients.

REFERENCES

[1] "Wikipedia."

[2] J. W. Jeff Morris, "EPA Nanotechnology Whitepaper," February 2007.

[3] A. D. Yoffe, "Low-Dimensional Systems - Quantum-Size Effects and Electronic-Properties of Semiconductor Microcrystallites (Zero-Dimensional Systems) and Some Quasi-2-Dimensional Systems," *Advances in Physics,* vol. 42, pp. 173-266, Mar-Apr 1993.

[4] L. E. Brus, "Electron Electron and Electron-Hole Interactions in Small Semiconductor Crystallites - the Size Dependence of the Lowest Excited Electronic State," *Journal of Chemical Physics,* vol. 80, pp. 4403-4409, 1984.

[5] A. P. Alivisatos, "Semiconductor clusters, nanocrystals, and quantum dots," *Science,* vol. 271, pp. 933-937, Feb 16 1996.

[6] S. Iijima, "Helical Microtubules of Graphitic Carbon," *Nature,* vol. 354, pp. 56-58, Nov 7 1991.

[7] P. C. Tsai, Y. R. Jeng, and T. H. Fang, "Coalescence, melting, and mechanical characteristics of carbon nanotube junctions," *Physical Review B,* vol. 74, pp. -, Jul 2006.

[8] D. K. Ferry, "Materials science - Nanowires in nanoelectronics," *Science,* vol. 319, pp. 579-580, Feb 1 2008.

[9] "The Project on Emerging Nanotechnologies."

[10] A. Shalleck, "Nanotech industry approaches massive growth phase," *Small Times Media,* 2004.

[11] X. D. Wang, J. H. Song, J. Liu, and Z. L. Wang, "Direct-current nanogenerator driven by ultrasonic waves," *Science,* vol. 316, pp. 102-105, Apr 6 2007.

[12] K. B. Lee, "Urine-activated paper batteries for biosystems," *Journal of Micromechanics and Microengineering,* vol. 15, pp. S210-S214, Sep 2005.

[13] P. Ball, "Nanowire sensors pass drugs test," *Nature Nanozone News,* 2005.

[14] R. J. Mannix, S. Kumar, F. Cassiola, M. Montoya-Zavala, E. Feinstein, M. Prentiss, and D. E. Ingber, "Nanomagnetic actuation of receptor-mediated signal transduction," *Nature Nanotechnology,* vol. 3, pp. 36-40, Jan 2008.

[15] K. Bullis, "Nanotechnology - Nanowires in the brain," *Technology Review,* vol. 109, pp. 16-16, Jul-Aug 2006.

[16] R. R. Llinas, K. D. Walton, M. Nakao, I. Hunter, and P. A. Anquetil, "Neuro-vascular central nervous recording/stimulating system: Using nanotechnology probes," *Journal of Nanoparticle Research,* vol. 7, pp. 111-127, Jun 2005.

[17] H. S. Sharma, S. F. Ali, W. Dong, Z. R. Tian, R. Patnaik, S. Patnaik, A. Sharma, A. Boman, P. Lek, E. Seifert, and T. Lundstedt, "Drug delivery to the spinal cord tagged with nanowire enhances neuroprotective efficacy and functional recovery following trauma to the rat spinal cord," *Neuroprotective Agents: Eighth International Neuroprotection Society Meeting,* vol. 1122, pp. 197-218, 2007.

[18] J. R. H. Foran, S. Steinman, I. Barash, H. G. Chambers, and R. L. Lieber, "Structural and mechanical alterations in spastic skeletal muscle," *Developmental Medicine and Child Neurology,* vol. 47, pp. 713-717, Oct 2005.

[19] R. L. Lieber, S. Steinman, I. A. Barash, and H. Chambers, "Structural and functional changes in spastic skeletal muscle," *Muscle & Nerve,* vol. 29, pp. 615-627, May 2004.

[20] F. Patolsky, B. P. Timko, G. H. Yu, Y. Fang, A. B. Greytak, G. F. Zheng, and C. M. Lieber, "Detection, stimulation, and inhibition of neuronal signals with high-density nanowire transistor arrays," *Science,* vol. 313, pp. 1100-1104, Aug 25 2006.

[21] F. Patolsky, B. P. Timko, G. F. Zheng, and C. M. Lieber, "Nanowire-based nanoelectronic devices in the life sciences," *Mrs Bulletin,* vol. 32, pp. 142-149, Feb 2007.

[22] *Forbes/Wolfe Nanotech Report.*

[23] V. I. Klimov, A. A. Mikhailovsky, S. Xu, A. Malko, J. A. Hollingsworth, C. A. Leatherdale, H. J. Eisler, and M. G. Bawendi, "Optical gain and stimulated emission in nanocrystal quantum dots," *Science,* vol. 290, pp. 314-317, Oct 13 2000.

[24] V. S. Trubetskoy, "Polymeric micelles as carriers of diagnostic agents," *Advanced Drug Delivery Reviews,* vol. 37, pp. 81-88, May 4 1999.

[25] D. L. Klein, R. Roth, A. K. L. Lim, A. P. Alivisatos, and P. L. McEuen, "A single-electron transistor made from a cadmium selenide nanocrystal," *Nature,* vol. 389, pp. 699-701, Oct 16 1997.

[26] P. Y. Yiying Wu, "Direct Observation of Vapor-Liquid-Solid Nanowire Growth," *Journal of the American Chemical Society,* vol. 123, pp. 3165-3166, December 20, 2000 2000.

[27] C. M. Lieber, "Nanoscale Science and Technology: Building a Big Future from Small Things," *MRS Bulletin,* pp. 486-491, July 2003 2003.

[28] R. S. Wagner, C. J. Doherty, and S. M. Arnold, "Cinephotomicrographic Study of Vls Growth of Silicon Whisker Crystals," *Journal of Metals,* vol. 17, pp. 1031-&, 1965.

[29] C. M. Lieber, "One-dimensional nanostructures: Chemistry, physics & applications," *Solid State Communications,* vol. 107, pp. 607-616, 1998.

[30] A. B. Greytak, L. J. Lauhon, M. S. Gudiksen, and C. M. Lieber, "Growth and transport properties of complementary germanium nanowire field-effect transistors," *Applied Physics Letters,* vol. 84, pp. 4176-4178, May 24 2004.

[31] C. Ma, ""Systematic investigation on the growth of one-dimensional wurtzite nanostructures,"" *Ph.D. Atlanta: Georgia Institute of Technology,* 2005.

[32] Z. W. P. Zu Rong Dai, Zhong L. Wang, "Novel Nanostructures of Functional Oxides Synthesized by Thermal Evaporation," *Advanced Functional Materials,* vol. 13, pp. 9-24, 2003.

[33] J. C. Q.A. Pankhurst, S.K. Jones, J. Dobson, "Applications of magnetic nanoparticles in biomedicine," *Journal of Physics D: Applied Physics,* vol. 36, pp. R167-R181, June 18, 2003 2003.

[34] C. Coulon, R. Clerac, W. Wernsdorfer, T. Colin, A. Saitoh, N. Motokawa, and H. Miyasaka, "Effect of an applied magnetic field on the relaxation time of single-chain magnets," *Physical Review B,* vol. 76, pp. -, Dec 2007.

[35] L. He, W. Z. Zheng, W. Zhou, H. L. Du, C. P. Chen, and L. Guo, "Size-dependent magnetic properties of nickel nanochains," *Journal of Physics-Condensed Matter,* vol. 19, pp. -, Jan 24 2007.

[36] M. Hernandez-Velez, "Nanowires and 1D arrays fabrication: An overview," *Thin Solid Films,* vol. 495, pp. 51-63, Jan 20 2006.

[37] H. Katayama-Yoshida, K. Sato, T. Fukushima, M. Toyoda, H. Kizaki, V. A. Dinh, and P. H. Dederichs, "Computational nano-materials design for high-T-C ferromagnetism in wide-gap magnetic semiconductors," *Journal of Magnetism and Magnetic Materials,* vol. 310, pp. 2070-2077, Mar 2007.

[38] S. O. Kasap, "Electronic Materials and Devices," pp. 598-663, 2002.

[39] A. J. E. Joel S. Miller, "Molecule-Based Magnets - An Overview," *MRS Bulletin,* pp. 21-28, November 2000 2000.

[40] G. Group, "Magnetism," *DISCovering Science,* 1996.

[41] J. Dobson, "Magnetism in Matter and Magnetic Biomaterials," 2000.

[42] H. Coetzee, "Biomagnetism and Bioelectromagnetism: The Foundation of Life," *The Academy for Future Science*.

[43] S. W. Marcelo Blatt, Eytan Domany, "Data Clustering Using a Model Granular Magnet," *Neural Computation,* vol. 9, pp. 1805-1842, 1997 1997.

[44] L. P. I. Bakonyi, V. Weihnacht, J. Toth, L. F. Kiss, C. M. Schneider, "Giant Magnetoresistance in Electrodeposited Multilayer Films. The Influence of Superparamagnetic Regions," *Journal of Optoelectronics and Advanced Materials,* vol. 7, pp. 589-598, April 2005 2005.

[45] D. E. L. M. E. McHenry, "Nano-scale materials development for future magnetic applications," *Acta Materialia,* vol. 48, pp. 223-238, July 15, 1999 1999.

[46] H. Z. Shouheng Sun, "Size-controlled synthesis of magnetite nanoparticles," *Journal of the American Chemical Society,* vol. 124, pp. 8204-8205, April 11, 2002 2002.

[47] S. Yamaguchi, "Determination of the easy magnetization direction of a ferrite by reflection electron diffraction," *British Journal of Applied Physics,* vol. 1, pp. 369-370, October 10, 1967 1968.

[48] G. F. Goya, T. S. Berquo, F. C. Fonseca, and M. P. Morales, "Static and dynamic magnetic properties of spherical magnetite nanoparticles," *Journal of Applied Physics,* vol. 94, pp. 3520-3528, Sep 1 2003.

[49] D. Z. Zuqin Liu, Song Han, Chao Li, Bo Lei, Weigang Lu, Jiye Fang, Chongwu Zhou, "Single Crystalline Magnetite Nanorods," *Journal of the American Chemical Society,* vol. 127, pp. 6-7, September 10 2004 2004.

[50] Q. A. Pankhurst, J. Connolly, S. K. Jones, and J. Dobson, "Applications of magnetic nanoparticles in biomedicine," *Journal of Physics D-Applied Physics,* vol. 36, pp. R167-R181, Jul 7 2003.

[51] C. C. Berry and A. S. G. Curtis, "Functionalisation of magnetic nanoparticles for applications in biomedicine," *Journal of Physics D-Applied Physics,* vol. 36, pp. R198-R206, Jul 7 2003.

[52] B. Fang, G. F. Wang, W. Z. Zhang, M. G. Li, and X. W. Kan, "Fabrication of Fe3O4 nanoparticles modified electrode and its application for voltammetric sensing of dopamine," *Electroanalysis,* vol. 17, pp. 744-748, May 2005.

[53] L. M. Rossi, A. D. Quach, and Z. Rosenzweig, "Glucose oxidase-magnetite nanoparticle bioconjugate for glucose sensing," *Analytical and Bioanalytical Chemistry,* vol. 380, pp. 606-613, Oct 2004.

[54] N. Morishita, H. Nakagami, R. Morishita, S. Takeda, F. Mishima, B. Terazono, S. Nishijima, Y. Kaneda, and N. Tanaka, "Magnetic nanoparticles with surface

modification enhanced gene delivery of HVJ-E vector," *Biochemical and Biophysical Research Communications,* vol. 334, pp. 1121-1126, Sep 9 2005.

[55] M. Shinkai, M. Yanase, M. Suzuki, H. Honda, T. Wakabayashi, J. Yoshida, and T. Kobayashi, "Intracellular hyperthermia for cancer using magnetite cationic liposomes," *Journal of Magnetism and Magnetic Materials,* vol. 194, pp. 176-184, Apr 1999.

[56] N. Nitin, L. E. W. LaConte, O. Zurkiya, X. Hu, and G. Bao, "Functionalization and peptide-based delivery of magnetic nanoparticles as an intracellular MRI contrast agent," *Journal of Biological Inorganic Chemistry,* vol. 9, pp. 706-712, Sep 2004.

[57] R. Weissleder, G. Elizondo, J. Wittenberg, C. A. Rabito, H. H. Bengele, and L. Josephson, "Ultrasmall Superparamagnetic Iron-Oxide - Characterization of a New Class of Contrast Agents for Mr Imaging," *Radiology,* vol. 175, pp. 489-493, May 1990.

[58] T. Ohmori, H. Takahashi, H. Mametsuka, and E. Suzuki, "Photocatalytic oxygen evolution on alpha-Fe2O3 films using Fe3+ ion as a sacrificial oxidizing agent," *Physical Chemistry Chemical Physics,* vol. 2, pp. 3519-3522, 2000.

[59] T. Fried, G. Shemer, and G. Markovich, "Ordered two-dimensional arrays of ferrite nanoparticles," *Advanced Materials,* vol. 13, pp. 1158-+, Aug 3 2001.

[60] S. P. Gubin, Y. I. Spichkin, G. Y. Yurkov, and A. M. Tishin, "Nanomaterial for high-density magnetic data storage," *Russian Journal of Inorganic Chemistry,* vol. 47, pp. S32-S67, 2002.

[61] R. S. Chen, E. K. N. Yung, F. Ji, and W. B. Dou, "Development of the microstrip circulator with a magnetized ferrite sphere in millimeter waveband," *International Journal of Infrared and Millimeter Waves,* vol. 24, pp. 813-828, May 2003.

[62] J. Jin, K. Hashimoto, and S. Ohkoshi, "Formation of spherical and rod-shaped epsilon-Fe2O3 nanocrystals with a large coercive field," *Journal of Materials Chemistry,* vol. 15, pp. 1067-1071, 2005.

[63] S. Ohkoshi, S. Sakurai, J. Jin, and K. Hashimoto, "The addition effects of alkaline earth ions in the chemical synthesis of epsilon-Fe2O3 nanocrystals that exhibit a huge coercive field," *Journal of Applied Physics,* vol. 97, pp. -, May 15 2005.

[64] M. Gich, A. Roig, C. Frontera, E. Molins, J. Sort, M. Popovici, G. Chouteau, D. M. Y. Marero, and J. Nogues, "Large coercivity and low-temperature magnetic reorientation in epsilon-Fe2O3 nanoparticles," *Journal of Applied Physics,* vol. 98, pp. -, Aug 15 2005.

[65] E. Tronc, C. Chaneac, and J. P. Jolivet, "Structural and magnetic characterization of epsilon-Fe2O3," *Journal of Solid State Chemistry,* vol. 139, pp. 93-104, Aug 1998.

[66] M. Gich, C. Frontera, A. Roig, J. Fontcuberta, E. Molins, N. Bellido, C. Simon, and C. Fleta, "Magnetoelectric coupling in epsilon-Fe2O3 nanoparticles," *Nanotechnology,* vol. 17, pp. 687-691, Feb 14 2006.

[67] C. C. Berry, "Possible exploitation of magnetic nanoparticle-cell interaction for biomedical applications," *Journal of Materials Chemistry,* vol. 15, pp. 543-547, 2005.

[68] I. Hilger, W. Andra, R. Hergt, R. Hiergeist, and W. A. Kaiser, "Magnetic thermotherapy of breast tumors: An experimental therapeutic approach," *Rofo-Fortschritte Auf Dem Gebiet Der Rontgenstrahlen Und Der Bildgebenden Verfahren,* vol. 177, pp. 507-515, Apr 2005.

[69] Y. Y. Xu, X. F. Rui, Y. Y. Fu, and H. Zhang, "Magnetic properties of alpha-Fe2O3 nanowires," *Chemical Physics Letters,* vol. 410, pp. 36-38, Jul 10 2005.

[70] D. S. Xue, L. Y. Zhang, C. X. Gao, X. F. Xu, and A. B. Gui, "Synthesis, Mossbauer Spectra and Magnetic Properties of Quasi-One-Dimensional Fe3O4 Nanowires," *Chinese Physics Letters,* vol. 21, pp. 733-736, December 4 2003 2003.

[71] M. A. C. Terrier, C. Arm, S. Serrano-Guisan, L. Gravier, J.-Ph. Ansernet, "Fe3O4 nanowires synthesized by electroprecipitation in templates," *Journal of Applied Physics,* vol. 98, pp. 086102-1 - 086102-3, September 2005 2005.

[72] J. Wang, Z. Peng, Y. Huang, and Q. Chen, "Growth of magnetite nanorods along its easy-magnetization axis of [110]," *Journal of Crystal Growth,* vol. 263, pp. 616-619, November 28 2003 2003.

[73] P. Gould, "Nanoparticles probe biosystems," *Materialstoday,* February 2004 2004.

[74] T. O. Paine, L. I. Mendelsohn, and F. E. Luborsky, "Effect of Shape Anisotropy on the Coercive Force of Elongated Single-Magnetic-Domain Iron Particles," *Physical Review,* vol. 100, pp. 1055-1059, 1955.

[75] S. K. Young-Yeal Song, Carl E. Patton, "Optimized pulsed laser deposited barium ferrite thin films with narrow ferromagnetic resonance linewidths," *Journal of Applied Physics,* vol. 94, pp. 5103-5110, October 15, 2003 2003.

[76] K. V. P. M. Shafi, I. Felner, Y. Mastai, and A. Gedanken, "Olympic ring formation from newly prepared barium hexaferrite nanoparticle suspension," *Journal of Physical Chemistry B,* vol. 103, pp. 3358-3360, Apr 29 1999.

[77] F. T. P. D. T. Margulies, F. E. Spada, R. S. Goldman, J. Li, R. Sinclair, A. E. Berkowitz, "Anomalous moment and anisotropy behavior in Fe3O4 films," *Physical Review B,* vol. 53, pp. 9175-9187, April 1 1996 1996.

[78] S. G. J. B. Moussy, A. Bataille, M. J. Guittet, M. Gautier-Soyer, F. Felille, B. Dieny, F. Ott, T. D. Doan, P. Warin, P, Bayle-Guillemaud, C. Gatel, E. Snoeck, "Thickness dependence of anomalous magnetic behavior in epitaxial Fe3O4 (111) thin films: Effect of density of antiphase bounaries," *Physical Review B,* vol. 70, pp. 174448-174457, 2004.

[79] A. H. M. Koichi Haneda, "Magnetic Properties of BaFe12O19 Small Particles," *IEEE Transactions on Magnetics,* vol. 25, pp. 2597-2601, January 9, 1989 1989.

[80] H. C. Y. Wanquan Jiang, S. Y. Yang, H. E. Horng, J. C. Hung, Y. C. Chen, Chen-Yih Hong, "Preparation and properties of superparamagnetic nanoparticles with narrow size distribution and biocompatible," *Journa of Magnetism, and Magnetic Materials,* vol. 283, pp. 210-214, May 17 2004 2004.

[81] P. Gould, "Nanopartilces probe biosystems," *Materialstoday,* February 2004 2004.

[82] N. S. G. R. N. Panda, G. Balaji, "Magnetic properties of single domain Fe3O4 particles," *Journal of Alloys and Compounds,* vol. 326, pp. 50-53, December 20 2000 2000.

[83] V. R. P. Deepa Thapa, M. B. Kurup, S. K. Malik, "Properties of magnetite nanoparticles synthesized through a novel chemical route," *Condensed Matter e-prints,* 2004.

[84] R. H. I. Hilger, W.A. Kaiser, "Use of magnetic nanoparticle heating in the treatment of breast cancer," *IEE Proceedings - Nanobiotechnology,* vol. 152, pp. 33-39, February 2005 2005.

[85] D. Szabo, H. Keyzer, H. E. Kaiser, and J. Molnar, "Reversal of multidrug resistance of tumor cells," *Anticancer Research,* vol. 20, pp. 4261-4274, Nov-Dec 2000.

[86] G. Barnett, A. M. Jakobsen, M. Tas, K. Rice, J. Carmichael, and J. C. Murray, "Prostate adenocarcinoma cells release the novel proinflammatory polypeptide EMAP-II in response to stress," *Cancer Research,* vol. 60, pp. 2850-2857, Jun 1 2000.

[87] C. J. Bakkenist, J. Koreth, C. S. M. Williams, N. C. A. Hunt, and J. O. McGee, "Heat Shock Cognate 70 mutations in sporadic breast carcinoma," *Cancer Research,* vol. 59, pp. 4219-4221, Sep 1 1999.

[88] A. S. G. C. Catherine C. Berry, "Functionalization of magnetic nanopartices for applications in biomedicine," *Journal of Physics D: Applied Physics,* vol. 36, pp. R198-R206, June 18 2003 2003.

[89] I. H. El-Sayed, X. H. Huang, and M. A. El-Sayed, "Surface plasmon resonance scattering and absorption of anti-EGFR antibody conjugated gold nanoparticles in cancer diagnostics: Applications in oral cancer," *Nano Letters,* vol. 5, pp. 829-834, May 2005.

[90] I. H. El-Sayed, X. H. Huang, and M. A. El-Sayed, "Selective laser photo-thermal therapy of epithelial carcinoma using anti-EGFR antibody conjugated gold nanoparticles," *Cancer Letters,* vol. 239, pp. 129-135, Jul 28 2006.

[91] C. Stuart, "Treatment could remove toxins in blood before damage occurs," *Smalltimes: big news in small tech,* 2004.

[92] G. Fasol, "Nanowires: Small is Beautiful," *Science Magzine,* vol. 280, pp. 545-546, April 24 1998 1998.

[93] X. L. Lei Fu, Yi Zhang, Vinayak P. Dravid, Chad A. Mirkin, "Nanopatterning of "Hard" Magnetic Nanostructures via Dip-Pen Nanolithography and a Sol-Based Ink," *Nano Letters,* vol. 3, pp. 757-760, April 8, 2003 2003.

[94] J. W. Shan Che, Qianwang Chen, "Soft magnetic nanoparticles of BaFe12O19 fabricated under mild conditions," *Journal of Physics: Condensed Matter,* vol. 15, pp. L335-L339, May 23 2003 2003.

[95] C. H. L. Cheng Tzu Kuo, An Ya Lo, "Feasibility studies of magnetic particle-embedded carbon nanotubes for perpendicular recording media," *Diamond and related materials,* vol. 12, pp. 799-805, 2003.

[96] Z. J. Z. Qing Song, "Shape Control and Associated Magnetic Properties of Spinel Cobalt Ferrite Nanocrystals," *Journal of the American Chemical Society,* vol. 126, pp. 6164-6168, January 5, 2004 2004.

[97] D. F. G. A. A. Eliseev, D. D. Zaitsev, A. V. Lukashin, A. V. Knotko, Yu. D. Tretyakov, P. Gornert, "Preparation of strontium hexaferrite nanowires in the mesoporous silica matrix (MCM-41)," *Journal of Magnetism and Magnetic Materials,* vol. 290-291, pp. 106-109, December 8 2004 2004.

[98] D. S. X. L. Y. Zhang, A. B. Gui, C. X. Gai, "The fabrication and magnetic properties of nanowire-like iron oxide," *Journal of Physics: Condensed Matter,* vol. 16, pp. 4541-4548, June 11 2004 2004.

[99] Z. L.-Y. Xue De-Sheng, Gao Cun-Xu, Xu Xue-Fei, Gui An-Biao, "Synthesis, Mossbauer Spectra and Magnetic Properties of Quasi-One-Dimensional Fe3O4 Nanowires," *Chinese Physics Letters,* vol. 21, pp. 733-736, December 4 2003 2003.

[100] Y. L. Hou, J. F. Yu, and S. Gao, "Solvothermal reduction synthesis and characterization of superparamagnetic magnetite nanoparticles," *Journal of Materials Chemistry,* vol. 13, pp. 1983-1987, 2003.

[101] R. V. Kumar, Yu Koltypin et al, "Fabrication of magnetite nanorods by ultrasound irradiation," *Journal of Applied Physics,* vol. 89, pp. 6324-6328, 2001.

[102] C. M. 3.2, "Model Library," 2005.

[103] Y. Peng, H. L. Zhang, S. L. Pan, and H. L. Li, "Magnetic properties and magnetization reversal of alpha-Fe nanowires deposited in alumina film," *Journal of Applied Physics,* vol. 87, pp. 7405-7408, May 15 2000.

[104] M. Ferrari, "Cancer nanotechnology: Opportunities and challenges," *Nature Reviews Cancer,* vol. 5, pp. 161-171, Mar 2005.

[105] L. J. Goldstein and E. B. Rypins, "Blood-Vessel Modeling," *International Journal of Bio-Medical Computing,* vol. 29, pp. 23-29, Oct 1991.

[106] F. Kajiya, S. Matsuoka, Y. Ogasawara, O. Hiramatsu, S. Kanazawa, Y. Wada, S. Tadaoka, K. Tsujioka, T. Fujiwara, and M. Zamir, "Velocity Profiles and Phasic Flow Patterns in the Non-Stenotic Human Left Anterior Descending Coronary-Artery during Cardiac-Surgery," *Cardiovascular Research,* vol. 27, pp. 845-850, May 1993.

[107] R. Mittal, S. P. Simmons, and F. Najjar, "Numerical study of pulsatile flow in a constricted channel," *Journal of Fluid Mechanics,* vol. 485, pp. 337-378, Jun 25 2003.

[108] H. S. Lew and Y. C. Fung, "Plug Effect of Erythrocytes in Capillary Blood Vessels," *Biophysical Journal,* vol. 10, pp. 80-&, 1970.

[109] Z. L. Daihua Zhang, Song Han, Chao Li, Bo Lei, Michael P. Stewart, James M. Tour, Chongwu Zhou, "Magnetite (Fe3O4) Core-Shell Nanowires: Synthesis and Magnetoresistance," *Nano Letters,* vol. 4, pp. 2151-2155, October 1, 2004 2005.

[110] X. G. Wen, S. H. Wang, Y. Ding, Z. L. Wang, and S. H. Yang, "Controlled growth of large-area, uniform, vertically aligned arrays of alpha-Fe2O3 nanobelts and nanowires," *Journal of Physical Chemistry B,* vol. 109, pp. 215-220, Jan 13 2005.

[111] D. Zhang, L. Zuquin, S. Han, C. Li, B. Lei, M. Stewart, J. Tour, and C. Zhou, "Magnetite (Fe3O4) Core-Shell Nanowires: Synthesis and Magnetoresistance," *Nano Letters,* vol. 4, pp. 2151-2155, October 1, 2004 2005.

[112] Z. M. Liao, Y. D. Li, J. Xu, J. M. Zhang, K. Xia, and D. P. Yu, "Spin-Filter Effect in Magnetite Nanowire," *Nano Letters,* vol. 6, pp. 1087-1091, 2006.

[113] K. Kelm and W. Mader, "Synthesis and structural analysis of epsilon-Fe2O3," *Zeitschrift Fur Anorganische Und Allgemeine Chemie,* vol. 631, pp. 2383-2389, 2005.

[114] H. X. J.B. Yang, S. X. You, X. D. Zhou, C. S. Wang, W. B. Yelon, W. J. James, "Large scale growth and magnetic properties of Fe and Fe3O4 nanowires," *Journal of Applied Physics,* vol. 99, pp. 08Q507-1 - 08Q507-3, 2006.

[115] P. X. Gao and Z. L. Wang, "Mesoporous polyhedral cages and shells formed by textured self-assembly of ZnO nanocrystals," *Journal of the American Chemical Society,* vol. 125, pp. 11299-11305, Sep 17 2003.

[116] Z. L. Wang, "Zinc oxide nanostructures: growth, properties and applications," *Journal of Physics-Condensed Matter,* vol. 16, pp. R829-R858, Jun 30 2004.

[117] D. F. Moore, Y. Ding, and Z. L. Wang, "Crystal orientation-ordered ZnS nanowire bundles," *Journal of the American Chemical Society,* vol. 126, pp. 14372-14373, Nov 10 2004.

[118] Y. Ding, X. D. Wang, and Z. L. Wang, "Phase controlled synthesis of ZnS nanobelts: zinc blende vs wurtzite," *Chemical Physics Letters,* vol. 398, pp. 32-36, Nov 1 2004.

[119] C. Ma and Z. L. Wang, "Road map for the controlled synthesis of CdSe nanowires, nanobelts, and nanosaws - A step towards nanomanufacturing," *Advanced Materials,* vol. 17, pp. 2635-2639, Nov 4 2005.

[120] C. Ma, Y. Ding, D. Moore, X. D. Wang, and Z. L. Wang, "Single-crystal CdSe nanosaws," *Journal of the American Chemical Society,* vol. 126, pp. 708-709, Jan 28 2004.

[121] Z. Liu, D. Zhang, S. Han, B. Li, C. Lei, W. Lu, J. Fang, and C. Zhou, "Single Crystalline Magnetite Nanorods," *Journal of the American Chemical Society,* vol. 127, pp. 6-7, September 10 2004 2004.

[122] A. Reilly, C. Allmond, S. Watson, J. Gammon, and J. G. Kim, "Pulsed laser deposition with a high average power free electron laser: Benefits of subpicosecond pulses with high repetition rate," *Journal of Applied Physics,* vol. 93, pp. 3098-3101, Mar 1 2003.

[123] F. Bodker, M. F. Hansen, C. B. Koch, K. Lefmann, and S. Morup, "Magnetic properties of hematite nanoparticles," *Physical Review B,* vol. 61, pp. 6826-6838, Mar 1 2000.

[124] Y. Ding, J. R. Morber, R. L. Snyder, and Z. L. Wang, "Nanowire structural evolution from Fe3O4 to epsilon-Fe2O3," *Advanced Functional Materials,* vol. 17, pp. 1172-1178, May 7 2007.

[125] L. A. Bursill and R. L. Withers, "Twinning Dislocations in Hematite Iron-Ore," *Philosophical Magazine a-Physics of Condensed Matter Structure Defects and Mechanical Properties,* vol. 40, pp. 213-232, 1979.

[126] L. A. Bursill and R. L. Withers, "Multiple Orientation Relationships between Hematite and Magnetite," *Journal of Applied Crystallography,* vol. 12, pp. 279-286, 1979.

[127] G. A. Ferguson and M. Hass, "Magnetic Structure and Vacancy Distribution in Gamma-Fe2o3 by Neutron Diffraction," *Physical Review Letters,* vol. 1, pp. 384-384, 1958.

[128] C. Greaves, "A Powder Neutron-Diffraction Investigation of Vacancy Ordering and Covalence in Gamma-Fe2O3," *Journal of Solid State Chemistry,* vol. 49, pp. 325-333, 1983.

[129] M. Boudeulle, H. Batislandoulsi, C. Leclercq, and P. Vergnon, "Structure of Gamma-Fe2o3 Micro-Crystals - Vacancy Distribution and Superstructure," *Journal of Solid State Chemistry,* vol. 48, pp. 21-32, 1983.

[130] G. G.-G. H. Forestier, *C. R. Acad. Sci. (Paris)* vol. 199, p. 720, 1934.

[131] R. Zboril, M. Mashlan, K. Barcova, and M. Vujtek, "Thermally induced solid-state syntheses of gamma-Fe2O3 nanoparticles and their transformation to alpha-Fe2O3 via epsilon-Fe2O3," *Hyperfine Interactions,* vol. 139, pp. 597-606, 2002.

[132] R. Zboril, M. Mashlan, and D. Petridis, "Iron(III) oxides from thermal processes-synthesis, structural and magnetic properties, Mossbauer spectroscopy characterization, and applications," *Chemistry of Materials,* vol. 14, pp. 969-982, Mar 2002.

[133] R. Zboril, M. Mashlan, D. Petridis, D. Krausova, and P. Pikal, "The role of intermediates in the process of red ferric pigment manufacture from FeSO4 center dot 7H(2)O," *Hyperfine Interactions,* vol. 139, pp. 437-445, 2002.

[134] A. Ito, M. Shinkai, H. Honda, and T. Kobayashi, "Medical application of functionalized magnetic nanoparticles," *Journal of Bioscience and Bioengineering,* vol. 100, pp. 1-11, Jul 2005.

[135] O. Suzuki, S. Miyachi, T. Okamoto, A. Ito, M. Shinkai, H. Honda, T. Kobayashi, M. Negoro, and J. Yoshida, "Local hyperthermia enhances thrombosis in aneurysms containing platinum coils," *Interventional Neuroradiology,* vol. 10, pp. 203-211, Sep 2004.

[136] H. Taguchi, "Recent improvements of ferrite magnets," *Journal De Physique Iv,* vol. 7, pp. 299-302, Mar 1997.

[137] V. Pillai and D. O. Shah, "Synthesis of high-coercivity cobalt ferrite particles using water-in-oil microemulsions," *Journal of Magnetism and Magnetic Materials,* vol. 163, pp. 243-248, Oct 1996.

[138] S. Ohkoshi, T. Nuida, T. Matsuda, H. Tokoro, and K. Hashimoto, "The dielectric constant in a thermal phase transition magnetic material composed of rubidium manganese hexacyanoferrate observed by spectroscopic ellipsometry," *Journal of Materials Chemistry,* vol. 15, pp. 3291-3295, 2005.

[139] S. Sakurai, J. Jin, K. Hashimoto, and S. Ohkoshi, "Reorientation phenomenon in a magnetic phase of epsilon-Fe2O3 nanocrystal," *Journal of the Physical Society of Japan,* vol. 74, pp. 1946-1949, Jul 2005.

[140] M. Popovici, M. Gich, A. Roig, L. Casas, E. Molins, C. Savii, D. Becherescu, J. Sort, S. Surinach, J. S. Munoz, M. D. Baro, and J. Nogues, "Ultraporous single phase iron oxide-silica nanostructured aerogels from ferrous precursors," *Langmuir,* vol. 20, pp. 1425-1429, Feb 17 2004.

[141] J. R. Morber, Y. Ding, M. S. Haluska, Y. Li, P. Liu, Z. L. Wang, and R. L. Snyder, "PLD-assisted VLS growth of aligned ferrite nanorods, nanowires, and nanobelts-synthesis, and properties," *Journal of Physical Chemistry B,* vol. 110, pp. 21672-21679, Nov 2 2006.

[142] J. M. Cowley and A. F. Moodie, "Possibilities for the Direct Observation of Crystal Structures," *Acta Crystallographica,* vol. 10, pp. 752-753, 1957.

[143] J. M. Cowley and A. F. Moodie, "A New Approach to Electron-Diffraction Theory, with Applications to Structure Analysis," *Acta Crystallographica,* vol. 10, pp. 859-859, 1957.

[144] M. E. Fleet, "The Structure of Magnetite," *Acta Crystallographica Section B-Structural Science,* vol. 37, pp. 917-920, 1981.

[145] R. L. Withers and L. A. Bursill, "Higher-Order Structural Relationships between Hematite and Magnetite," *Journal of Applied Crystallography,* vol. 13, pp. 346-353, 1980.

[146] R. S. Wagner, C. J. Doherty, and W. C. Ellis, "Preparation + Morphology of Crystals of Silicon + Germanium Grown by Vapor-Liquid-Solid Mechanism," *Jom-Journal of Metals,* vol. 16, pp. 761-&, 1964.

[147] R. S. Wagner and W. C. Ellis, "Vapor-Liquid-Solid Mechanism of Crystal Growth," *Jom-Journal of Metals,* vol. 16, pp. 761-&, 1964.

[148] R. S. Wagner, W. C. Ellis, S. M. Arnold, and K. A. Jackson, "Study of Filamentary Growth of Silicon Crystals from Vapor," *Journal of Applied Physics,* vol. 35, pp. 2993-&, 1964.

[149] J. H. He, Y. Y. Zhang, J. Liu, D. Moore, G. Bao, and Z. L. Wang, "ZnS/Silica nanocable field effect transistors as biological and chemical nanosensors," *Journal of Physical Chemistry C,* vol. 111, pp. 12152-12156, Aug 23 2007.

[150] R. A. Freitas, "Nanomedicine, Volume IIA: Biocompatibility," 2003.

[151] C. N. King, "Electroluminescent displays," *Journal of Vacuum Science & Technology a-Vacuum Surfaces and Films,* vol. 14, pp. 1729-1735, May-Jun 1996.

[152] R. A. Rosenberg, G. K. Shenoy, F. Heigl, S. T. Lee, P. S. G. Kim, X. T. Zhou, and T. K. Sham, "Effects of in situ vacuum annealing on the surface and luminescent properties of ZnS nanowires," *Applied Physics Letters,* vol. 86, pp. -, Jun 27 2005.

[153] X. J. Xu, G. T. Fei, W. H. Yu, X. W. Wang, L. Chen, and L. D. Zhang, "Preparation and formation mechanism of ZnS semiconductor nanowires made by the electrochemical deposition method," *Nanotechnology,* vol. 17, pp. 426-429, Jan 28 2006.

[154] S. C. Erwin, L. J. Zu, M. I. Haftel, A. L. Efros, T. A. Kennedy, and D. J. Norris, "Doping semiconductor nanocrystals," *Nature,* vol. 436, pp. 91-94, Jul 7 2005.

[155] J. Q. Hu, Y. Bando, Z. W. Liu, J. H. Zhan, D. Golberg, and T. Sekiguchi, "Synthesis of crystalline silicon tubular nanostructures with ZnS nanowires as removable templates," *Angewandte Chemie-International Edition,* vol. 43, pp. 63-66, 2004.

[156] Y. N. Xia, P. D. Yang, Y. G. Sun, Y. Y. Wu, B. Mayers, B. Gates, Y. D. Yin, F. Kim, and Y. Q. Yan, "One-dimensional nanostructures: Synthesis, characterization, and applications," *Advanced Materials,* vol. 15, pp. 353-389, Mar 4 2003.

[157] X. S. Fang, C. H. Ye, L. D. Zhang, Y. H. Wang, and Y. C. Wu, "Temperature-controlled catalytic growth of ZnS nanostructures by the evaporation of ZnS nanopowders," *Advanced Functional Materials,* vol. 15, pp. 63-68, Jan 2005.

[158] X. S. Fang and L. D. Zhang, "One-dimensional (1D) ZnS nanomaterials and nanostructures," *Journal of Materials Science & Technology,* vol. 22, pp. 721-+, Nov 2006.

[159] M. Lin, T. Sudhiranjan, C. Boothroyd, and K. P. Loh, "Influence of Au catalyst on the growth of ZnS nanowires," *Chemical Physics Letters,* vol. 400, pp. 175-178, Dec 11 2004.

[160] X. Fan, X. M. Meng, X. H. Zhang, S. K. Wu, and S. T. Lee, "Formation of ZnS/SiO2 nanocables," *Applied Physics Letters,* vol. 86, pp. -, Apr 25 2005.

[161] A. M. Morales and C. M. Lieber, "A laser ablation method for the synthesis of crystalline semiconductor nanowires," *Science,* vol. 279, pp. 208-211, Jan 9 1998.

[162] S. Ravindran, S. Chaudhary, B. Colburn, M. Ozkan, and C. S. Ozkan, "Covalent coupling of quantum dots to multiwalled carbon nanotubes for electronic device applications," *Nano Letters,* vol. 3, pp. 447-453, Apr 2003.

[163] X. Michalet, F. F. Pinaud, L. A. Bentolila, J. M. Tsay, S. Doose, J. J. Li, G. Sundaresan, A. M. Wu, S. S. Gambhir, and S. Weiss, "Quantum dots for live cells, in vivo imaging, and diagnostics," *Science,* vol. 307, pp. 538-544, Jan 28 2005.

[164] H. Mattoussi, J. M. Mauro, E. R. Goldman, G. P. Anderson, V. C. Sundar, F. V. Mikulec, and M. G. Bawendi, "Self-assembly of CdSe-ZnS quantum dot bioconjugates using an engineered recombinant protein," *Journal of the American Chemical Society,* vol. 122, pp. 12142-12150, Dec 13 2000.

[165] M. E. Akerman, W. C. W. Chan, P. Laakkonen, S. N. Bhatia, and E. Ruoslahti, "Nanocrystal targeting in vivo," *Proceedings of the National Academy of Sciences of the United States of America,* vol. 99, pp. 12617-12621, Oct 1 2002.

[166] F. Patolsky, G. F. Zheng, and C. M. Lieber, "Nanowire-based biosensors," *Analytical Chemistry,* vol. 78, pp. 4260-4269, Jul 1 2006.

[167] R. S. Wagner and W. C. Ellis, "Vapor-Liquid-Solid Mechanism of Single Crystal Growth (New Method Growth Catalysis from Impurity Whisker Epitaxial + Large Crystals Si E)," *Applied Physics Letters,* vol. 4, pp. 89-&, 1964.

[168] E. I. Givargizov, "Fundamental Aspects of Vls Growth," *Journal of Crystal Growth,* vol. 31, pp. 20-30, 1975.

[169] J. W. Dailey, J. Taraci, T. Clement, D. J. Smith, J. Drucker, and S. T. Picraux, "Vapor-liquid-solid growth of germanium nanostructures on silicon," *Journal of Applied Physics,* vol. 96, pp. 7556-7567, Dec 15 2004.

[170] A. I. Persson, M. W. Larsson, S. Stenstrom, B. J. Ohlsson, L. Samuelson, and L. R. Wallenberg, "Solid-phase diffusion mechanism for GaAs nanowire growth," *Nature Materials,* vol. 3, pp. 677-681, Oct 2004.

[171] Y. W. Wang, L. D. Zhang, C. H. Liang, G. Z. Wang, and X. S. Peng, "Catalytic growth and photoluminescence properties of semiconductor single-crystal ZnS nanowires," *Chemical Physics Letters,* vol. 357, pp. 314-318, May 10 2002.

[172] Y. J. Li, L. P. You, R. Duan, P. B. Shi, H. L. Du, Y. P. Qiao, and G. G. Qin, "Straight ZnS nanobelts with wurtzite structure synthesized by the vapour phase transport process and their crystallization and photoluminescence properties," *Nanotechnology,* vol. 15, pp. 581-585, May 2004.

[173] Z. W. Wang, L. L. Daemen, Y. S. Zhao, C. S. Zha, R. T. Downs, X. D. Wang, Z. L. Wang, and R. J. Hemley, "Morphology-tuned wurtzite-type ZnS nanobelts," *Nature Materials,* vol. 4, pp. 922-927, Dec 2005.

[174] F. H. Chung, "Quantitative Interpretation of X-Ray-Diffraction Patterns of Mixtures .1. Matrix-Flushing Method for Quantitative Multicomponent Analysis," *Journal of Applied Crystallography,* vol. 7, pp. 519-525, 1974.

[175] A. V. Murugan, O. Y. Heng, V. Ravi, A. K. Viswanath, and V. Saaminathan, "Photoluminescence properties of nanocrystalline ZnS on nanoporous silicon," *Journal of Materials Science,* vol. 41, pp. 1459-1464, Mar 2006.

[176] M. Leone, S. Agnello, R. Boscaino, M. Cannas, and F. M. Gelardi, "Conformational disorder in vitreous systems probed by photoluminescence activity in SiO2," *Physical Review B,* vol. 60, pp. 11475-11481, Oct 15 1999.

[177] K. A. Dick, K. Deppert, T. Martensson, B. Mandl, L. Samuelson, and W. Seifert, "Failure of the vapor-liquid-solid mechanism in Au-assisted MOVPE growth of InAs nanowires," *Nano Letters,* vol. 5, pp. 761-764, Apr 2005.

[178] P. X. Gao, Y. Ding, and I. L. Wang, "Crystallographic orientation-aligned ZnO nanorods grown by a tin catalyst," *Nano Letters,* vol. 3, pp. 1315-1320, Sep 2003.

[179] P. X. Gao and Z. L. Wang, "Substrate atomic-termination-induced anisotropic growth of ZnO nanowires/nanorods by the VLS process," *Journal of Physical Chemistry B,* vol. 108, pp. 7534-7537, Jun 10 2004.

[180] S. Kodambaka, J. Tersoff, M. C. Reuter, and F. M. Ross, "Diameter-independent kinetics in the vapor-liquid-solid growth of Si nanowires," *Physical Review Letters,* vol. 96, pp. -, Mar 10 2006.

[181] J. D. Holmes, K. P. Johnston, R. C. Doty, and B. A. Korgel, "Control of thickness and orientation of solution-grown silicon nanowires," *Science,* vol. 287, pp. 1471-1473, Feb 2000.

[182] J. Westwater, D. P. Gosain, and S. Usui, "Si nanowires grown via the vapour-liquid-solid reaction," *Physica Status Solidi a-Applied Research,* vol. 165, pp. 37-42, Jan 1998.

[183] J. H. Song, X. D. Wang, E. Riedo, and Z. L. Wang, "Systematic study on experimental conditions for large-scale growth of aligned ZnO nanwires on nitrides," *Journal of Physical Chemistry B,* vol. 109, pp. 9869-9872, May 26 2005.

[184] S. J. Kwon and J. G. Park, "Theoretical analysis of the radius of semiconductor nanowires grown by the catalytic vapour-liquid-solid mechanism," *Journal of Physics-Condensed Matter,* vol. 18, pp. 3875-3885, Apr 2006.

[185] E. L. Cussler, *Diffusion : mass transfer in fluid systems*, 2nd ed. New York: Cambridge University Press, 1997.

[186] H. Y. Wang and G. S. Fischman, "Role Of liquid droplet surface-diffusion in the vapor-liquid-solid whisker growth mechanism," *Journal of Applied Physics,* vol. 76, pp. 1557-1562, Aug 1994.

[187] Y. W. Wang, V. Schmidt, S. Senz, and U. Gosele, "Epitaxial growth of silicon nanowires using an aluminium catalyst," *Nature Nanotechnology,* vol. 1, pp. 186-189, Dec 2006.

[188] M. Kirkham, X. D. Wang, Z. L. Wang, and R. L. Snyder, "Solid Au nanoparticles as a catalyst for growing aligned ZnO nanowires: a new understanding of the vapour-liquid-solid process," *Nanotechnology,* vol. 18, pp. -, Sep 12 2007.

[189] M. Z. D. Calestani, G. Salviati, L. Lazzarini, L. Zanotti, E. Comini, G. Sberveglieri, "Nucleation and growth of SnO2 nanowires," *Journal of Crystal Growth*
vol. 275, pp. e2083-e2087 February 15, 2005 2005.

[190] Y. Y. Wu and P. D. Yang, "Direct observation of vapor-liquid-solid nanowire growth," *Journal of the American Chemical Society,* vol. 123, pp. 3165-3166, Apr 4 2001.

[191] Z. W. Pan, Z. R. Dai, C. Ma, and Z. L. Wang, "Molten gallium as a catalyst for the large-scale growth of highly aligned silica nanowires," *Journal of the American Chemical Society,* vol. 124, pp. 1817-1822, Feb 27 2002.

[192] R. S. Yang and Z. L. Wang, "Interpenetrative and transverse growth process of self-catalyzed ZnO nanorods," *Solid State Communications,* vol. 134, pp. 741-745, Jun 2005.

[193] C. R. R. Ernest M. Levin, Howard F. McMurdie, "Phase Diagrams for Ceramists," 1964.

[194] W. L. N. Harold Kirkemo, and Roger P. Ashley, "Gold," *United States Geological Survey,* 1997.

[195] Z. L. Wang, "Nanostructures of Zinc Oxide " *Materialstoday,* pp. 26-33, June 2004 2004.

[196] Y. Ding, C. Ma, and Z. L. Wang, "Self-catalysis and phase transformation in the formation of CdSe nanosaws," *Advanced Materials,* vol. 16, pp. 1740-+, Oct 4 2004.

[197] P. Buffat and J. P. Borel, "Size Effect on Melting Temperature of Gold Particles," *Physical Review A,* vol. 13, pp. 2287-2298, 1976.

[198] J. P. v. d. E. a. O. S. L. Bruinsma, "Science and Technology of Crystal Growth," pp. 123-136, 1995.

[199] G. H. P. M. Swinkels, Kersten, H., Deutsch, H., Kroesen, G.M.W. , "Microcalorimetry of Dust Particles in a Radio-Frequency Plasma

" *Journal of Applied Physics,* vol. 88, pp. 1255-1747, 2000.

[200] A. Colli, S. Hofmann, A. C. Ferrari, C. Ducati, F. Martelli, S. Rubini, S. Cabrini, A. Franciosi, and J. Robertson, "Low-temperature synthesis of ZnSe nanowires and nanosaws by catalyst-assisted molecular-beam epitaxy," *Applied Physics Letters,* vol. 86, pp. -, Apr 11 2005.

[201] P. L. Gai, R. Sharma, and F. M. Ross, "Environmental (S)TEM studies of gas-liquid-solid interactions under reaction conditions," *Mrs Bulletin,* vol. 33, pp. 107-114, Feb 2008.

[202] J. G. Lee, H. Mori, and H. Yasuda, "In situ high-resolution electron microscope observation of phase change in nanometer-sized alloy particles," *Journal of Materials Research,* vol. 20, pp. 1708-1721, Jul 2005.

[203] H. Saka, T. Kamino, S. Arai, and K. Sasaki, "In situ heating transmission electron microscopy," *Mrs Bulletin,* vol. 33, pp. 93-100, Feb 2008.

[204] S. Kodambaka, J. Tersoff, M. C. Reuter, and F. M. Ross, "Germanium nanowire growth below the eutectic temperature," *Science,* vol. 316, pp. 729-732, May 4 2007.

[205] Y. Lilach, J. P. Zhang, M. Moskovits, and A. Kolmakov, "Encoding morphology in oxide nanostructures during their growth," *Nano Letters,* vol. 5, pp. 2019-2022, Oct 2005.

[206] S. V. Kalinin, J. Shin, S. Jesse, D. Geohegan, A. P. Baddorf, Y. Lilach, M. Moskovits, and A. Kolmakov, "Electronic transport imaging in a multiwire SnO2 chemical field-effect transistor device," *Journal of Applied Physics,* vol. 98, pp. -, Aug 15 2005.

[207] J. G. Fan, X. J. Tang, and Y. P. Zhao, "Water contact angles of vertically aligned Si nanorod arrays," *Nanotechnology,* vol. 15, pp. 501-504, May 2004.

[208] Y. Ding, P. X. Gao, and Z. L. Wang, "Catalyst-nanostructure interfacial lattice mismatch in determining the shape of VLS grown nanowires and nanobelts: A case of Sn/ZnO," *Journal of the American Chemical Society,* vol. 126, pp. 2066-2072, Feb 25 2004.

[209] M. T. Borgstrom, G. Immink, B. Ketelaars, R. Algra, and E. P. A. M. Bakkers, "Synergetic nanowire growth," *Nature Nanotechnology,* vol. 2, pp. 541-544, Sep 2007.

[210] S. Vaddiraju, A. Mohite, A. Chin, M. Meyyappan, G. Sumanasekera, B. W. Alphenaar, and M. K. Sunkara, "Mechanisms of 1D crystal growth in reactive vapor transport: Indium nitride nanowires," *Nano Letters,* vol. 5, pp. 1625-1631, Aug 2005.

[211] J. B. Hannon, S. Kodambaka, F. M. Ross, and R. M. Tromp, "The influence of the surface migration of gold on the growth of silicon nanowires," *Nature,* vol. 440, pp. 69-71, Mar 2006.

[212] X. D. Wang, C. J. Summers, and Z. L. Wang, "Large-scale hexagonal-patterned growth of aligned ZnO nanorods for nano-optoelectronics and nanosensor arrays," *Nano Letters,* vol. 4, pp. 423-426, Mar 2004.

[213] D. Stolcic, M. Fischer, G. Gantefor, Y. D. Kim, Q. Sun, and P. Jena, "Direct observation of key reaction intermediates on gold clusters," *Journal of the American Chemical Society,* vol. 125, pp. 2848-2849, Mar 12 2003.

[214] Q. Sun, P. Jena, Y. D. Kim, M. Fischer, and G. Gantefor, "Interactions of Au cluster anions with oxygen," *Journal of Chemical Physics,* vol. 120, pp. 6510-6515, Apr 8 2004.

[215] M. M. Maye, N. N. Kariuki, J. Luo, L. Han, P. Njoki, L. Y. Wang, Y. Lin, H. R. Naslund, and C. J. Zhong, "Electrocatalytic reduction of oxygen: Gold and gold-platinum nanoparticle catalysts prepared by two-phase protocol," *Gold Bulletin,* vol. 37, pp. 217-+, 2004.

[216] F. M. Ross, J. Tersoff, and M. C. Reuter, "Sawtooth faceting in silicon nanowires," *Physical Review Letters,* vol. 95, Sep 2005.

[217] X. L. Chen, Y. C. Lan, J. Y. Li, Y. G. Cao, and M. He, "Radial growth dynamics of nanowires," *Journal of Crystal Growth,* vol. 222, pp. 586-590, Jan 2001.

[218] X. H. Gao and S. M. Nie, "Molecular profiling of single cells and tissue specimens with quantum dots," *Trends in Biotechnology,* vol. 21, pp. 371-373, Sep 2003.

[219] B. A. Kairdolf, M. C. Mancini, A. M. Smith, and S. M. Nie, "Minimizing nonspecific cellular binding of quantum dots with hydroxyl-derivatizied surface coatings," *Analytical Chemistry,* vol. 80, pp. 3029-3034, Apr 15 2008.

[220] A. M. Smith, S. Dave, S. M. Nie, L. True, and X. H. Gao, "Multicolor quantum dots for molecular diagnostics of cancer," *Expert Review of Molecular Diagnostics,* vol. 6, pp. 231-244, Mar 2006.

[221] Y. Xing, T. Nomura, V. A. Odero-Marah, F. Habib, R. Wang, S. Nie, L. W. K. Chung, and H. E. Zhau, "Multiplexing quantum dot nanoparticles to detect epithelial to mesenchymal transition in human prostate cancer," *Journal of Urology,* vol. 175, pp. 267-267, Apr 2006.

[222] M. V. Yezhelyev, A. Al-Hajj, C. Morris, A. I. Marcus, T. Liu, M. Lewis, C. Cohen, P. Zrazhevskiy, J. W. Simons, A. Rogatko, S. Nie, X. Gao, and R. M. O'Regan, "In situ molecular profiling of breast cancer biomarkers with multicolor quantum dots," *Advanced Materials,* vol. 19, pp. 3146-+, Oct 19 2007.

[223] M. B. Ujiki, B. Milam, X. Z. Ding, A. B. Roginsky, M. R. Salabat, M. S. Talamonti, R. H. Bell, W. X. Gu, R. B. Silverman, and T. E. Adrian, "A novel peptide sansalvamide analogue inhibits pancreatic cancer cell growth through G0/G1 cell-cycle arrest," *Biochemical and Biophysical Research Communications,* vol. 340, pp. 1224-1228, Feb 24 2006.

[224] O. Salta, "Applications of nanoparticles in biology and medicine," *Journal of Nanobiotechnology,* vol. 2, April, 30 2004 2004.

[225] C. C. Berry, "Possible Exploitation of Magnetic Nanoparticle-Cell Interaction for Biomedical Applications," *Journal of Materials Chemistry,* vol. 15, pp. 543-547, 2005.

[226] R. Singh, D. Pantarotto, L. Lacerda, G. Pastorin, C. Klumpp, M. Prato, A. Bianco, and K. Kostarelos, "Tissue biodistribution and blood clearance rates of intravenously administered carbon nanotube radiotracers," *Proceedings of the National Academy of Sciences of the United States of America,* vol. 103, pp. 3357-3362, Feb 28 2006.

[227] S. Garibaldi, C. Brunelli, V. Bavastrello, G. Ghigliotti, and C. Nicolini, "Carbon nanotube biocompatibility with cardiac muscle cells," *Nanotechnology,* vol. 17, pp. 391-397, Jan 28 2006.

[228] J. S. Tsuji, A. D. Maynard, P. C. Howard, J. T. James, C. W. Lam, D. B. Warheit, and A. B. Santamaria, "Research strategies for safety evaluation of nanomaterials, part IV: Risk assessment of nanoparticles," *Toxicological Sciences,* vol. 89, pp. 42-50, Jan 2006.

[229] M. Bottini, S. Bruckner, K. Nika, N. Bottini, S. Bellucci, A. Magrini, A. Bergamaschi, and T. Mustelin, "Multi-walled carbon nanotubes induce T lymphocyte apoptosis," *Toxicology Letters,* vol. 160, pp. 121-126, Jan 5 2006.

[230] S. K. Manna, S. Sarkar, J. Barr, K. Wise, E. V. Barrera, O. Jejelowo, A. C. Rice-Ficht, and G. T. Ramesh, "Single-walled carbon nanotube induces oxidative stress and activates nuclear transcription factor-kappa B in human keratinocytes," *Nano Letters,* vol. 5, pp. 1676-1684, Sep 2005.

[231] K. Kostarelos, L. Lacerda, C. D. Partidos, M. Prato, and A. Blanco, "Carbon nanotube-mediated delivery of peptides and genes to cells: translating nanobiotechnology to therapeutics," *Journal of Drug Delivery Science and Technology,* vol. 15, pp. 41-47, Jan-Feb 2005.

[232] N. A. Monteiro-Riviere, R. J. Nemanich, A. O. Inman, Y. Y. Y. Wang, and J. E. Riviere, "Multi-walled carbon nanotube interactions with human epidermal keratinocytes," *Toxicology Letters,* vol. 155, pp. 377-384, Mar 15 2005.

[233] D. X. Cui, F. R. Tian, C. S. Ozkan, M. Wang, and H. J. Gao, "Effect of single wall carbon nanotubes on human HEK293 cells," *Toxicology Letters,* vol. 155, pp. 73-85, Jan 15 2005.

[234] Y. Lin, S. Taylor, H. P. Li, K. A. S. Fernando, L. W. Qu, W. Wang, L. R. Gu, B. Zhou, and Y. P. Sun, "Advances toward bioapplications of carbon nanotubes," *Journal of Materials Chemistry,* vol. 14, pp. 527-541, Feb 21 2004.

[235] G. Jia, H. F. Wang, L. Yan, X. Wang, R. J. Pei, T. Yan, Y. L. Zhao, and X. B. Guo, "Cytotoxicity of carbon nanomaterials: Single-wall nanotube, multi-wall nanotube, and fullerene," *Environmental Science & Technology,* vol. 39, pp. 1378-1383, Mar 1 2005.

[236] M. Z. Atashbar, B. E. Bejcek, and S. Singamaneni, "Carbon nanotube network-based biomolecule detection," *Ieee Sensors Journal,* vol. 6, pp. 524-528, Jun 2006.

[237] L. Q. Guo, R. Wang, H. M. Xu, and J. Liang, "Measuring the adhesion forces of ligand-receptor bonds using functionalized carbon nanotube atomic force microscopic tips," *Chinese Journal of Analytical Chemistry,* vol. 34, pp. 359-361, Mar 2006.

[238] B. J. Hinds, N. Chopra, T. Rantell, R. Andrews, V. Gavalas, and L. G. Bachas, "Aligned multiwalled carbon nanotube membranes," *Science,* vol. 303, pp. 62-65, Jan 2 2004.

[239] P. Nednoor, N. Chopra, V. Gavalas, L. G. Bachas, and B. J. Hinds, "Reversible biochemical switching of ionic transport through aligned carbon nanotube membranes," *Chemistry of Materials,* vol. 17, pp. 3595-3599, Jul 12 2005.

[240] J. Wang, G. D. Liu, M. R. Jan, and Q. Y. Zhu, "Electrochemical detection of DNA hybridization based on carbon-nanotubes loaded with CdS tags," *Electrochemistry Communications,* vol. 5, pp. 1000-1004, Dec 2003.

[241] S. Woo, Y. Lee, V. Sunkara, R. K. Cheedarala, H. S. Shin, H. C. Choi, and J. W. Park, ""Fingertip"-Guided noncovalent functionalization of carbon nanotubes by dendrons," *Langmuir,* vol. 23, pp. 11373-11376, Nov 6 2007.

[242] J. R. Wolpaw and e. al., "Brain-computer interfaces for communication and control," *Clinical Neurophysiology,* vol. 113, pp. 767-791, 2002.

[243] J. W. B. R. A. Andersen, S. Musallam, B. Pesaran, J. G. Cham, "Cognitive Neural Prosthetics," *TRENDS in cognitive science,* vol. 8, pp. 486-493, November 2004 2004.

[244] A. Kubler, N. Neumann, B. Wilhelm, T. Hinterberger, and N. Birbaumer, "Brain-computer predictability of brain-computer communication," *Journal of Psychophysiology,* vol. 18, pp. 121-129, 2004.

[245] M. A. L. Nicolelis, "Actions from Thoughts," *Nature,* vol. 409, pp. 403-407, 2004.

[246] J. D. Millan and J. Mourino, "Asynchronous BCI and local neural classifiers: An overview of the adaptive brain interface project," *Ieee Transactions on Neural Systems and Rehabilitation Engineering,* vol. 11, pp. 159-161, Jun 2003.

[247] M. J. S. Eleanor A. Curran, "Learning to control brain activity: A review of the production and control of EEG components for driving brain-computer interface (BCI) systems," *Brain and Cognition,* vol. 51, pp. 326-336, 2002.

[248] M. A. L. N. Dana Cohen, "Reduction of Single-Neuron Firing Uncertainty by Cortical Ensembles during Motor Skill Learning," *The Journal of Neuroscience,* vol. 24, pp. 3574-3582, 2004.

[249] Y.-T. Kim, "Chronic response of adult rat brain tissue to implants anchored to the skull," *Biomaterials,* vol. 25, pp. 2229-2237, 2004.

[250] J. P. Donoghue, "Connecting cortex to machines: recent advances in brain interfaces," *Nature Neuroscience Suppliment,* vol. 5, pp. 1085-1088, 2002.

[251] D. Graham-Rowe, "Moving brain implant seeks out signals," *Newscientist.com,* 2004.

[252] Y. W. Wang, G. W. Meng, L. D. Zhang, C. H. Liang, and J. Zhang, "Catalytic growth of large-scale single-crystal CdS nanowires by physical evaporation and their photoluminescence," *Chemistry of Materials,* vol. 14, pp. 1773-1777, Apr 2002.

[253] Z. L. Wang, X. Y. Kong, Y. Ding, P. X. Gao, W. L. Hughes, R. S. Yang, and Y. Zhang, "Semiconducting and piezoelectric oxide nanostructures induced by polar surfaces," *Advanced Functional Materials,* vol. 14, pp. 943-956, Oct 2004.

VITA

JENNY RUTH MORBER

J. MORBER was born in St. Louis, Missouri to Nancy and Keith Harrison, but her family moved to Mobile Alabama before she entered primary school. There she attended both public and private facilities and spent many happy days along the coast. Apparently fortunate to have escaped from Alabama without a noticeable accent and with a few pairs of decent shoes, she then attended the Georgia Institute of Technology, where she received a BS in Materials Science and Engineering, *magna cum laude*. Having gained useful undergraduate research experience, she remained at Georgia Tech to pursue her doctorate. Her initial motivation to study nanoscience stemmed from her curiosity regarding the unusual behaviors of once familiar materials, and her desire to help put these to good use. She continues to be generally fascinated by the way the world works. When she is not working on research she can usually be found outdoors with her husband and two dogs. She also enjoys reading, painting, writing, and training for athletic events. Most recently she has been incubating another human and looking forward to her status as “doctor.”